Title

Identification of Features of Response and Resistance to Anti-Programmed-Death-1 Immunotherapy in Melanoma

Author

Zaretsky, Jesse Meir

Publication Date

2017

UNIVERSITY OF CALIFORNIA

Los Angeles

Identification of Features of Response and Resistance to Anti-Programmed-Death-1 Immunotherapy in Melanoma

A dissertation submitted in partial satisfaction of the requirements for the degree

Doctor of Philosophy in Molecular and Medical Pharmacology

by

Jesse Meir Zaretsky

2017

ABSTRACT OF THE DISSERTATION

Identification of Features of Response and Resistance to Anti-Programmed-Death-1 Immunotherapy in Melanoma

by

Jesse Meir Zaretsky

Doctor of Philosophy in Molecular and Medical Pharmacology

University of California, Los Angeles, 2017

Professor Antoni Ribas, Chair

Checkpoint blockade immunotherapy takes advantage of an endogenous anti-cancer immune response and promotes tumor killing by altering the balance of signals that control T-cell activity. Dramatic and durable responses have led to FDA approvals for anti-programmed-death-1 (anti-PD1) therapy across a broad range of cancer types, however only a fraction of patients benefit and some with an initial response will later progress. The specific mechanisms of tumor-immune evasion or resistance in this setting are not well established, but understanding them will be critical for accurate prognosis, proper therapy selection, and identification of next-generation drug targets.

To investigate mechanistic correlates of anti-PD1 response and resistance in melanoma, we used high-throughput sequencing to analyze genomic, transcriptomic, and T-cell data in whole-tumor biopsies and early passage cell lines from 1) longitudinally sampled lesions from patients with an initial response followed by late progression (acquired resistance) and 2) pre-treatment lesions in cohorts of patients with or without response (primary resistance).

Whole exome sequencing from four cases of late acquired resistance revealed evidence of *in-situ* clonal selection for new homozygous loss-of-function mutations in the interferon-receptor associated kinases JAK1 and JAK2 and in beta-2-microglobulin (B2M, a co-factor required for class I antigen presentation). These JAK mutations abolished sensitivity to interferon-gamma (IFNγ), including IFNγ-induced PD-L1 expression and growth arrest. In complementary work, we evaluated the frequency of interferon insensitivity (or lack of PD-L1 inducibility) and interferon pathway mutations in PD1-therapy naïve cohorts. Among the handful of JAK homozygous loss-of-function mutations we identified from patients with response data, all were found in non-responders.

Two other retrospective cohort studies revealed additional response-correlated insights. Transcriptomic data from pre-treatment biopsies showed enrichment for a coordinated set of genes associated with epithelial-to-mesenchymal transition (EMT), wound-healing, angiogenesis, and hypoxia in PD1 non-responders. By contrast, we found the rare desmoplastic melanoma subtype (DM) was unusually sensitive to anti-PD1 therapy, with a 70% response rate double that of unselected cutaneous melanoma. While often a histological diagnosis, we observed our DM cohort was characterized by a high mutational load and NF1 driver subtype.

Finally, we worked with colleagues at Caltech on enabling studies with a new technology for sensitive identification of neo-antigen specific T-cell responses that is optimized for downstream T-cell capture and receptor cloning. Here, the goal was to aid in assessment of the diversity and dynamics of defined tumor antigen-specific T-cells and to allow for their ex-vivo production.

The dissertation of Jesse Meir Zaretsky is approved.

Thomas G. Graeber

Roger S. Lo

Michael Alan Teitell

Owen N. Witte

Antoni Ribas, Committee Chair

University of California, Los Angeles

2017

TABLE OF CONTENTS

List of Figures

Chapter 1

Chapter 2

Chapter 3

Chapter 4

Chapter 5

Chapter 6

List of Tables

Chapter 1

Chapter 2*

Chapter 3

Chapter 4

Chapter 5*

Chapter 6

*Tables for these chapters attached as excel spreadsheets, page number indicates first reference

Acknowledgments

First and foremost, I would like to thank my mentor Dr Antoni Ribas for his unwavering support and guidance that significantly pre-dates my time in the lab, and that has grown with new challenges and opportunities that I did not dream were possible at the start. Toni, your trust, encouragement and optimism, indefatigable work ethic, collaborative spirit, and kindness and respect for your patients and colleagues inspires those of us who work with you and sets a superb example that I strive to emulate.

I owe an enormous debt of gratitude to members of the Ribas lab (past and present), the Lo lab, Graeber lab, the team at the UCLA sequencing Core, my committee, and my collaborators across campus, at Caltech, and at other institutions near and far. I won't/can't name every name, but you know who you are. Iron sharpens iron, and I am moved by both the academic richness of our interactions and the new friendships developed along the way.

To my family (Mom, Dad, Abbie, Kaile, and Marcelo) and my dear friends, thank you for your patience and understanding, for the balance you bring to my life, and for keeping me humble; Brian gets special mention for asking, "So have you cured cancer yet?" every time we meet.
I love you all, far more that I probably usually express.

Finally, I need to thank the patients and their families whom I consider true partners in research, and the funding sources that have supported me and our lab and make this work possible, including the National Institute of Health via the UCLA Medical Scientist Training Program Training Grant (GM08042) and grant R35 CA197633 to Antoni Ribas, the Grimaldi Family

Fund , the Garcia-Corsini Family Fund, Stand Up to Cancer, the Parker Institute for Cancer Immunotherapy, and the American Association for Cancer Research.

Chapter 1 contains a figure reproduced with permission from “Oncology meets immunology: the cancer-immunity cycle” published in *Immunity*. Copyright Elsevier.

Chapter 2 was reproduced with permission from Zaretsky JM, Garcia-Diaz A, Shin DS et al, Mutations associated with acquired resistance 22 to anti-PD1 immunotherapy in melanoma. *New Engl J Med* (2016) 375(9):819-29, Copyright Massachusetts Medical Society.

Chapter 3 was reproduced with permission Shin DS, Zaretsky JM, Escuin-Ordinas H, et al, Primary Resistance to PD-1 Blockade Mediated by JAK1/2 Mutations. *Cancer Discov* (2017) 7(2):188-201.

Chapter 4 is adapted from “High response rate to PD-1 blockade in desmoplastic melanomas” by Zeynep Eroglu*, Jesse M. Zaretsky*, Siwen Hu-Lieskovan*ɣ, Dae Won Kim, Alain Algazi, Douglas B. Johnson, Elizabeth Liniker, Ben Kong, Rodrigo Munhoz, Suthee Rapisuwon, Pier Federico Gherardini, Bartosz Chmielowski, Xiaoyan Wang, I. Peter Shintaku, Cody Wei, Jeffrey A. Sosman, Richard Joseph, Michael A. Postow, Jane Messina, Richard A. Scolyer, Alistair J. Cochran, Matteo S Carlino, Wen-Jen Hwu, Georgina V. Long, Antoni Ribas ɣ
Submitted to *Nature* May 2017

Chapter 5 was reproduced with permission from Hugo W*, Zaretsky JM*, Sun L, et al. Genomic and transcriptomic features of response to anti-PD-1 therapy in metastatic melanoma. *Cell* (2016) 165(1):35-44. Copyright Elsevier.

Chapter 6 is adapted from “Sensitive, non-destructive detection and analysis of neoantigen-specific T cell populations from tumors and blood”, by Songming Peng*, Jesse M. Zaretsky*, Michael T. Bethune, Alice Hsu, Elizabeth Holman, Xiaozhe Ding, Katherine Guo, Jungwoo Kim, Alexander M. Xu, John E. Heath, Won Jun Noh, Jing Zhou, Yapeng Su, Jami McLaughlin, Donghui Cheng, Owen N. Witte, David Baltimore, Antoni Ribas, and James R. Heath ɣ
Submitted to *Cell* April 2017

*Equal contribution as first authors, ɣ corresponding authors

VITA

EDUCATION

2011-Current	David Geffen School of Medicine at UCLA Medical Scientist Training Program Department of Molecular and Medical Pharmacology Expected date of completion 2019 MD matriculation 2011 PhD matriculation 2013
2005 to 2009	University of California, Los Angeles B.S. in Microbiology, Immunology and Molecular Genetics Minor in Biomedical Research College Honors, Magna Cum Laude

HONORS AND AWARDS

2017	American Association for Cancer Research Next Gen Star Award
2016	UCLA Molecular and Medical Pharmacology Retreat Prize for Oral Presentation
2007-2009	Howard Hughes Medical Institute Undergraduate Research Program, UCLA

PRESENTATIONS

Oral Presentations:

2017
CRI-CIMT-EATI-AACR International Cancer Immunotherapy Conference
(Upcoming 09/2017), Frankfurt, Germany
AACR National Meeting, Major Symposium, Next Gen Star Award
Molecular Medicine Tri Conference

2016
UCLA Molecular and Medical Pharmacology Departmental Retreat

2014-2016
UCLA Engineered Immunity Consortium Quarterly Retreats

Poster Presentations:

2016
UCLA Molecular and Medical Pharmacology Retreat
2015
American Society of Clinical Oncology (ASCO) National Meeting, Chicago IL
UCLA Molecular and Medical Pharmacology Departmental Retreat

PUBLICATIONS

A Garcia-Diaz, DS Shin, BH Moreno, J Saco, H Escuin-Ordinas, GA Rodriguez, **JM Zaretsky**, L Sun, W Hugo, X Wang, G Parisi, CP Saus, DY Torrejon, TG Graeber, B Comin-Anduix, S Hu-Lieskovan, R Damoiseaux, RS Lo, A Ribas. Interferon Receptor Signaling Pathways Regulating PD-L1 and PD-L2 Expression.. *Cell Rep* **19**, 1189-1201 (2017).

DS Shin, **JM Zaretsky**, H Escuin-Ordinas, A Garcia-Diaz, S Hu-Lieskovan, A Kalbasi, CS Grasso, W Hugo, S Sandoval, DY Torrejon, N Palaskas, GA Rodriguez, G Parisi, A Azhdam, B Chmielowski, G Cherry, E Seja, B Berent-Maoz, IP Shintaku, DT Le, DM Pardoll, LA Jr Diaz, PC Tumeh, TG Graeber, RS Lo, B Comin-Anduix, A Ribas. Primary Resistance to PD-1 Blockade Mediated by JAK1/2 Mutations.. *Cancer Discov* **7**, 188-201 (2017).

Moreno B Homet, **JM Zaretsky**, A Garcia-Diaz, J Tsoi, G Parisi, L Robert, K Meeth, A Ndoye, M Bosenberg, AT Weeraratna, TG Graeber, B Comin-Anduix, S Hu-Lieskovan, A Ribas. Response to Programmed Cell Death-1 Blockade in a Murine Melanoma Syngeneic Model Requires Costimulation, CD4, and CD8 T Cells.. *Cancer Immunol Res* **4**, 845-857 (2016).

JM Zaretsky, A Garcia-Diaz, DS Shin, H Escuin-Ordinas, W Hugo, S Hu-Lieskovan, DY Torrejon, G Abril-Rodriguez, S Sandoval, L Barthly, J Saco, Moreno B Homet, R Mezzadra, B Chmielowski, K Ruchalski, IP Shintaku, PJ Sanchez, C Puig-Saus, G Cherry, E Seja, X Kong, J Pang, B Berent-Maoz, B Comin-Anduix, TG Graeber, PC Tumeh, TN Schumacher, RS Lo, A Ribas. Mutations Associated with Acquired Resistance to PD-1 Blockade in Melanoma.. *N Engl J Med* **375**, 819-29 (2016).

W Hugo*, **JM Zaretsky***, L Sun, C Song, BH Moreno, S Hu-Lieskovan, B Berent-Maoz, J Pang, B Chmielowski, G Cherry, E Seja, S Lomeli, X Kong, MC Kelley, JA Sosman, DB Johnson, A Ribas, RS Lo. Genomic and Transcriptomic Features of Response to Anti-PD-1 Therapy in Metastatic Melanoma..*Cell* 165, 35-44 (2016).

A Ribas, DS Shin, **J Zaretsky**, J Frederiksen, A Cornish, E Avramis, E Seja, C Kivork, J Siebert, P Kaplan-Lefko, X Wang, B Chmielowski, JA Glaspy, PC Tumeh, T Chodon, D Pe'er, B Comin-Anduix. PD-1 Blockade Expands Intratumoral Memory T Cells.. *Cancer Immunol Res* **4**, 194-203 (2016).

A Snyder, V Makarov, T Merghoub, J Yuan**, JM Zaretsky**, A Desrichard, LA Walsh, MA Postow, P Wong, TS Ho, TJ Hollmann, C Bruggeman, K Kannan, Y Li, C Elipenahli, C Liu, CT Harbison, L Wang, A Ribas, JD Wolchok, TA Chan. Genetic basis for clinical response to CTLA-4 blockade in melanoma.. *N Engl J Med* 371, 2189-99 (2014).

Call GB, Olson JM, Chen J, Villarasa N, Ngo KT,…**Zaretsky JM**.. et al 2007 Genome wide clonal analysis of lethal mutations in the Drosophila melanogaster eye: comparison of the X chromosome and autosomes *Genetics*. 177(2):689-97 (2007)

* equal contribution

Chapter 1:
Introduction

1. Anti-PD-1 checkpoint blockade in the clinic

Melanoma is predicted to be responsible for 9730, or 1.6% of all cancer deaths in 2017, and the 5-year survival rate between 2007 and 2013 for Stage IV metastatic disease was 16% [1]. Melanoma has historically been resistant to chemotherapy, and the development of target therapy for BRAF mutant melanoma marked a revolution in the field, with combination BRAF + MEK inhibitors currently achieving ~70% overall response rates (ORR) and estimated 3-year progression free/overall survival (PFS/OS) of ~20%/42% respectively [2]. Melanoma was also one of the first to be identified as sensitive to immunotherapy. High dose IL-2 and interferon alpha (IFNa) were FDA approved based on their ability to produce dramatic tumor regression and durable response in a small number of patients, with long experience at the NIH yielding 49-72% overall response rate (ORR) and 22% complete responses (CR) in patients with bulky, naturally immunogenic tumors amenable to in-vitro expansion of autologous tumor-infiltrating lymphocytes (TILs)[3].

Checkpoint inhibitor therapy blocks the interaction between T-cells and suppressive ligands, which reinvigorates their anti-tumor activity. Ipilimumab, a monoclonal anti-CTLA4 antibody, was the first approved checkpoint inhibitor and is similarly to IL-2/IFNa therapy with respect to low response rate (~10%) effecting durable control, but produced less toxicity. In a meta-analysis of 4846 patients from the ipilimumab clinical trials and expanded access program, median OS was 9.5 months with 21% 3-year survival and a notable plateau in survival at 3 years [4].

Anti-PD1 checkpoint inhibitor therapy significantly improved upon those response rates, and monotherapy with pembrolizumab or nivolumab produces objective responses (RECIST complete or partial response, >30% tumor reduction) of between 22-40% in melanoma, while combination anti-PD1/anti-CTLA4 therapy pushes the ORR to 58% (Table 1). Subgroups at the higher end of the response range include treatment-naive, Stage M1b disease, and smaller tumor burden [5], and pooled meta-analysis showed no difference in response between BRAF WT and BRAF mutant melanoma [6]. Responses are also durable, and in two studies with extended follow-up data (median 21 and 24 months), 74% and 80% of patients with an initial response remained progression-free [5, 7].

The promise of anti-PD1 immunotherapy lies not only in the high frequency and long durability of responses, but also in its broad applicability to other cancer types, though response rate vary widely. To date, FDA approval has been granted for non-small-cell lung cancer (20% ORR, 45% ORR if PD-L1+), squamous head and neck cancer (13.3-16% ORR), Hodgkin lymphoma (ORR 65-69%), renal cell carcinoma (ORR 21.5%), and urothelial carcinoma (ORR 19.6%). Clinical trials are underway in gastric, liver, thymic, breast, brain, and MSI-high colorectal cancers, and a recent pre-clinical study showed promising synergistic effects between tyrosine kinase, PI3K/mTOR, and checkpoint inhibitors in a mouse model of castration-resistant prostate cancer [8].

While these results represent a seismic shift in onclogic practice, the majority of patients still do not respond to immunotherapy, and our ability to predict response is poor. Additionally, some patients (currently 25-30% at 2 years) with objective tumor response eventually develop progressive disease. Greater mechanistic insight into tumor, T-cell, and microenvironment interactions will be required to identify reliable biomarkers, and rationally design second generation combination therapies that broaden response rate and act synergistically to prevent escape and recurrence.

Table 1 Summary of Objective Response Rate in anti-PD1 clinical trials

Drug	Study	Selection Criteria	% BRAF WT	Phase	Control	**# PD1 tx**	**ORR**	Control ORR	**Response Ongoing @ 2yrs**	Refs
Nivo	CA209-003	NA	NA	I	NA	107	31%	NA	58%	[9]; [10]
Pembro	Keynote-001	NA	78%	I	NA	581	33%	NA	75%	[5]
Pembro	Keynote-002	Ipi pre-tx	77%	II	Chemo	361	23%	4%	N A	[11]
Nivo	Checkmate-037	Ipi pre-tx	78%	III	Chemo	120	32%	10%	NA	[12]
Pembro	Keynote-006	NA	65%	III	Ipi	556	33%	13%	NA	[13]
Nivo	Checkmate-066	Tx naive	100%	III	Chemo	210	40%	14%	NA	[14]
Nivo + Ipi	Checkmate-69	Tx naive	77%	II	Ipi	95	59%	11%	80%	[15]; [7]
Nivo + Ipi	Checkmate-067	Tx naive	68%	III	Nivo,Ipi	314	57.6%	44%	NA	[16]

2. Tumor-immune dynamics in the tumor microenvironment

Generation of an effective anti-tumor T-cell response depends on antigen presentation and recognition by T-cells in the context of co-stimulatory activation signals, trafficking to target site, and interaction with the target tumor cell and killing. This process has been called the "cancer immunity cycle" [17] (Figure 1). However tumor, stromal, and other immune cells react to and alter T-cell activity in complex positive and negative feedback loops, and the dynamics between tumor elimination, equilibrium, and escape define the immunoediting process [18].

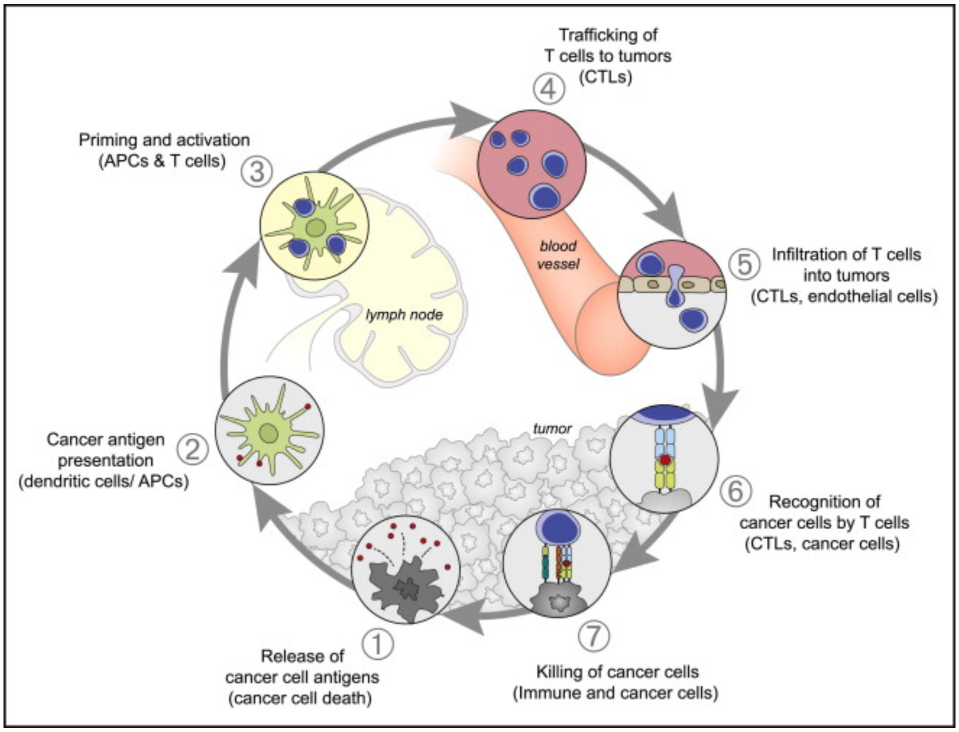

Figure 1. The Cancer-Immunity Cycle, Reprinted from DS Chen et al 2013, with kind permission from Elsevier, USA, copyright 2013

2-1. T-cell recognition of tumor antigens

Recognition of tumor antigens presented in a peptide-MHC complex is required for initial T-cell activation and again on their target cells for direct killing. Antigens can be derived from over-expressed differentiation-specific proteins (MART-1, tyrosinase), aberrantly re-expressed following de-differentiation and/or epigenetic dysregualtion (embryonic or testes-specific antigens, i.e. NY-ESO1, CEA), viral-derived proteins (from HPV- or EBV-related cancers), or mutated endogenous proteins.

However, studies in humans have suggested that T-cell responses to known “shared” antigens occur at relatively low frequency, and currently mutated “neo-antigens” are thought to play a larger role. Methylcolanthrene-induced tumors in syngeneic mouse models have used for almost 30 years to prove the immunogenicity of mutated proteins, and mutant-peptide vaccine is able to provide protection against tumor challenge in mice. [19-21].   Whole-exome sequencing (WES) has made identification of mutant neoantigen candidates a high throughput endeavor. [21-23], but identification of the antigens actually recognized by T-cells still remains a challenge. Initial brute force methods for screening include transfection of autologous or HLA-matched APCs with a tumor-derived cDNA library or collections of synthetic tandem mini-genes encoding peptides from all identified mutations [24]. Hits are identified by target cell lysis or IFN-gamma production after T-cell/APC co-culture. Alternatively, mutant-peptide binding to MHC can be predicted by trained machine learning algorithms as a first proxy for antigenic potential [25], along with RNA expression cutoffs and/or proteosmal cleavability scoring [26]. Then a subset of ranked candidates can be made into peptide-MHC tetramers and screened for T-cell binding [27]. While potentially enriching for positive hits, the false-negative rate from this approach is unknown, and a multi-center collaborative study through the Parker Institute for Cancer

Immunotherapy is currently underway to test the efficacy of various algorithms. Both co-culture and pMHC methods require screening of T-cells, and use of expanded or unexpanded T-cells from TIL, leukaphoresis, or routine blood draw depends on assay sensitivity and throughput.

Neoantigen responses in humans have now been been identified and proven therapeutically in relevant in TIL therapy and checkpoint blockade [28-30]. Even adoptive transfer of T-cells with a single predominant specificity have been shown to produce substantial tumor regression and long term remission [31, 32]. However, immune-selective pressure for antigen loss is a significant risk. This has been seen in melanoma de-differentiation following ACT with MART-1-specific TCRs [33]. Pre-existing heterogeneity or continued tumor evolution (DNA level copy loss, epigenetic/expression changes) may also allow tumors to escape depending on the penetrance (trunk vs clonal branches) and diversity of the antigens recognized [34-36]. Loss of passenger mutations may not carry much fitness cost for a tumor, and so finding or engineering T-cell responses to core driver mutations may be advantageous. However these too can be escaped by loss/downregulation of the presenting HLA allele as was seen for responses against a KRAS G12D mutation [31]. In general, loss of HLA or genes involved in antigen presentation (B2M, TAP1/2) has long been hypothesized to lead to tumor immune escape [37-38].

Checkpoint blockade is a systemic, non-specific therapy whose main toxicity is the awakening of cryptic auto-immune responses. Though typically manageable, these often carry significant morbidity. There is therefore a strong rational basis for engineering a defined neo-antigen specific (and therefore tumor-specific) response against multiple targets and spread over mutliple HLA-specificities within a patient. This is currently being pursued in Phase I clinical trial as a vaccine (NEO-PV-01, NCT01970358). The effectiveness of a vaccine will depend on a robust endogenous immune response. Therefore there may be indication for an expanded, neo-antigen selected TIL-based ACT (NEO-PTC-01) or TCR-engineered ACT of defined T-cell dose and phenotype.

2-2. T-cell activation and functional phenotype

The presence of activated T-cells at the tumor margin long been associated with increased survival in many cancer types, and was one of the first positive prognostic markers for response to anti-PD-1 therapy [39]. Assuming that a T-cell exists with tumor-antigen-specific TCR, the process of T-cell activation and licensure for killing is finely controlled by a dynamic interplay between T-cell intrinsic and extrinsic positive and negative feedback signals. It is the balance of these signals that contributes to the equilibrium and escape phases of immunoediting, and that is manipulated by checkpoint blockade therapy.

Naive T-cells are primed for killing by TCR binding to peptide-MHC (signal 1) and co-stimulation from CD28-CD80/86 interaction (signal 2). This initial activation then induces the upregulates of a host of further co-stimulatory receptors (ICOS, 4-1BB, CD137, OX40, GITR), or co-inhibitory molecules (CTLA4, PD1, TIM3, LAG3, BTLA, VISTA, etc.) [40], almost all of which are being targeted for clinical development [41]. CTLA4 is thought to compete with CD28 for CD80/86 binding, but PD1's mechanism of action is still under active investigation. One recent study suggests that upon ligation PD1 recruits SHP2 phosphatase which preferentially dephosphorylates and inactivates CD28 rather than TCR signaling as previously thought [42]. Two reports using the chronic LCMV infection model (where T-cell exhaustion was first described) showed that CD28 was required for PD1 blockade based re-invigoration [43], and that a PD1+ CXCR5+ stem-like T-cell population with high expression of memory makers and co-stimulatory molecules (including CD28) selectively proliferate after PD-1 therapy [44]. This is consistent with work in mouse models from our lab and others that showed lack of dendritic cells activity impaired anti-PD1 tumor control [45-47, 22]. However, PD-L1 knockout specifically within tumor cells also abolishes tumor control by anti-PD1 therapy, re-affirming the importance of direct PD1/PD-L1 interactions between the T-cell and the tumor [48, 49].

Data on the phenotype of *human* tumor-reactive T-cells indicates that antigen-specific TILs are PD1+, LAG3+ , TIM3+, undergo oligoclonal expansion, and were responsible for killing upon co-culture rather than PD1-negative TIL [50]. These PD1+ antigen specific TIL can make up 32-75% of the CD8+ TIL population. Similarly, CD8+, PD1+ T-cells in the peripheral blood were also found to be tumor-reactive, though present at much lower frequency (<5%) and lacking co-expression of LAG3/TIM3 [51]. And finally, data from a prospective human anti-PD1 clinical trial in melanoma showed these CD8+ PD1+ peripheral T-cells population become Ki67+ at high frequency upon anti-PD1 therapy [52].

2-3. Interferon gamma control of pro-and anti-inflammatory signals in the tumor microenvironment

Interferon gamma (IFNγ) is produced by activated T-cells and is often used as the primary marker of T-cell activation. Similar to the the way T-cell activation simultaneously upregulates co-inhibitory receptors, interferon gamma induces both pro- and anti-inflammatory gene programs. The IFN-gamma receptor (IFNGR) is expressed on almost all nucleated cells, including tumor cells from diverse cancer types [53]. However CD8+ and Th1 CD4+ T-cells themselves lack INFGR2 expression. The IFNGR1/2 complexes with the JAK1 and JAK2 kinases to activate STAT transcription factors (primarily STAT1 homodimers) which in turn induce Interferon Regulatory Factors (IRFs). IFNγ has direct pro-apoptotic/anti-proliferative effects on target cells, while its pro-inflammatory effects include promoting Th1 type CD4 helper differentiation, enhancing antigen presentation through MHC and TAP1 upregulation, and inducing chemokine (CXCL9, 10, 11) and ICAM expression for T-cell recruitment [53]. Anti-inflammatory effects of IFNg include: upregulation of IDO to degrades tryptophan, an essential nutrient for T-cell proliferation; SOCS1 which helps tag JAKs for ubiquitin-mediated degredation; and CSF1 which recruits suppressive tumor-associated macrophages that impair immunotherapy[54].

However one of the most important negative regulatory effects of IFNγ is the induction of PD-L1. This co-dependent T-cell/target cell negative feedback mechanism is termed adaptive immune resistance [55]. In the immuno-editing process, early studies showed MCA-induced sarcomas rejected by wild-type mice would grow if either the tumor or host mouse was interferon gamma insensitive [56], highlighting the role of IFNγ in acute tumor elimination. However, in the equilibrium and escape phase, where cancer is more akin to a chronic infection, induction of PD-L1 may play the larger role. In the following chapters, we present evidence that when PD-1 blockade re-activates the anti-tumor immune response, the cancer-immunity cycle is reset and acquired interferon-insenitivity can make make melanoma resistant to elimination.

Many of these features of the cancer-immune cycle (Figure 1) have been incorporated into a “cancer immunogram” that provides a framework for integrating individual biomarkers into a snapshot of tumor-immune status[57].

3. Clinical biomarkers of response and resistance to PD-1 blockade

Despite decades of research into anti-tumor immunity and our current understanding of immune biology, few biomarkers have emerged for determining response or resistance to immunotherapy, and only one has entered clinical practice.

3.1 Mutational load

High mutational load was predicted to be favorable marker by increasing the chances for T-cell neoepitope recognition. Mutational load differences are also often discussed as a possible explanation for the different immune-responsiveness between cancer types. Indeed, high mutational load correlates with response and longer survival in CTLA4-treated melanoma[58], PD-1 treated lung cancer[28], and PD1-treated MSI-high colorectal cancer[59]. Yet while mutational load trended with PD1 response in two studies of PD1-treated melanoma it did not reach statistical significance in either [60,61]. Furthermore, while there was a difference in population mean in all these studies, no cutoff gave good positive or negative predictive value, and high mutational load nonresponders and low mutational load responders were frequently observed.

3.2 Inflamed Microenvironment

Several factors that together suggest an inflamed tumor environment are also predictive of response. T-cell infiltration has been a positive prognostic factor for survival in many cancer types even before the widespread use of immunotherapy. Our group showed an association between response to PD1 therapy in melanoma and the presence of infiltrating, clonally expanded T-cells [39] while markers of T-cell activity, including RNA expression of a two gene proxy (Granzyme A, Perforin) or a 28-gene IFNγ -related RNA signature correlated with better survival across many TCGA cancer types and with clinical benefit to anti-PD1 therapy in melanoma, head and neck, and gastric cancer [62, 63]. Notably early on-treatment measurement of these markers in melanoma showed an even stronger association, with less overlap between responders/nonresponders than at baseline[64].

3.3 PD-L1 Expression

Logically, PD-L1 expression is generally correlated with response to PD1 blockade, and PD-L1 positive lung cancer and melanoma showed response rates >40% vs ~11% for PD-L1 negative tumors in two large representative clinical trials [65, 16]. However due to poor negative predictive value, clinical use is limited to determining whether PD1 therapy should be first or second line for non-small cell lung cancer. PD-L1 expression can also represent variable biology. In addition to adaptive induction by interferons, constitutive tumor expression has been reported secondary to various genetic derangements, including focal amplification of the PD-L1 locus [66], MYC overexprssion [67], 3’UTR mutation [68], or PTEN loss [69]. In different cancer types, theses PD-L1 modulation alterations can be associated with opposite response patterns to PD1 blockade, such as response in PD-L1 amplified Hodgkin’s lympohma , and resistance with PTEN loss [70,71].

4. Investigation into genetic features of response and resistance to PD1 blockade in melanoma

In the following chapters we will discuss investigations using melanoma biopsy samples from anti-PD1 treated cohorts to investigate features associate with primary or late acquired resistance. WES is used to assess mutational load, driving oncogenic mutations, and response-associated mutations. Analysis of pre/post therapy genetic evolution and selection proved particularly fruitful, as it has been for identification of resistance mechanisms to targeted therapy in the past [72]. We also assessed transcriptomics, immunohistochemistry, and T-cell repertoires in these cohorts.

References

1. Siegel RL, Miller KD, Jemal A. Cancer Statistics, 2017. *CA Cancer J Clin* 2017; **67**:7–30.

2. Long GV, Weber JS, Infante JR, *et al.*. Overall Survival and Durable Responses in Patients With BRAF V600-Mutant Metastatic Melanoma Receiving Dabrafenib Combined With Trametinib.. *J Clin Oncol* 2016; **34**:871–8.

3. Rosenberg SA, Yang JC, Sherry RM, *et al.*. Durable complete responses in heavily pretreated patients with metastatic melanoma using T-cell transfer immunotherapy.. *Clin Cancer Res* 2011; **17**:4550–7.

4. Schadendorf D, Hodi FS, Robert C, *et al.*. Pooled Analysis of Long-Term Survival Data From Phase II and Phase III Trials of Ipilimumab in Unresectable or Metastatic Melanoma.. *J Clin Oncol* 2015; **33**:1889–94.

5. Ribas A, Hamid O, Daud A, *et al.*. Association of Pembrolizumab With Tumor Response and Survival Among Patients With Advanced Melanoma.. *JAMA* 2016; **315**:1600–9.

6. Larkin J, Lao CD, Urba WJ, *et al.*. Efficacy and Safety of Nivolumab in Patients With BRAF V600 Mutant and BRAF Wild-Type Advanced Melanoma: A Pooled Analysis of 4 Clinical Trials.. *JAMA Oncol* 2015; **1**:433–40.

7. Hodi FS, Chesney J, Pavlick AC, *et al.*. Combined nivolumab and ipilimumab versus ipilimumab alone in patients with advanced melanoma: 2-year overall survival outcomes in a multicentre, randomised, controlled, phase 2 trial.. *Lancet Oncol* 2016; **17**:1558–1568.

8. Lu X, Horner JW, Paul E, *et al.*. Effective combinatorial immunotherapy for castration-resistant prostate cancer.. *Nature* 2017; **543**:728–732.

9. Topalian SL, Hodi FS, Brahmer JR, *et al.*. Safety, activity, and immune correlates of anti-PD-1 antibody in cancer.. *N Engl J Med* 2012; **366**:2443–54.

10. Topalian SL, Sznol M, McDermott DF, *et al.*. Survival, durable tumor remission, and long-term safety in patients with advanced melanoma receiving nivolumab.. *J Clin Oncol* 2014; **32**:1020–30.

11. Ribas A, Puzanov I, Dummer R, *et al.*. Pembrolizumab versus investigator-choice chemotherapy for ipilimumab-refractory melanoma (KEYNOTE-002): a randomised, controlled, phase 2 trial.. *Lancet Oncol* 2015; **16**:908–18.

12. Weber JS, D'Angelo SP, Minor D, *et al.*. Nivolumab versus chemotherapy in patients with advanced melanoma who progressed after anti-CTLA-4 treatment (CheckMate 037): a randomised, controlled, open-label, phase 3 trial.. *Lancet Oncol* 2015; **16**:375–84.

13. Robert C, Schachter J, Long GV, *et al.*. Pembrolizumab versus Ipilimumab in Advanced Melanoma.. *N Engl J Med* 2015; **372**:2521–32.

14. Robert C, Long GV, Brady B, *et al.*. Nivolumab in previously untreated melanoma without BRAF mutation.. *N Engl J Med* 2015; **372**:320–30.

15. Postow MA, Chesney J, Pavlick AC, *et al.*. Nivolumab and ipilimumab versus ipilimumab in untreated melanoma.. *N Engl J Med* 2015; **372**:2006–17.

16. Larkin J, Chiarion-Sileni V, Gonzalez R, *et al.*. Combined Nivolumab and Ipilimumab or Monotherapy in Untreated Melanoma.. *N Engl J Med* 2015; **373**:23–34.

17. Chen DS, Mellman I. Oncology meets immunology: the cancer-immunity cycle.. *Immunity* 2013; **39**:1–10.

18. Dunn GP, Old LJ, Schreiber RD. The three Es of cancer immunoediting.. *Annu Rev Immunol* 2004; **22**:329–60.

19. Ikeda H, Ohta N, Furukawa K, *et al.*. Mutated mitogen-activated protein kinase: a tumor rejection antigen of mouse sarcoma.. *Proc Natl Acad Sci U S A* 1997; **94**:6375–9.

20. De PE, Lurquin C, Van PA, *et al.*. Immunogenic (tum-) variants of mouse tumor P815: cloning of the gene of tum- antigen P91A and identification of the tum- mutation.. *Proc Natl Acad Sci U S A* 1988; **85**:2274–8.

21. Matsushita H, Vesely MD, Koboldt DC, *et al.*. Cancer exome analysis reveals a T-cell-dependent mechanism of cancer immunoediting.. *Nature* 2012; **482**:400–4.

22. Gubin MM, Zhang X, Schuster H, *et al.*. Checkpoint blockade cancer immunotherapy targets tumour-specific mutant antigens.. *Nature* 2014; **515**:577–81.

23. Castle JC, Kreiter S, Diekmann J, *et al.*. Exploiting the mutanome for tumor vaccination.. *Cancer Res* 2012; **72**:1081–91.

24. Lu YC, Yao X, Crystal JS, *et al.*. Efficient identification of mutated cancer antigens recognized by T cells associated with durable tumor regressions.. *Clin Cancer Res* 2014; **20**:3401–10.

25. Andreatta M, Nielsen M. Gapped sequence alignment using artificial neural networks: application to the MHC class I system.. *Bioinformatics* 2016; **32**:511–7.

26. Abelin JG, Keskin DB, Sarkizova S, *et al.*. Mass Spectrometry Profiling of HLA-Associated Peptidomes in Mono-allelic Cells Enables More Accurate Epitope Prediction.. *Immunity* 2017; **46**:315–326.

27. Andersen RS, Kvistborg P, Frøsig TM, *et al.*. Parallel detection of antigen-specific T cell responses by combinatorial encoding of MHC multimers.. *Nat Protoc* 2012; **7**:891–902.

28. Rizvi NA, Hellmann MD, Snyder A, *et al.*. Cancer immunology. Mutational landscape determines sensitivity to PD-1 blockade in non-small cell lung cancer.. *Science* 2015; **348**:124–8.

29. Parkhurst M, Gros A, Pasetto A, *et al.*. Isolation of T-Cell Receptors Specifically Reactive with Mutated Tumor-Associated Antigens from Tumor-Infiltrating Lymphocytes Based on CD137 Expression.. *Clin Cancer Res* 2017; **23**:2491–2505.

30. Pasetto A, Gros A, Robbins PF, *et al.*. Tumor- and Neoantigen-Reactive T-cell Receptors Can Be Identified Based on Their Frequency in Fresh Tumor.. *Cancer Immunol Res* 2016; **4**:734–43.

31. Tran E, Robbins PF, Lu YC, *et al.*. T-Cell Transfer Therapy Targeting Mutant KRAS in Cancer.. *N Engl J Med* 2016; **375**:2255–2262.

32. Tran E, Turcotte S, Gros A, *et al.*. Cancer immunotherapy based on mutation-specific CD4+ T cells in a patient with epithelial cancer.. *Science* 2014; **344**:641–5.

33. Landsberg J, Kohlmeyer J, Renn M, *et al.*. Melanomas resist T-cell therapy through inflammation-induced reversible dedifferentiation.. *Nature* 2012; **490**:412–6.

34. McGranahan N, Furness AJ, Rosenthal R, *et al.*. Clonal neoantigens elicit T cell immunoreactivity and sensitivity to immune checkpoint blockade.. *Science* 2016; **351**:1463–9.

35. Anagnostou V, Smith KN, Forde PM, *et al.*. Evolution of Neoantigen Landscape during Immune Checkpoint Blockade in Non-Small Cell Lung Cancer.. *Cancer Discov* 2017; **7**:264–276.

36. Verdegaal EM, de MNF, Visser M, *et al.*. Neoantigen landscape dynamics during human melanoma-T cell interactions.. *Nature* 2016; **536**:91–5.

37. D'Urso CM, Wang ZG, Cao Y, Tatake R, Zeff RA, Ferrone S. Lack of HLA class I antigen expression by cultured melanoma cells FO-1 due to a defect in B2m gene expression.. *J Clin Invest* 1991; **87**:284–92.

38. Restifo NP, Marincola FM, Kawakami Y, Taubenberger J, Yannelli JR, Rosenberg SA. Loss of functional beta 2-microglobulin in metastatic melanomas from five patients receiving immunotherapy.. *J Natl Cancer Inst* 1996; **88**:100–8.

39. Tumeh PC, Harview CL, Yearley JH, *et al.*. PD-1 blockade induces responses by inhibiting adaptive immune resistance.. *Nature* 2014; **515**:568–71.

40. Chen L, Flies DB. Molecular mechanisms of T cell co-stimulation and co-inhibition.. *Nat Rev Immunol* 2013; **13**:227–42.

41. Sharma P, Hu-Lieskovan S, Wargo JA, Ribas A. Primary, Adaptive, and Acquired Resistance to Cancer Immunotherapy.. *Cell* 2017; **168**:707–723.

42. Hui E, Cheung J, Zhu J, *et al.*. T cell costimulatory receptor CD28 is a primary target for PD-1-mediated inhibition.. *Science* 2017; **355**:1428–1433.

43. Kamphorst AO, Wieland A, Nasti T, *et al.*. Rescue of exhausted CD8 T cells by PD-1-targeted therapies is CD28-dependent.. *Science* 2017; **355**:1423–1427.

44. Im SJ, Hashimoto M, Gerner MY, *et al.*. Defining CD8+ T cells that provide the proliferative burst after PD-1 therapy.. *Nature* 2016; **537**:417–421.

45. Homet MB, Zaretsky JM, Garcia-Diaz A, *et al.*. Response to Programmed Cell Death-1 Blockade in a Murine Melanoma Syngeneic Model Requires Costimulation, CD4, and CD8 T Cells.. *Cancer Immunol Res* 2016; **4**:845–857.

46. Spranger S, Bao R, Gajewski TF. Melanoma-intrinsic β-catenin signalling prevents anti-tumour immunity.. *Nature* 2015; **523**:231–5.

47. Salmon H, Idoyaga J, Rahman A, *et al.*. Expansion and Activation of CD103(+) Dendritic Cell Progenitors at the Tumor Site Enhances Tumor Responses to Therapeutic PD-L1 and BRAF Inhibition.. *Immunity* 2016; **44**:924–38.

48. Noguchi T, Ward JP, Gubin MM, et al. Temporally Distinct PD-L1 Epxression by Tumor and Host Cells Contributes to Immune Escape. *Cancer Immunol Res* 2017 **5**:106-117

49. Juneja VR, McGurie KA, Mangruso RT, et al. PD-L1 on tumor cells is sufficient for immune evasion in immunogenic tumors and inhibits CD8 T cell cytotoxicity. *J Exp Med* 2017 **214**:895-904

50. Gros A, Robbins PF, Yao X, *et al.*. PD-1 identifies the patient-specific CD8$^+$ tumor-reactive repertoire infiltrating human tumors.. *J Clin Invest* 2014; **124**:2246–59.

51. Gros A, Parkhurst MR, Tran E, *et al.*. Prospective identification of neoantigen-specific lymphocytes in the peripheral blood of melanoma patients.. *Nat Med* 2016; **22**:433–8.

52. Huang AC, Postow MA, Orlowski RJ, *et al.*. T-cell invigoration to tumour burden ratio associated with anti-PD-1 response.. *Nature* 2017; **545**:60–65.

53. Dunn GP, Koebel CM, Schreiber RD. Interferons, immunity and cancer immunoediting.. *Nat Rev Immunol* 2006; **6**:836–48.

54. Mok S, Koya RC, Tsui C, *et al.*. Inhibition of CSF-1 receptor improves the antitumor efficacy of adoptive cell transfer immunotherapy.. *Cancer Res* 2014; **74**:153–61.

55. Ribas A. Adaptive Immune Resistance: How Cancer Protects from Immune Attack.. *Cancer Discov* 2015; **5**:915–9.

56. Kaplan DH, Shankaran V, Dighe AS, *et al.*. Demonstration of an interferon gamma-dependent tumor surveillance system in immunocompetent mice.. *Proc Natl Acad Sci U S A* 1998; **95**:7556–61.

57. Blank CU, Haanen JB, Ribas A, Schumacher TN. CANCER IMMUNOLOGY. The cancer immunogram.. *Science* 2016; **352**:658–60.

58. Van AEM, Miao D, Schilling B, *et al.*. Genomic correlates of response to CTLA-4 blockade in metastatic melanoma.. *Science* 2015; **350**:207–11.

59. Le DT, Uram JN, Wang H, *et al.*. PD-1 Blockade in Tumors with Mismatch-Repair Deficiency.. *N Engl J Med* 2015; **372**:2509–20.

60. Hugo W, Zaretsky JM, Sun L, *et al.*. Genomic and Transcriptomic Features of Response to Anti-PD-1 Therapy in Metastatic Melanoma.. *Cell* 2016; **165**:35–44.

61. Roh W, Chen PL, Reuben A, *et al.*. Integrated molecular analysis of tumor biopsies on sequential CTLA-4 and PD-1 blockade reveals markers of response and resistance.. *Sci Transl Med* 2017; **9**.

62. Rooney MS, Shukla SA, Wu CJ, Getz G, Hacohen N. Molecular and genetic properties of tumors associated with local immune cytolytic activity.. *Cell* 2015; **160**:48–61.

63. Ayers M, Lunceford J, Nebozhyn M, *et al.*. Relationship between immune gene signatures and clinical response to PD-1 blockade with pembrolizumab (MK-3475) in patients with advanced solid tumors. *Journal for ImmunoTherapy of Cancer* 2015; **3**:P80.

64. Chen PL, Roh W, Reuben A, *et al.*. Analysis of Immune Signatures in Longitudinal Tumor Samples Yields Insight into Biomarkers of Response and Mechanisms of Resistance to Immune Checkpoint Blockade.. *Cancer Discov* 2016; **6**:827–37.

65. Garon EB, Rizvi NA, Hui R, *et al.*. Pembrolizumab for the treatment of non-small-cell lung cancer.. *N Engl J Med* 2015; **372**:2018–28.

66. Ansell SM, Lesokhin AM, Borrello I, et al. PD-1 blockade with nivolumab in relapsed or refractory Hodgkin's lymphoma. *N Engl J Med* 2015, **372**:311-319

67. Casey SC, Tong L, Li Y, *et al.*. MYC regulates the antitumor immune response through CD47 and PD-L1.. *Science* 2016; **352**:227–31.

68. Kataoka K, Shiraishi Y, Takeda Y, *et al.*. Aberrant PD-L1 expression through 3'-UTR disruption in multiple cancers.. *Nature* 2016; **534**:402–6.

69. Parsa AT, Waldron JS, Panner A, *et al.*. Loss of tumor suppressor PTEN function increases B7-H1 expression and immunoresistance in glioma.. *Nat Med* 2007; **13**:84–8.

70 Peng W, Chen JQ, Liu C, *et al.*. Loss of PTEN Promotes Resistance to T Cell-Mediated Immunotherapy.. *Cancer Discov* 2016; **6**:202–16.

71. George S, Miao D, Demetri GD, *et al.*. Loss of PTEN Is Associated with Resistance to Anti-PD-1 Checkpoint Blockade Therapy in Metastatic Uterine Leiomyosarcoma.. *Immunity* 2017; **46**:197–204.

72. Shi H, Hugo W, Kong X, et al. Acquired resistance and clonal evolution during BRAF inhibitor therapy. *Cancer Discov* 2014 **4**:80-93

Chapter 2:

Mutations associated with acquired resistance to anti-PD1 immunotherapy in melanoma

The NEW ENGLAND JOURNAL *of* MEDICINE

ORIGINAL ARTICLE

Mutations Associated with Acquired Resistance to PD-1 Blockade in Melanoma

Jesse M. Zaretsky, B.S., Angel Garcia-Diaz, Ph.D., Daniel S. Shin, M.D.,
Helena Escuin-Ordinas, Ph.D., Willy Hugo, Ph.D.,
Siwen Hu-Lieskovan, M.D., Ph.D., Davis Y. Torrejon, M.D.,
Gabriel Abril-Rodriguez, M.Sc., Salemiz Sandoval, Ph.D., Lucas Barthly, M.Sc.,
Justin Saco, B.S., Blanca Homet Moreno, M.D., Riccardo Mezzadra, M.Sc.,
Bartosz Chmielowski, M.D., Ph.D., Kathleen Ruchalski, M.D.,
I. Peter Shintaku, Ph.D., Phillip J. Sanchez, Ph.D., Cristina Puig-Saus, Ph.D.,
Grace Cherry, R.N., N.P., Elizabeth Seja, B.A., Xiangju Kong, M.Sc., Jia Pang, B.S.,
Beata Berent-Maoz, Ph.D., Begoña Comin-Anduix, Ph.D.,
Thomas G. Graeber, Ph.D., Paul C. Tumeh, M.D., Ton N.M. Schumacher, Ph.D.,
Roger S. Lo, M.D., Ph.D., and Antoni Ribas, M.D., Ph.D.

ABSTRACT

BACKGROUND

Approximately 75% of objective responses to anti–programmed death 1 (PD-1) therapy in patients with melanoma are durable, lasting for years, but delayed relapses have been noted long after initial objective tumor regression despite continuous therapy. Mechanisms of immune escape in this context are unknown.

METHODS

We analyzed biopsy samples from paired baseline and relapsing lesions in four patients with metastatic melanoma who had had an initial objective tumor regression in response to anti–PD-1 therapy (pembrolizumab) followed by disease progression months to years later.

RESULTS

Whole-exome sequencing detected clonal selection and outgrowth of the acquired resistant tumors and, in two of the four patients, revealed resistance-associated loss-of-function mutations in the genes encoding interferon-receptor–associated Janus kinase 1 (*JAK1*) or Janus kinase 2 (*JAK2*), concurrent with deletion of the wild-type allele. A truncating mutation in the gene encoding the antigen-presenting protein beta-2-microglobulin (*B2M*) was identified in a third patient. *JAK1* and *JAK2* truncating mutations resulted in a lack of response to interferon gamma, including insensitivity to its antiproliferative effects on cancer cells. The *B2M* truncating mutation led to loss of surface expression of major histocompatibility complex class I.

CONCLUSIONS

In this study, acquired resistance to PD-1 blockade immunotherapy in patients with melanoma was associated with defects in the pathways involved in interferon-receptor signaling and in antigen presentation. (Funded by the National Institutes of Health and others.)

From the University of California, Los Angeles (UCLA) (J.M.Z., A.G.-D., D.S.S., H.E.-O., W.H., S.H.-L., D.Y.T., G.A.-R., S.S., L.B., J.S., B.H.M., B.C., K.R., I.P.S., P.J.S., C.P.-S., G.C., E.S., X.K., J.P., B.B.-M., B.C.-A., T.G.G., P.C.T., R.S.L., A.R.), and Jonsson Comprehensive Cancer Center (B.C., B.C.-A., T.G.G., P.C.T., R.S.L., A.R.) — both in Los Angeles; and the Division of Immunology, Netherlands Cancer Institute, Amsterdam (R.M., T.N.M.S.). Address reprint requests to Dr. Ribas at the Department of Medicine, Division of Hematology–Oncology, Jonsson Comprehensive Cancer Center at UCLA, 11-934 Factor Bldg., 10833 Le Conte Ave., Los Angeles, CA 90095-1782, or at aribas@mednet.ucla.edu.

DOI: 10.1056/NEJMoa1604958

Durable responses in metastatic cancers have been achieved with a variety of immunotherapies such as interleukin-2, adoptive cell transfer of tumor-infiltrating lymphocytes, antibodies that block cytotoxic T-lymphocyte–associated antigen 4 (CTLA4),[1-5] and antibodies that block programmed death 1 (PD-1).[6-10] However, in a recent study, approximately 25% of patients with melanoma who had had an objective response to PD-1 blockade therapy had disease progression at a median follow-up of 21 months.[11]

The mechanisms of immune-resistant cancer progression are mostly unknown. Previous studies involving humans examined the loss of beta-2-microglobulin as a mechanism of acquired resistance to several forms of cancer immunotherapy.[12-14] In preclinical models, defects in the interferon signaling pathway have been proposed as a potential mechanism of cancer escape (insensitivity) to immunotherapy.[15,16] In the current study, we assessed the effect of anti–PD-1 therapy on cancer genomic evolution, including acquired mutations in the genes affecting the interferon pathway and antigen-presentation pathway, in an effort to determine genetic mechanisms of acquired resistance to PD-1 blockade therapy.

METHODS

PATIENTS, RESPONSE ASSESSMENT, AND TUMOR BIOPSIES

Of 78 patients with metastatic melanoma who were treated with the anti–PD-1 antibody pembrolizumab at the University of California, Los Angeles (UCLA), 42 had an objective response, of whom 15 went on to have disease progression. Four of these 15 patients met all three selection criteria for this analysis. First, they must have had an objective tumor response while participating in a clinical trial with single-agent pembrolizumab.[6,7,10,11] Tumor responses were evaluated at 12 weeks and confirmed 4 weeks later, and patients were assessed by imaging every 12 weeks thereafter with the use of both the Response Evaluation Criteria in Solid Tumors[17] and the immune-related response criteria.[18] Second, patients had to have late acquired resistance, defined as in situ recurrence or new lesion development, despite continuous dosing, after more than 6 months of tumor response. Third, patients had to have adequate biopsy material for whole-exome sequencing at two time points: before the initiation of pembrolizumab therapy and after disease progression. We processed tumor biopsy samples as described previously to perform pathological analyses, obtain DNA and RNA, and attempt to establish cell lines.[19,20]

IMMUNOHISTOCHEMICAL, IMMUNOFLUORESCENCE, WESTERN BLOT, AND FLOW-CYTOMETRIC ANALYSES

Immunohistochemical and immunofluorescence analyses[19] as well as Western blot and flow-cytometric analyses[21] were performed and analyzed as described previously. Full methods are included in the Supplementary Appendix, available with the full text of this article at NEJM.org.

GENETIC AND TRANSCRIPTIONAL-PROFILING ANALYSES

Whole-exome sequencing was performed at the UCLA Clinical Microarray Core with the use of the NimbleGen SeqCap EZ Human Exome Library, version 3.0 (Roche). Mutation calling was performed as described previously.[22] Selected gene-expression profiling on interferon exposure was performed with the use of nCounter (NanoString Technologies). Whole-exome sequencing data have been deposited in the National Center for Biotechnology Information Sequence Read Archive under the accession number SRP076315.

FUNCTIONAL STUDIES

Patient-derived and previously established human melanoma cell lines were used to analyze recognition by T-cell receptor transgenic T cells[23] with the use of in vitro coculture assays that detect antigen-induced release of interferon-γ assessed by enzyme-linked immunosorbent assay. Cell-proliferation and growth-inhibition assays were performed with the use of an automated live-cell imaging system (IncuCyte, Essen BioScience) with or without exposure to interferons. Full methods are described in the Supplementary Appendix.

STUDY OVERSIGHT

Data generated and collected by the study investigators were analyzed by the last author, who vouches for the completeness and accuracy of the data, analyses, and reported results. Summaries of the clinical protocol have been reported by Hamid et al.[6] and Robert et al.[10]

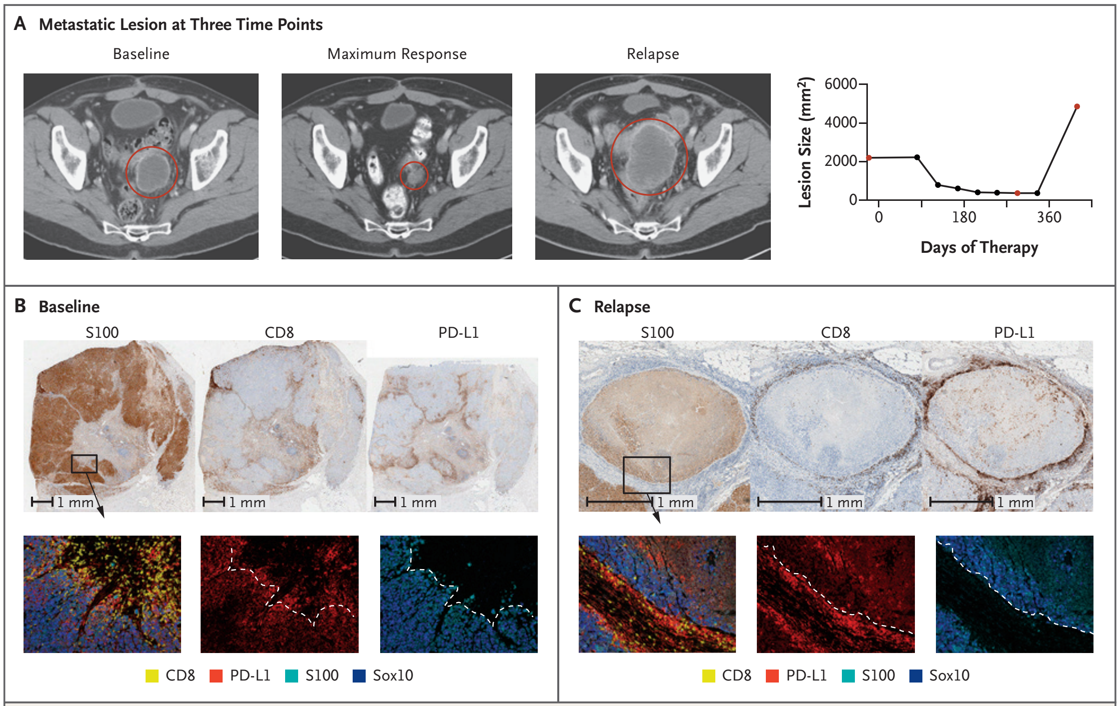

Figure 1. Clinical Pattern of Acquired Resistance to Anti–Programmed Death 1 (PD-1) Therapy in Patient 1.

In Panel A, computed tomographic images show a melanoma small-bowel metastasis at baseline, at the time of maximum response, and at the time of an in situ relapse after a year of minimal residual disease; the red dots in the graph on the right indicate these three time points. Immunohistochemical staining and multiplexed immunofluorescence analysis showed abundant CD8 T-cell infiltrates and programmed death ligand 1 (PD-L1) expression at baseline and again at the time of relapse at the tumor margin in Panels B and C, respectively. In the immunofluorescence images, red indicates PD-L1, yellow CD8 T cells, light blue the melanoma marker S100 (cytoplasmic staining), and dark blue the melanoma marker Sox10 (nuclear staining).

STATISTICAL ANALYSIS

Student's t-test and a two-way analysis of variance were used for cell-culture experiments, with Dunnett's correction applied for multiple comparisons with untreated controls.

RESULTS

CLINICAL COURSE AND IMMUNE INFILTRATES

We analyzed paired tumor samples from four (nonconsecutive) selected patients with metastatic melanoma who had had a relapse while receiving PD-1–inhibition therapy with pembrolizumab (Tables S1 and S2 in the Supplementary Appendix). All four patients met objective criteria for a partial response,[17,18] though with slightly different kinetics (Fig. 1, and Figs. S1, S2, and S3 in the Supplementary Appendix). The mean time to relapse was 624 days (range, 419 to 888). The baseline biopsy samples were obtained just before the initiation of pembrolizumab therapy in Patients 2, 3, and 4, whereas for Patient 1, the only available baseline biopsy sample was obtained before an earlier course of therapy with the BRAF inhibitor vemurafenib. The baseline biopsy samples from Patients 1, 2, and 3 showed preexisting CD8 T-cell infiltrates at the invasive margin that colocalized with programmed death ligand 1 (PD-L1) expression on surrounding macrophages and melanoma cells (Fig. 1B, and Figs. S1B and S2B in the Supplementary Appendix). The biopsy samples obtained at the time of response in Patients 2, 3, and 4 showed a marked increase in intratumoral CD8 T-cell infiltrates

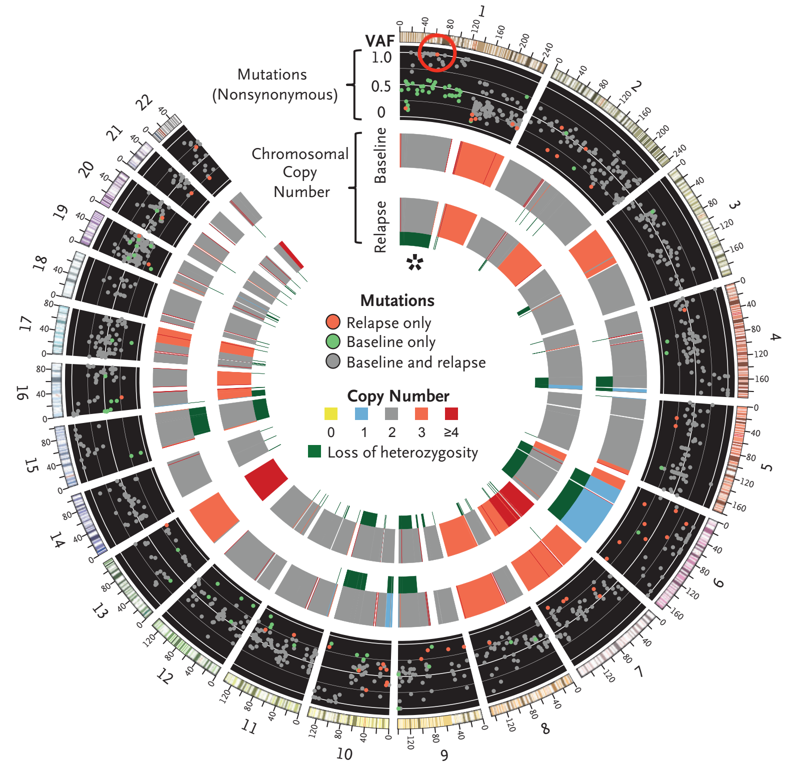

A Genetic Changes between Baseline Tumor and Relapse Tumor

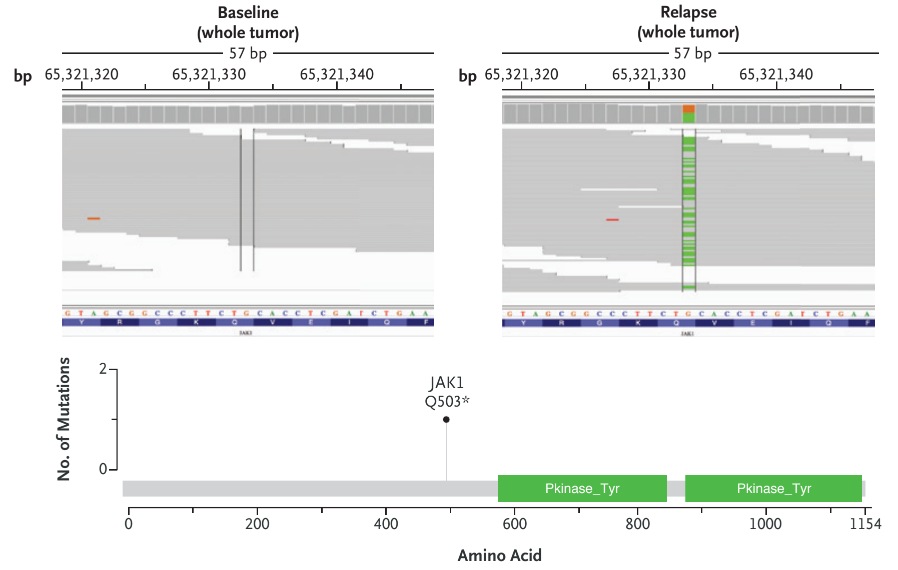

B IGV Plots and cBioPortal Diagram

Figure 2 (facing page). Acquired *JAK1* Loss-of-Function Mutation at Relapse, with Accompanying Loss of Heterozygosity.

In Panel A, a Circos plot[25] of Patient 1 shows differences in whole-exome sequencing between the pre-pembrolizumab and post-relapse biopsies. The red circle highlights a new, high-allele-frequency, relapse-specific mutation in the gene encoding Janus kinase 1 (*JAK1*) in the context of chromosomal loss of heterozygosity (asterisk). Each wedge represents a chromosome. In the outer track (black background), each point represents a nonsynonymous mutation, with most detected in both biopsy samples (gray) rather than at relapse only (red) or baseline only (green). The y-axis position indicates the variant allele frequency (VAF) at relapse, unless baseline-specific. The middle and inner tracks show copy-number status for the baseline and relapse biopsy, respectively; dark green in the subtrack indicates loss of heterozygosity. In Panel B, Integrative Genomics Viewer (IGV) plots (top) show that the *JAK1* Q503* nonsense mutation is relapse-specific, and the cBioPortal[26] diagram (bottom) shows that the JAK1 mutation is upstream of the kinase domains.

(Figs. S1C, S2C, and S3C and Table S3 in the Supplementary Appendix; no biopsy sample during therapy was available for Patient 1). At the time of relapse, all four biopsy samples showed CD8 T-cell infiltration and PD-L1 expression concentrated at the tumor margins again (Fig. 1C and Figs. S1D, S2D, and S3D in the Supplementary Appendix). Multiplex immunofluorescence assays revealed that melanoma cells at the time of relapse in Patients 1 and 2 were negative for PD-L1 even when directly adjacent to T cells, whereas macrophages and stromal cells were positive for PD-L1.

GENETIC CHANGES IN RELAPSE BIOPSY SAMPLES

The pattern of a strong initial response, long dormancy, and rapid late progression led us to hypothesize that relapse in these patients resulted from immune-mediated clonal selection and tumor outgrowth.[24] To identify mutations that might confer immune resistance, we extracted DNA from bulk-tumor biopsy samples or early-passage primary cell lines (Table S2 in the Supplementary Appendix) and performed whole-exome sequencing to compare baseline and matched relapsed tissues. We achieved a median coverage of 149×, and the percent of tumor cells (as compared with stromal cells) was more than 40% in all samples (Table S2 in the Supplementary Appendix). Nonsynonymous mutations for all samples are shown in Table S4 in the Supplementary Appendix.

JAK MUTATIONS WITH CONCURRENT LOSS OF HETEROZYGOSITY AT RELAPSE

We found strong evidence that the relapsed tumors were closely genetically related to their baseline counterparts, despite up to 2 years between biopsies. In the case of Patients 1 and 2, of 1173 and 240 nonsynonymous mutations, respectively, originally identified in the baseline sample, 92.5% and 95.8% were also seen in the resistant tumor (Fig. 2A, and Fig. S4 in the Supplementary Appendix). The relapsing tumors also contained the same chromosomal loss-of-heterozygosity events as the baseline tumors, and all differences were due to further loss in the relapse samples. In the relapse biopsy samples from both patients, we identified new homozygous loss-of-function mutations in the kinases associated with the interferon-receptor pathway, with a Q503* nonsense mutation in the gene encoding Janus kinase 1 (*JAK1*) in Patient 1 (Fig. 2A and 2B) and a F547 splice-site mutation in the gene encoding Janus kinase 2 (*JAK2*) in Patient 2 (Fig. S4 in the Supplementary Appendix). RNA sequencing showed that the *JAK2* splice-site mutation caused intron inclusion, producing an in-frame stop codon 10 bp after exon 12 (Fig. S5 in the Supplementary Appendix). Therefore, both mutations were upstream of the kinase domains and probably truncated the protein or caused nonsense-mediated decay. Neither mutation was seen at baseline in the exome sequencing reads, by Sanger sequencing, or by targeted amplicon resequencing (Fig. S6 in the Supplementary Appendix).

The *JAK2* mutation was the only homozygous mutation (adjusted variant allele frequency, >85%) of 76 new nonsynonymous mutations in Patient 2, and the *JAK1* mutation was 1 of only 3 homozygous mutations among 53 new mutations in Patient 1 (Table S5 in the Supplementary Appendix). To become homozygous, both *JAK* mutations were acquired in the context of a copy-number–neutral nondisjunction event, resulting in loss of the wild-type chromosome and duplication of the mutated allele. This is seen clearly in Patient 1: at relapse, chromosome 1p (containing *JAK1*) showed a decrease in minor-allele frequencies for germline single-nucleotide polymorphisms relative to baseline (Fig. S7 in the Supplementary Appendix), was missing 36 heterozygous baseline mutations (presumably on the lost allele), and contained 20 mutations (presumably on the amplified allele) that became homozygous (adjusted variant allele frequency, >85%, with change of >35 percentage points from baseline). A similar loss-of-heterozygosity event occurred for chromosome 9 in Patient 2 (Fig. S8 and Table S5 in the Supplementary Appendix). Together, these data suggest that the tumors resistant to anti–PD-1 are a relatively homogenous population derived directly from the baseline tumor and that acquisition of the *JAK* mutations was an early founder event before clonal selection and relapse despite the fact that the mutation was not detected in pretreatment tumor tissue.

FUNCTIONAL EFFECTS OF *JAK2* MUTATION

To assess the functional consequences of the observed *JAK* mutations, we focused on the *JAK2* mutation from Patient 2 using two cell lines established at baseline (M420, wild-type *JAK2*) and at the time of relapse (M464, *JAK2* F547 splice-site mutation). Whole-exome sequencing confirmed that the original bulk tumor was well represented by M464 (Fig. S9 in the Supplementary Appendix). Western blot analysis showed that the baseline cell line responded to interferon alfa, beta, and gamma with the expected signal transduction, including an increase in signal transducer and activator of transcription 1 (STAT1) and interferon regulatory factor (IRF) expression, STAT1 phosphorylation (pSTAT1), and the production of downstream interferon targets such as PD-L1, transporter associated with antigen processing 1 (TAP1), and major histocompatibility complex (MHC) class I (Fig. 3A). However, the cell line from the progressing lesion showed a total loss of JAK2 protein (Fig. 3A), resulting in a lack of response to interferon gamma, without change in sensitivity to interferon alfa or beta. This was true of the pSTAT1 response (Fig. 3A) and the expression of PD-L1 and MHC class I molecules (Fig. 3A and 3B). The progressing cell line also failed to up-regulate a wider panel of interferon-induced transcripts involved in antigen presentation and T-cell chemotaxis (Fig. 3C, and Table S6 in the Supplementary Appendix). Together, these data indicate a total loss of functional response to interferon gamma and are consistent with JAK2 being required for signaling through the interferon-γ receptor, as opposed to the interferon-α/β receptor, which uses TYK2 and JAK1.[27-29]

LOSS OF INTERFERON GAMMA–INDUCED GROWTH ARREST THROUGH ACQUIRED *JAK* MUTATIONS

We hypothesized that inactivating *JAK* mutations may result in a functional advantage for the progressive tumors because the lack of interferon signaling either decreased antigen presentation or allowed escape from interferon-induced inhibition of growth. In addition to using M420 and M464, we engineered the human melanoma cell line M407 by means of the CRISPR (clustered regularly interspaced short palindromic repeats)–Cas9 approach to create sublines without expression of *JAK1* or *JAK2* (Figs. S10 and S11 in the Supplementary Appendix). These created truncating mutations analogous to those from Patients 1 and 2, and M407 is positive for HLA-A*02:01 and expresses the cancer–testis antigen NY-ESO-1, which allowed us to model T-cell recognition using T cells genetically modified to express an NY-ESO-1–specific T-cell receptor.[23] M407 and both *JAK*-loss sublines were equally recognized by NY-ESO-1–specific T cells, leading to high levels of interferon-γ production (Fig. 4A).

When cultured in recombinant interferon alfa, beta, or gamma, the M420 and M407 parental cell lines showed interferon-induced growth inhibition in a dose-dependent manner (Fig. S12 in the Supplementary Appendix). However, both the *JAK2*-deficient M464 cell line (from Patient 2 at relapse) and the M407 *JAK2*-knockout subline were insensitive specifically to interferon gamma–induced growth arrest, yet remained sensitive to type I interferons alfa and beta; in contrast, the M407 *JAK1*-mutated subline was resistant to all three interferons (Fig. 4B). This is again consistent with the specific association of *JAK2* with the interferon-γ receptor and the common use of JAK1 by all three interferon receptors.[27-29] As an orthogonal test of these effects, we treated our cell lines with 2′3′-cGAMP (cyclic guanosine monophosphate–adenosine monophosphate); this dinucleotide, which is produced in response to

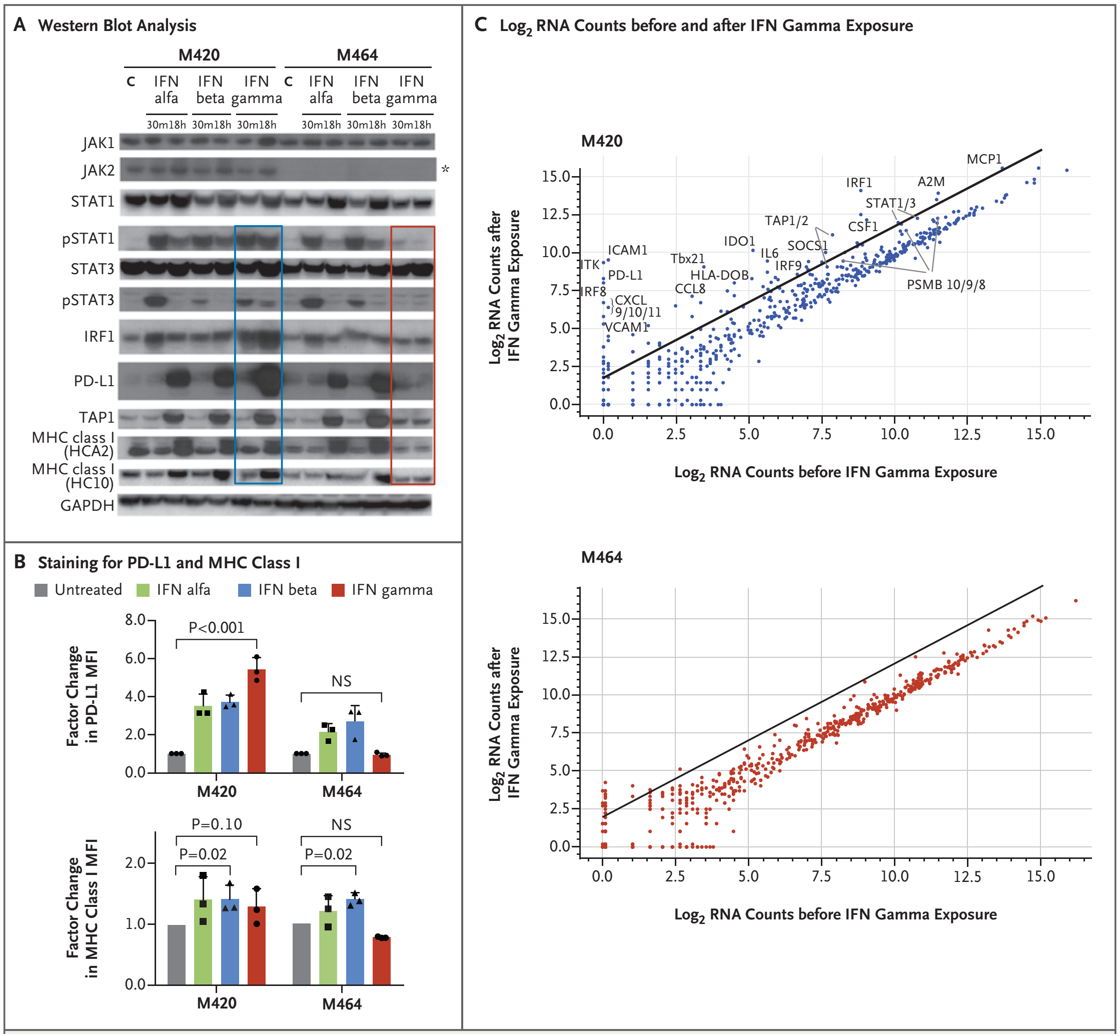

Figure 3. **Loss of Interferon Gamma–Induced Signaling and Gene-Expression Changes through Acquired *JAK2* Mutation.**

In Panel A, Western blot analysis of lysates from cell lines M420 (Patient 2, baseline) and M464 (Patient 2, relapse) shows Janus kinase (JAK)–signal transducer and activator of transcription (STAT) signaling events and downstream target induction after either 30 minutes (m) or 18 hours (h) of exposure to interferon (IFN) alfa, beta, or gamma (C indicates untreated control). Janus kinase 2 (JAK2) protein expression was absent in the relapse cell line (asterisk), and M464 failed to phosphorylate intermediate signaling components STAT1 and STAT3 or to up-regulate interferon-response targets TAP1, PD-L1, and major histocompatibility complex (MHC) class I after treatment specifically with interferon gamma (red box), as compared with intact signaling in M420 (blue box). There was no change in response to interferon alfa or beta. As shown in Panel B, a lack of response to interferon gamma exposure was also seen in surface staining for PD-L1 and MHC class I by flow cytometry. Each point represents an independent experiment, T bars represent standard deviations, and P values are for a two-way analysis of variance with Dunnett's correction. MFI denotes mean fluorescent intensity, and NS not significant. Panel C shows $\log_2$ RNA counts of expression for 790 immune-related genes on exposure to interferon gamma or vehicle control. The baseline cell line M420 (top) showed up-regulation of many interferon-stimulated genes (line represents an increase by a factor of 4), whereas the *JAK2* mutated progression cell line M464 (bottom) lacked a similar response.

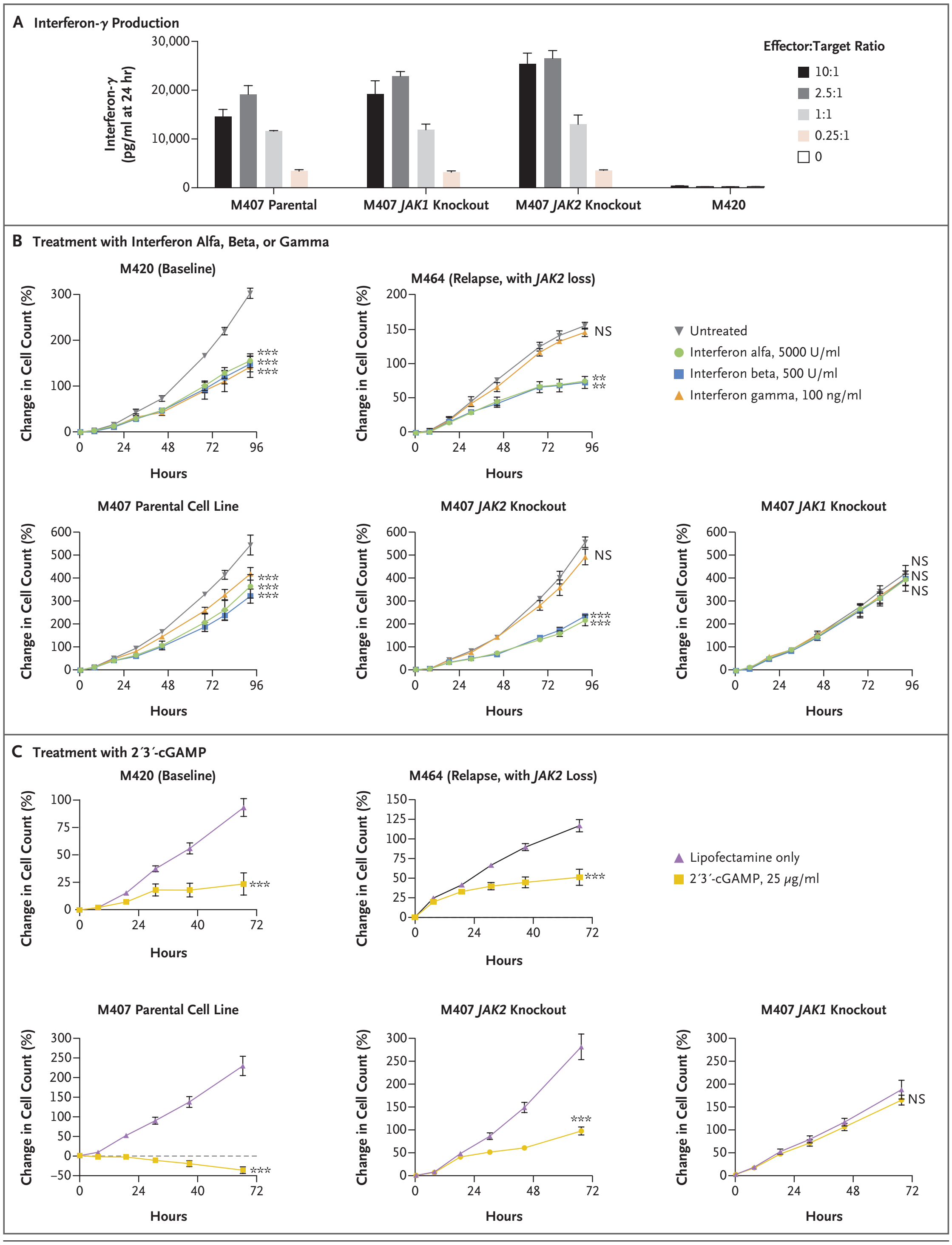
A Interferon-γ Production
Interferon-γ (pg/ml at 24 hr)
30,000
20,000
10,000
0
M407 Parental
M407 JAK1 Knockout
M407 JAK2 Knockout
M420
Effector:Target Ratio
10:1
2.5:1
1:1
0.25:1
0
B Treatment with Interferon Alfa, Beta, or Gamma
M420 (Baseline)
M464 (Relapse, with JAK2 loss)
Change in Cell Count (%)
Hours
0
24
48
72
96
***
NS
**
Untreated
Interferon alfa, 5000 U/ml
Interferon beta, 500 U/ml
Interferon gamma, 100 ng/ml
M407 Parental Cell Line
M407 JAK2 Knockout
M407 JAK1 Knockout
C Treatment with 2′3′-cGAMP
M420 (Baseline)
M464 (Relapse, with JAK2 Loss)
Lipofectamine only
2′3′-cGAMP, 25 μg/ml
M407 Parental Cell Line
M407 JAK2 Knockout
M407 JAK1 Knockout
Change in Cell Count (%)
Hours
***
NS

Figure 4 (facing page). Loss of Interferon Gamma–Induced Growth Arrest through Acquired *JAK* Mutations.

In Panel A, the M407 parental cell line as well as the M407 *JAK1*-knockout and *JAK2*-knockout sublines were recognized by NY-ESO-1–specific, HLA-A*02:01–restricted T cells, as assessed by interferon-γ production after 24 hours of in vitro coculture. M420 is negative for HLA-A*02:01 and served as a negative control. In Panel B, cell lines M420 and M407 showed growth inhibition in response to direct in vitro treatment with interferon alfa, beta, or gamma (left), whereas the *JAK2*-deficient counterpart M464 and the M407 *JAK2* knockout were insensitive specifically to interferon gamma (middle). The M407 *JAK1* knockout was insensitive to all three interferons (right). In Panel C, treatment with 2′3′-cGAMP (cyclic guanosine monophosphate–adenosine monophosphate), a direct cytosolic agonist of the stimulator of interferon genes (STING), was able to produce growth arrest in all cell lines, regardless of *JAK2* status, yet had no effect in M407 with *JAK1* knockout. Growth curves represent the percent change in the number of melanoma cells over time as measured by IncuCyte continuous live-cell imaging in one of three independent experiments. I bars in Panels A, B, and C indicate standard deviations for three replicate wells. Three asterisks indicate P<0.001 and two asterisks P<0.01 for the percent change in growth with the treatment shown at the 72-hour end point as compared with the untreated control, with Dunnett's multiple-comparison correction applied in Panel B. NS denotes not significant.

cytosolic double-stranded DNA, directly activates the stimulator of interferon genes (STING) and leads to interferon-β production through activation of interferon regulatory factor 3 (IRF-3).[30] After 2′3′-cGAMP treatment, we observed growth arrest in all cell lines independent of JAK2 status but no effect in the *JAK1*-knockout subline (Fig. 4C). Therefore, the *JAK1* and *JAK2* loss-of-function mutations did not decrease in vitro T-cell recognition but selectively blocked the interferon-γ signaling that leads to cell-growth inhibition, which for *JAK2* loss could be corrected by type I pathway activation or a STING agonist.

FUNCTIONAL EFFECTS OF MUTATION IN THE GENE ENCODING BETA-2-MICROGLOBULIN (*B2M*)

In Patient 3, whole-exome sequencing of the baseline and progressive lesions showed a 4-bp S14 frame-shift deletion in exon 1 of the beta-2-microglobulin component of MHC class I as 1 of only 24 new relapse-specific mutations and the only such mutation that was homozygous (Fig. S13A and S13B in the Supplementary Appendix). Immunohistochemical analysis for MHC class I heavy chains revealed loss of outer-membrane localization as compared with adjacent stroma or the baseline tumor, even though diffuse intracellular staining indicated continued production of MHC class I molecules (Fig. S14 in the Supplementary Appendix). This finding is in line with the role of beta-2-microglobulin in proper MHC class I folding and transport to the cell surface, and its deficiency has long been recognized as a genetic mechanism of acquired resistance to immunotherapy.[12-14] Both the baseline and relapse biopsy samples were negative for MHC class II expression (Fig. S14 in the Supplementary Appendix), which suggests a lack of compensatory MHC up-regulation.

We could not find defined genetic alterations in Patient 4 that had clear potential to result in acquired resistance to T cells, but cancer cells in the baseline and relapse biopsy samples did not express PD-L1 despite proximity to T cells and PD-L1–expressing stroma (Fig. S3D in the Supplementary Appendix). These findings suggest possible nongenetic mechanisms of altered expression of interferon-inducible genes.[16]

DISCUSSION

With the approval of PD-1 checkpoint-blockade agents for the treatment of patients with melanoma, lung cancer, and other cancers, it is anticipated that cases of late relapse after initial response will increase. Understanding the molecular mechanisms of acquired resistance by focused comparison of biopsy samples from paired baseline and relapsing lesions may open options for the rational design of salvage combination therapies or preventive interventions and may guide mechanistic biomarker studies for the selection of patients, before the initiation of treatment, who are unlikely to have a response.

Tumor-infiltrating T cells are the effectors that kill cancer cells during PD-1 blockade therapy.[19,31] We found it striking that after intratumoral CD8 T-cell infiltration during active response, CD8 T cells were usually still present and abundant at the time of relapse, though they were restricted to the tumor margin. This observation suggested to us that the T cells were no longer able to exert their cytotoxic activity, because of either a lack of tumor antigen recognition and activation or a loss of sensitivity to their effector molecules by the cancer cells. The general possibilities are loss of mutational or shared tumor antigens that are recognized by T cells, loss of antigen-presenting machinery components (e.g., beta-2-microglobulin and HLA),[12-14] tumor-cell–induced or myeloid-cell–induced inactivation of T-cell signaling,[32,33] or insensitivity to the proapoptotic effects of toxic granules (e.g., perforin and granzymes), death receptors (e.g., Fas and tumor necrosis factor–related apoptosis-inducing ligand [TRAIL]), or interferons.[34] Any of these escape mechanisms would be hypothesized to be fostered by the selective pressure of CD8 attack, which would be particularly active during the new round of immunoediting[35] that is unleashed after PD-1 blockade.

The inactivation of *JAK1* or *JAK2*, as noted in two of the patients, may be particularly advantageous to cancer cells in the context of anti–PD-1 therapy as compared with other immunotherapies. The interferon-induced adaptive expression of PD-L1, which allows the cancer to inactivate adjacent CD8 T cells,[36] would be of no use after the PD-1–PD-L1 interaction is blocked by therapeutic antibodies. We propose that without this benefit, the advantage for cancer cells tilts toward abolishing interferon signaling in order to avoid the detrimental increase in antigen presentation and direct antiproliferative effects.[27] Although we identified inactivating mutations in *JAK1* and *JAK2*, which are receptor-level signaling bottlenecks, interferon insensitivity through other means — such as epigenetic silencing of interferon-signaling components as previously documented in lung-cancer and prostate-cancer cell lines[15,16] or increased expression of negative regulators[37] — might lead to the same end. We also documented one case of beta-2-microglobulin inactivation, which corroborates a previously described mechanism of acquired resistance to cancer immunotherapy in humans through loss of this shared component of all human MHC class I molecules that is required for CD8 T-cell recognition.[12-14]

In conclusion, the nearly identical mechanism of acquisition, functional consequence, and evidence of clonal selection for *JAK1* or *JAK2* mutations in two independent cases with a similar clinical course of acquired resistance suggests that resistance to interferon gamma contributes to immune resistance and escape. This genetic alteration of immune resistance joins the previously described loss of *B2M* in decreasing immune-cell recognition of cancer cells, leading to acquired resistance to cancer immunotherapy. Although we have identified four cases and worked out a potential mechanism of resistance in three of them, additional cases will need to be closely examined to assess the generalizability of these findings.

Supported in part by National Institutes of Health (NIH) grants R35 CA197633, P01 CA168585, 1U54 CA199090, and R01 CA170689 (to Dr. Ribas). Dr. Ribas was supported by the Ressler Family Foundation, the Dr. Robert Vigen Memorial Fund, the Grimaldi Family Fund, the Samuels Family Fund, the Ruby Family Fund, and the Garcia-Corsini Family Fund. Drs. Ribas and Schumacher were supported by a Stand Up To Cancer–Cancer Research Institute Cancer Immunology Dream Team Translational Research Grant (SU2C-AACR-DT1012); Stand Up To Cancer is a program of the Entertainment Industry Foundation administered by the American Association for Cancer Research. Mr. Zaretsky is part of the UCLA Medical Scientist Training Program supported by NIH training grant GM08042. Dr. Shin was supported by the Oncology (5T32CA009297-30), Dermatology (5T32AR058921-05), and Tumor Immunology (5T32CA009120-39) training grants and a Tower Cancer Research Foundation Grant. Dr. Hu-Lieskovan was supported by a Young Investigator Award and a Career Development Award from the American Society of Clinical Oncology, a Tower Cancer Research Foundation Grant, and a Dr. Charles Coltman Fellowship Award from the Hope Foundation. Dr. Homet Moreno was supported in part by the Rio Hortega Scholarship (08/142) from Hospital 12 de Octubre, Madrid. Dr. Torrejon was supported by a grant from the Spanish Society of Medical Oncology for Translational Research in Reference Centers. Dr. Hugo was supported by the American Skin Association. Dr. Graeber was supported by a Melanoma Research Alliance Established Investigator Award (20120279) and an American Cancer Society Research Scholar Award (RSG-12-257-01-TBE). Dr. Lo was supported by the Steven C. Gordon Family Foundation, the Wade F.B. Thompson/Cancer Research Institute Clinic and Laboratory Integration Program Grant, the Ressler Family Foundation, the Grimaldi Family Fund, and the Ian Copeland Melanoma Fund.

Disclosure forms provided by the authors are available with the full text of this article at NEJM.org.

We thank the staff of the Translational Pathology Core Laboratory and Rongqing Guo and Wang Li from UCLA for blood and biopsy processing; Xinmin Li, Ling Dong, Janice Yoshizawa, and Jamie Zhou from the UCLA Clinical Microarray Core for sequencing expertise; and members of Dr. Ribas's laboratory, Pia Kvistborg and Marit van Buuren from the Netherlands Cancer Institute, Jordan Freeman from FLX Bio, and Leticia Corrales and Thomas Gajewski from the University of Chicago for useful discussions.

REFERENCES

1. Atkins MB, Kunkel L, Sznol M, Rosenberg SA. High-dose recombinant interleukin-2 therapy in patients with metastatic melanoma: long-term survival update. Cancer J Sci Am 2000;6:Suppl 1:S11-4.

2. Rosenberg SA, Yang JC, Sherry RM, et al. Durable complete responses in heavily pretreated patients with metastatic melanoma using T-cell transfer immunotherapy. Clin Cancer Res 2011;17:4550-7.

3. Prieto PA, Yang JC, Sherry RM, et al. CTLA-4 blockade with ipilimumab: long-term follow-up of 177 patients with metastatic melanoma. Clin Cancer Res 2012; 18:2039-47.

4. Eroglu Z, Kim DW, Wang X, et al. Long term survival with cytotoxic T lymphocyte-associated antigen 4 blockade using tremelimumab. Eur J Cancer 2015; 51:2689-97.

5. Schadendorf D, Hodi FS, Robert C, et al. Pooled analysis of long-term survival data from phase II and phase III trials of ipilimumab in unresectable or metastatic melanoma. J Clin Oncol 2015;33:1889-94.

6. Hamid O, Robert C, Daud A, et al. Safety and tumor responses with lambrolizumab (anti–PD-1) in melanoma. N Engl J Med 2013;369:134-44.

7. Robert C, Ribas A, Wolchok JD, et al. Anti-programmed-death-receptor-1 treatment with pembrolizumab in ipilimumab-refractory advanced melanoma: a randomised dose-comparison cohort of a phase 1 trial. Lancet 2014;384:1109-17.

8. Ansell SM, Lesokhin AM, Borrello I, et al. PD-1 blockade with nivolumab in relapsed or refractory Hodgkin's lymphoma. N Engl J Med 2015;372:311-9.

9. Robert C, Long GV, Brady B, et al. Nivolumab in previously untreated melanoma without *BRAF* mutation. N Engl J Med 2015;372:320-30.

10. Robert C, Schachter J, Long GV, et al. Pembrolizumab versus ipilimumab in advanced melanoma. N Engl J Med 2015; 372:2521-32.

11. Ribas A, Hamid O, Daud A, et al. Association of pembrolizumab with tumor response and survival among patients with advanced melanoma. JAMA 2016; 315:1600-9.

12. Restifo NP, Marincola FM, Kawakami Y, Taubenberger J, Yannelli JR, Rosenberg SA. Loss of functional beta 2-microglobulin in metastatic melanomas from five patients receiving immunotherapy. J Natl Cancer Inst 1996;88:100-8.

13. D'Urso CM, Wang ZG, Cao Y, Tatake R, Zeff RA, Ferrone S. Lack of HLA class I antigen expression by cultured melanoma cells FO-1 due to a defect in B2m gene expression. J Clin Invest 1991;87: 284-92.

14. Sucker A, Zhao F, Real B, et al. Genetic evolution of T-cell resistance in the course of melanoma progression. Clin Cancer Res 2014;20:6593-604.

15. Kaplan DH, Shankaran V, Dighe AS, et al. Demonstration of an interferon gamma-dependent tumor surveillance system in immunocompetent mice. Proc Natl Acad Sci USA 1998;95:7556-61.

16. Dunn GP, Sheehan KC, Old LJ, Schreiber RD. IFN unresponsiveness in LNCaP cells due to the lack of JAK1 gene expression. Cancer Res 2005;65: 3447-53.

17. Eisenhauer EA, Therasse P, Bogaerts J, et al. New response evaluation criteria in solid tumours: revised RECIST guideline (version 1.1). Eur J Cancer 2009;45: 228-47.

18. Wolchok JD, Hoos A, O'Day S, et al. Guidelines for the evaluation of immune therapy activity in solid tumors: immune-related response criteria. Clin Cancer Res 2009;15:7412-20.

19. Tumeh PC, Harview CL, Yearley JH, et al. PD-1 blockade induces responses by inhibiting adaptive immune resistance. Nature 2014;515:568-71.

20. Nazarian R, Shi H, Wang Q, et al. Melanomas acquire resistance to B-RAF(V600E) inhibition by RTK or N-RAS upregulation. Nature 2010;468:973-7.

21. Atefi M, Avramis E, Lassen A, et al. Effects of MAPK and PI3K pathways on PD-L1 expression in melanoma. Clin Cancer Res 2014;20:3446-57.

22. Shi H, Hugo W, Kong X, et al. Acquired resistance and clonal evolution in melanoma during BRAF inhibitor therapy. Cancer Discov 2014;4:80-93.

23. Robbins PF, Morgan RA, Feldman SA, et al. Tumor regression in patients with metastatic synovial cell sarcoma and melanoma using genetically engineered lymphocytes reactive with NY-ESO-1. J Clin Oncol 2011;29:917-24.

24. Dunn GP, Bruce AT, Ikeda H, Old LJ, Schreiber RD. Cancer immunoediting: from immunosurveillance to tumor escape. Nat Immunol 2002;3:991-8.

25. Krzywinski M, Schein J, Birol I, et al. Circos: an information aesthetic for comparative genomics. Genome Res 2009;19: 1639-45.

26. Cerami E, Gao J, Dogrusoz U, et al. The cBio Cancer Genomics Portal: an open platform for exploring multidimensional cancer genomics data. Cancer Discov 2012;2:401-4.

27. Bach EA, Aguet M, Schreiber RD. The IFN gamma receptor: a paradigm for cytokine receptor signaling. Annu Rev Immunol 1997;15:563-91.

28. Müller M, Briscoe J, Laxton C, et al. The protein tyrosine kinase JAK1 complements defects in interferon-alpha/beta and -gamma signal transduction. Nature 1993;366:129-35.

29. Watling D, Guschin D, Müller M, et al. Complementation by the protein tyrosine kinase JAK2 of a mutant cell line defective in the interferon-gamma signal transduction pathway. Nature 1993;366: 166-70.

30. Corrales L, Gajewski TF. Endogenous and pharmacologic targeting of the STING pathway in cancer immunotherapy. Cytokine 2016;77:245-7.

31. Pardoll DM. The blockade of immune checkpoints in cancer immunotherapy. Nat Rev Cancer 2012;12:252-64.

32. Finke JH, Zea AH, Stanley J, et al. Loss of T-cell receptor zeta chain and p56lck in T-cells infiltrating human renal cell carcinoma. Cancer Res 1993;53:5613-6.

33. Marvel D, Gabrilovich DI. Myeloid-derived suppressor cells in the tumor microenvironment: expect the unexpected. J Clin Invest 2015;125:3356-64.

34. Marincola FM, Jaffee EM, Hicklin DJ, Ferrone S. Escape of human solid tumors from T-cell recognition: molecular mechanisms and functional significance. Adv Immunol 2000;74:181-273.

35. Dunn GP, Old LJ, Schreiber RD. The three Es of cancer immunoediting. Annu Rev Immunol 2004;22:329-60.

36. Ribas A. Adaptive immune resistance: how cancer protects from immune attack. Cancer Discov 2015;5:915-9.

37. Fish EN, Platanias LC. Interferon receptor signaling in malignancy: a network of cellular pathways defining biological outcomes. Mol Cancer Res 2014; 12:1691-703.

Supplemental Appendix

Acquired resistance to PD-1 blockade through interferon pathway mutations

List of Investigators:

Jesse M. Zaretsky B.S., Angel Garcia-Diaz Ph.D., Daniel Sanghoon Shin M.D., Helena Escuin-Ordinas Ph.D., Willy Hugo Ph.D., Siwen Hu-Lieskovan MD Ph.D., Davis Y. Torrejon M.D., Gabriel Abril-Rodriguez M.Sc., Salemiz Sandoval Ph.D., Lucas Barthly M.Sc., Justin Saco B.S., Blanca Homet Moreno M.D., Riccardo Mezzadra M.Sc., Bartosz Chmielowski M.D. Ph.D., Kathleen Ruchalski M.D., I. Peter Shintaku Ph.D., Phillip J. Sanchez Ph.D., Cristina Puig-Saus Ph.D., Grace Cherry R.N. N.P., Elizabeth Seja B.A., Xiangju Kong M.Sc., Jia Pang B.S., Beata Berent-Maoz Ph.D., Begoña Comin-Anduix Ph.D., Thomas G. Graeber Ph.D., Paul C. Tumeh M.D. Ph.D., Ton N.M. Schumacher Ph.D., Roger S. Lo M.D. Ph.D., Antoni Ribas M.D. Ph.D.

Supplementary Appendix

Table of Contents

1) Supplementary Methods

2) Supplementary Figures

3) Supplementary Tables

4) Supplementary References

Supplementary Methods

Tumour samples and cell lines

Patients underwent baseline biopsies before starting on therapy, early on therapy biopsies[1-3] (in some patients), and upon progression. When feasible, biopsy samples were split into three with one aliquot immediately fixed in formalin followed by paraffin embedding for pathological analyses, a second aliquot snap frozen by immediate immersion in liquid nitrogen for genetic analyses, and if there was residual tissue it was sterily processed in the laboratory to establish a cell line as previously described[4,5] . Cell lines were periodically authenticated using GenePrint® 10 System (Promega, Madison, WI), and were matched with the earliest passage cell lines. Tumour biopsy and peripheral blood cell collection and analyses were approved by UCLA IRBs 11-001918 and 11-003066. Snap frozen samples were disrupted in lysis buffer by BeadBug microtube homogenizer (Benchmark Scientific, Edison, NJ) using disposable stainless steel beads. DNA and RNA from snap frozen samples and cell lines were extracted concurrently using the Qiagen All-Prep kit (Qiagen, , Benelux B.V., Venlo, The Netherlands) and mirVana miRNA isolation kit (ThermoFisher, Canoga Park, CA). Ambion RecoverAll kit (also ThermoFisher) was used for DNA extraction from FFPE slides.

Immunohistochemistry and Immunofluorescence

Slides were stained for immunohistochemistry with S100 (Dako, Carpinteria, CA, CD8 (Dako), PD-L1 (all clone SP142, Spring Bio, Pleasanton, CA, except the PD-L1 in Figs S1B, S2B, and S2C which were previously stained[3] with clone 22C3, Merck). Staining was performed at the UCLA Anatomic Pathology IHC Laboratory. Immunostaining was performed on Leica Bond III autostainers using Leica Bond ancillary reagents and REFINE polymer DAB detection system as previously described[3]. Staining for MHC Class I (clone HC 10, Saphirre NA, Ann Arbor, MI) and MHC Class II (HLA-DR, sc-53319, Santa Cruz

Biotechnology, Santa Cruz, CA) was performed by the UCLA Translational Pathology Core Laboratory. Slides were scanned at 40X on an Aperio ScanScope AT (Leica Biosystems, Buffalo Grove, IL) and analyzed on the Halo Platform (Indica Labs, Corrales, NM). Immnofluoresecnce was performed with OPAL-5-plex reagents, imaged at 20X on the Vectra Automated Quantitative Pathology Imaging System, and analyzed using inForm software (all from Perkin-Elmer, Waltham, MA). Staining used the following antibodies: S100 (DAKO), CD8 (DAKO), PD-L1 (all clone SP142, Spring Bio), and Sox10 (Biocare Medical, Concord, CA).

Genetic analyses

Exon capture and library preparation were performed at the UCLA Clinical Microarray Core using the Roche Nimblegen SeqCap EZ Human Exome Library v3.0 targeting 64 Mb of genome. 2x100bp paired-end sequencing was carried out on the HiSeq 2000 platform (Illumina, San Diego, CA) and sequences were aligned to the UCSC hg19 reference using BWA-mem (v0.7.9). Sequencing for tumors and matched normal DNA from peripheral blood mononuclear cells was performed to a target depth of 150X (actual: minimum 90X, maximum 348X, median 143X). Pre-processing followed the Genome Analysis Toolkit (GATK) Best Practices Workflow v3, including duplicate removal, indel realignment, and base quality score recalibration.

Somatic mutations were called against a paired normal sample with methods as previously reported[6]. In brief, high-confidence mutations were retained if identified by at least two out of three programs between: MuTect (v1.1.7)[7], Varscan2 Somatic (v2.3.6)[8], and a one-sided Fisher's Exact Test (P value cut-off ≤ 0.01) for GATK-HaplotypeCaller (HC) calls between tumour/normal pairs for single nucleotide variants. Insertions/deletions were included if called by both Varscan2 and the GATK-HC. Variants were annotated by a stand-alone version of Oncotator[9] using the Dec112014 datasource. Non-synonymous mutations were those classified as nonsense, missense, splice_site, or nonstop mutations, frame_shift, in_frame_, or start_codon altering insertions/deletions. Purity, ploidy, and allele-specific copy number status was determined by Sequenza[10] with default settings. Adjusted variant allele frequency was calculated according to the following equation to adjust for stromal content and copy number, with tumor/stromal fractions and local copy number from Sequenza output.

$$VAFadjusted = VAFobserved * [1 + (2 * Stromal\ Fraction)/(Tumor\ Fraction * Local\ Copy\ Number)]$$

Sanger validation of JAK and B2M mutations and Targeted Amplicon Re-Sequencing

The following primers pairs were used for PCR amplification of the mutation-containing region of JAK1, JAK2 and B2M from cases #1, #2, and #3 respectively.

JAK1 296bp: 5’ caatgccttctcctggacctt 3’ and 5’ ccgaaccgtgcagactgtag 3’

JAk2 241bp: 5’ acctcaccaacattacagaggc 3’ and 5’ acatctaacacaaggttggca 3’

B2M 257bp: 5’ cttgtcctgattggctgggc 3’ and 5’ acttggagaagggaagtcacg 3’

PCR was performed with 250ng input genomic DNA using the AccuPrime Taq DNA Polymerase System (ThermoFisher, Canoga Park, CA) and cycling protocol 94°C 2 min, [94°C 30 sec, 52°C 1min, 68°C 1min] X 35 cycles , 68°C 10min, 4°C hold.

Products were purified by agarose gel elecrtophoresis and submitted for either Sanger sequencing (Laragen, Culver City, CA) or Illumina deep sequencing with the UCLA Clinical Microarray Core. Library prep of PCR products was performed without fragmentation using the KAPA Hyper Prep kit (Kapa Biosystems, Wilmington, MA), and sequenced on an Illumina Miseq 2x150bp or NextSeq 1x75bp. All sequencing reactions produced >1 million mapped reads per locus.

Western blot and flow cytometry analyses

Melanoma cell lines were maintained in 10 cm culture dishes and analyzed when approximately 70% confluent. Western blot and flow cytometry was performed as previously described[11-12] upon exposure to interferon alpha, beta or gamma (BD Bioscience, San Jose, CA) for 30 minutes or 18 hours. Experiments were performed at least twice for each cell line.

Primary antibodies included JAK1, JAK2, pSTAT1 (Tyr701), pSTAT3 (Tyr705), STAT1 and STAT3 total protein; IRF-1, PD-L1, TAP1 and GAPDH (all from Cell Signaling Technology, Danvers, MA) as well as MHC class I heavy chain clones HCA2 for HLA-A and clone HC10 for HLA-B/C (both from Sapphire NA, Ann Arbor, MI). Immuno-reactivity was revealed with an ECL-Plus kit (Amersham Biosciences Co, Piscataway, NJ), using the ChemiDoc MP system (Bio-Rad Laboratories, Hercules, CA).

Transcriptional Profiling Analysis

Total RNA was extracted from human melanoma cell lines in the absence or presence of interferon-gamma (100 IU/ml) at 3 hours according to the manufacturer's protocol (Qiagen, Benelux B.V., Venlo, The Netherlands). nCounter (NanoString Technologies, Seattle, WA) analysis was performed at the Center for Systems Biomedicine, a part of the Integrated Molecular Technologies Core (IMTC) at UCLA using the nCounter PanCancer immune profiling panel, including 769 genes to which we added 21 custom genes to capture the known interferon response genes. Through the use of color-coded probe pairs, mRNA transcripts of specific cellular genes, including housekeeping genes for normalization, were quantified in untreated M420 and M464 cells and after 3 hours of interferon gamma exposure. The list of genes included in the analysis appears in Table S4.

For RNA-seq analysis of JAK2 splicing in M420 and M464, paired-end transcriptome reads were mapped to the UCSC hg19 reference genome using Tophat2[13].

JAK CRISPR/Cas9-mediated Knockout

M407 with CRISPR/Cas9 mediated JAK1 and JAK2 knock-outs were generated by lentiviral transduction using particles encoding guide RNAs, a fully functional CAS9 cassette, green fluorescent protein, and puromycin as selectable markers (Sigma-Aldrich, St. Louis, MI). Two guide sequences were used per gene, targeting exon 4 (ccaagctctggtatgctccaaa) and exon 5 (ccaattggcatggaaccaacga) for JAK1, and exon 1 (cctgccttacgatgacagaaat) and 2 (ccaggcataatgtactctacag) for JAK2. GFP positive single cell clones were isolated using a FACSARIA sorter (Becton-Dickinson, Franklin Lakes, NJ). Clones were screened by PCR with the following primers, and reading-frame disruption was confirmed by Sanger sequencing with TIDE analysis (Tracking of Indels by Decomposition, NKI, The Netherlands, https://tide.nki.nl).

JAK1 Exon4 : 5' agtcctttctcacatcaagca 3' and 5' gccaggaatttgtttgcatgt 3'
JAK1 Exon 5: 5' cagggttgtctgcctgcttc 3' and 5' gaagctggagtttgtgggat 3'
JAK2 Exon 1: 5' acttctgggctcaagctatctg 3' and 5' cttgggaaatctgaggcaga 3'
JAK2 Exon2: 5' ggtgctgacagacttactagattc 3' and 5' gatattgctggtttgtgcagcg 3'

Finally, knockout was confirmed by Western blot.

JAK Functional Studies with T-cell Co-culture and Interferon Treatment

Parental and M407 JAK2 knock-out cells were co-cultured with human peripheral blood mononuclear cells transduced with an NY-ESO1 specific TCR[14]. Interferon-gamma release was measured in supernatant at 24 hours by ELISA (eBioscience, San Diego, CA). Proliferation assays were conducted by real-time live cell imaging in an IncuCyte ZOOM (Essen Biosciences, Ann Arbor, MI). Cell lines were stably transfected with a nuclear-localizing RFP (NucLight Red Lentivirus EF1a Reagent, Essen Bioseinces) to facilitate cell counts. Recombinant human interferon gamma (BD Bioscience, San Jose, CA), human interferon alpha and beta (EMD Millipore, Temecula, CA), and 2'3'-cGAMP (IngivoGen, San Diego, CA) were applied once to approx. 5000 cells per well seeded the previous day in a 96-well plate plate. Cells were maintained without media change for the duration of the experiments. 2'3'-cGAMP was complexed with Lipofectamine 2000 (1:500 dilution, Invitrogen, Carlsbad, CA) for cytosolic exposure. All experiments were performed with wells in triplicate at in a minimum of three independent runs. Graph production and statistical data were analyzed via Prism software (Graphpad, La Jolla, CA).

Figure S1. Clinical pattern of acquired resistance to anti-PD-1 therapy in case #2.

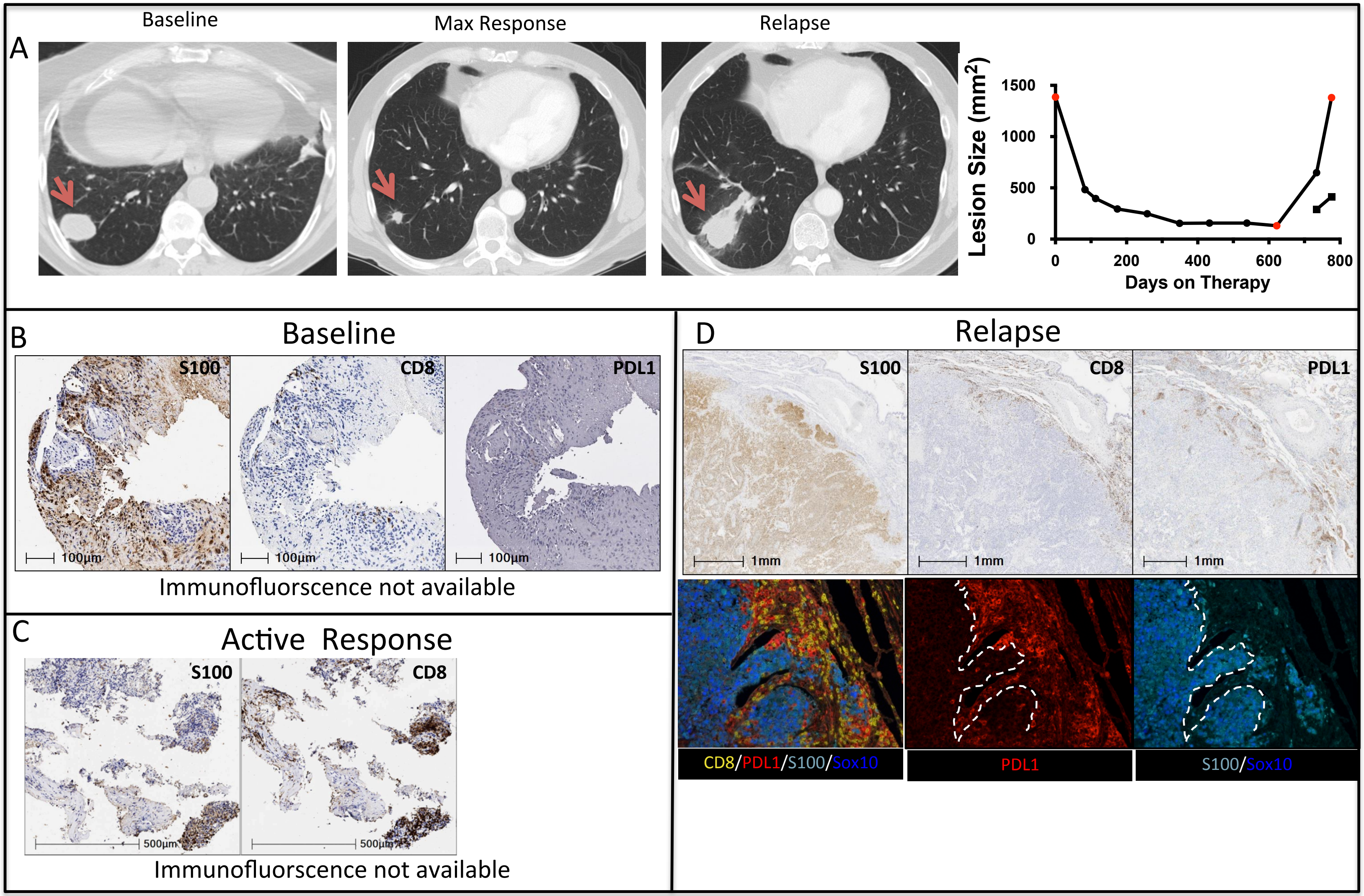

Patient #2 exhibited a 90% response in a solitary lung metastasis, followed by relapse in-situ after almost two years of minimal residual disease. Panel A shows CT images from time-points indicated by colored dots on the graph at right. Panels B-D show immunohistochemical staining of S100, CD8, and PDL1. CD8 T-cells were present at baseline (B), increased at relapse (C), and were abundant but primarily found at the tumor margin at relapse (D). At relapse, PD-L1 was not expressed on the cancer cells (Panel D). In the immunofluorescence images, red shows PD-L1, yellow shows CD8 T cells, while light blue (cytoplasmic) and dark blue (nuclear) indicate tumor markers S100 and SOX10, respectively.

Figure S2. Clinical pattern of acquired resistance to anti-PD-1 therapy in case #3.

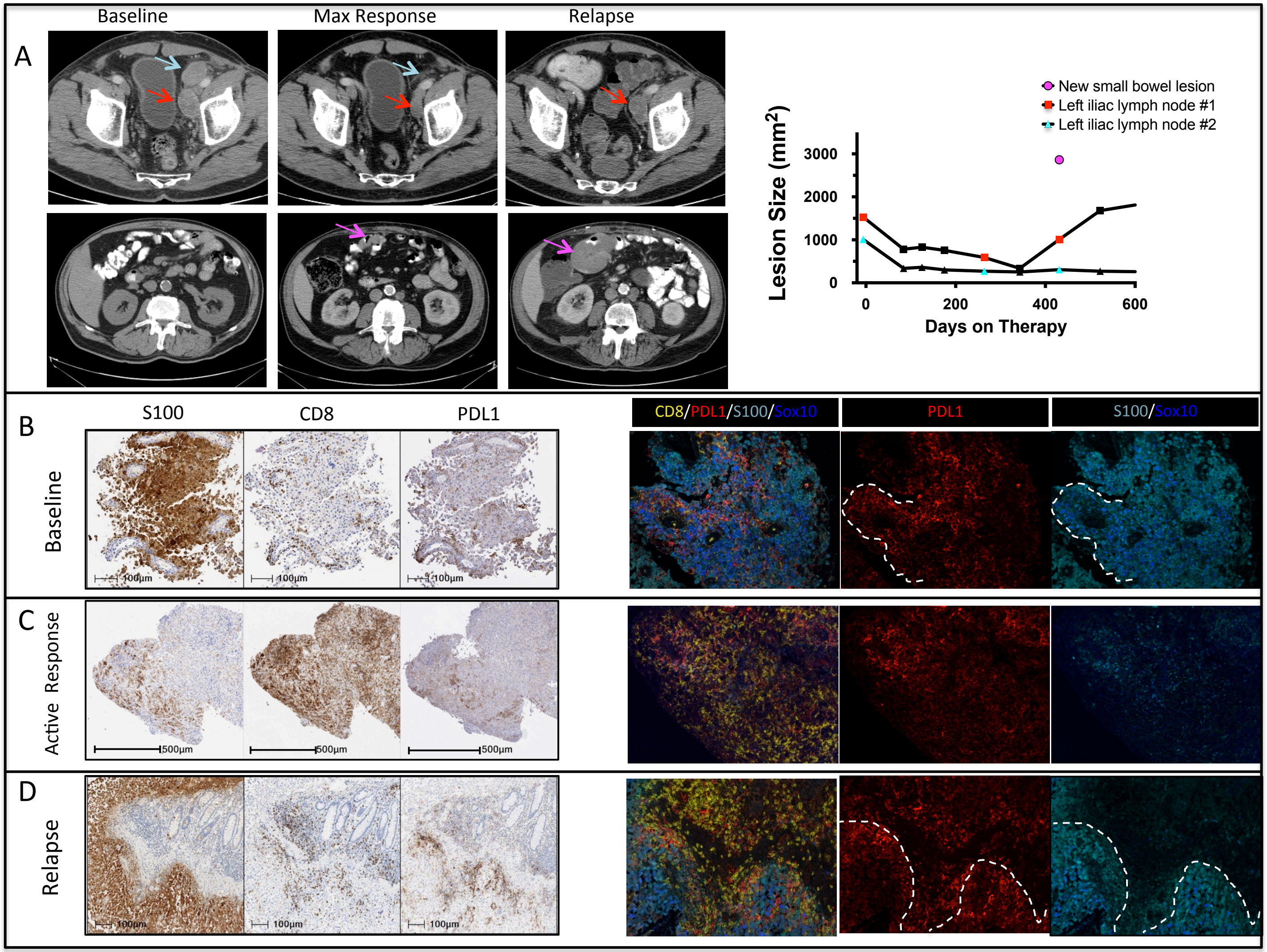

In Panel A, CT images correspond time-points indicated by colored dots on the graph at right. Inguinal lesions from baseline showed partial (red arrow) or complete (cyan arrow) regression. The relapse biopsy comes from a small bowel lesion first visualized at 264 days, with clear progression 453 days from therapy start. Panels B-D show immunohistochemical staining of S100, CD8, and PDL1 at baseline (B), during active response (day 39, C) and relapse (D), with massive CD8 infiltration during response. In the immunofluorescence images, red shows PD-L1, yellow shows CD8 T cells, while light blue (cytoplasmic) and dark blue (nuclear) indicate tumor markers S100 and SOX10, respectively.

Figure S3. Clinical pattern of acquired resistance to anti-PD-1 therapy in case #4.

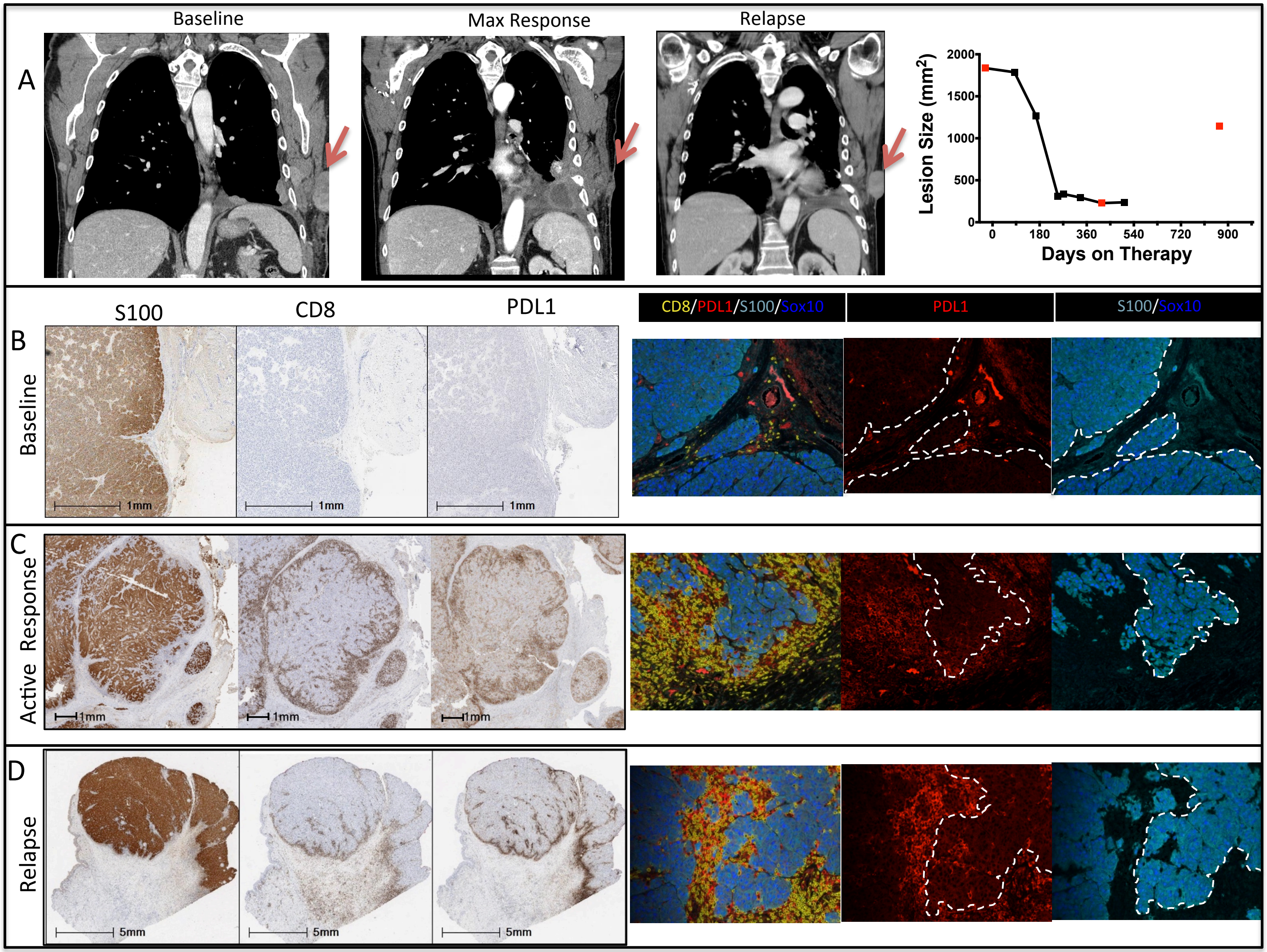

In Panel A, CT images corresponds to time-points indicated by colored dots on the graph at right. Panels B-D show immunohistochemical staining of S100, CD8, and PDL1 at baseline (B), during active response (day 187, C) and relapse (D). Case #4 had a very small pre-existing T-cell infiltrate which increased over time, corresponding to an initial pseudoprogression followed by a tumor response, as previously described[3]. The progressing tumor at relapse shows equally strong CD8 infiltration and local PD-L1 expression as active response, though PD-L1 is not expressed on the cancer cells at either timepoint. In the immunofluorescence images, red shows PD-L1, yellow shows CD8 T cells, while light blue (cytoplasmic) and dark blue (nuclear) indicate tumor markers S100 and SOX10, respectively.

Figure S4. Relapse-specific JAK2 splice site mutation causes near universal intron inclusion.

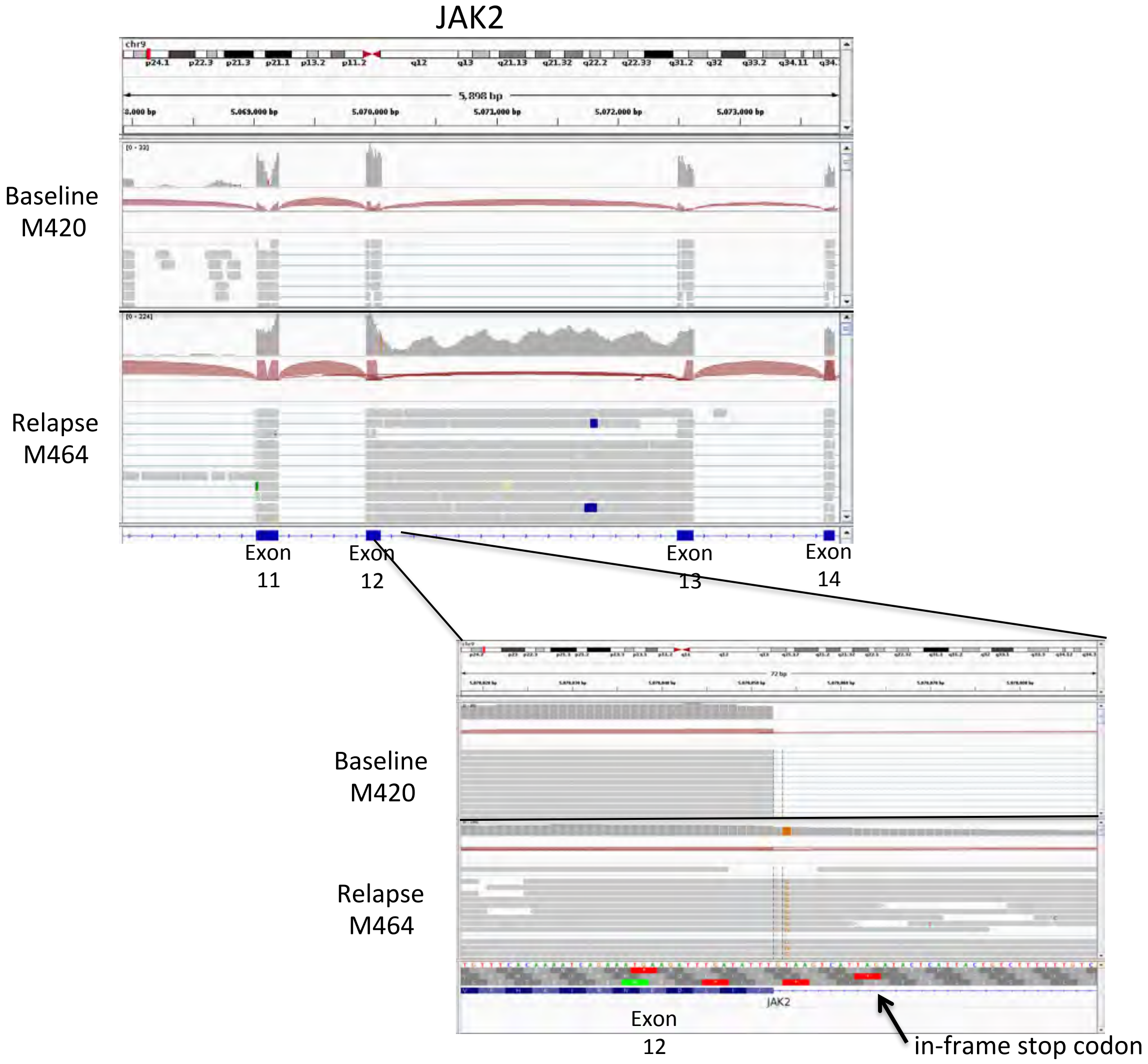

IGV plot of RNA-Seq reads for JAK2 exons 11-14 from the baseline and relapse cell lines from case #2. Intron-inclusion is only seen at relapse. Magnified locus shows RNA reads containing the splice site mutations continuing through the exon 12 exon/intron junction in the relapse cell line, compared to those at baseline that span the exon 12/13 splice junction (Reads with abrupt end at exon 12 with blue line indicating continuation of the RNA read at exon13). Intron inclusion introduces an in-frame stop codon within 10 base pairs of intron (arrow).

Figure S5. Relapse-specific JAK1, JAK2, and B2M mutations are not found at baseline by Sanger or Illumina deep amplicon sequencing

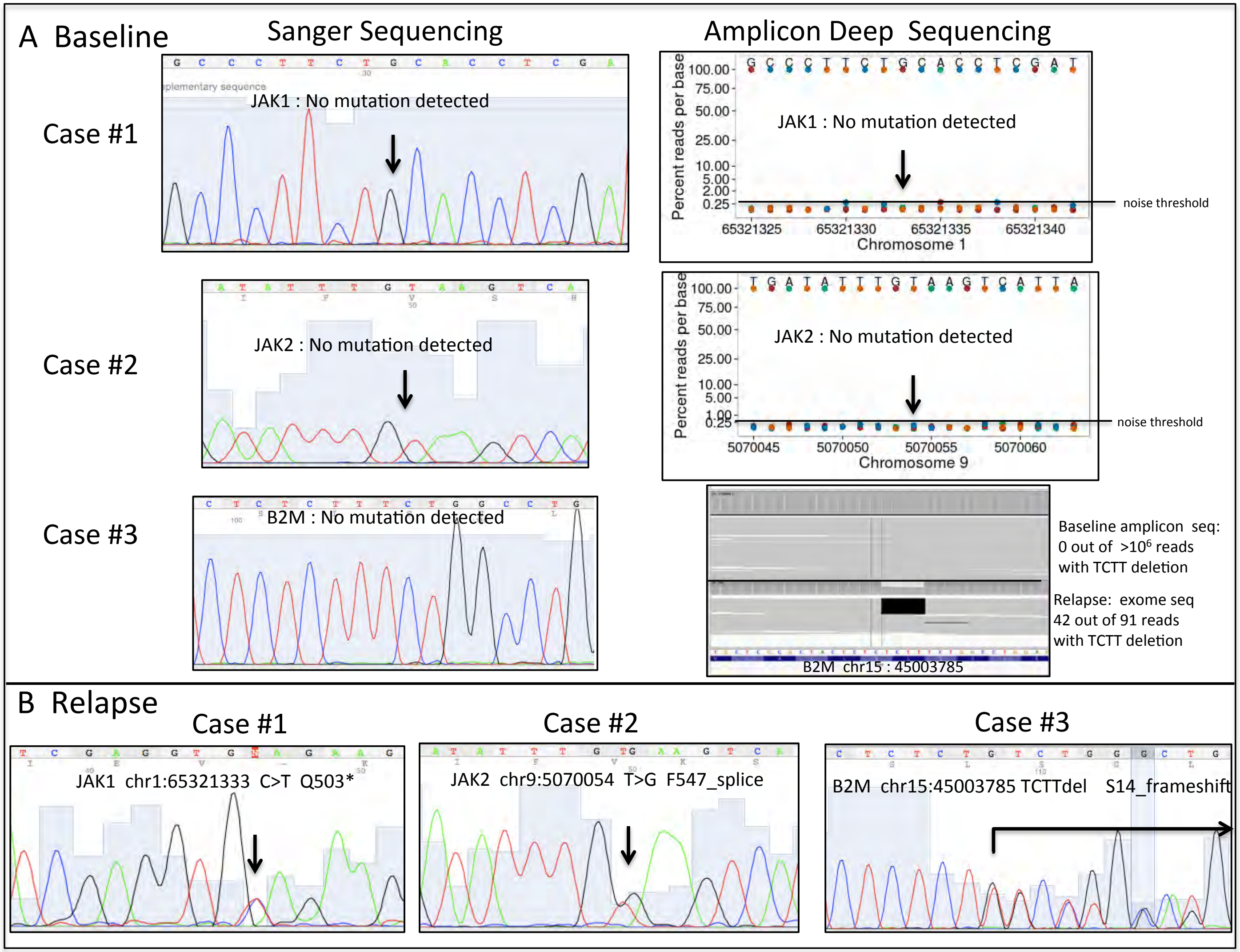

Panel A shows the JAK1, JAK2 and B2M mutations identified at relapse were not observed in PCR amplified genomic DNA from the baseline samples for case #1, #2, and #3 respectively, either by Sanger sequencing (left) or Illumina amplicon re-sequencing (right). For case #1 and #2, graphs show the percentage of each base per position out of 1 million mapped reads. No mutations were observed above the background error rate of ~0.25%. The case #3 baseline sample also had 0 detectable reads with the 4 basepair B2M deletion out of 1.6 million mapped reads examined. IGV plot shows representative sampling, with the relapse mutation for reference. In Panel B, Sanger sequencing of PCR products from genomic DNA of the relapse biopsies confirms the presence of the indicated mutations.

Figure S6. Changes in germline SNP allele frequency shows loss-of-heterozygosity upon relapse on chromosome 1p.

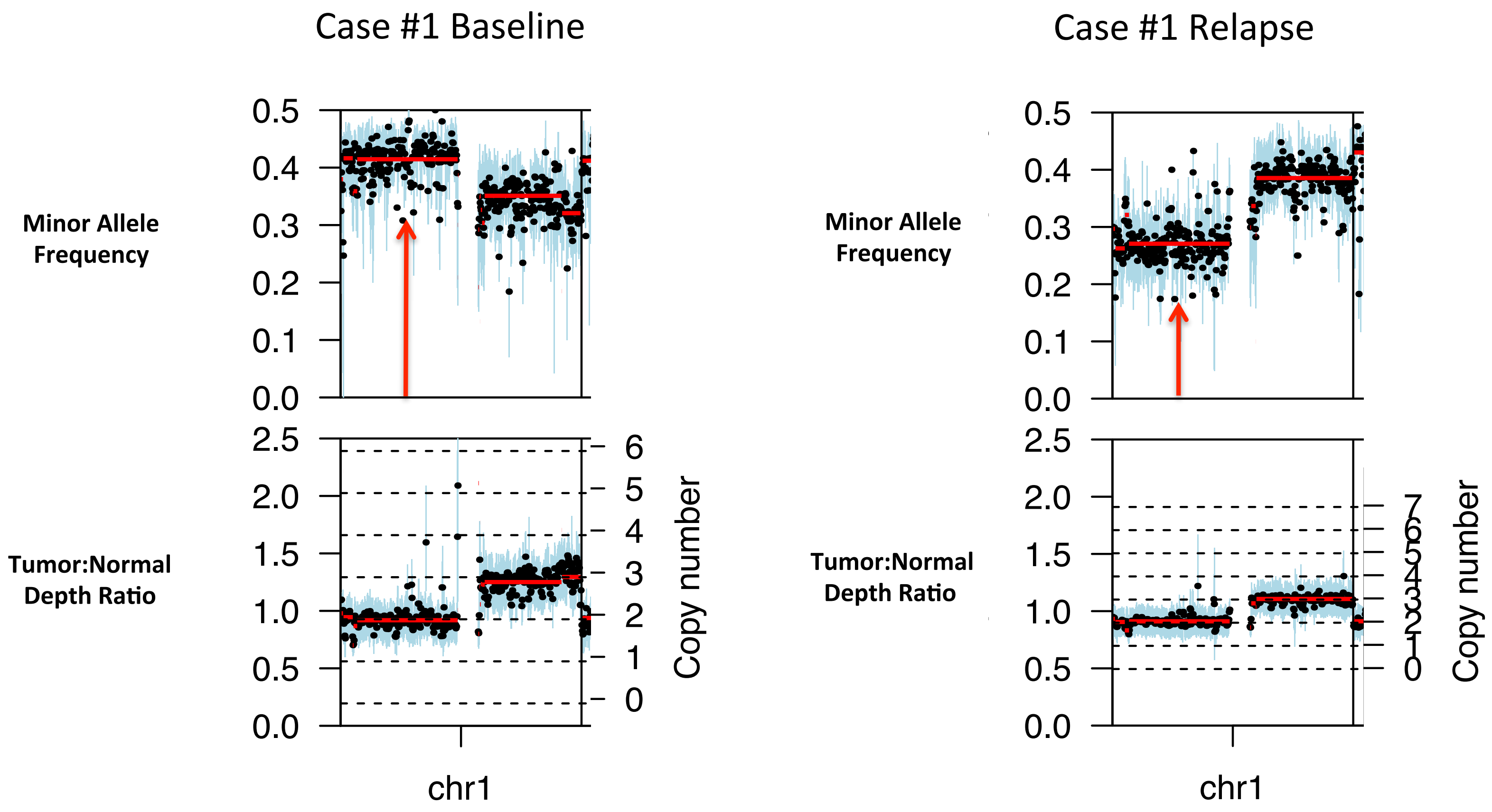

Sequenza output with upper plot showing the minor allele frequencies for germline single nucleotide polymorphisms (SNPs) on chromosome 1, and the lower plot showing the read depth ratio and stroma-adjusted copy number estimate. There is a decrease in SNP frequency for chromosome 1p upon relapse, yet there is no change in relative depth ratio (bottom panel), indicating stable overall copy number. Together, they suggest a copy-number neutral loss of heterozygosity event.

Figure S7. Model schematic of JAK mutation acquisition in the setting of copy-number neutral loss-of-heterozygosity events.

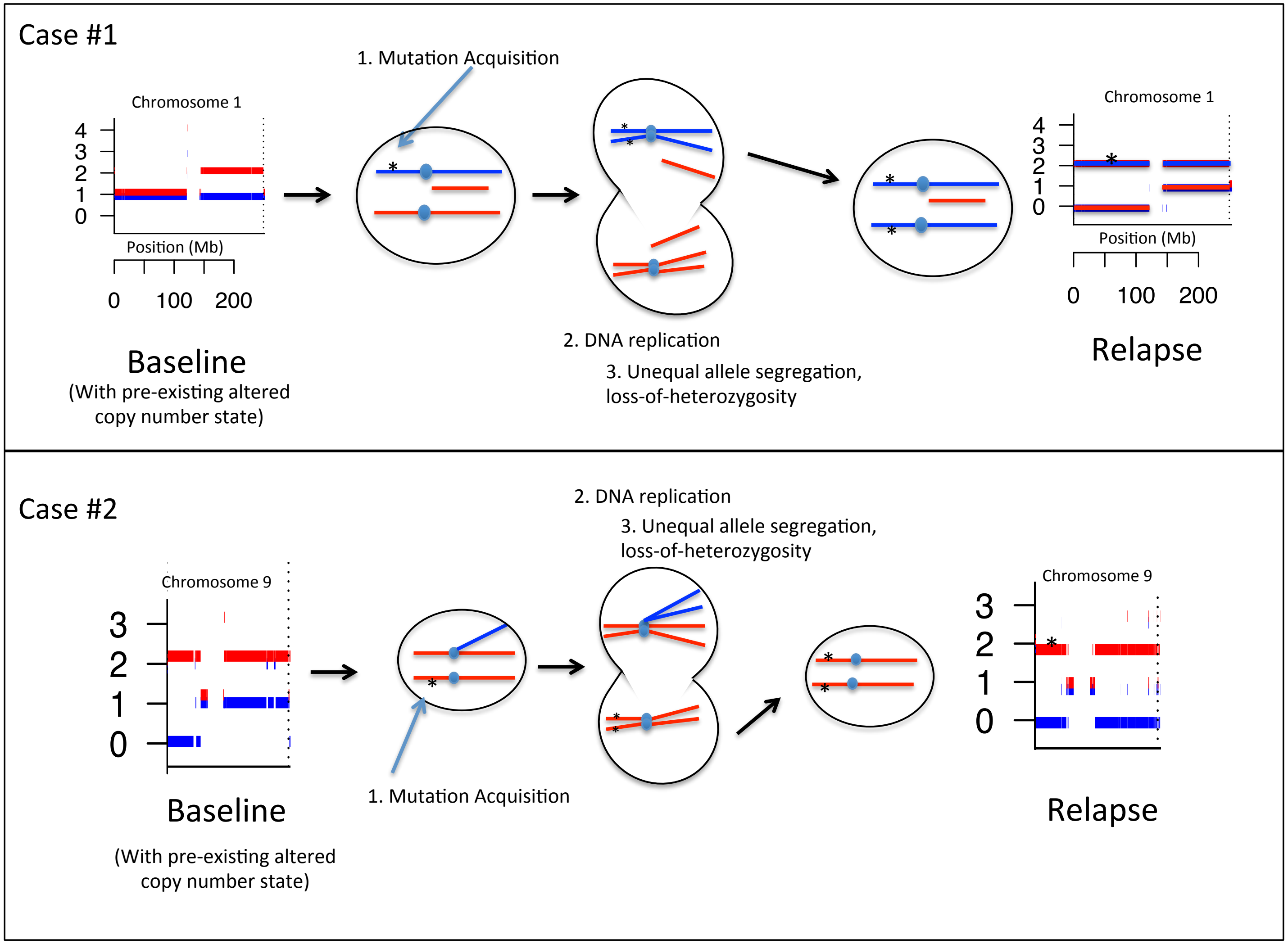

The JAK mutations in case #1 and case #2 were not observed at baseline, but were seen at homozygous allele frequency at relapse. We suggest the mutations were likely first acquired, then later followed by DNA replication and unequal allele segregation, resulting in loss of heterozygosity (and loss of the wild-type allele) without overall copy number change. This is modeled in the top panel for chromosome 1 in case #1, and in the bottom panel for chromosome 9 in case #2. Red and blue represent the maternal and paternal alleles, with arbitrary coloring.

Figure S8. Cell line M464 derived from case #2 relapse is almost identical to the snap-frozen tumor.

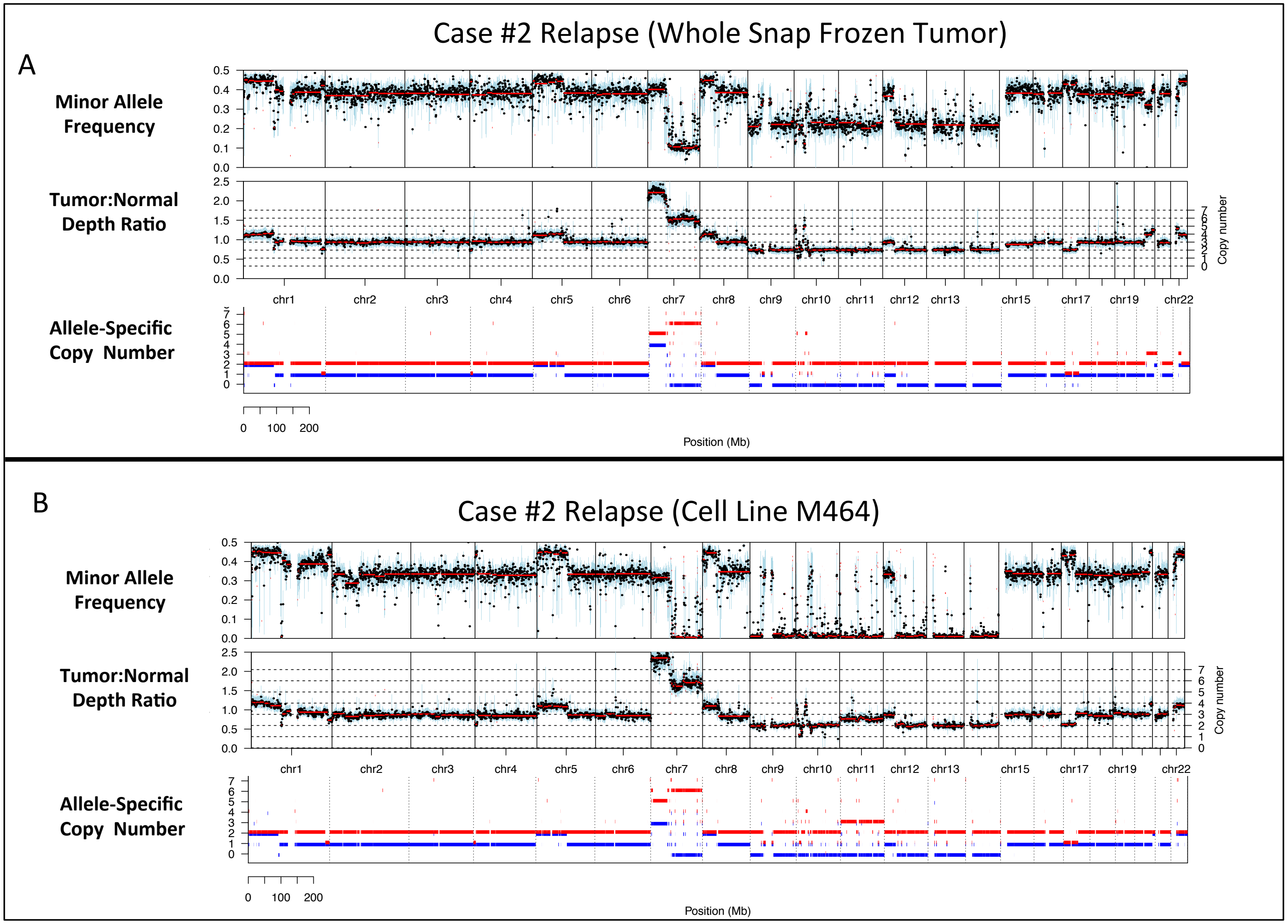

Genome-wide Sequenza plots show the minor-allele frequency, depth ratio, and allele-specific copy number from sequencing of both the snap-frozen whole tumor (Panel A) and the cell line (M464, Panel B) derived from the relapse biopsy in case #2. After model-fit adjustment for the 44% contaminating normal DNA in the bulk tumor (from lung stroma, immune infiltrates, etc), the allele-specific copy number estimates (bottom red/blue track) are nearly identical across most chromosomes between the bulk tumor and cell line.

Figure S9 CRISPR/Cas-9 knockout of JAK1 in M407.

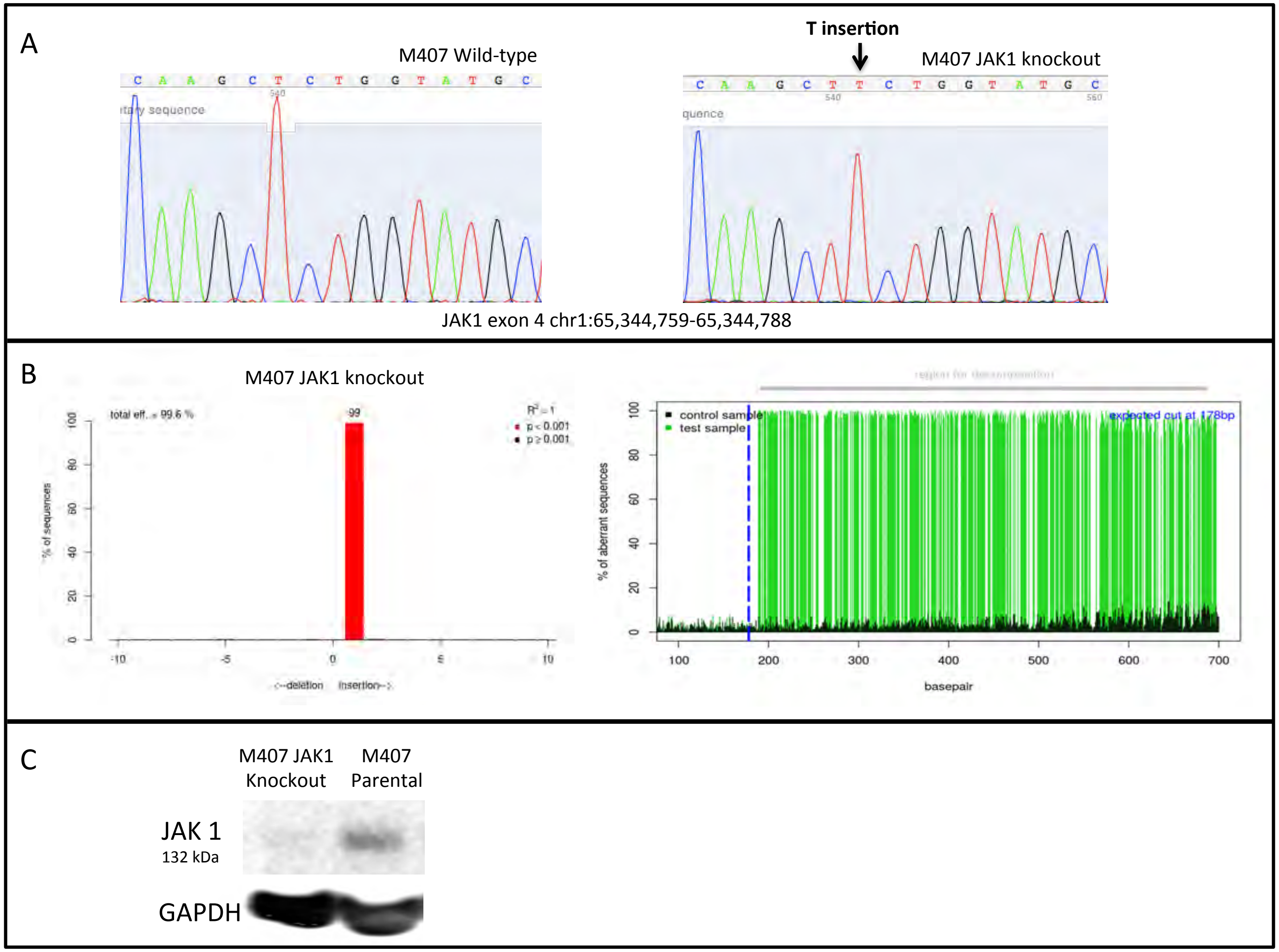

Panel A shows Sanger sequence of JAK1 exon 4 in the M407 parental cell line (left) versus the CRISPR/Cas9 edited subline (right.) showing insertion of a single thymine at the cutpoint. Panel B shows trace decomposition analysis of the JAK1 mutation by TIDE[15], showing 99% of alleles of sequences contain the one basepair insertion. Panel C shows total loss of JAK1 protein by western blot in this cell line.

Figure S10 CRISPR/Cas-9 knockout of JAK2 in M407.

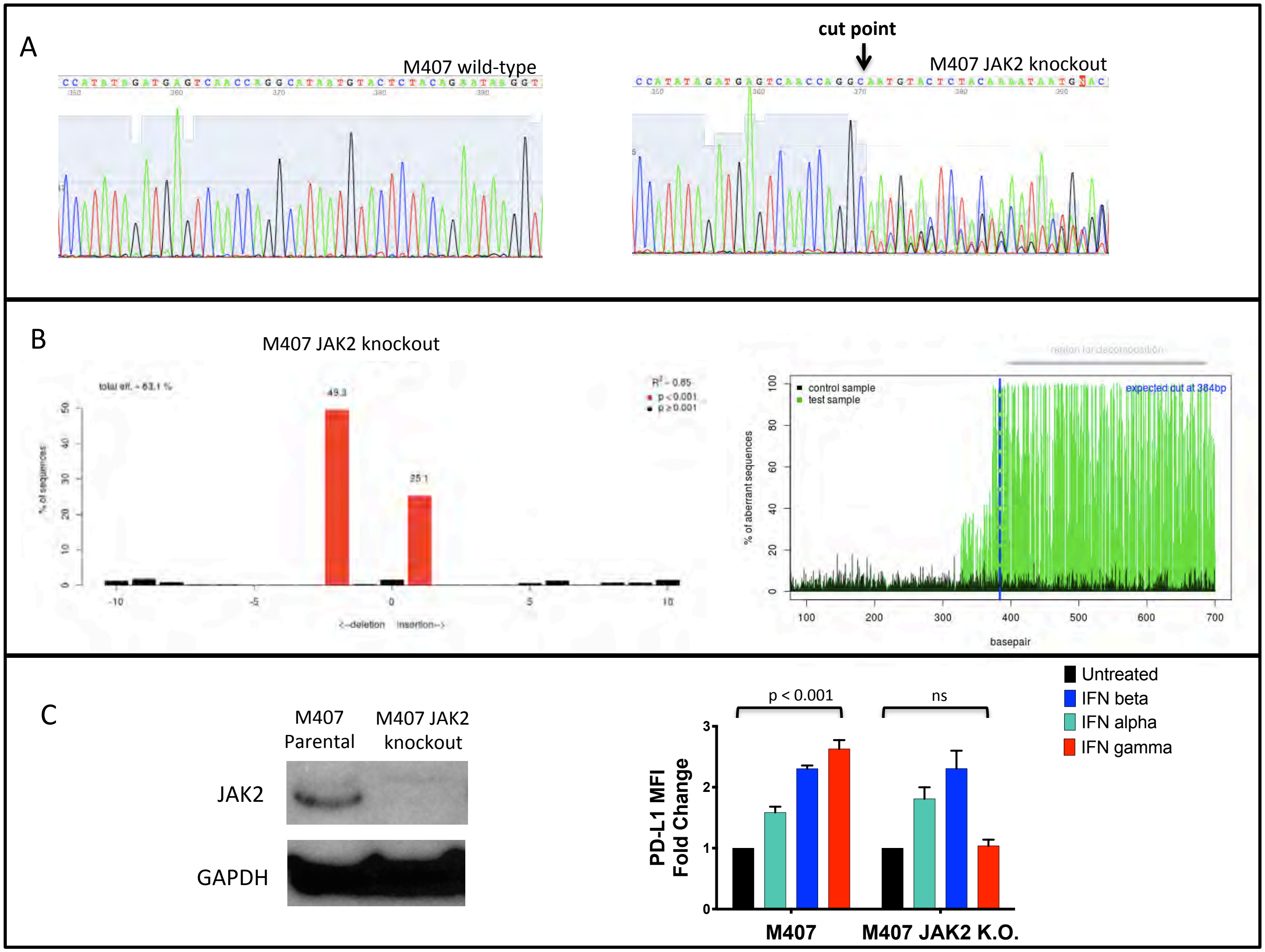

Panel A shows Sanger sequence of JAK2 exon 2 in the M407 parental cell line (left) versus the CRISPR/Cas9 edited subline (right.) Arrow shows the main breakpoint. Panel B shows trace decomposition analysis of the JAK2 mutation by TIDE[15]. Panel C shows total loss of JAK2 protein by western blot, and lack of PD-L1 upregulation in response interferon-gamma compared to parental cell line, with no change in response to interferon alpha or beta.

Figure S11. Dose-dependent growth inhibition of M420 and M407 by interferon alpha, beta, and gamma

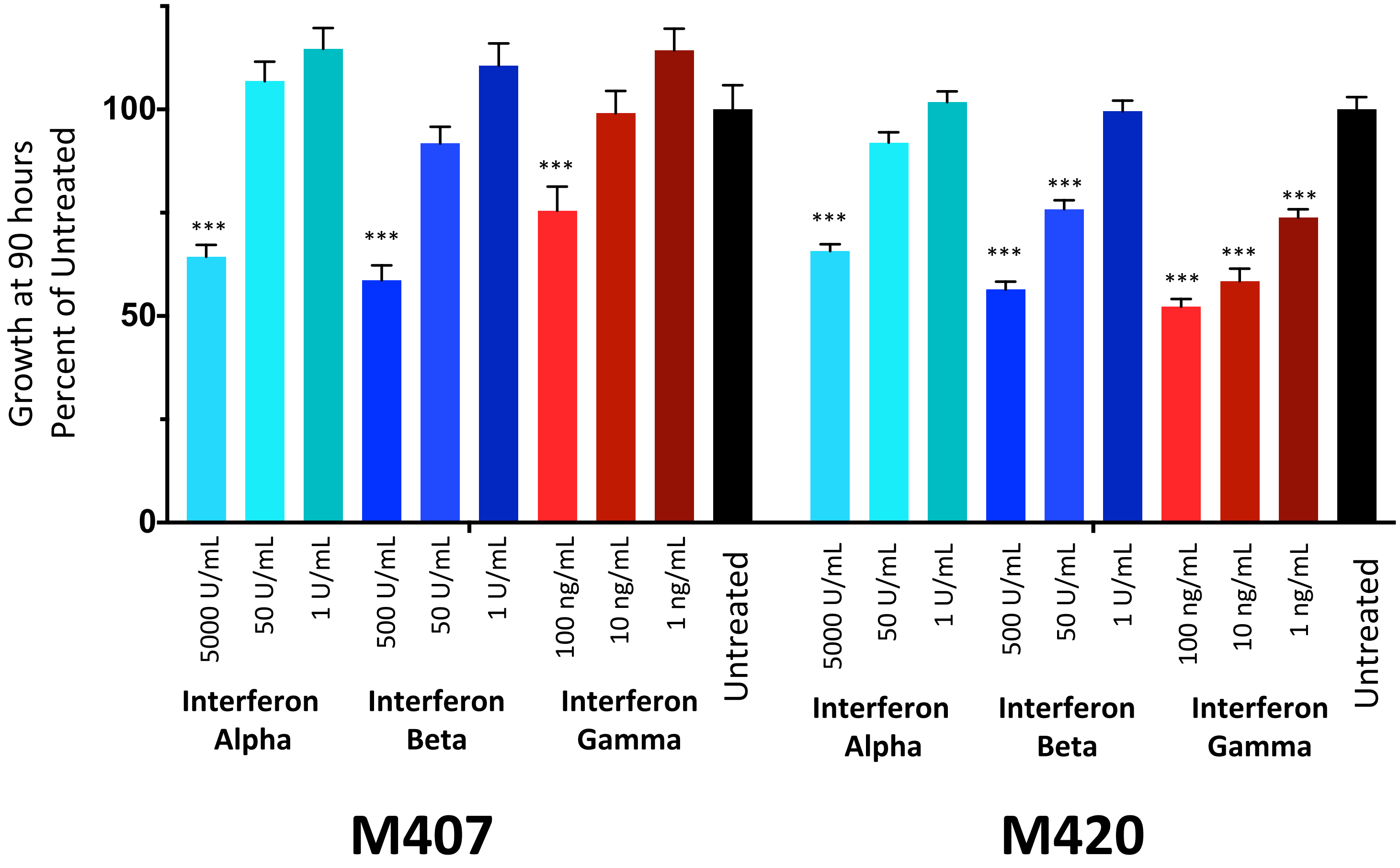

Cell lines M420 and M407 were cultured in-vitro with recombinant human interferon alpha, beta, or gamma. Both cell lines showed significant (~50%) decrease in growth at the 90hr endpoint compared to untreated cells at the highest doses. M420 showed significant dose-sensitive inhibition at lower concentrations for beta and gamma, though there was a dose-sensitive trend for all interferons in both cell lines. Results are shown for a single representative experiment, three replicate wells per condition. Error bars show standard error of the mean. *** = p-value < 0.001 with Dunnett's multiple comparison correction. All others not significant.

Figure S12. Class II MHC immunohistochemistry and additional example of loss of Class I MHC membrane localization in Case #3 relapse biopsy with B2M mutation.

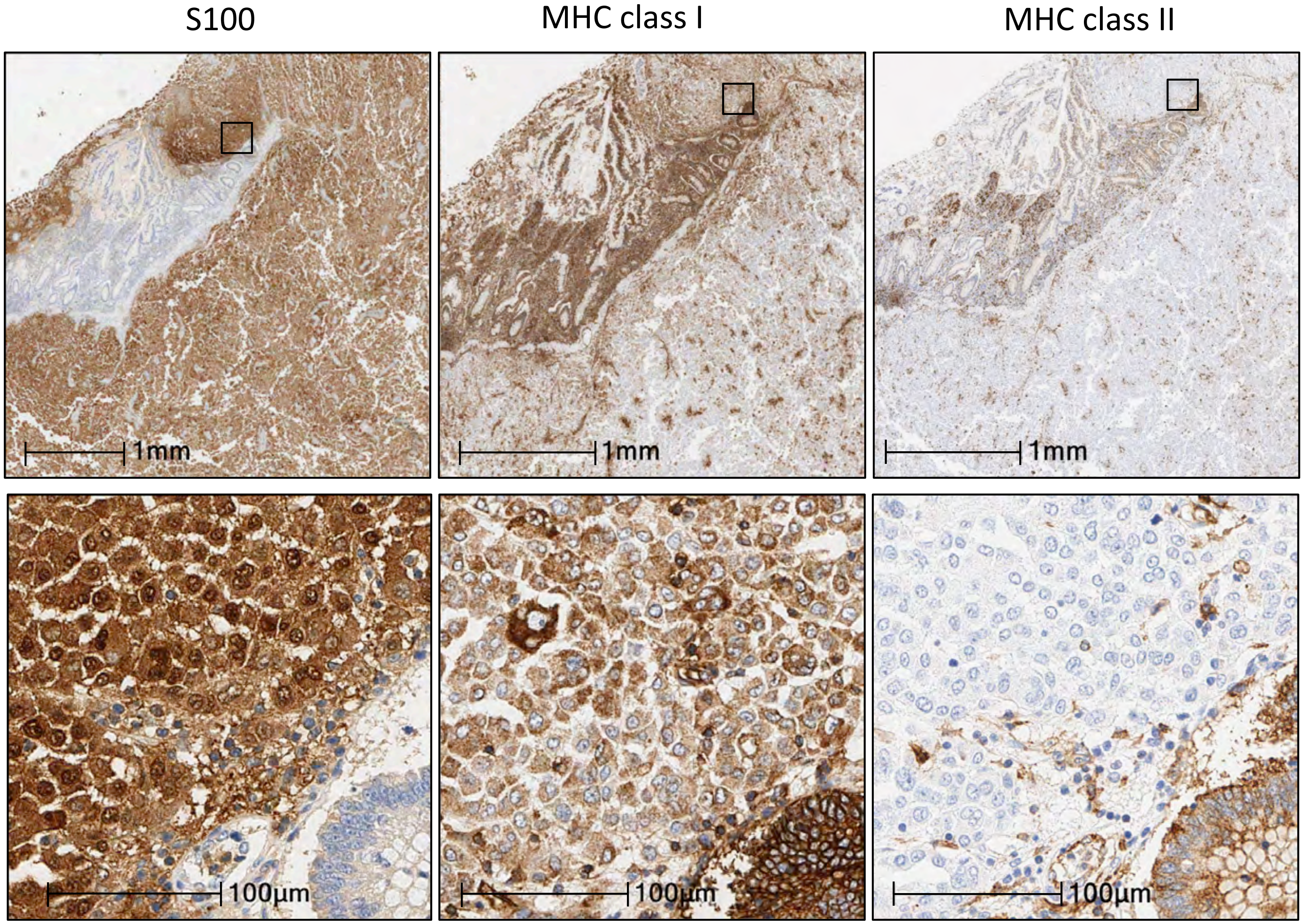

Immunohistochemical staining of MHC class I (clone HC10, specific for some HLA-A, and all HLA-B/C heavy chains) shows lack of localization to the outer cell membrane of S100-positive tumor cells, especially as contrasted to normal adjacent bowel tissue. By contrast, the tumor appears negative for MHC class II. Lower panel represents boxed insets from upper panel.

Chapter 3:

Primary resistance to PD-1 blockade mediated by JAK1/2 mutations.

RESEARCH ARTICLE

Primary Resistance to PD-1 Blockade Mediated by *JAK1/2* Mutations

Daniel Sanghoon Shin[1], Jesse M. Zaretsky[1], Helena Escuin-Ordinas[1], Angel Garcia-Diaz[1], Siwen Hu-Lieskovan[1], Anusha Kalbasi[1], Catherine S. Grasso[1], Willy Hugo[1], Salemiz Sandoval[1], Davis Y. Torrejon[1], Nicolaos Palaskas[1], Gabriel Abril-Rodriguez[1], Giulia Parisi[1], Ariel Azhdam[1], Bartosz Chmielowski[1,2], Grace Cherry[1], Elizabeth Seja[1], Beata Berent-Maoz[1], I. Peter Shintaku[1], Dung T. Le[3], Drew M. Pardoll[3], Luis A. Diaz, Jr[3], Paul C. Tumeh[1], Thomas G. Graeber[1,2], Roger S. Lo[1,2], Begoña Comin-Anduix[1,2], and Antoni Ribas[1,2]

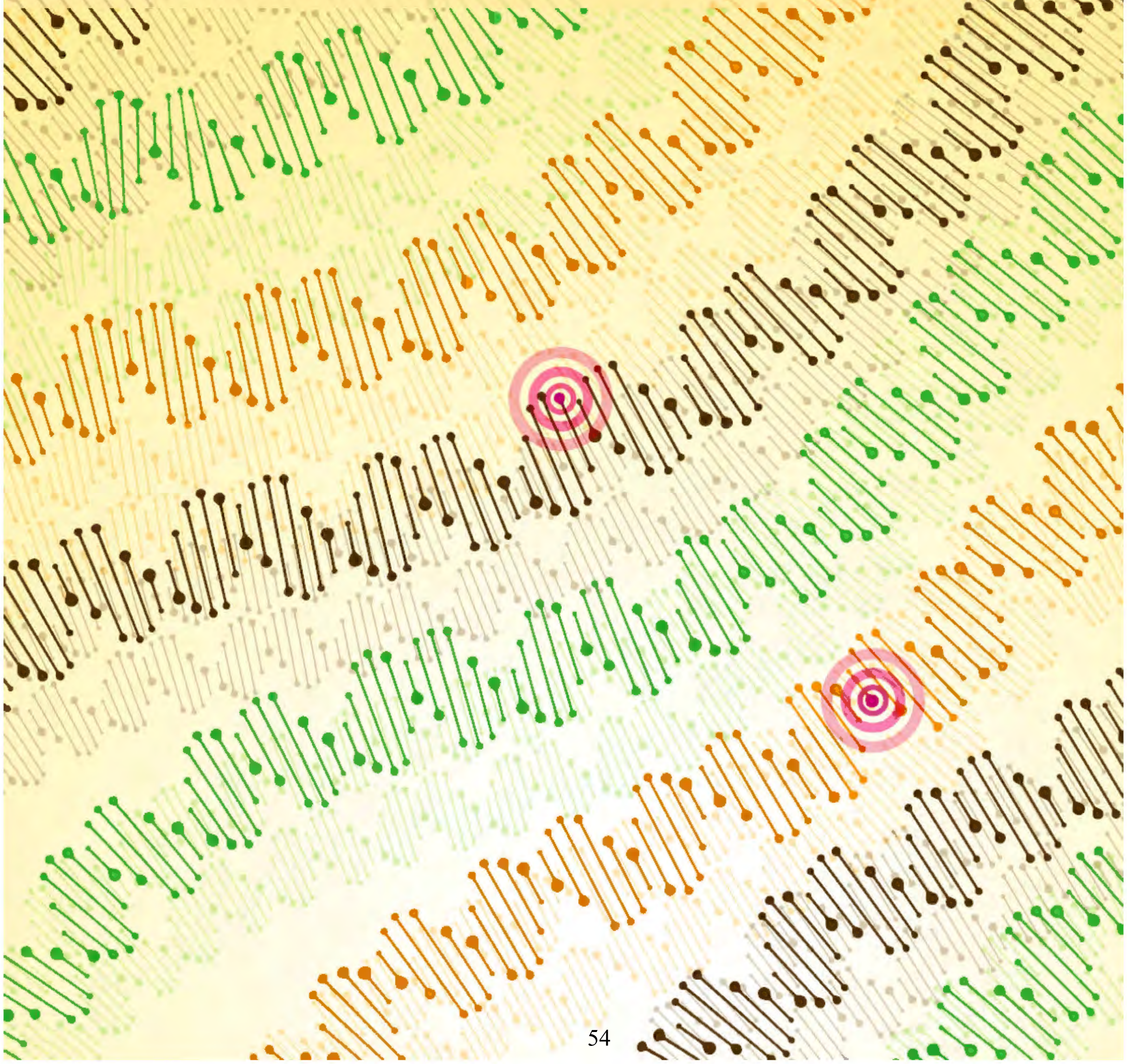

ABSTRACT Loss-of-function mutations in *JAK1/2* can lead to acquired resistance to anti–programmed death protein 1 (PD-1) therapy. We reasoned that they may also be involved in primary resistance to anti–PD-1 therapy. *JAK1/2*-inactivating mutations were noted in tumor biopsies of 1 of 23 patients with melanoma and in 1 of 16 patients with mismatch repair–deficient colon cancer treated with PD-1 blockade. Both cases had a high mutational load but did not respond to anti–PD-1 therapy. Two out of 48 human melanoma cell lines had *JAK1/2* mutations, which led to a lack of PD-L1 expression upon interferon gamma exposure mediated by an inability to signal through the interferon gamma receptor pathway. *JAK1/2* loss-of-function alterations in The Cancer Genome Atlas confer adverse outcomes in patients. We propose that *JAK1/2* loss-of-function mutations are a genetic mechanism of lack of reactive PD-L1 expression and response to interferon gamma, leading to primary resistance to PD-1 blockade therapy.

SIGNIFICANCE: A key functional result from somatic *JAK1/2* mutations in a cancer cell is the inability to respond to interferon gamma by expressing PD-L1 and many other interferon-stimulated genes. These mutations result in a genetic mechanism for the absence of reactive PD-L1 expression, and patients harboring such tumors would be unlikely to respond to PD-1 blockade therapy. *Cancer Discov; 7(2); 188–201. ©2016 AACR.*

See related commentary by Marabelle et al., p. 128.

INTRODUCTION

Blocking the programmed death 1 (PD-1) negative immune receptor results in unprecedented rates of long-lasting antitumor activity in patients with metastatic cancers of different histologies, including melanoma, Hodgkin disease, Merkel cell carcinoma, and head and neck, lung, esophageal, gastric, liver, kidney, ovarian, bladder, and high mutational load cancers with defective mismatch repair, among others, in a rapidly growing list (1–8). This remarkable antitumor activity is explained by the reactivation of tumor antigen–specific T cells that were previously inactive due to the interaction between PD-1 and its ligand PD-L1 expressed by cancer cells (1, 9–12). Upon tumor antigen recognition, T cells produce interferon gamma, which through the interferon gamma receptor, the Janus kinases JAK1 and JAK2, and the signal transducers and activators of transcription (STAT) results in the expression of a large number of interferon-stimulated genes. Most of these genes lead to beneficial antitumor effects, such as increased antigen presentation through inducible proteasome subunits, transporters associated with antigen processing (TAP), and the major histocompatibility complex (MHC), as well as increased production of chemokines that attract T cells and direct tumor growth arrest and apoptosis (13). However, interferon gamma also provides the signal that allows cancer cells to inactivate antitumor T cells by the adaptive expression of PD-L1 (9), thereby specifically escaping their cytotoxic effects (12).

Acquired resistance to PD-1 blockade in patients with advanced melanoma can be associated with loss-of-function mutations with loss of heterozygosity in *JAK1/2* or in beta 2-microglobulin (*B2M*; ref. 14). The complex genetic changes leading to acquired resistance to PD-1 blockade, wherein one *JAK1/2* allele was mutated and amplified and the other was lost, suggest a strong selective pressure induced by the therapeutic immune response. Similar events leading to lack of sensitivity to interferon gamma have been reported in the cancer immune-editing process and acquired resistance to immunotherapy in mouse models (15–17) and in patients treated with the anti–CTLA-4 antibody ipilimumab who did not respond to therapy (18). Therefore, lack of interferon gamma responsiveness allows cancer cells to escape from antitumor T cells, and in the context of anti–PD-1/PD-L1 therapy, results in the loss of PD-L1 expression, the target of PD-1 blockade therapy, which would abrogate the antitumor efficacy of this approach.

In order to explore the role of *JAK1* and *JAK2* disruption in primary resistance to PD-1 blockade therapy, we performed a genetic analysis of tumors from patients with melanoma and colon cancer who did not respond to PD-1 blockade therapy despite having a high mutational load. We identified tumors with homozygous loss-of-function mutations in *JAK1* and *JAK2* and studied the functional effects of deficient interferon gamma receptor signaling that lead to a genetically mediated absence of PD-L1 expression upon interferon gamma exposure.

RESULTS

JAK Loss-of-Function Mutations in Primary Resistance to PD-1 Blockade in Patients with Metastatic Melanoma

Recent data indicate that tumors with a high mutational burden are more likely to have clinical responses to PD-1

---

[1]University of California, Los Angeles (UCLA), Los Angeles, California. [2]Jonsson Comprehensive Cancer Center, Los Angeles, California. [3]Johns Hopkins Sidney Kimmel Comprehensive Cancer Center, Baltimore, Maryland.

Note: Supplementary data for this article are available at Cancer Discovery Online (http://cancerdiscovery.aacrjournals.org/).

Corresponding Author: Antoni Ribas, Department of Medicine, Division of Hematology-Oncology, UCLA, 11-934 Factor Building, 10833 Le Conte Avenue, Los Angeles, CA 90095-1782. Phone: 310-206-3928; Fax: 310-825-2493; E-mail: aribas@mednet.ucla.edu

doi: 10.1158/2159-8290.CD-16-1223

blockade therapy (6, 19–21). However, in all of these series some patients failed to respond despite having a high mutational load. We performed whole-exome sequencing (WES) of 23 pretreatment biopsies from patients with advanced melanoma treated with anti–PD-1 therapy, which included 14 patients with a tumor response by immune-related RECIST (irRECIST) criteria and 9 without a response (Supplementary Table S1). Even though the mean mutational load was higher in responders than nonresponders, as reported for lung, colon, and bladder cancers (6, 19, 21), some patients with a tumor response had a low mutational load and some patients without a tumor response had a high mutational load (Fig. 1A).

We then assessed whether loss-of-function mutations in interferon receptor signaling molecules, which would prevent adaptive expression of PD-L1, might be present in tumors with a relatively high mutational load that did not respond to therapy. A melanoma biopsy from the patient with the highest mutational load among the 9 nonresponders (patient #15) had a somatic P429S missense mutation in the src-homology (SH2) domain of *JAK1* (Fig. 1B). WES of an early passage cell line derived from this tumor (M431) showed an amplification of chromosome 1p, including the *JAK1* locus, and a 4:1 mutant:wild-type allele ratio was observed at both the DNA and RNA level (Supplementary Fig. S1A–S1E and Supplementary Database S1). None of the tumors from the other 22 patients had homozygous loss-of-function mutations or deletions in the interferon receptor pathway. Rather, the other *JAK2* mutations found in biopsies of responders had low variant allele frequency (VAF) as shown in Fig. 1B and were likely heterozygous. These mutations would not carry the same functional significance, as signaling would still occur upon interferon exposure through the wild-type JAK protein from the nonmutated allele. Two nonresponders had *IFNGR* mutations, also of low allele frequency and therefore uncertain significance. We also analyzed potential mutations in genes involved in the antigen-presenting machinery and did not find any loss-of-function mutations that were homozygous (Supplementary Fig. S2).

As expected, tumors from patients who responded had a higher density of CD8 cells and PD-L1 in the center and invasive tumor margin (Fig. 1C and D). In contrast, the baseline biopsy from patient #15 with a high mutational load but with the *JAK1*^{P429S} missense mutation had undetectable CD8 infiltrates, PD-1 and PD-L1 expression (Supplementary Fig. S3). The amplification of *PD-L1*, *PD-L2*, and *JAK2* (PDJ amplicon), which has been associated with a high response rate in Hodgkin disease (4), was noted only in patient #16, who did not respond to PD-1 blockade therapy despite having the second highest mutational load and a high level of PD-L1 expression (Fig. 1B, D and E).

Functional Analyses of the Role of *JAK* Loss-of-Function Mutations in Regulating PD-L1 Expression

We next sought to characterize the interferon response of M431, the melanoma cell line established from a biopsy of patient #15 with high mutational load and no response to therapy. First, we optimized flow cytometry conditions in selected human melanoma cell lines (Supplementary Figs. S4A–S4F, S5A–S5D, S6A–S6H, and S7A–S7C). PD-L1 expression increased less than 1.5-fold interferon gamma exposure in M431 (Fig. 2A), versus 5.1-fold in M438, a cell line established from patient #8 used as a positive control in this same series. Phosphorylated STAT1 (pSTAT1) was induced at 30 minutes in M431, but the signal dissipated at 18 hours, faster than in cell lines with more durable responses to interferon gamma leading to PD-L1 upregulation (Fig. 2B, C compared with Supplementary Fig. S8A–S8C). These data are consistent with the 4:1 *JAK1* mutant:wild-type allele frequency in the M431 cell line (Supplementary Fig. S1A–S1E).

We then screened a panel of 48 human melanoma cell lines for absolute absence of PD-L1 induction by either type I (alpha and beta) or type II (gamma) interferons. Among the three interferons, interferon gamma most potently induced PD-L1 expression (Fig. 2D; Supplementary Fig. S9A and S9B for type I interferons). Two cell lines had *JAK1/2* homozygous loss-of-function mutations and did not respond to interferon gamma with upregulation of surface PD-L1 expression. M368 had a mutation in *JAK2* (20 out of 22 reads, VAF = 0.91) that is predicted to disrupt and shift the D313 splice-site acceptor in exon 8 by one nucleotide, changing the reading frame, and had loss of the wild-type allele (Fig. 3A; Supplementary Fig. S10A and S10B). M395 had an inactivating *JAK1*^{D775N} kinase domain mutation in exon 17 and loss of the other allele (140 out of 143 reads, variant allele frequency 0.98; Fig. 3B).

We then analyzed signaling in response to interferon alpha, beta, and gamma in these two cell lines. M368, which harbored the *JAK2* loss-of-function mutation, maintained signaling in response to interferon alpha and beta, but did not respond to interferon gamma (Fig. 3C), which resulted in the ability of M368 to upregulate PD-L1 when exposed to interferon alpha and beta, but not to interferon gamma (Fig. 3C; Supplementary Fig. S9A and S9B). M395, which harbored the *JAK1* loss-of-function mutation, did not respond to downstream signaling to interferon alpha, beta, or gamma (Fig. 3D), and equally did not upregulate PD-L1 in response to any of these cytokines (Fig. 3D; Supplementary Fig. S9A and S9B). We were able to retrieve the tumor from which the cell line M395 had been established, and this tumor exhibited an absence of CD8 infiltration similar to the finding in patient #15 with a *JAK1* loss-of-function mutation who did not respond to anti–PD-1 therapy (Supplementary Fig. S11). Taken together, these data are consistent with the knowledge that JAK1 (disabled in M395) is required to propagate signaling downstream of the interferon alpha/beta and gamma receptors, whereas JAK2 (disabled in M368) is required for signaling downstream only from the interferon gamma receptor (22–24).

To assess a causal relationship between loss of adaptive PD-L1 expression and loss-of-function *JAK* mutations, we transduced the M395 and M431 cell lines with a lentivirus vector expressing *JAK1* wild-type (Supplementary Fig. S12A–S12C). Reintroduction of wild-type JAK1 rescued PD-L1 expression in M395 cells, which exhibited a 4-fold increase in PD-L1 surface expression after interferon gamma exposure (Fig. 3E). For M431, the magnitude of change in PD-L1 expression after 18-hour interferon gamma exposure for M431 was modest after reintroducing the JAK1 wild-type protein (approximately 2-fold, compared with a 1.5-fold in the untransduced cell line; Fig. 3F). However, the difference between untransduced and

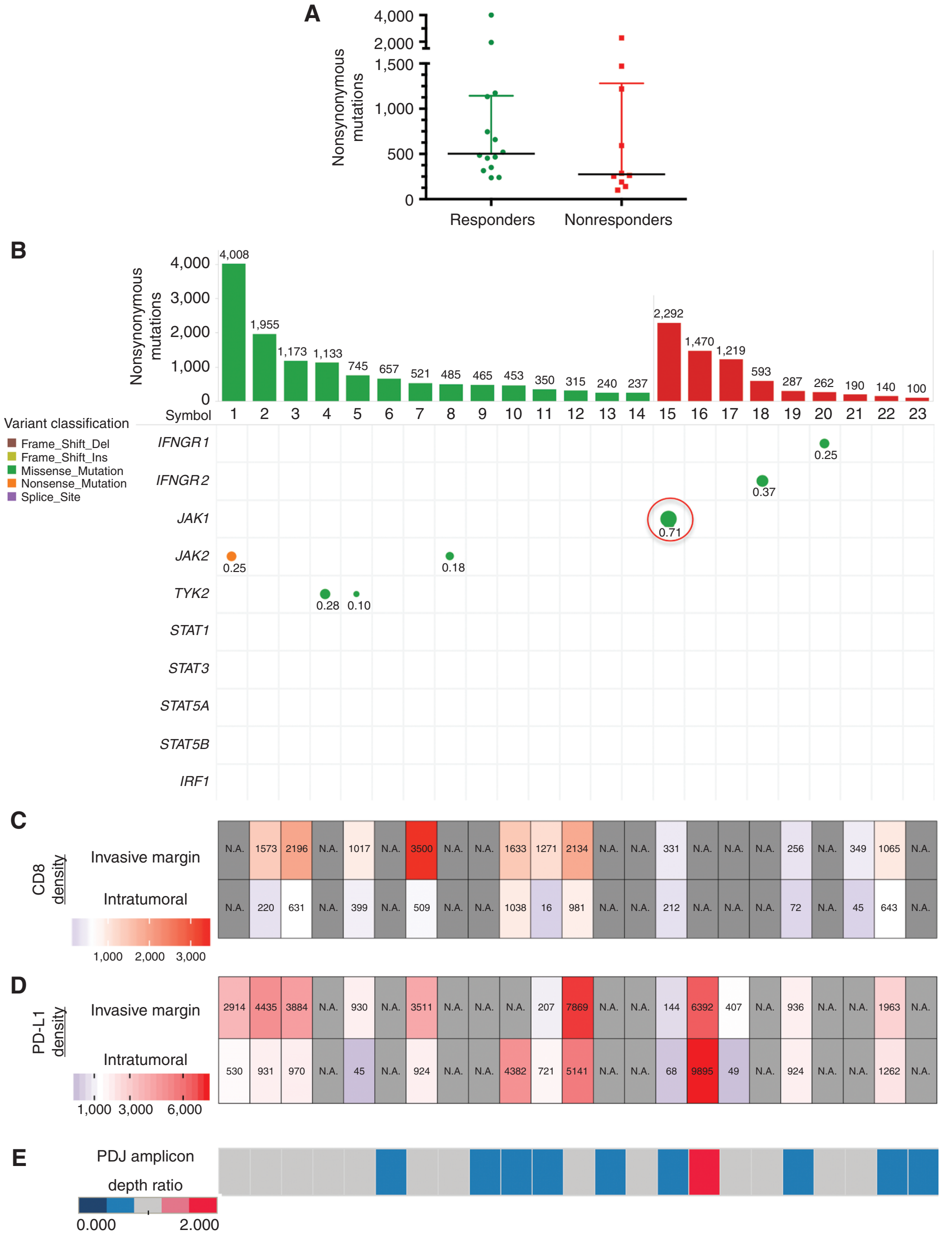

C

CD8 density	1	2	3	4	5	6	7	8	9	10	11	12	13	14	15	16	17	18	19	20	21	22	23
Invasive margin	N.A.	1573	2196	N.A.	1017	N.A.	3500	N.A.	N.A.	1633	1271	2134	N.A.	N.A.	331	N.A.	N.A.	N.A.	256	N.A.	349	1065	N.A.
Intratumoral	N.A.	220	631	N.A.	399	N.A.	509	N.A.	N.A.	1038	16	981	N.A.	N.A.	212	N.A.	N.A.	N.A.	72	N.A.	45	643	N.A.

D

PD-L1 density	1	2	3	4	5	6	7	8	9	10	11	12	13	14	15	16	17	18	19	20	21	22	23
Invasive margin	2914	4435	3884	N.A.	930	N.A.	3511	N.A.	N.A.	N.A.	207	7869	N.A.	N.A.	144	6392	407	N.A.	936	N.A.	N.A.	1963	N.A.
Intratumoral	530	931	970	N.A.	45	N.A.	924	N.A.	N.A.	4382	721	5141	N.A.	N.A.	68	9895	49	N.A.	924	N.A.	N.A.	1262	N.A.

Figure 1. Mutational load and mutations in the interferon signaling pathway among patients with advanced melanoma with or without response to anti–PD-1 blockade therapy. **A,** Total nonsynonymous mutations per tumor from biopsies of patients with response ($n = 14$) or without response ($n = 9$) to anti–PD-1 per RECIST 1.1 criteria (median 503 vs. 274, $P = 0.27$ by Mann–Whitney). Median and interquartile range are shown, with value for each individual tumor shown as dots. **B–D,** Each column corresponds to an individual case from **A**. **B,** Depiction of mutational load (bar graph) and mutations in interferon receptor pathway genes. The size of circles and adjacent labels represents the tumor VAF after adjustment for stromal content. Color represents predicted functional effect. Green, missense; orange, nonsense. Red circle highlights amplified *JAK1* mutation in one patient who did not respond to anti–PD-1 therapy. All the tumor sequences were compared to normal germline sequences. **C,** Heat map of the density of CD8 T cells in the invasive margin or intratumor compartment analyzed in baseline tumor biopsies by immunohistochemistry. **D,** Heat map of density of PD-L1 expression in available tissue samples. **E,** Genetic amplification of the chr9p24.1 (*PD-L1*, *PD-L2*, and *JAK2* locus, termed the PDJ amplicon) was noted in one biopsy from a nonresponding patient. Heat map represents average read depth ratio versus paired germline normal.

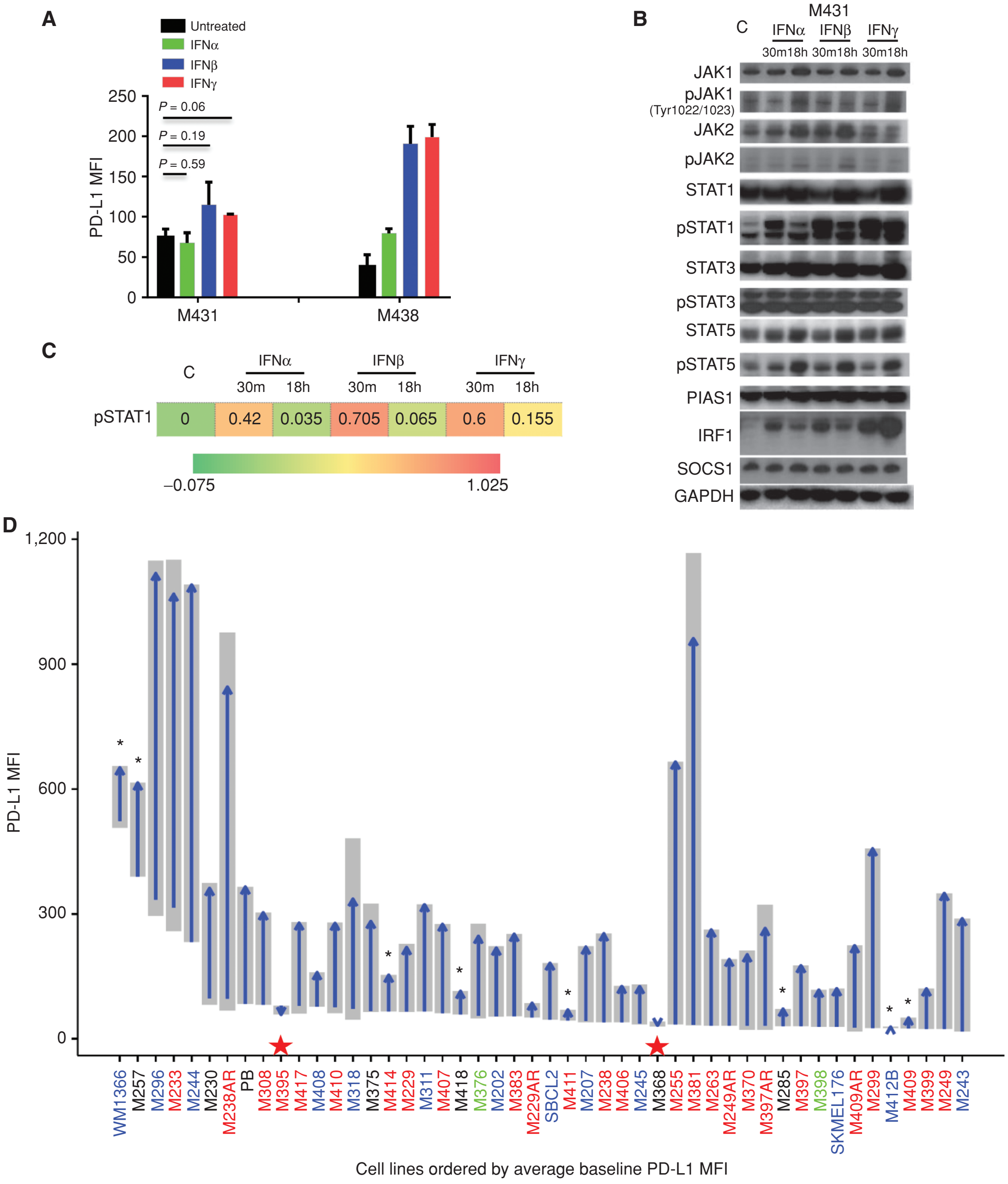

Figure 2. Altered interferon signaling with *JAK1* loss-of-function mutation in M431 and interferon gamma-inducible PD-L1 expression by 48 melanoma cell lines. **A,** Mean fluorescent intensity (MFI) of PD-L1 expression by flow cytometry upon interferon alpha, beta, or gamma exposure over 18 hours in M431 (established from patient #15) compared with M438 (established from patient #8). **B,** Corresponding Western blot analyses for M431 upon interferon exposure for 30 minutes or 18 hours. **C,** Phosphorylated STAT1 (pSTAT1) flow cytometry for M431 upon interferon exposure for 30 minutes or 18 hours (same color scale as in Fig. 3C and D, Supplementary Fig. S8A–S8C). The numbers in the heat map of pSTAT1 indicate the average Arcsinh ratio from two independent phospho-flow cytometry experiments. **D,** PD-L1 response to interferon gamma. Blue arrows represent average change from baseline upon interferon gamma exposure. Grey shades show the full range of measured values ($n = 2$ or 3). Red stars indicate cell lines with no response due to having a JAK loss-of-function mutation, and black stars indicate cell lines with poor response to interferons. Red, *BRAF* mutated; blue, *NRAS* mutated; green, *BRAF* and *NRAS* mutated; black, *BRAF* wild-type, *NRAS* wild-type.

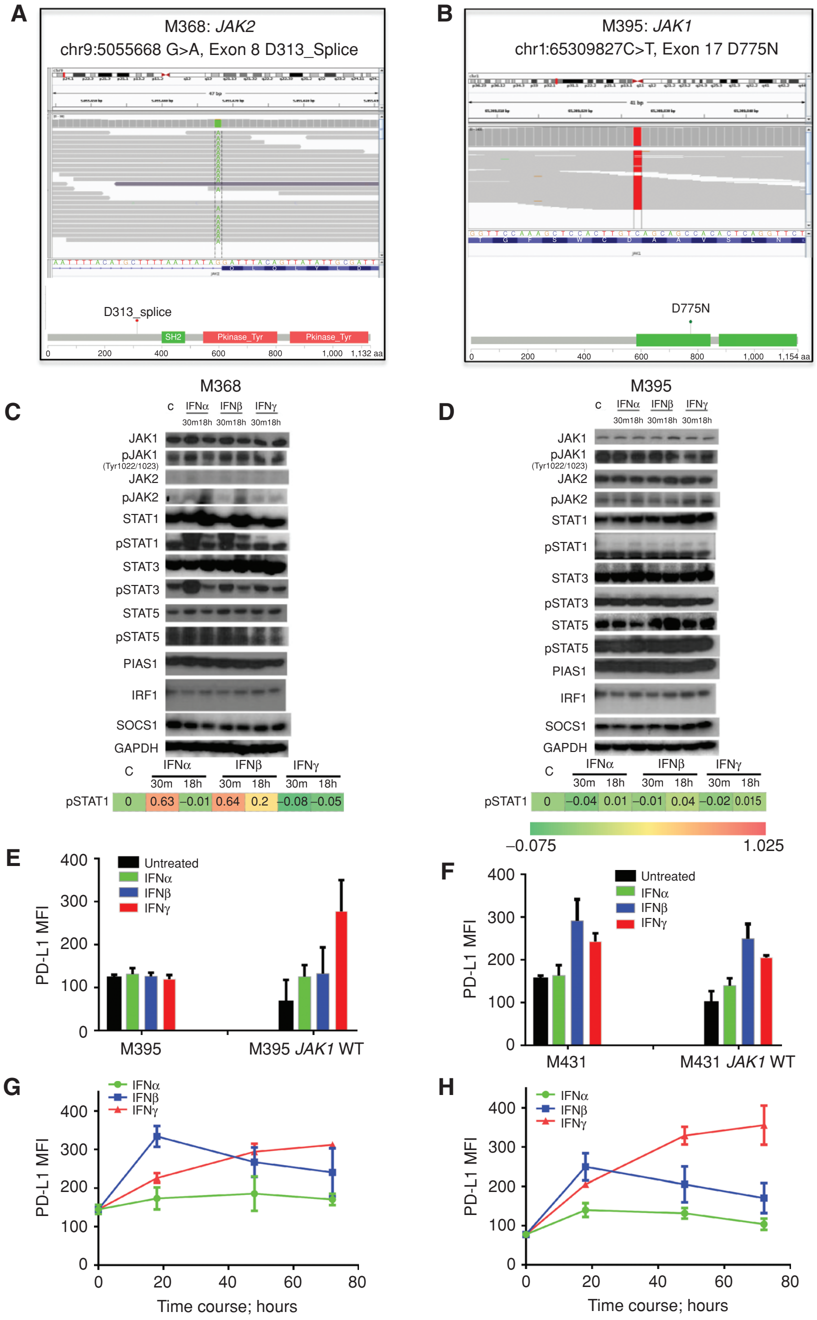

Figure 3. Defects in the interferon receptor signaling pathway with *JAK* homozygous loss-of-function mutations in M368 and M395. **A** and **B,** Exome sequencing data showing *JAK2*^{D313} spice-site mutation in exon 8 in M368 (**A**), and *JAK1*^{D775N} kinase domain mutation in exon 17 in M395 (**B**). Top, individual sequencing reads using the Integrated Genomics Viewer; bottom, position relative to kinase domains using the cBioPortal Mutation Mapper. **C** and **D,** For each cell line, cells were cultured with interferon alpha, interferon beta, or interferon gamma for either 30 minutes or 18 hours, or with vehicle control (c, first column from the left in Western blots and phospho-flow data). Phosphorylated STAT1 (pSTAT1) detected by Western blotting (top) or phospho-flow cytometry data (bottom). The numbers in the heat map of pSTAT1 indicate the average Arcsinh ratio from two independent phospho-flow experiments. Blots represent two independent replicate experiments. **E** and **F,** PD-L1 expression after interferon exposure on M395 and M431 after *JAK1* wild-type (WT) lentiviral transduction respectively. **G** and **H,** Time course PD-L1 expression for M431 and *JAK1* wild-type lentiviral vector transduced M431, respectively.

JAK1 wild-type transduced M431 was more distinct when observed over a longer time course (Fig. 3G and 3H).

JAK Loss-of-Function Mutations in Primary Resistance to PD-1 Blockade in Patients with Metastatic Colon Carcinoma

To determine whether *JAK1/2* loss-of-function mutations are present and relate to response to PD-1 blockade therapy in another cancer histology, we analyzed WES data from 16 biopsies of patients with colon cancer, many with a high mutational load resultant from mismatch-repair deficiency (6). One of the biopsies of a rare patient with high mutational load with neither an objective response nor disease control with anti–PD-1 had a homozygous *JAK1*^{W690*} nonsense loss-of-function mutation, expected to truncate the protein within the first kinase domain, and an accompanying loss of heterozygosity at the *JAK1* locus (Fig. 4A–D). No mutations in antigen presentation machinery were detected in this sample (Supplementary Fig. S13). Although we observed other interferon pathway and antigen presentation mutations in the high mutational load patients with a response to therapy in this cohort, they appeared to be heterozygous by allele frequency (adjusted VAF < 0.6) after adjustment for stromal content. Most were splice-site mutations or frameshift insertions/deletions unlikely to create a dominant-negative effect. Several samples bore two mutations in *JAK1/2* or *B2M*, but either retained at least one wild-type copy (subjects #4 and #5), were too far apart to determine cis versus trans status (subject #6), or were of uncertain significance (subject #1, both near c-terminus).

Frequency of *JAK* Loss-of-Function Mutations in Cell Lines of Multiple Histologies

We then analyzed data from the Cancer Cell Line Encyclopedia (CCLE) from cBioPortal to determine the frequency of homozygous putative loss-of-function mutations in *JAK1/2* in 905 cancer cell lines (25). For this analysis, we considered a homozygous mutation when the VAF was 0.8 or greater, as previously described (26). Approximately 0.7% of cell lines have loss-of-function mutations that may predict lack of response to interferons (Fig. 5A and 5B). The highest frequency of mutations was in endometrial cancers, as described previously (26). None of these cell lines had *POLE* or *POLD1* mutations, but microsatellite instability and DNA-damage gene mutations were present in the *JAK1/2* mutant cell lines (Supplementary Fig. S14). The frequency of *JAK1/2* mutations across all cancers suggests that there is a fitness gain with loss of interferon responsiveness.

JAK1/2 Loss-of-Function Alterations in The Cancer Genome Atlas

Analysis of WES, RNA sequencing (RNA-seq), and reverse-phase protein array (RPPA) data from tissue specimens from 472 patients in The Cancer Genome Atlas (TCGA) Skin Cutaneous Melanoma dataset revealed that 6% (28 of 472) and 11% (50 of 472) harbored alterations in *JAK1* and *JAK2*, respectively. These include loss-of-function alterations in either *JAK1* or *JAK2* that would putatively diminish JAK1 or JAK2 signaling (homodeletions, truncating mutations, or gene or protein downregulation).

There was no survival difference in patients in the TCGA Skin Cutaneous Melanoma dataset harboring any *JAK1* or *JAK2* alteration (Fig. 6A). However, when considering only loss-of-function *JAK1* or *JAK2* alterations (homodeletions, truncating mutations, or gene or protein downregulation), patients with tumors that had *JAK1* or *JAK2* alterations had significantly decreased overall survival ($P = 0.009$, log-rank test). When considered separately, the 8 patients with truncating mutations in *JAK1* or *JAK2* and the 18 patients with *JAK1* or *JAK2* gene or protein downregulation also had significantly decreased overall survival ($P = 0.016$ and $P < 0.001$, respectively).

To assess the relevance of these findings in a broader set of malignancies, we examined the frequency of *JAK1* and *JAK2* alterations and their association with clinical outcome in TCGA datasets for four common malignancies (breast invasive carcinoma, prostate adenocarcinoma, lung adenocarcinoma, and colorectal adenocarcinoma). Similar to findings in melanoma, alterations in *JAK1* were found in 6%, 8%, 10%, and 10% of patients with breast invasive carcinoma, prostate adenocarcinoma, lung adenocarcinoma, and colorectal adenocarcinoma, respectively. Likewise, alterations in *JAK2* were found in 12%, 7%, 12%, and 5% of these respective malignancies.

Consistent with our findings in melanoma, *JAK1* or *JAK2* alterations as a whole were not associated with a difference in survival in any of the four additional TCGA datasets. However, for patients with breast invasive carcinoma harboring truncating mutations, there was an association with decreased survival ($P = 0.006$, log-rank test; Fig. 6B). Likewise, patients with prostate adenocarcinoma harboring truncating mutations had worse overall survival ($P = 0.009$, log-rank test; Fig. 6C), with a similar trend noted in patients harboring any loss-of-function *JAK1* or *JAK2* alterations ($P = 0.083$, Fig. 6C). We did not observe differences in survival in patients with lung adenocarcinoma or colorectal adenocarcinoma harboring *JAK1* or *JAK2* loss-of-function alterations, when considered either separately or as a whole (Supplementary Fig. S15A and S15B).

DISCUSSION

For this work, we hypothesized that if cancer cells evolved to disable inducible PD-L1 expression upon interferon exposure due to selective immune pressure as demonstrated in preclinical models of cancer immune-editing (15, 16), then it would be superfluous to attempt to treat these cases with anti–PD-1/PD-L1 antibody therapy (Supplementary Fig. S16A and S16B). The premise of therapy with anti–PD-1– or anti–PD-L1–blocking antibodies is that T cells with specificity for cancer antigens recognize their target on cancer cells and produce interferon gamma. The cancer cell then finds a way to specifically protect itself from the T-cell attack by reactively expressing PD-L1 upon interferon gamma signaling. This reactive process is termed adaptive immune resistance, and it requires signaling through the interferon gamma receptor (12). By understanding this process, it is then logical to anticipate that a genetically acquired insensitivity to interferon gamma signaling could represent an immune resistance mechanism; these tumors would be expected to be incapable of upregulating either antigen-presenting machinery or PD-L1 even in the presence of a robust preexisting repertoire of tumor-specific T cells. With a genetic mechanism of lack

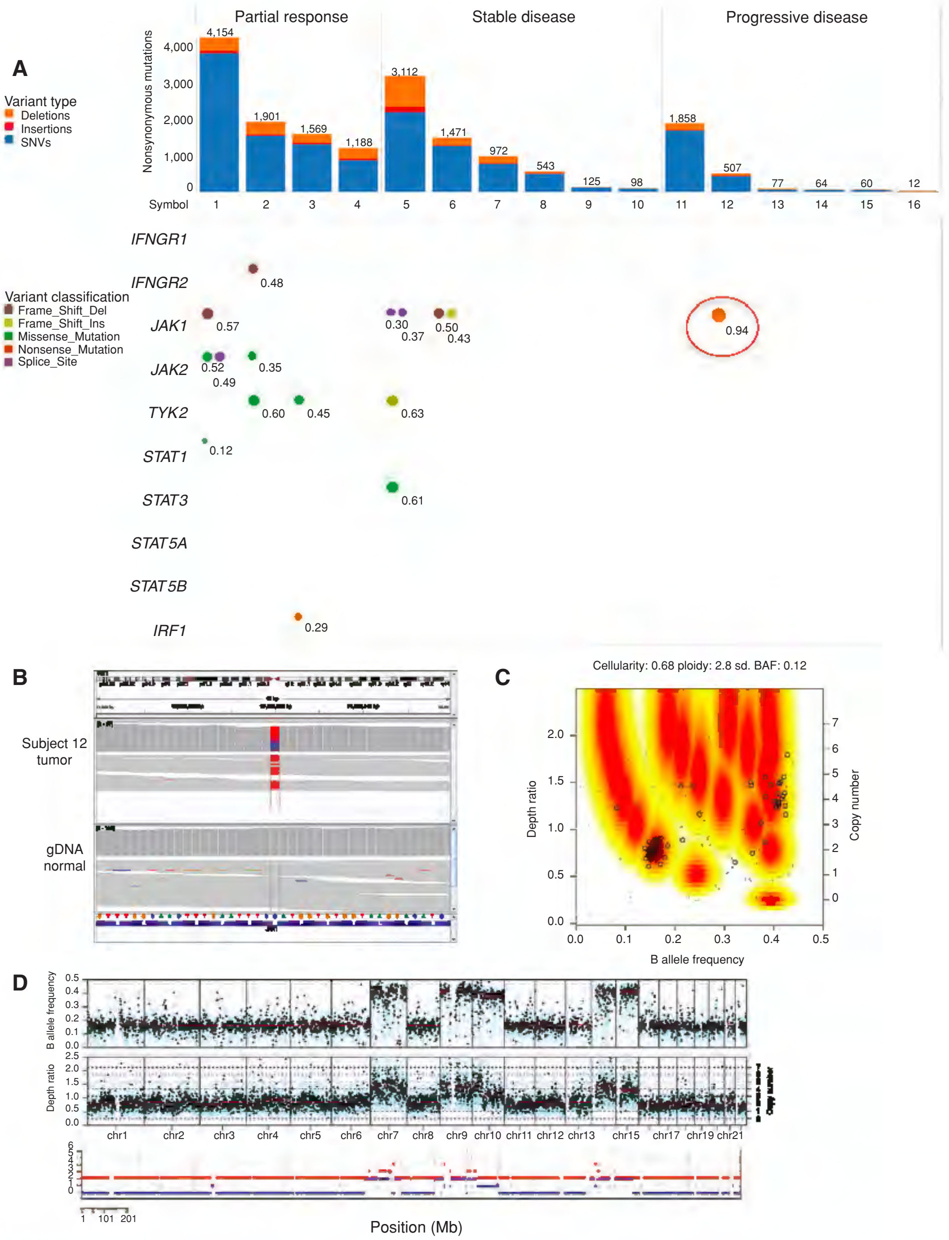

Figure 4. Mutational burden of somatic, protein-altering mutations per subject from WES for patients with advanced colon cancer who participated in PD-1 blockade clinical trial. **A,** Similar to Fig. 1B, bar graph shows mutational load in individual cases [fraction single nucleotide variants (SNV), blue; insertions, red; deletions, orange] divided by response to PD-1 blockade therapy. Bottom panel depicts mutations, insertions, or deletions in the interferon receptor pathway. Color represents predicted functional effect. The size of circles and adjacent labels correspond to tumor VAF after adjusting for stromal content. Red circle highlights homozygous nonsense mutation in *JAK1* from one patient who did not respond to anti–PD-1 therapy. **B,** Sequencing reads of *JAK1* mutation in nonresponder subject #12. **C,** Mutation observed in 51 reads out of 80 (VAF 0.64), which corresponds to a homozygous mutation (adjusted VAF 0.94) when adjusted for a tumor purity of 68%. **D,** Copy-number profile reveals loss of heterozygosity across most of the genome, including chromosome 1/*JAK1*.

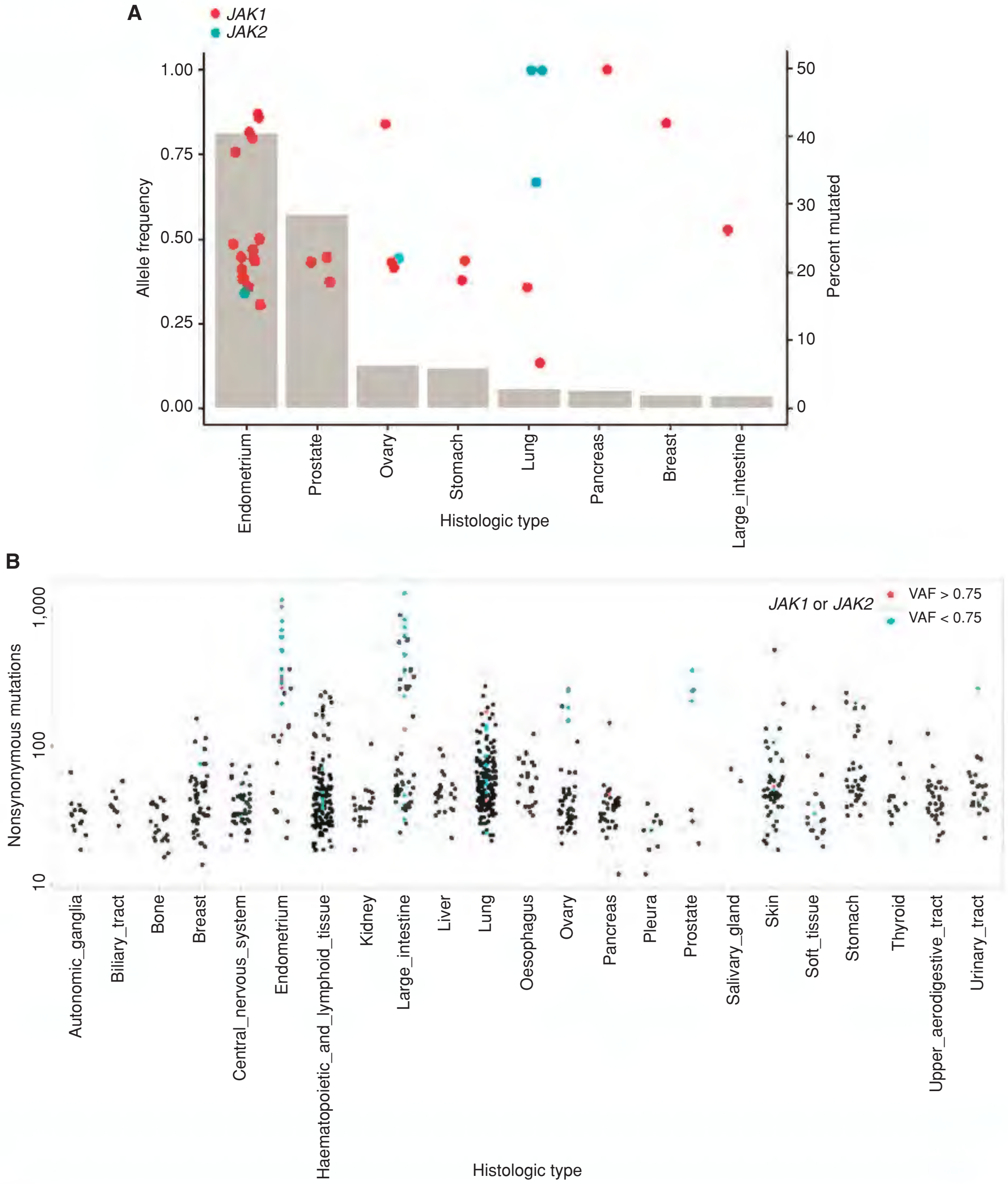

Figure 5. Analysis of *JAK1* and *JAK2* mutations in the CCLE database. **A,** Variant allele frequency (left axis, red and blue points) and percentage of tumors with mutations in *JAK1* or *JAK2* (right axis, gray bars) in the CCLE database from the cBioPortal. **B,** Nonsynonymous mutational burden was analyzed for individual cell lines (each dot represents cell line) and plotted for each histologic type. *JAK1* or *JAK2* mutated cell lines were color coded (red, VAF>0.75; blue, VAF<0.75).

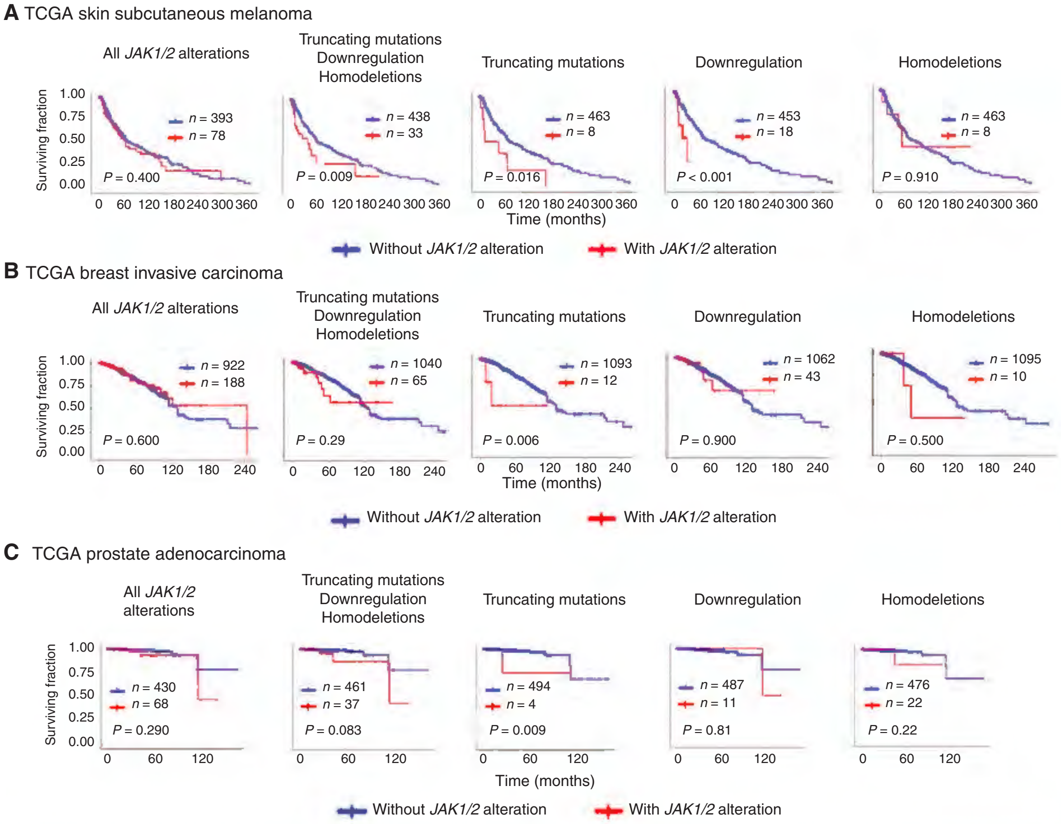

Figure 6. Frequency of *JAK1* and *JAK2* alterations and their association with overall survival in TCGA datasets. Kaplan–Meier survival analysis of TCGA skin cutaneous melanoma (**A**), breast invasive carcinoma (**B**), and prostate adenocarcinoma (**C**) provisional datasets, comparing control patients (blue) and patients harboring specified alterations in *JAK1* and *JAK2* (red). Frequency and distribution of combined *JAK1* and *JAK2* alterations are shown within each set of Kaplan–Meier plots. Significance testing of overall survival was performed using log-rank analysis.

of interferon gamma signaling, a T-cell response with interferon gamma production would not lead to reactive PD-L1 expression and therefore these would be cases that would be considered constitutively PD-L1 negative.

JAK kinases mediate signaling from many cytokine receptors, but the commonality between *JAK1* and *JAK2* homozygous loss-of-function mutations is that they are both required for signaling upon exposure to interferon gamma (27). Interferon gamma is a major cytokine produced by T cells upon recognizing their cognate antigen, and it has multiple effects on target cells. In the setting of acquired resistance to PD-1 blockade therapy in patients who progressed while on continuous anti–PD-1 therapy, the tumor's insensitivity to interferon gamma provides a selective advantage for the relapsed cancer to grow, as it no longer is sensitive to the antiproliferative effects of interferon gamma (14). In that setting, T cells continued to recognize cancer cells with *JAK1* or *JAK2* mutations despite the known role of interferon gamma signaling in upregulating a series of genes involved in the antigen-presenting machinery. However, as the baseline expression of MHC class I, proteasome subunits and TAP transporters is unchanged, tumor antigen presentation to T cells was not impaired (14).

In primary resistance to checkpoint blockade therapy with the anti–CTLA-4 antibody ipilimumab, there is a higher frequency of mutations in the several molecules involved in the interferon signaling pathway (18). It is hypothesized that cancer cells lacking interferon receptor signaling would have a selective advantage because they evade T cells activated by CTLA-4 blockade, in particular through decreased antigen presentation and resistance to the antiproliferative effects of interferons. The same processes may have an important role in the lack of response to anti–PD-1 therapy in the cancers with *JAK1/2* loss-of-function mutations in our series, as antitumor T cells would be anticipated to have lower ability to recognize and kill cancer cells. Loss-of-function mutations in *JAK1/2* would likewise prevent the antitumor activity of any immunotherapy that results in the activation of T cells to attack cancer cells. But in the setting of anti–PD-1/PD-L1 therapy, it has the additional important effect of preventing PD-L1 expression upon interferon gamma exposure, thereby making it futile to pharmacologically inhibit the PD-L1/PD-1 interaction.

As the interferon gamma receptor pathway downstream of JAK1/2 controls the expression of chemokines with a potent chemoattractant effect on T cells, such as CXCL9, CXCL10, and CXCL11 (28), it is possible that an important effect of *JAK1/2* loss may result in a lack of T-cell infiltrates. Indeed, both the patient in the melanoma series with a *JAK1* loss of function and the biopsy from which we had derived a melanoma cell line with a *JAK1* mutation were completely devoid of T-cell infiltrates. As preexisting T cells in the tumor are a requisite for response to anti–PD-1 therapy (11), a *JAK1/2* mutation may result in lack of response not only because PD-L1 cannot be reactively expressed but also because the cancer fails to attract T cells due to lack of chemokine production.

Beyond a genetic mutation that prevented expression of *JAK1/2*, it is also possible that epigenetic silencing of *JAK*s could result in lack of response to interferon gamma, as previously reported for the LNCaP cell line (29). In this case, loss of JAK1/2 expression could then be corrected with exposure to a demethylating agent. This evidence suggests that the frequency of loss of function in *JAK1/2* may be higher than can be estimated by exome-sequencing analyses, as it could occur epigenetically, and in these cases it would provide an option for pharmacologic intervention.

In conclusion, we propose that *JAK1/2* mutations that lead to loss of interferon gamma signaling and prevent adaptive PD-L1 expression upon interferon gamma exposure represent an immunoediting process that defines patients with cancer who would not be good candidates for PD-1 blockade therapy. This mechanism would add to other multiple explanations that may lead to primary resistance to PD-1 blockade therapy, including a tumor that lacks antigens that can be a target for a T-cell response, the presence of immune suppressive factors in the tumor microenvironment that exclude T cells in tumors or that lead to alteration of T-cell function, presence of immune suppressive cells such as T regulatory or myeloid-derived suppressor cells, or cancers that have specific genetic signaling or transcriptomes that are not permissive to T-cell infiltrates (20, 30, 31). The recognition that *JAK1/2* loss-of-function mutations would lead to lack of response to PD-1 blockade therapy could be incorporated in oncogenic sequencing panels used to select patients for precision cancer treatments.

METHODS

Tumor Samples

Tumor biopsies were obtained from a subset of patients enrolled in a phase I expansion clinical trial with pembrolizumab after signing a written informed consent (32). Patients were selected for this analysis by having adequate tumor biopsy samples and clinical follow-up. Baseline biopsies of metastatic tumors were obtained within 30 days of starting on treatment, except for one in a patient with an eventual complete response (Fig. 3B, subject #4) collected after 84 days on treatment. Samples were immediately fixed in formalin followed by paraffin embedding, and when there was an additional sterile piece of the tumor, processed for snap-freezing in liquid nitrogen and to establish a cell line as previously described (33–35). Tumor biopsy and peripheral blood cell collection and analyses were approved by UCLA Institutional Review Boards 11-001918 and 11-003066.

Treatment and Response Assessment

Patients received single-agent pembrolizumab intravenously in one of three dosing regimens: 2 mg/kg every 3 weeks (2Q3W), 10 mg/kg every 3 weeks (10Q3W), or 10 mg/kg every 2 weeks (10Q2W; ref. 32). Tumor responses to pembrolizumab were evaluated at 12 weeks after the first infusion (confirmed at 16 weeks), and every 12 weeks thereafter. The RECIST version 1.1 was used to define objective clinical responses. The protocol was allowed to proceed beyond initial progression at the restaging scans at 12 weeks and have repeated imaging scans 4 weeks later following the immune-related response criteria (irRC; ref. 36).

IHC Staining

For CD8 T-cell density, 5 of the 11 cases were reanalyzed blindly from IHC samples already used in our prior work (11), and the other 6 cases were newly stained cases also analyzed blindly. Slides were stained with hematoxylin and eosin, S100, CD8, CD68, PD-1, and PD-L1 at the UCLA Anatomic Pathology IHC Laboratory. Immunostaining was performed on Leica Bond III autostainers using Leica Bond ancillary reagents and the REFINE polymer DAB detection system as previously described (11). Cell density (cells/mm^2) in the invasive margin or intratumoral area was calculated using the Indica Labs Halo platform as previously described (11).

Cell Lines, Cell Culture, and Conditions

Patient-derived melanoma cell lines were generated as reported previously and characterized for their oncogenic mutational status (33–35). Each melanoma cell line was thawed and maintained in RPMI-1640 medium supplemented with 10% FBS, 100 units/mL penicillin, and 100 μg/mL streptomycin at 37°C in a humidified atmosphere of 5% CO_2. Cells were subject to experimental conditions after reaching two passages from thawing. Cell lines were periodically authenticated using GenePrint 10 System (Promega) and were matched with the earliest passage cell lines. Selected melanoma cell lines were subjected to *Mycoplasma* tests periodically (every 2–3 months) with the MycoAlert Mycoplasma Detection Kit (Lonza).

Surface Flow Cytometry Analysis for PD-L1 and MHC Class I

Melanoma cells were seeded into 6-well plates on day 1, ranging from 420,000 to 485,000 depending on their doubling time, targeting 70% to 80% of confluence at the time of trypsinization after 18 hours of exposure to interferons. For 48-hour exposure, 225,000 to 280,000 cells were seeded, and 185,000 to 200,000 cells were seeded for 72-hour exposure. After trypsinization, cells were incubated at 37°C for 2 hours with media containing different concentrations of interferons. Concentrations of each interferon were determined after optimization process (dose–response curves were generated with representative cell lines as shown in Supplementary Fig. S5B–S5D). After 2 hours of incubation, the media were removed by centrifugation and cells were resuspended with 100% FBS and stained with APC anti–PD-L1 antibody on ice for 20 minutes. The staining was halted by washing with 3 mL of PBS, which was removed by centrifugation at 500 × *g* for 4 minutes. The cells were resuspended with 300 μL of PBS, and 7-AAD for dead cell discrimination was added to samples prior to data acquisition by LSRII. The data were analyzed by FlowJo software (Version 10.0.8r1, Tree Star Inc.). Experiments were performed at least twice for each cell line; some cell lines with high assay variability were analyzed three times.

Phosphoflow Signaling Analyses

Cells were seeded into two 6-well plates for each cell line for single phospho-proteomics study. After 30-minute or 18-hour exposure to interferon alpha, beta, or gamma, cells were trypsinized and resuspended with 1 mL of PBS per 1 to 3 million cells and stained with live/dead agent at room temperature in the dark for 30 minutes.

Cells were then fixed with paraformaldehyde at room temperature for 10 minutes in the dark, permeabilized by methanol, and stained with pSTAT1. Cells were incubated at room temperature in the dark for 30 minutes, washed with phospho-flow cytometry buffer, and resuspended with 300 to 500 μL of the same buffer and analyzed with an LSRII. The flow cytometry standard (FCS) files obtained by LSRII were analyzed using the online flow cytometry program (Cytobank; ref. 37). The raw FCS files were deconvoluted into four different conditions, three of which were exposed to interferon alpha, beta, and gamma and compared with an untreated condition at each time point. Data represented as Arcsinh ratio, which is one of transformed ratio of cytometry data (inverse hyperbolic sine) analyses; each data point was compared with its control [Value = arcsinh((x – control)/scale_argument)].

Western Blot Analyses

Selected melanoma cells were maintained in 10-cm cell culture dishes and exposed to interferon alpha, beta, or gamma (same concentrations as above) for 30 minutes or 18 hours. Western blotting was performed as described previously (38). Primary antibodies included pJAK1 (Tyr1022/1023), pJAK2 (Tyr221), pSTAT1 (Tyr701), pSTAT3 (Tyr705), pSTAT5 (Tyr695), and their total proteins; PIAS1, IRF1, SOCS1, and GAPDH (all from Cell Signaling Technology). Antibodies were diluted to 1:1,000 ratio for each blot. Immunoreactivity was revealed with an ECL-Plus Kit (Amersham Biosciences Co.), using the ChemiDoc MP system (Bio-rad Laboratories).

Lentiviral Vector Production and Gene Transfer

Lentivirus production was performed by transient cotransfection of 293T cells (ATCC). The lentiviral vectors pLenti-C-mGFP and pLenti-C-JAK1-mGFP were purchased from Origen (cat# RC213878L2). In brief, T175 tissue culture flasks coated with poly-L-lysine (Sigma Aldrich) containing 6×10^6 293T cells were used for each transfection. The constructs required for the packaging of third-generation self-inactivating lentiviral vectors pLenti-C-mGFP and pLenti-C-JAK1-mGFP (60 μg), pMDLGg/p (39 μg), pRSV–REV (15 μg), and pMD.G (21 μg) were dissolved in water in a total volume of 2.7 mL. A total of 300 μL of 2.5 mol/L $CaCl_2$ (Sigma Aldrich) was added to the DNA mixture. A total of 2.8 mL of the DNA/$CaCl_2$ mix was added dropwise to 2.8 mL of 2× HBS buffer, pH 7.12 (280 nmol/L NaCl, 1.5 mmol/L Na_2HPO_4, 100 mmol/L HEPES). The DNA/$CaPO_4$ suspension was added to each flask and incubated in a 5% CO_2 incubator at 37°C overnight. The next morning, the medium was discarded, the cells were washed, and 15 mL DMEM with 10% FBS containing 20 mmol/L HEPES (Invitrogen) and 10 mmol/L sodium butyrate (Sigma Aldrich) was added, and the flask was incubated at 37°C for 8 to 12 hours. After that, the cells were washed once, and 10 mL fresh DMEM medium with 20 mmol/L HEPES was added onto the 293T cells, which were further incubated in a 5% CO_2 incubator at 37°C for 12 hours. The medium supernatants were then collected, filtered through 0.2 μmol/L filters, and cryopreserved at minus 80°C. Virus supernatant was added at different concentrations into 6-well plates containing 5×10^5 cells per well. Protamine sulphate (Sigma Aldrich) was added at a final concentration of 5 μg/mL, and the transduction plates were incubated at 37°C in 5% CO_2 overnight.

Whole-Exome Sequencing

Exon capture and library preparation were performed at the UCLA Clinical Microarray Core using the Roche Nimblegen SeqCap EZ Human Exome Library v3.0 targeting 65 Mb of genome. Paired-end sequencing (2 × 100 bp) was carried out on the HiSeq 2000 platform (Illumina) and sequences were aligned to the UCSC hg19 reference using BWA-mem (v0.7.9). Sequencing for tumors was performed to a target depth of 150× (actual min. 91×, max. 162×, mean 130×). Preprocessing followed the Genome Analysis Toolkit (GATK) Best Practices Workflow v3, including duplicate removal (PicardTools), indel realignment, and base quality score recalibration.

Somatic mutations were called by comparison to sequencing of matched normals for the PD1-treated whole-tumor patient samples. Methods were modified from ref. 39; specifically, the substitution the GATK-HaplotypeCaller (HC, v3.3) for the UnifiedGenotyper. gVCF outputs from GATK-HC for all 23 tumor/normal exomes, and cell lines M395 and M431, were jointly genotyped and submitted for variant quality score recalibration. Somatic variants were determined using one-sided Fisher exact test (P value cutoff ≤ 0.01) between tumor/normal pairs with depth >10 reads. Only high-confidence mutations were retained for final consideration, defined as those identified by at least two out of three programs [MuTect (v1.1.7; ref. 40), Varscan2 Somatic (v2.3.6; ref. 41), and the GATK-HC] for single nucleotide variants, and those called by both Varscan2 and the GATK-HC for insertions/deletions. Variants were annotated by Oncotator (42), with nonsynonymous mutations for mutational load being those classified as nonsense, missense, splice_site, or nonstop mutations, as well as frame_shift, in_frame_, or start_codon altering insertions/deletions. Adjusted variant allele frequency was calculated according to the following equation:

$$\mathit{VAF\ adjusted} = n_{\mathrm{mut}}/\mathrm{CN}_t = \mathit{VAF}*[1+(2*\mathit{Stromal\ Fraction})/(\mathit{Tumor\ Fraction}*\mathit{Local\ Copy\ Number})]$$

This is an algebraic rearrangement of the equation used in the clonal architecture analysis from McGranaham and colleagues (43) to calculate the fraction of mutated chromosomal copies while adjusting for the diluting contribution of stromal chromosomal copies. Local tumor copy number ($\mathrm{CN}_{t,}$) tumor fraction (purity, or p) and stromal fraction (1 – p) were produced by Sequenza (44), which uses both depth ratio and SNP minor B-allele frequencies to estimate tumor ploidy and percent tumor content, and perform allele-specific copy-number variation analysis.

PDJ amplification was considered tumor/normal depth ratio ≥ 2 standard deviations above length-weighted genome average. BAM files for the 16 colorectal cases were previously mapped to hg18, and sequencing and analysis were performed at Personal Genome Diagnostics. After preprocessing and somatic variant calling, positions were remapped to hg19 using the Ensembl Assembly Converter before annotation.

M431 and M395 were compared with matched normal samples, the other 47 cell lines lacked a paired normal sample. For detection of potential *JAK1* or *JAK2* mutations, variants were detected using the Haplotype Caller, noted for membership in dbSNP 146 and allele frequency from the 1000 Genomes project, and confirmed by visual inspection with the Integrated Genomics Viewer.

RT-PCR

Forward 5′-AACCTTCTCACCAGGATGCG-3′ and reverse 5′-CTCAGCACGTACATCCCCTC-3′ primers were designed to perform RT-PCR (700 base pair of target PCR product to cover the P429 region of the JAK1 protein) on the M431 cell line. Total RNA was extracted by the *mir*Vana miRNA Isolation Kit, with phenols as per the manufacturer's protocol (Thermo Fischer Scientific). RT-PCR was performed by utilizing ThermoScript RT-PCR Systems (Thermo Fisher Scientific, cat# 11146-057). PCR product was subject to Sanger sequencing at the UCLA core facility.

TCGA Analysis

To determine the relevance of *JAK1* and *JAK2* alterations in a broader set of patients, we queried the TCGA skin cutaneous melanoma provisional dataset for the frequency of genetic and expression alterations in *JAK1* and *JAK2*. We then extended our query to the breast invasive carcinoma, prostate adenocarcinoma, lung adenocarcinoma, and colorectal adenocarcinoma provisional TCGA datasets. We then examined the association of various *JAK1* and *JAK2* alterations with overall survival for each dataset. The results are based upon data generated by the TCGA Research Network and made available through the NCI Genomic Data Commons and cBioPortal (45, 46).

The mutation annotation format (MAF) files containing *JAK1* and *JAK2* mutations in the TCGA datasets were obtained from the

Genomic Data Commons. In addition, mutations, putative copy-number alterations, mRNA expression, protein expression, and survival data were obtained using the cBioPortal resource. The putative copy-number alterations (homodeletion events, in particular) available in cBioPortal were obtained from the TCGA datasets using Genomic Identification of Significant Targets in Cancer (GISTIC; ref. 47). The mRNA expression data available in cBioPortal were obtained from the TCGA datasets using RNA-seq (RNA Seq V2 RSEM). Upregulation and downregulation of *JAK1* and *JAK2* mRNA expression were determined using an mRNA *z*-score cutoff of 2.0. Protein expression data available in cBioPortal were obtained from the TCGA dataset using RPPA, with a *z*-score threshold of 2.0.

Mutation data between the MAF files and data from cBioPortal were combined. Genetic and expression alterations were characterized in one of six categories: amplifications, homodeletions, single-nucleotide polymorphisms, truncating mutations (stop codons and frameshift insertions and deletions), mRNA or protein downregulation, and mRNA or protein upregulation. The frequency of *JAK1* and *JAK2* alterations was determined using combined data from the *.MAF file and cBioPortal. Kaplan–Meier survival curves were generated in R, using the "survminer" package and the "ggsurvplot" function. Overall survival was determined using log-rank analysis.

Statistical Analysis

Statistical comparisons were performed by the unpaired two-tailed Student *t* test (GraphPad Prism, version 6.0 for Windows). Mutational load was compared by unpaired two-sided Mann–Whitney test. R programming was utilized to generate arrow graphs of PD-L1/MHC class I expression upon interferon exposures and the CCLE *JAK1/2* mutation frequency graph.

Disclosure of Potential Conflicts of Interest

B. Chmielowski reports receiving speakers bureau honoraria from Genentech and Janssen and is a consultant/advisory board member for Merck, Genentech, Eisai, Immunocore, BMS, and Amgen. D.T. Le reports receiving commercial research grants from Merck and BMS, and is a consultant/advisory board member for Merck. D.M. Pardoll reports receiving a commercial research grant from BMS. L.A. Diaz has ownership interest (including patents) in Personal Genome Diagnostics and PapGene, and is a consultant/advisory board member for Merck and Cell Design labs. No potential conflicts of interest were disclosed by the other authors.

Authors' Contributions

Conception and design: D.S. Shin, A. Garcia-Diaz, R.S. Lo, B. Comin-Anduix, A. Ribas

Development of methodology: D.S. Shin, H. Escuin-Ordinas, A. Garcia-Diaz, S. Sandoval, D.Y. Torrejon, G. Abril-Rodriguez, L.A. Diaz, Jr, P.C. Tumeh, R.S. Lo, A. Ribas

Acquisition of data (provided animals, acquired and managed patients, provided facilities, etc.): D.S. Shin, J.M. Zaretsky, S. Hu-Lieskovan, D.Y. Torrejon, B. Chmielowski, G. Cherry, E. Seja, I.P. Shintaku, D.T. Le, D.M. Pardoll, L.A. Diaz, Jr, P.C. Tumeh, A. Ribas

Analysis and interpretation of data (e.g., statistical analysis, biostatistics, computational analysis): D.S. Shin, J.M. Zaretsky, S. Hu-Lieskovan, A. Kalbasi, C.S. Grasso, W. Hugo, N. Palaskas, B. Chmielowski, D.M. Pardoll, L.A. Diaz, Jr, P.C. Tumeh, T.G. Graeber, R.S. Lo, B. Comin-Anduix, A. Ribas

Writing, review, and/or revision of the manuscript: D.S. Shin, J.M. Zaretsky, S. Hu-Lieskovan, A. Kalbasi, C.S. Grasso, W. Hugo, D.Y. Torrejon, N. Palaskas, G. Parisi, B. Chmielowski, D.T. Le, D.M. Pardoll, P.C. Tumeh, T.G. Graeber, R.S. Lo, B. Comin-Anduix, A. Ribas

Administrative, technical, or material support (i.e., reporting or organizing data, constructing databases): H. Escuin-Ordinas, S. Sandoval, B. Berent-Maoz, P.C. Tumeh, A. Ribas

Study supervision: B. Comin-Anduix, A. Ribas

Other (assisted with Western blot work): A. Azhdam

Acknowledgments

We acknowledge the UCLA Translational Pathology Core Laboratory (TPCL); Rongqing Guo, Jia Pang, and Wang Li from UCLA for blood and biopsy processing; and Matt Klinman, Thinle Chodon, and Charles Ng for establishing some of the cell lines.

Grant Support

This study was funded in part by the NIH grants R35 CA197633 and P01 CA168585, the Parker Institute for Cancer Immunotherapy (PICI), the Dr. Robert Vigen Memorial Fund, the Ruby Family Fund, and the Garcia-Corsini Family Fund (to A. Ribas); and P01 CA168585, the Ressler Family Fund, the Samuels Family Fund, and the Grimaldi Family Fund (to A. Ribas and R.S. Lo). D.S. Shin was supported by the Oncology (5T32CA009297-30), Dermatology (5T32AR058921-05), and Tumor Immunology (5T32CA009120-39 and 4T32CA009120-40) training grants, a 2016 Conquer Cancer Foundation ASCO Young Investigator Award, and a Tower Cancer Research Foundation Grant. A. Ribas and D.M. Pardoll were supported by a Stand Up To Cancer – Cancer Research Institute Cancer Immunology Dream Team Translational Research Grant (SU2C-AACR-DT1012). Stand Up To Cancer is a program of the Entertainment Industry Foundation administered by the American Association for Cancer Research. J.M. Zaretsky is part of the UCLA Medical Scientist Training Program supported by NIH training grant GM08042. S. Hu-Lieskovan was supported by a Conquer Cancer Foundation ASCO Young Investigator Award, a Conquer Cancer Foundation ASCO Career Development Award, and a Tower Cancer Foundation Research Grant. G. Parisi was supported by the V Foundation-Gil Nickel Family Endowed Fellowship in Melanoma Research and also in part by the Division of Medical Oncology and Immunotherapy (University Hospital of Siena). T.G. Graeber was supported by an American Cancer Society Research Scholar Award (RSG-12-257-01-TBE), a Melanoma Research Alliance Established Investigator Award (20120279), and the National Center for Advancing Translational Sciences UCLA CTSI Grant UL1TR000124. R.S. Lo was supported by the Steven C. Gordon Family Foundation and the Wade F.B. Thompson/Cancer Research Institute CLIP Grant. L.A. Diaz and D.T. Le were funded from the Swim Across America Laboratory and the Commonwealth Fund at Johns Hopkins. W. Hugo was supported by the 2016 Milstein Research Scholar Award from the American Skin Association and by the 2016 AACR-Amgen, Inc., Fellowship in Clinical/Translational Cancer Research (16-40-11-HUGO).

Received November 1, 2016; revised November 28, 2016; accepted November 28, 2016; published OnlineFirst November 30, 2016.

REFERENCES

1. Herbst RS, Soria JC, Kowanetz M, Fine GD, Hamid O, Gordon MS, et al. Predictive correlates of response to the anti-PD-L1 antibody MPDL3280A in cancer patients. Nature 2014;515:563–7.
2. Powles T, Eder JP, Fine GD, Braiteh FS, Loriot Y, Cruz C, et al. MPDL3280A (anti-PD-L1) treatment leads to clinical activity in metastatic bladder cancer. Nature 2014;515:558–62.
3. Robert C, Long GV, Brady B, Dutriaux C, Maio M, Mortier L, et al. Nivolumab in previously untreated melanoma without BRAF mutation. N Engl J Med 2015;372:320–30.
4. Ansell SM, Lesokhin AM, Borrello I, Halwani A, Scott EC, Gutierrez M, et al. PD-1 blockade with nivolumab in relapsed or refractory Hodgkin's lymphoma. N Engl J Med 2015;372:311–9.

5. Robert C, Schachter J, Long GV, Arance A, Grob JJ, Mortier L, et al. Pembrolizumab versus ipilimumab in advanced melanoma. N Engl J Med 2015;372:2521–32.
6. Le DT, Uram JN, Wang H, Bartlett BR, Kemberling H, Eyring AD, et al. PD-1 blockade in tumors with mismatch-repair deficiency. N Engl J Med 2015;372:2509–20.
7. Garon EB, Rizvi NA, Hui R, Leighl N, Balmanoukian AS, Eder JP, et al. Pembrolizumab for the treatment of non-small-cell lung cancer. N Engl J Med 2015;372:2018–28.
8. Nghiem PT, Bhatia S, Lipson EJ, Kudchadkar RR, Miller NJ, Annamalai L, et al. PD-1 blockade with pembrolizumab in advanced merkel-cell carcinoma. N Engl J Med 2016;374:2542–52.
9. Pardoll DM.The blockade of immune checkpoints in cancer immunotherapy. Nature reviews Cancer 2012;12:252–64.
10. Taube JM, Anders RA, Young GD, Xu H, Sharma R, McMiller TL, et al. Colocalization of inflammatory response with B7-h1 expression in human melanocytic lesions supports an adaptive resistance mechanism of immune escape. Sci Transl Med 2012;4:127ra37.
11. Tumeh PC, Harview CL, Yearley JH, Shintaku IP, Taylor EJ, Robert L, et al. PD-1 blockade induces responses by inhibiting adaptive immune resistance. Nature 2014;515:568–71.
12. Ribas A. Adaptive immune resistance: how cancer protects from immune attack. Cancer Discov 2015;5:915–9.
13. Bach EA, Aguet M, Schreiber RD. The IFN gamma receptor: a paradigm for cytokine receptor signaling. Annu Rev Immunol 1997;15: 563–91.
14. Zaretsky JM, Garcia-Diaz A, Shin DS, Escuin-Ordinas H, Hugo W, Hu-Lieskovan S, et al. Mutations associated with acquired resistance to PD-1 blockade in melanoma. N Engl J Med 2016;375:819–29.
15. Dunn GP, Bruce AT, Ikeda H, Old LJ, Schreiber RD. Cancer immunoediting: from immunosurveillance to tumor escape. Nat Immunol 2002;3:991–8.
16. Kaplan DH, Shankaran V, Dighe AS, Stockert E, Aguet M, Old LJ, et al. Demonstration of an interferon gamma-dependent tumor surveillance system in immunocompetent mice. Proc Natl Acad Sci U S A 1998;95:7556–61.
17. Mazzolini G, Narvaiza I, Martinez-Cruz LA, Arina A, Barajas M, Galofre JC, et al. Pancreatic cancer escape variants that evade immunogene therapy through loss of sensitivity to IFNgamma-induced apoptosis. Gene Ther 2003;10:1067–78.
18. Gao J, Shi LZ, Zhao H, Chen J, Xiong L, He Q, et al. Loss of IFN-gamma pathway genes in tumor cells as a mechanism of resistance to Anti-CTLA-4 Therapy. Cell 2016;167:397–404 e9.
19. Rizvi NA, Hellmann MD, Snyder A, Kvistborg P, Makarov V, Havel JJ, et al. Cancer immunology. Mutational landscape determines sensitivity to PD-1 blockade in non-small cell lung cancer. Science 2015;348:124–8.
20. Hugo W, Zaretsky JM, Sun L, Song C, Moreno BH, Hu-Lieskovan S, et al. Genomic and transcriptomic features of response to Anti-PD-1 therapy in metastatic melanoma. Cell 2016;165:35–44.
21. Rosenberg JE, Hoffman-Censits J, Powles T, van der Heijden MS, Balar AV, Necchi A, et al. Atezolizumab in patients with locally advanced and metastatic urothelial carcinoma who have progressed following treatment with platinum-based chemotherapy: a single-arm, multicentre, phase 2 trial. Lancet 2016;387:1909–20.
22. Rodig SJ, Meraz MA, White JM, Lampe PA, Riley JK, Arthur CD, et al. Disruption of the Jak1 gene demonstrates obligatory and nonredundant roles of the Jaks in cytokine-induced biologic responses. Cell 1998;93:373–83.
23. Muller M, Briscoe J, Laxton C, Guschin D, Ziemiecki A, Silvennoinen O, et al. The protein tyrosine kinase JAK1 complements defects in interferon-alpha/beta and -gamma signal transduction. Nature 1993;366:129–35.
24. Watling D, Guschin D, Muller M, Silvennoinen O, Witthuhn BA, Quelle FW, et al. Complementation by the protein tyrosine kinase JAK2 of a mutant cell line defective in the interferon-gamma signal transduction pathway. Nature 1993;366:166–70.
25. Barretina J, Caponigro G, Stransky N, Venkatesan K, Margolin AA, Kim S, et al. The cancer cell line encyclopedia enables predictive modelling of anticancer drug sensitivity. Nature 2012;483:603–7.
26. Ren Y, Zhang Y, Liu RZ, Fenstermacher DA, Wright KL, Teer JK, et al. JAK1 truncating mutations in gynecologic cancer define new role of cancer-associated protein tyrosine kinase aberrations. Scientific reports 2013;3:3042.
27. Platanias LC. Mechanisms of type-I- and type-II-interferon-mediated signalling. Nat Rev Immunol 2005;5:375–86.
28. Fish EN, Platanias LC. Interferon receptor signaling in malignancy: a network of cellular pathways defining biological outcomes. Mol Cancer Res 2014;12:1691–703.
29. Dunn GP, Sheehan KC, Old LJ, Schreiber RD. IFN unresponsiveness in LNCaP cells due to the lack of JAK1 gene expression. Cancer Res 2005;65:3447–53.
30. Spranger S, Bao R, Gajewski TF. Melanoma-intrinsic beta-catenin signalling prevents anti-tumour immunity. Nature 2015;523:231–5.
31. Sharma P, Allison JP. The future of immune checkpoint therapy. Science 2015;348:56–61.
32. Ribas A, Hamid O, Daud A, Hodi FS, Wolchok JD, Kefford R, et al. Association of pembrolizumab with tumor response and survival among patients with advanced melanoma. JAMA 2016;315:1600–9.
33. Nazarian R, Shi H, Wang Q, Kong X, Koya RC, Lee H, et al. Melanomas acquire resistance to B-RAF(V600E) inhibition by RTK or N-RAS upregulation. Nature 2010;468:973–7.
34. Atefi M, Avramis E, Lassen A, Wong DJ, Robert L, Foulad D, et al. Effects of MAPK and PI3K Pathways on PD-L1 expression in melanoma. Clin Cancer Res 2014;20:3446–57.
35. Wong DJ, Robert L, Atefi MS, Lassen A, Avarappatt G, Cerniglia M, et al. Antitumor activity of the ERK inhibitor SCH722984 against BRAF mutant, NRAS mutant and wild-type melanoma. Mol Cancer 2014;13:194.
36. Wolchok JD, Hoos A, O'Day S, Weber JS, Hamid O, Lebbe C, et al. Guidelines for the evaluation of immune therapy activity in solid tumors: immune-related response criteria. Clin Cancer Res 2009;15:7412–20.
37. Kotecha N, Krutzik PO, Irish JM. Web-based analysis and publication of flow cytometry experiments. Current protocols in cytometry/editorial board, J Paul Robinson managing editor [et al] 2010;Chapter 10:Unit10 7.
38. Escuin-Ordinas H, Atefi M, Fu Y, Cass A, Ng C, Huang RR, et al. COX-2 inhibition prevents the appearance of cutaneous squamous cell carcinomas accelerated by BRAF inhibitors. Mol Oncol 2014;8:250–60.
39. Shi H, Hugo W, Kong X, Hong A, Koya RC, Moriceau G, et al. Acquired resistance and clonal evolution in melanoma during BRAF inhibitor therapy. Cancer Discov 2014;4:80–93.
40. Cibulskis K, Lawrence MS, Carter SL, Sivachenko A, Jaffe D, Sougnez C, et al. Sensitive detection of somatic point mutations in impure and heterogeneous cancer samples. Nat Biotechnol 2013;31:213–9.
41. Koboldt DC, Zhang Q, Larson DE, Shen D, McLellan MD, Lin L, et al. VarScan 2: somatic mutation and copy number alteration discovery in cancer by exome sequencing. Genome research 2012;22:568–76.
42. Ramos AH, Lichtenstein L, Gupta M, Lawrence MS, Pugh TJ, Saksena G, et al. Oncotator: cancer variant annotation tool. Human mutation 2015;36:E2423–9.
43. McGranahan N, Furness AJ, Rosenthal R, Ramskov S, Lyngaa R, Saini SK, et al. Clonal neoantigens elicit T cell immunoreactivity and sensitivity to immune checkpoint blockade. Science 2016;351:1463–9.
44. Favero F, Joshi T, Marquard AM, Birkbak NJ, Krzystanek M, Li Q, et al. Sequenza: allele-specific copy number and mutation profiles from tumor sequencing data. Ann Oncol 2015;26:64–70.
45. Cerami E, Gao J, Dogrusoz U, Gross BE, Sumer SO, Aksoy BA, et al. The cBio cancer genomics portal: an open platform for exploring multidimensional cancer genomics data. Cancer Discov 2012;2:401–4.
46. Gao J, Aksoy BA, Dogrusoz U, Dresdner G, Gross B, Sumer SO, et al. Integrative analysis of complex cancer genomics and clinical profiles using the cBioPortal. Sci Signal 2013;6:pl1.
47. Beroukhim R, Getz G, Nghiemphu L, Barretina J, Hsueh T, Linhart D, et al. Assessing the significance of chromosomal aberrations in cancer: methodology and application to glioma. Proc Natl Acad Sci U S A 2007;104:20007–12.

Supplementary Data

Supplementary Data to: Shin DS, Zaretsky JM, Escuin-Ordinas H, et al: Primary resistance to PD-1 blockade mediated by *JAK1/2* mutations

Primary resistance to PD-1 blockade mediated by *JAK1/2* mutations

Daniel Sanghoon Shin[1], Jesse M. Zaretsky[1], Helena Escuin-Ordinas[1], Angel Garcia-Diaz[1], Siwen Hu-Lieskovan[1], Anusha Kalbasi[1], Catherine S. Grasso[1], Willy Hugo[1], Salemiz Sandoval[1], Davis Y. Torrejon[1], Nicolaos Palaskas[1], Gabriel Abril Rodriguez[1], Giulia Parisi[1], Ariel Azhdam[1], Bartosz Chmielowski[1,2], Grace Cherry[1], Elizabeth Seja[1], Beata Berent-Maoz[1], I. Peter Shintaku[1], Dung Thi Le[3], Drew M. Pardoll[3], Luis A. Diaz, Jr[3], Paul C. Tumeh[1], Thomas G. Graeber[1,2], Roger S. Lo[1,2], Begoña Comin-Anduix[1,2], Antoni Ribas[1,2]

Table of Contents

Supplementary Data Legends

Supplementary Figure 1. Exome sequencing and copy number changes in M431 and corresponding whole-tumor biopsy. A) Sequenza tumor purity (cellularity) inference in M431 and corresponding whole-tumor biopsy from Fig. 3B subject #15. Tumor purity was 0.32 for the whole-tumor extract (left) and 0.91 for the early-passage M431 cell line (right). B) IGV plot showing JAK1 chr1:65,325,837 G>A mutation (red box) and accompanying loss-of-heterozygosity (blue box). Top panel M431 cell line (unadjusted VAF 0.68), middle whole tumor (unadjusted VAF 0.30), bottom normal genomic DNA. C) Sanger sequencing of cDNA from RT-PCR of RNA from M431. JAK1 mutation predominates over wild-type allele. D) View of chromosome 1 for cell line M431; red arrows show JAK1 location (65 Mb), with inferred copy number 5 and 4:1 allele ratio. Top panel dots are individual mutations at their corresponding allele frequency. Middle and lower panel show SNP minor allele frequency and depth ratio respectively. Dotted lines show expected frequencies based on model-fit Copy Number assignment. E) Copy number profile is largely the same between whole tumor (upper series) and M431 (lower series). Figure reflects Sequenza output from tumor and cell line exome sequencing each compared to patient-matched blood-derived germline DNA. Top, middle, and lower panels display SNP minor-allele frequency, tumor:normal depth ratio, and inferred allele-specific copy number state respectively per chromosomal position. The whole tumor biopsy and M431 also displayed 2292 and 2202 non-synonymous mutations, respectively, with a 93.7% overlap between them (Supplementary Database 1).

Supplementary Figure 2. Mutations in antigen presentation machinery from anti-PD1 treated melanoma cohort. Subjects are ordered as in Fig1B, and top bar graph re-depicts mutational load for reference. The size of circles and adjacent labels represent the tumor variant allele frequency (VAF) of the mutation after adjustment for stromal content. Color represents predicted functional effect.

Supplementary Figure 3. Immunohistochemistry (IHC) analysis of biopsies from melanoma metastases with a JAK1 loss of function mutation. IHC analysis of the whole-tissue biopsy from which patient-derived cell line M431 was established. Sequentially cut pathology slides were stained for S100 to delineate the area of the tumor, CD8 for T cells, CD68 for macrophages, as well as for PD-1 and PD-L1.

Supplementary Figure 4. Selection of PD-L1 flow cytometry antibody and impact of phosphatase inhibitor as well as temperature on measuring surface PD-L1 expression and pAKT. A) PD-L1 surface staining with two different fluorochrome flow cytometry antibodies. The selected melanoma cells (M410) were harvested by trypsinization and stained with APC-PD-L1 and PE-PD-L1 flow cytometry antibodies. APC PD-L1 antibody shows a clearer distinction of signal between control and stained sample. B to D) Impact of phosphatase inhibitors and 2 hours of incubation at 37^{o}C after trypsinization on measuring surface PD-L1 expression and pAKT in melanoma cells. M233, M249 and M407 (E to D respectively) cells were trypsinized and re-suspended into three conditions. First two conditions were with and without phosphatase inhibitor then subjected to surface staining and intracellular staining with pAKT antibody. The third condition without phosphatase inhibitor, was incubated at 37^{o}C, then subjected to surface PD-L1 staining and followed by pAKT staining. E and F) Impact of temperature on measuring surface PD-L1 expression and pAKT in melanoma cells. M233 and M249 (E and F respectively) were trypsinized, re-suspended into three groups with and without phosphatase inhibitors, incubated at 37^{o}C for 2 hours, PD-L1 surface staining was performed at room temperature and on ice (without phosphatase inhibitor) anti-PD-L1 antibody. Based on these studies, the conditions chosen for further testing were without phosphatase inhibitor and on ice for 20 minutes.

Supplementary Figure 5. Flow cytometry gating strategy and dose response curve of interferon alpha, beta and gamma to determine the optimal concentrations. A) Representative gating strategy for PD-L1 measurement by flow cytometry after 18 hours exposure to interferon alpha, beta or gamma. Cells were stained with anti-PD-L1 for flow cytometry and the mean fluorescence intensity (MFI) was determined. B) Dose response curve of interferon alpha. The representative melanoma cells were seeded into 6 well plates in different numbers to target 70-80% confluence at the time of completion of treatment for set amount of time. Inset on right side represent a smaller dose range of the same data to better illustrate the curve change at low concentration ranges. C) Dose response curve of interferon beta. D) Dose response of interferon gamma. We selected interferon alpha: 5000 IU/mL, interferon beta: 500 IU/mL and interferon gamma 100 IU/mL as the optimal conditions for further testing.

Supplementary Figure 6. Time course of PD-L1 surface expression upon interferon alpha, beta and gamma treatment for selected cell lines to determine the optimal time point for the screening. A to H) The selected melanoma cell lines (M202, M230, M229, M233, M249, M263, M308 and M381) were seeded into 6 well plates on day 1 with target confluence of 70-80% at the time of measuring PD-L1 expression by LSRII flow cytometry. Cells were treated on day 2 with pre-determined concentrations, interferon alpha, beta and gamma as described above. Based on these experiments, the optimal screening time point was chosen at 18 hours.

Supplementary Figure 7. **Time course of PD-L1 expression upon interferon alpha, beta or gamma treatment for the cell lines with poor or no up-regulation upon 18 hours exposure.** Time course PD-L1 expression upon interferon alpha (A), beta (B) or gamma (C) exposure for 10 selected melanoma cell lines with poor or no up-regulation of PD-L1 at 18 hours exposure. M285, M414 and M418 cell lines (marked as diamond) did show increased up-regulation of PD-L1 over 2 fold from baseline upon 48 to 72 hours of interferon gamma exposure ($P<0.05$), but not with interferon alpha or beta. This experiment confirms that the three non-responding cell lines, M368, M395 and M412b, still did not up-regulate PD-L1 upon longer time exposure to interferon gamma.

Supplementary Figure 8. Interferon signalling pathway in good and poorly responding cell lines. Two responding cell lines M233 (A), and PB (B); a poorly responding cell line M257 (C). For each cell line, cells were cultured with interferon alpha, interferon beta or interferon gamma for either 30 minutes or 18 hours, or with vehicle control (c, first column from the left in Western blots and phosphoflow data). Phosphorylated STAT1 (pSTAT1) detected by Western blotting (top panel) or phospho-flow cytometry data (bottom panel). The numbers in the heat map of pSTAT1 indicate the average Arcsinh ratio from two independent phospho-flow experiments.

Supplementary Figure 9. PD-L1 expression upon interferon alpha and beta exposure. A and B) 48 melanoma cell lines were exposed with the pre-determined concentrations of interferon alpha (A) or beta (B) for 18 hours and PD-L1 expression was measured by flow cytometry. The cells are organized in order by average baseline expression; the arrow indicates the average changes upon interferon treatment, and the shaded grey area represents the full range of measurements from two independent experiments (three independent experiments were performed in some cell lines which showed large variation).

Supplementary Figure 10. Predicted functional consequences of M368 JAK2 D313 splice site mutation. A) Output from the Human Splice Finder 3.0 (http://www.umd.be/HSF3/). Chromosome 9 5055668 G>A mutation is predicted to break the existing splice acceptor and create a new one shifted by a single nucleotide, producing a frameshift outcome. Transcripts from Ensembl Release 70. B) Schematic of genomic locus at JAK2 exon 8. Lower case = intronic nucleotides, upper case = exonic. Red arrows point to G to A mutation.

Supplementary Figure 11. Immunohistochemistry (IHC) analysis of biopsies from melanoma metastases with a JAK1 loss of function mutation. IHC analysis of the whole-tissue biopsy from which patient-derived cell line M395 was established. Sequentially cut pathology slides were stained for S100 to delineate the area of the tumor, CD8 for T cells, CD68 for macrophages, as well as for PD-1 and PD-L1. The contour of the melanoma from the biopsy is delineated in yellow to highlight the intratumoral space.

Supplementary Figure 12. **JAK1 wild-type lentiviral vector transduction.** A) Schematic of the JAK1 wild-type expressing lentiviral vector. B and C) Gating strategies for sorting based on GFP signal for M431 and M395 after JAK1 wild-type lentiviral vector transduction respectively.

Supplementary Figure 13. Mutations in antigen presentation machinery from anti-PD1 treated colorectal cohort. Subjects are ordered as in Fig. 4A, and top bar graph re-depicts mutational load for reference. The size of circles and adjacent labels represent the tumor variant allele frequency (VAF) of the mutation after adjustment for stromal content. Color represents predicted functional effect.

Supplementary Figure 14. DNA damage repair gene mutations in endometrial cancer cell lines with *JAK1/2* mutations. Analysis of gene mutations involving DNA repair in the 11 endometrial carcinoma cell lines with JAK1/2 mutations, including POLE or POLD1 mutations, microsatellite instability and DNA damage gene mutations.

Supplementary Figure 15. Frequency of *JAK1* and *JAK2* alterations and their association with overall survival in additional TCGA datasets. Kaplan-Meier survival analysis of TCGA lung adenocarcinoma (A) and colorectal adenocarcinoma (B), comparing control patients (blue) and patients harboring specified alterations in *JAK1* and *JAK2* (red). Frequency and distribution of combined *JAK1* and *JAK2* alterations are shown within each set of Kaplan-Meier plots. Significance testing of overall survival was performed using log-rank analysis.

Supplementary Figure 16. Functional effect of genetic loss of reactive PD-L1 on responses to PD-1 blockade. A) Adaptive immune resistance is mediated by a T cell that recognizes cognate antigen and produces interferon gamma. This triggers the phosphorylation of JAK1 and JAK2, with both being necessary for downstream signaling and being a bottle neck in the pathway. The downstream effect is the expression of PD-L1, which then blocks the T cell that was attaching the cancer. In this setting, an anti-PD-1 or anti-PD-L1 blocking antibody would release this immune checkpoint and lead to a tumor response. B) Futility of using a PD-1/L1 blocking antibody if the interferon gamma response circuit is broken due to JAK1/2 loss of function mutations. A tumor that has evolved to lose the expression of JAK1 or JAK2 will not respond to interferon gamma by expressing PD-L1. If PD-L1 is not turning off the T cell, then blocking PD-1 or PD-L1 would be futile treatment. The circuit is broken leading to innate resistance to these class of agents, and being the only cases that we can truly say the cancer is PD-L1 negative. In all other cases where the cancer has this circuit intact, PD-L1 could be potentially re-expressed upon T cell infiltration and production of interferon gamma. Therefore, the majority of cases that we now call “PD-L1 negative” are not really negative unless they had

JAK1/2 loss of function mutations. All other could be re-expressed with combination immunotherapies that included PD-1 blockade with another immune activating therapy.

Supplementary Table 1. Demographic and baseline patient clinical characteristics.

Supplementary Database 1. Whole exome sequencing of 23 baseline biopsies from patients analyzed in Fig. 1, and whole exome sequencing of the M431 cell line (Accession code: SRP067938).

Supplementary Figure. 1

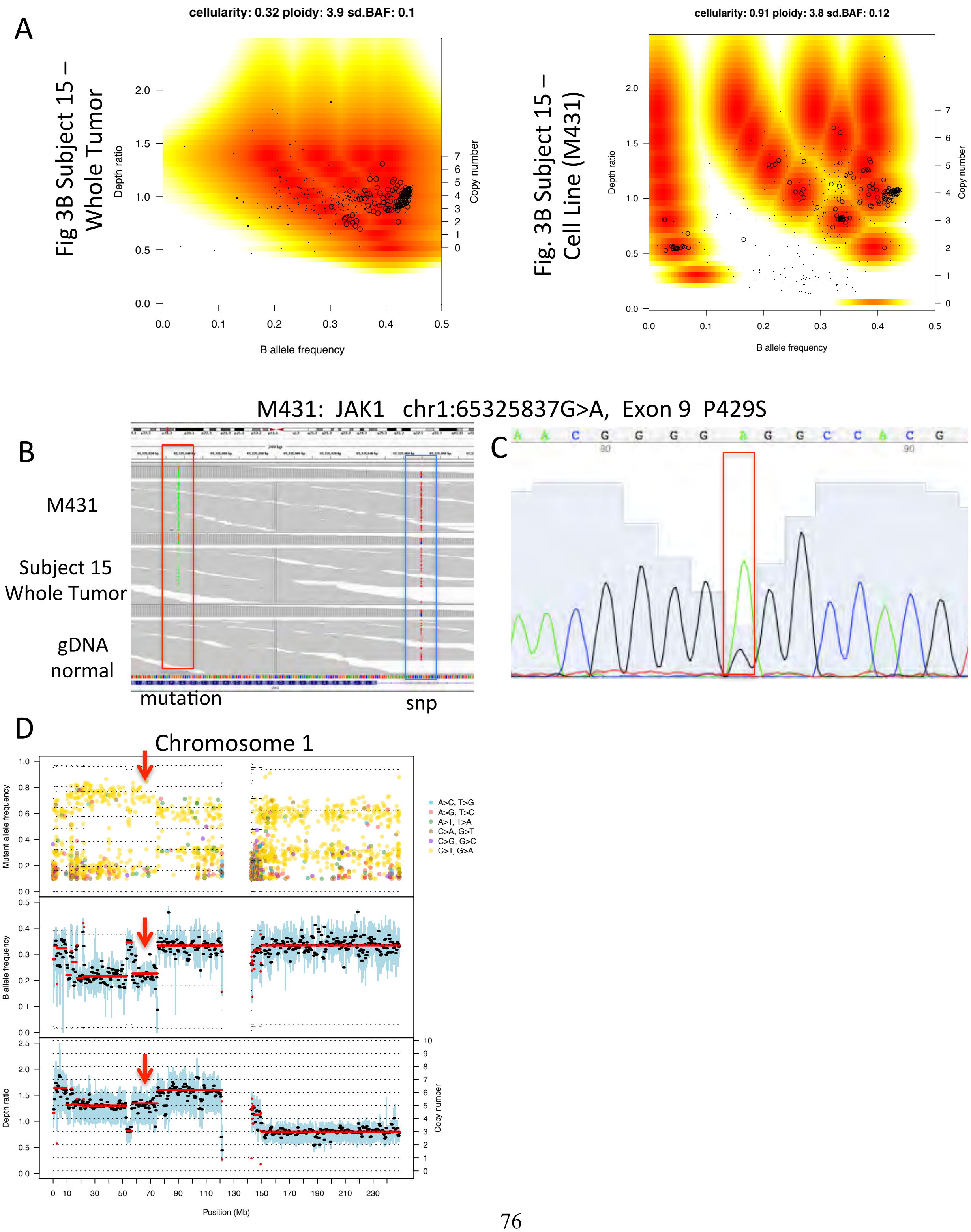

Supplementary Figure. 1 cont.

E

Subject 15 - Tumor

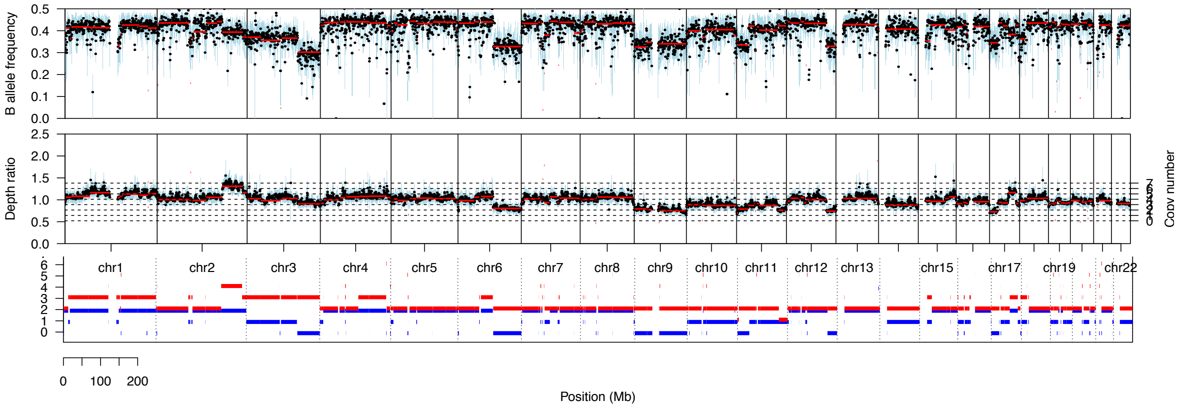

Subject 15 – Cell Line (M431)

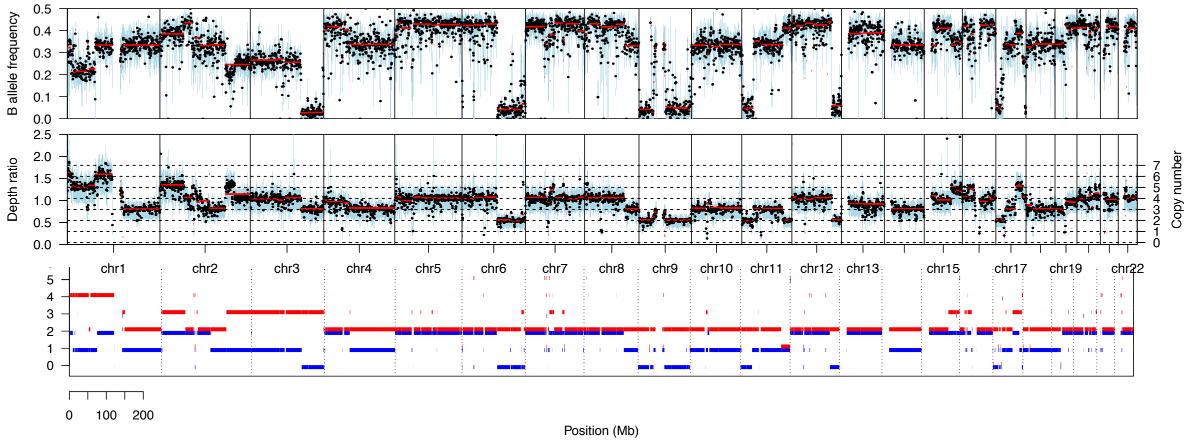

Supplementary Figure. 2

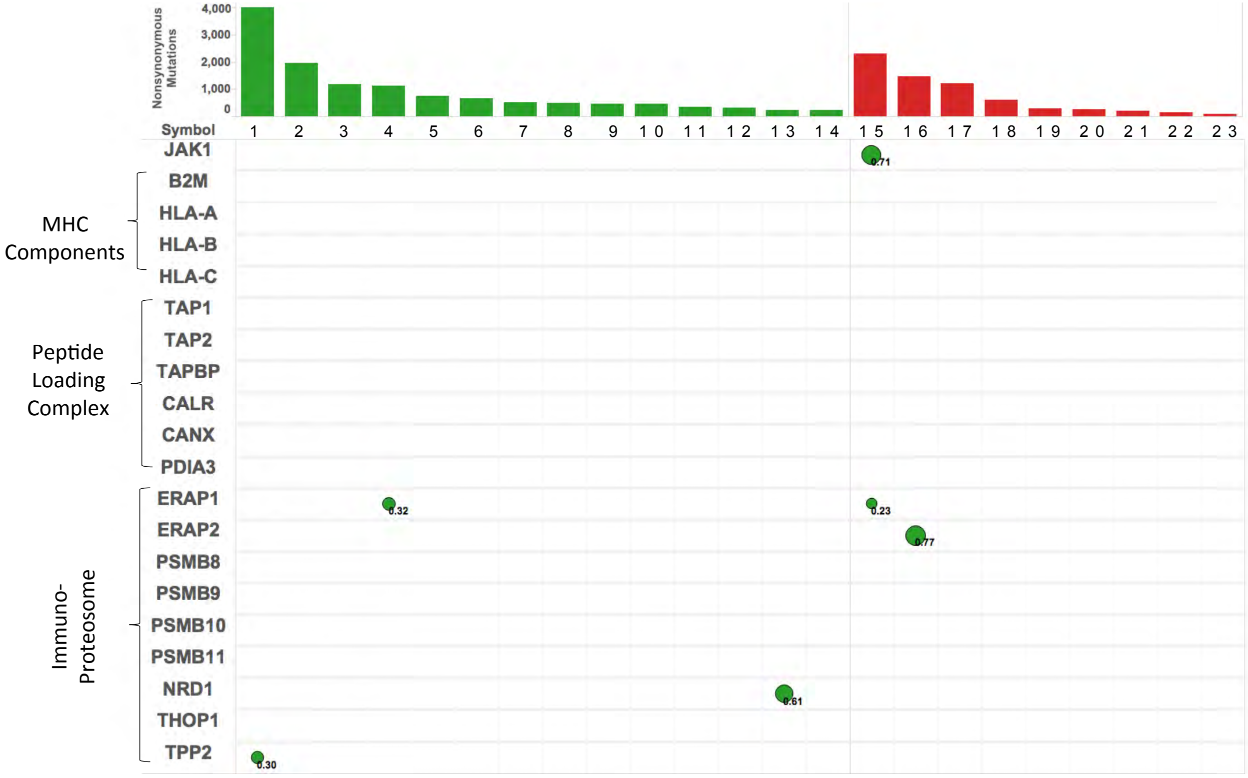

Supplementary Figure. 3

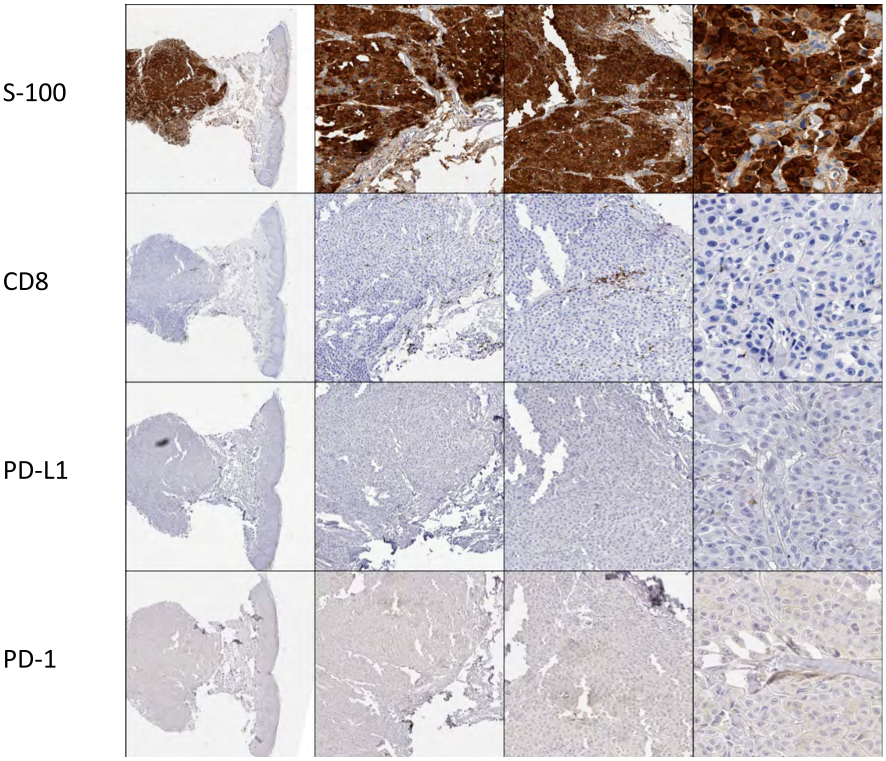

Supplementary Figure. 4

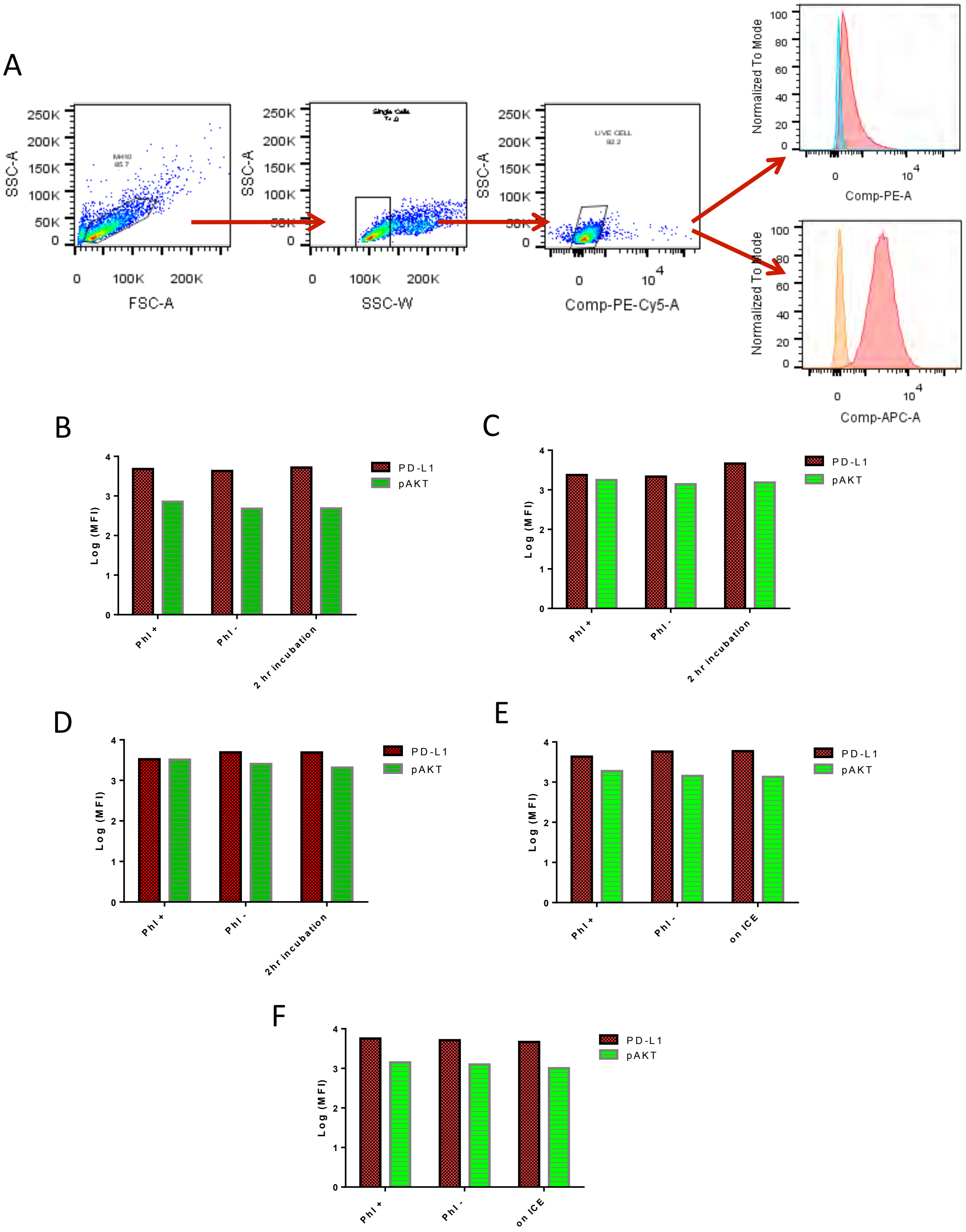

Supplementary Figure. 5

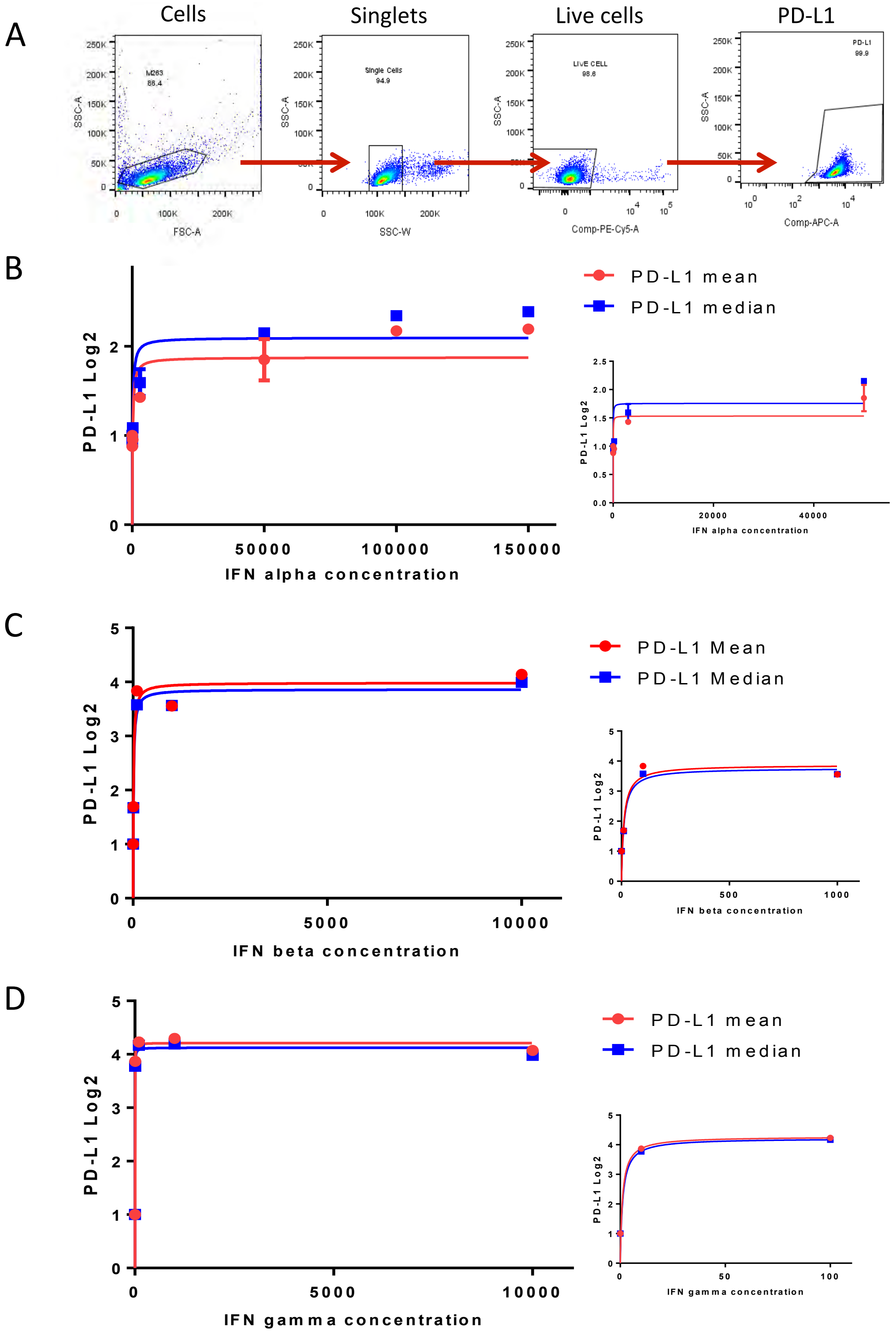

Supplementary Figure. 6

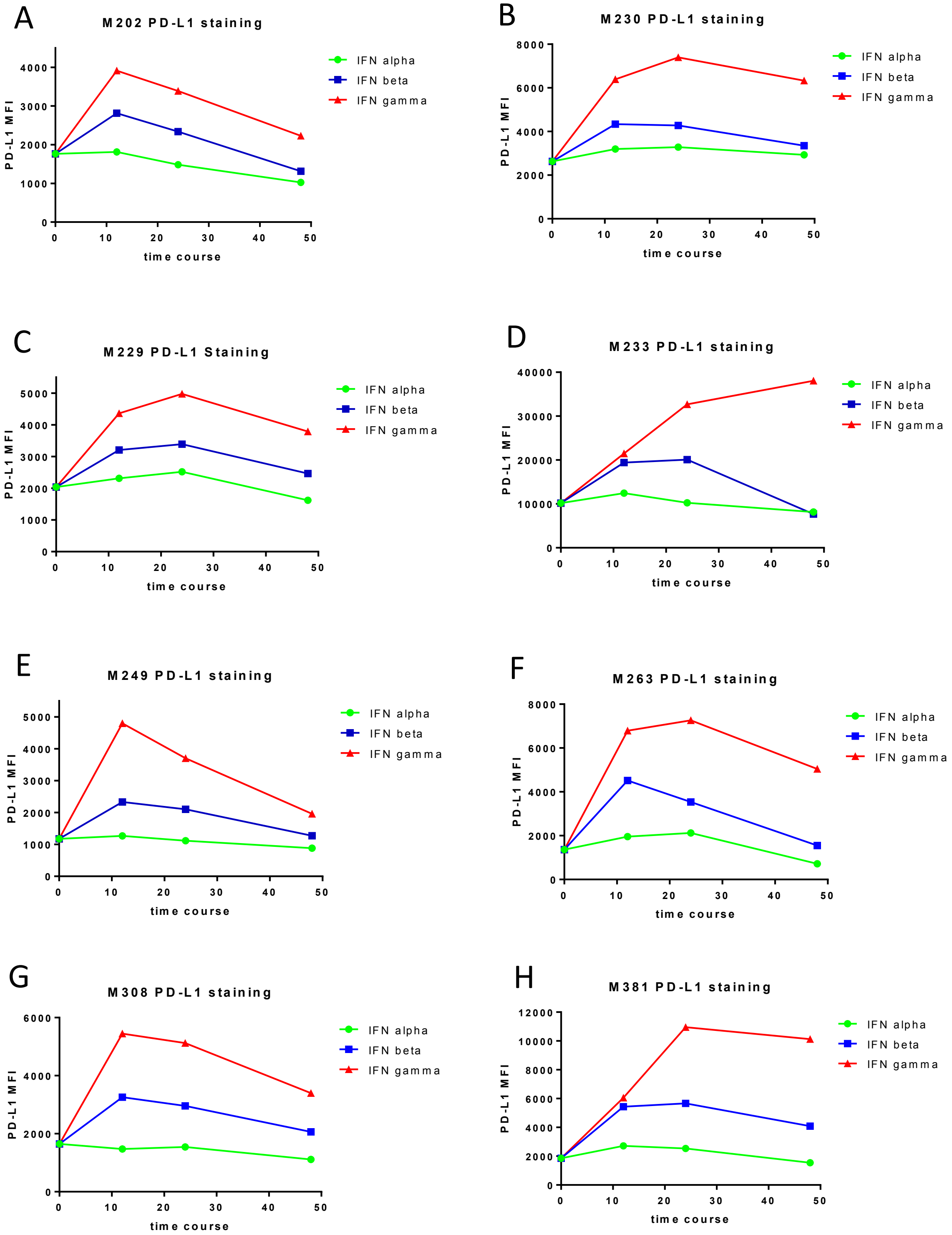

Supplementary Figure. 7

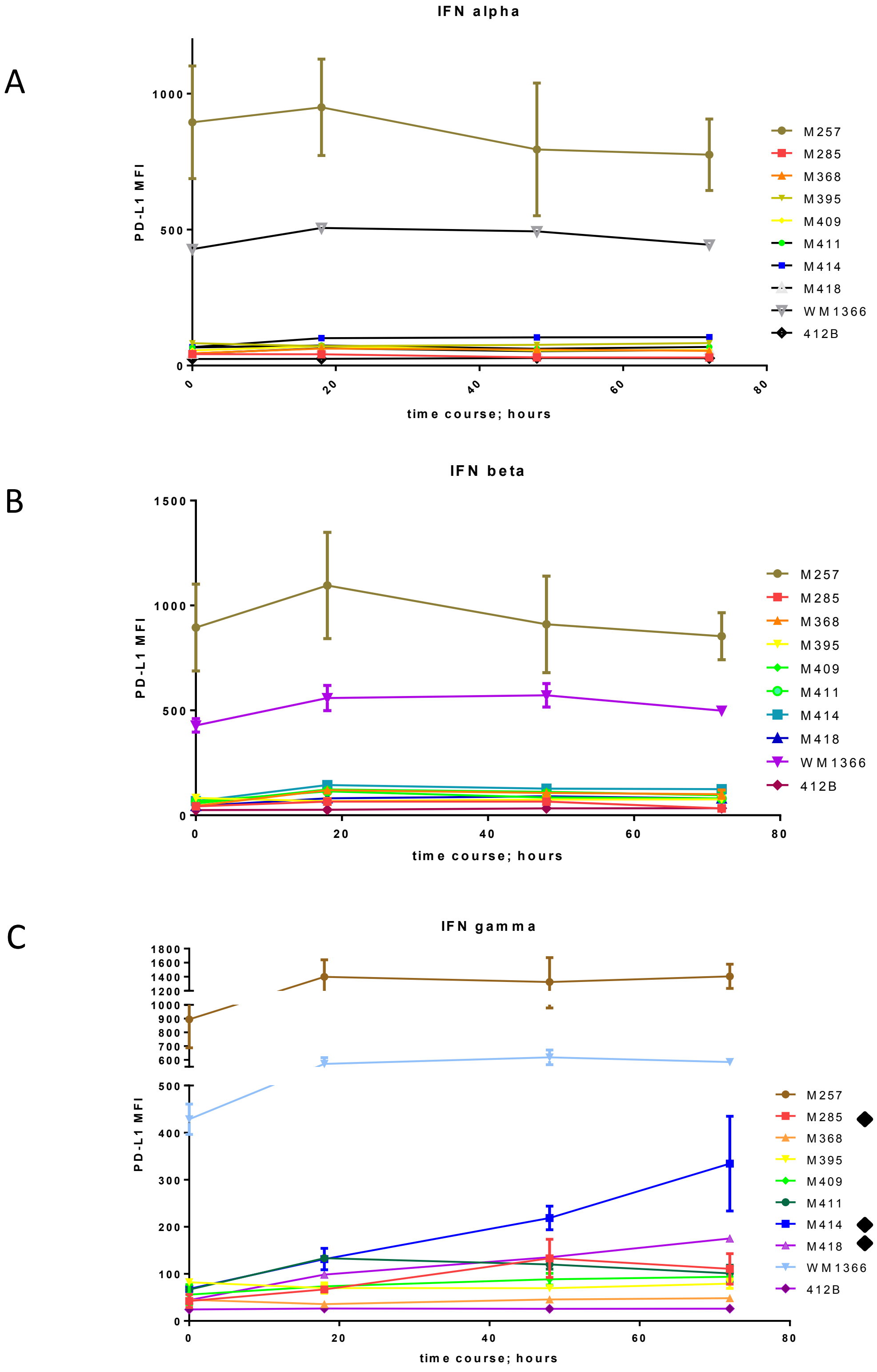

Supplementary Figure. 8

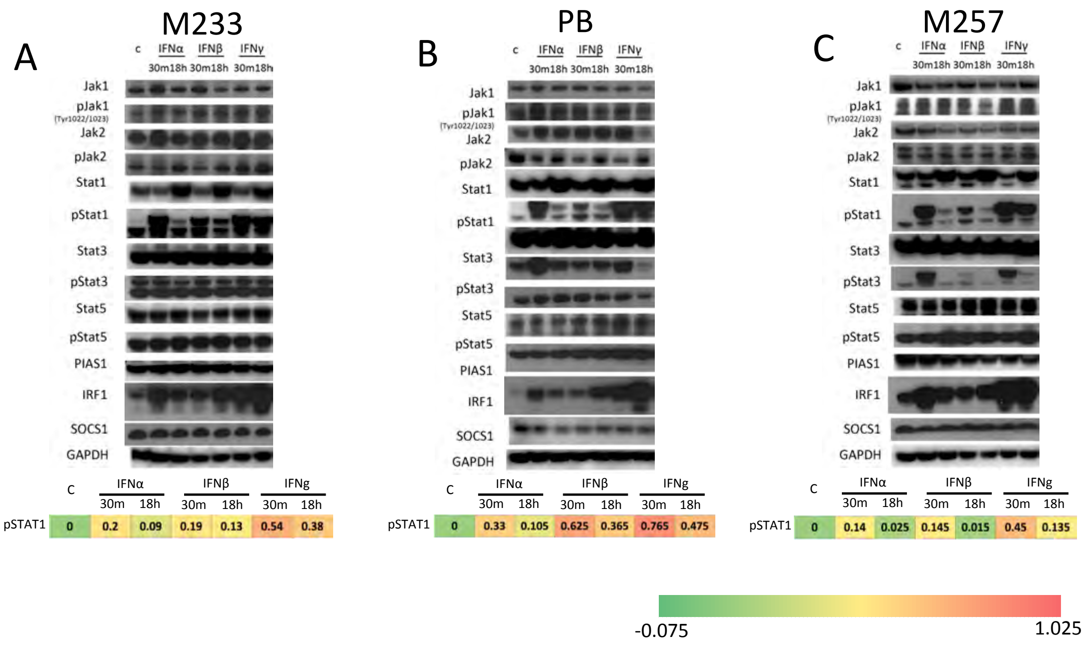

A

	C	IFNα		IFNβ		IFNg	
		30m	18h	30m	18h	30m	18h
pSTAT1	0	0.2	0.09	0.19	0.13	0.54	0.38

B

	C	IFNα		IFNβ		IFNg	
		30m	18h	30m	18h	30m	18h
pSTAT1	0	0.33	0.105	0.625	0.365	0.765	0.475

C

	C	IFNα		IFNβ		IFNg	
		30m	18h	30m	18h	30m	18h
pSTAT1	0	0.14	0.025	0.145	0.015	0.45	0.135

Supplementary Figure. 9

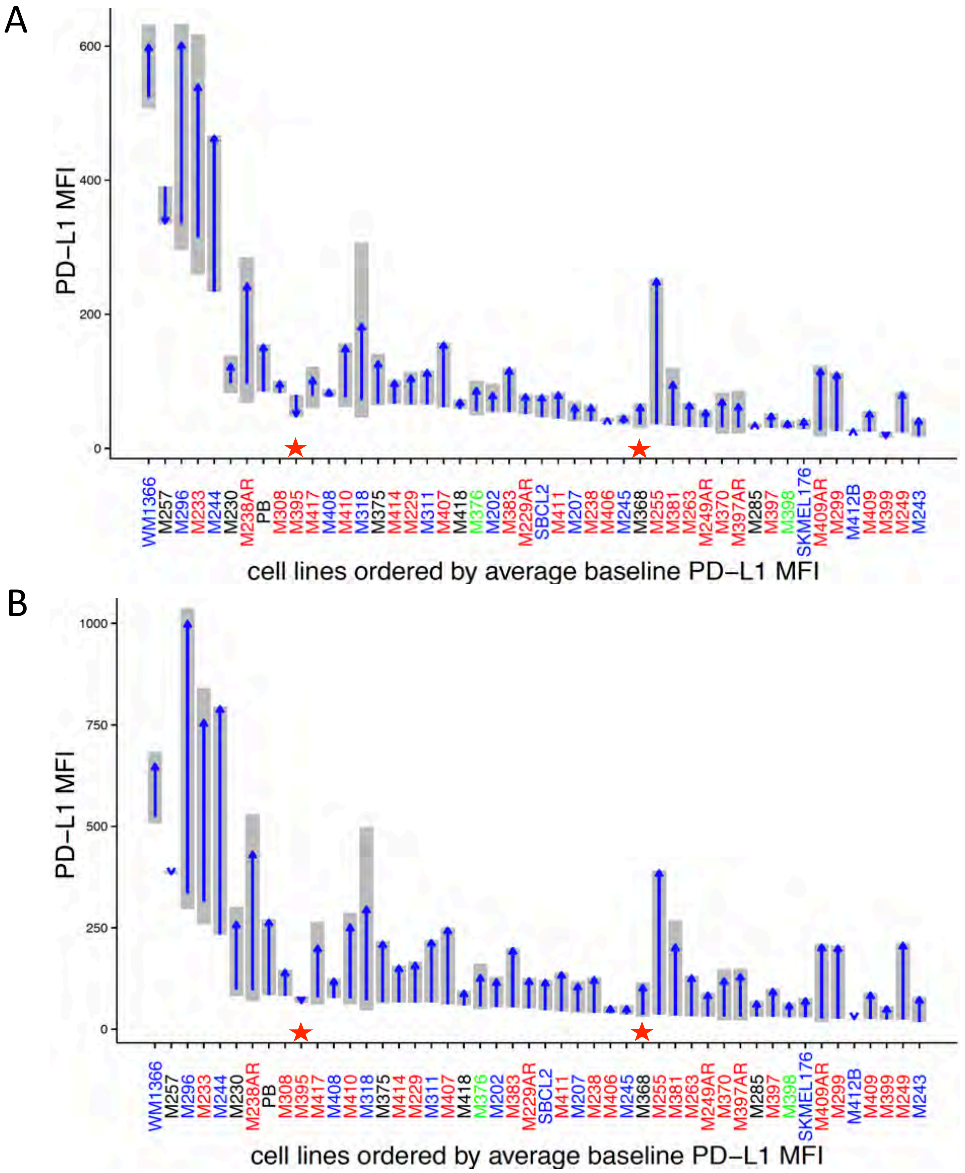

Supplementary Figure. 10

A.

Splice site type	Motif	New splice site	Wild Type	Mutant	Variation (%)
Acceptor	ttttaattatagGA	ttttaattataaGA	85.16	56.22	WT site broken -33.98
Acceptor	tttaattatagGAT	tttaattataagAT	47.43	76.37	New site +61.02

B. JAK2 Transcript ENST00000381652

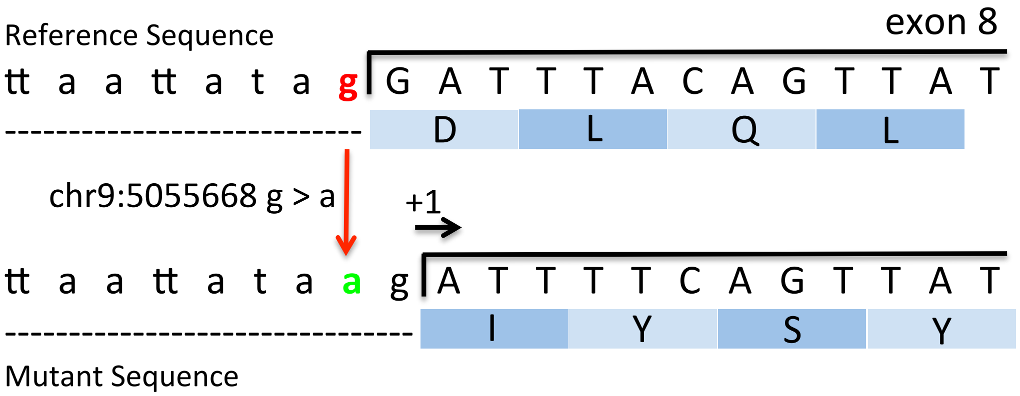

Supplementary Figure. 11

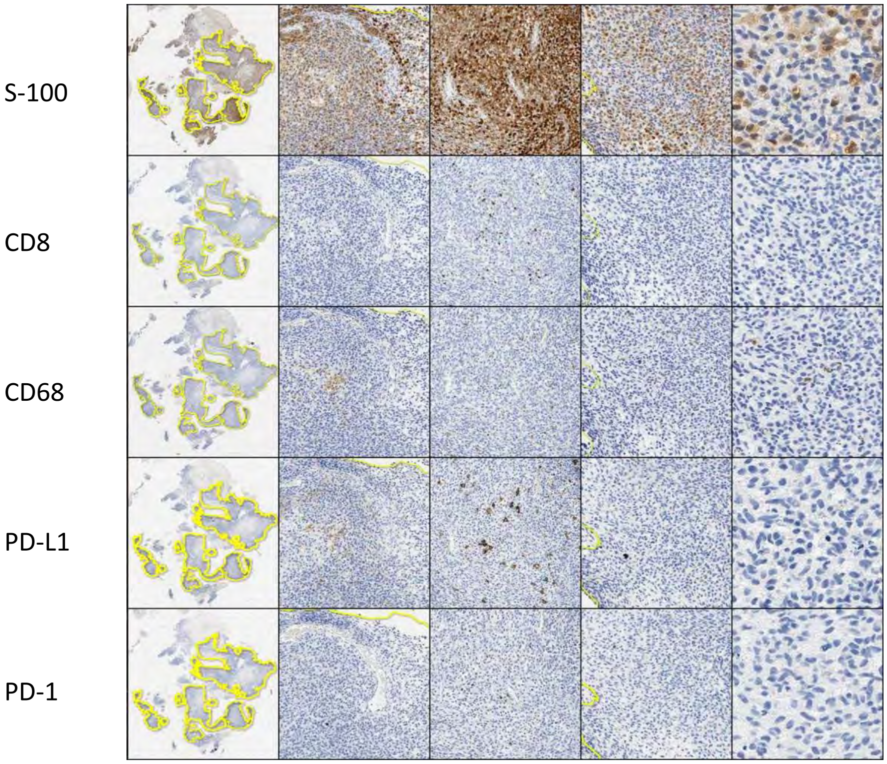

Supplementary Figure. 12

A

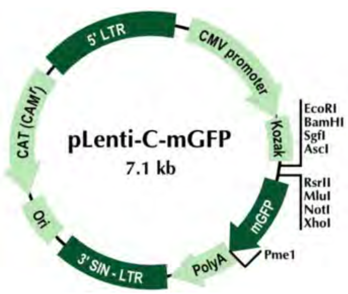

B

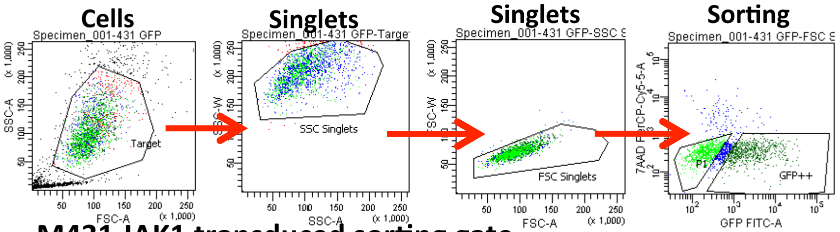

M431 JAK1 transduced sorting gate

C

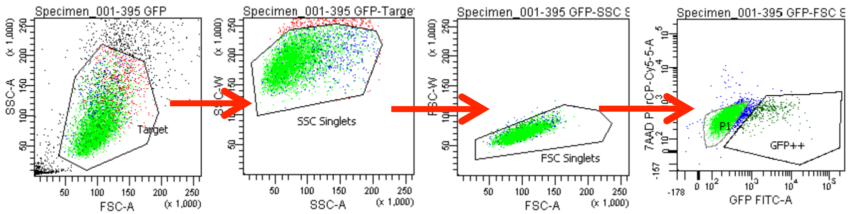

M395 JAK1 transduced sorting gate

Supplementary Figure. 13

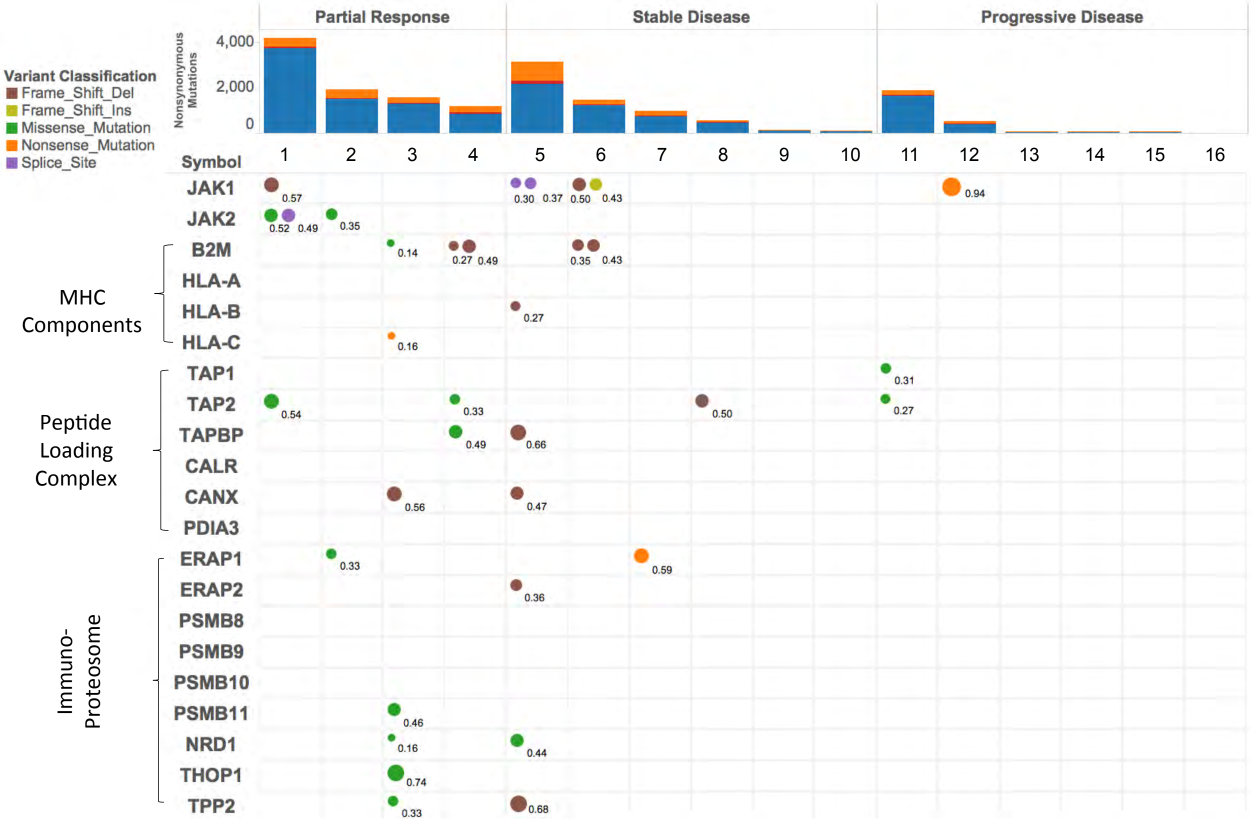

Supplementary Figure. 14

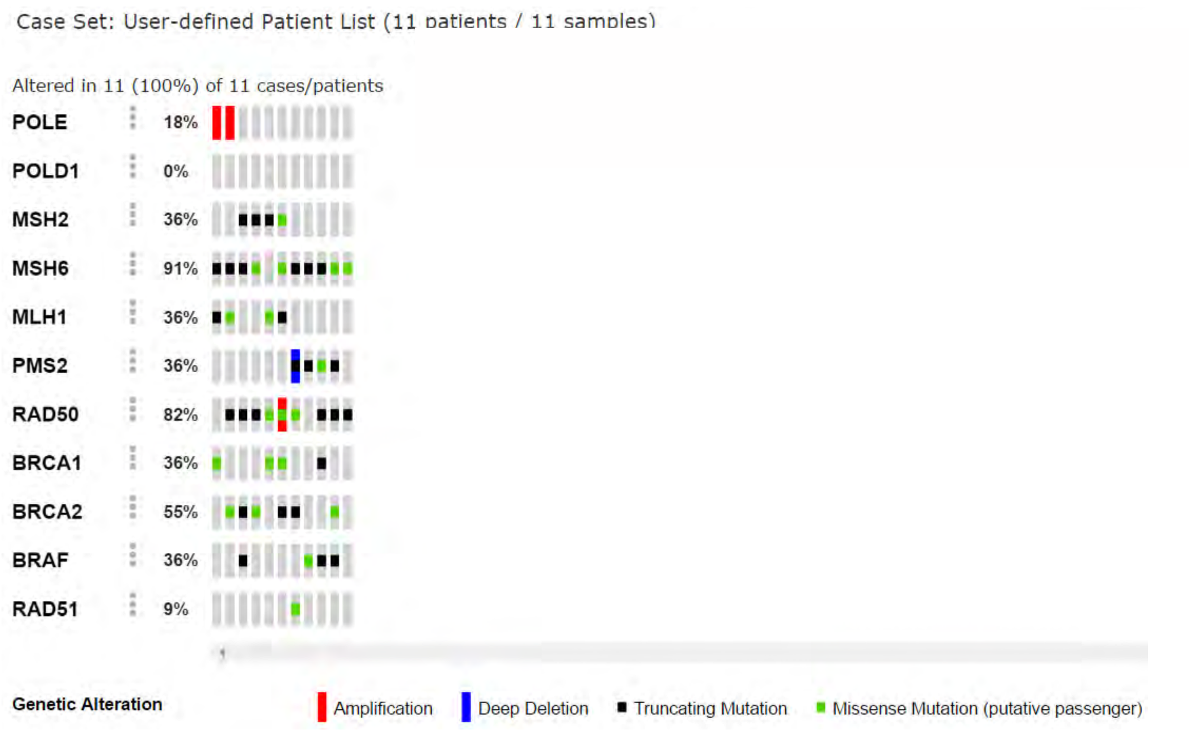

Case Set: User-defined Patient List (11 patients / 11 samples)

Altered in 11 (100%) of 11 cases/patients

Supplementary Figure. 15

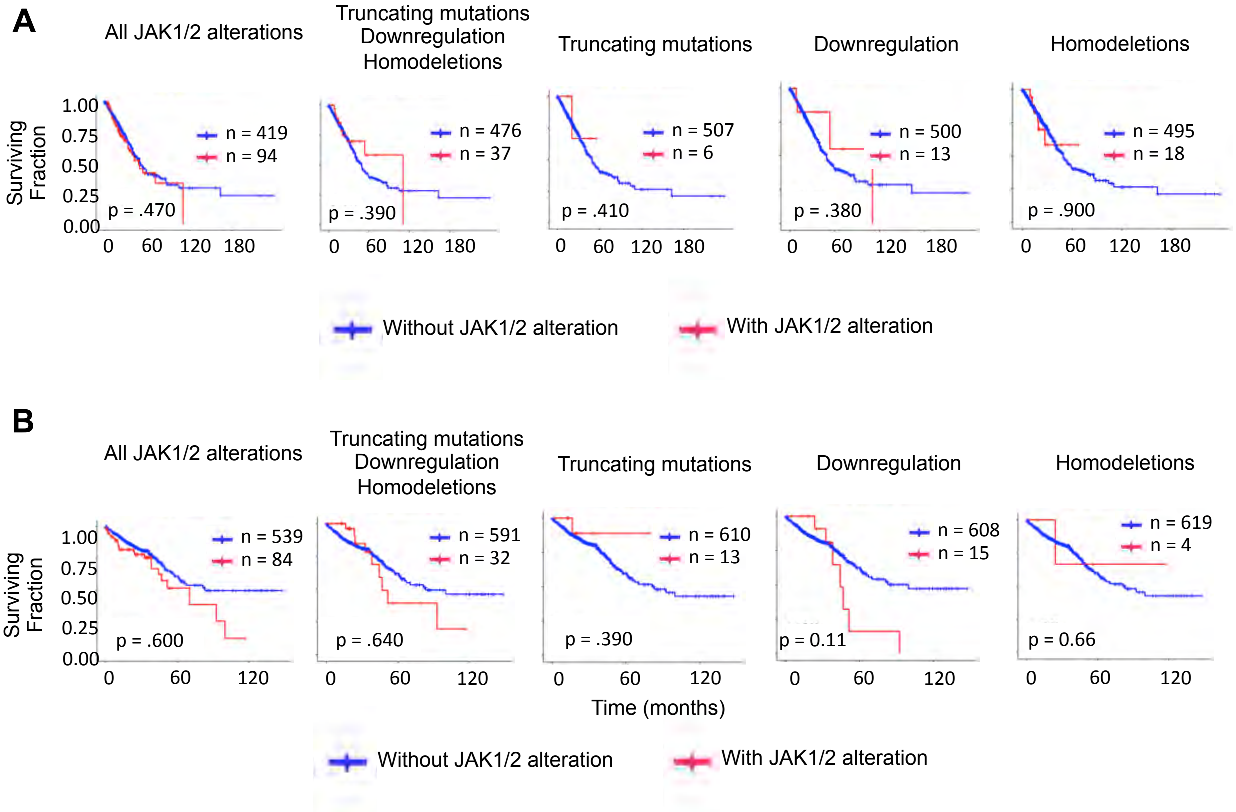

Supplementary Figure. 16

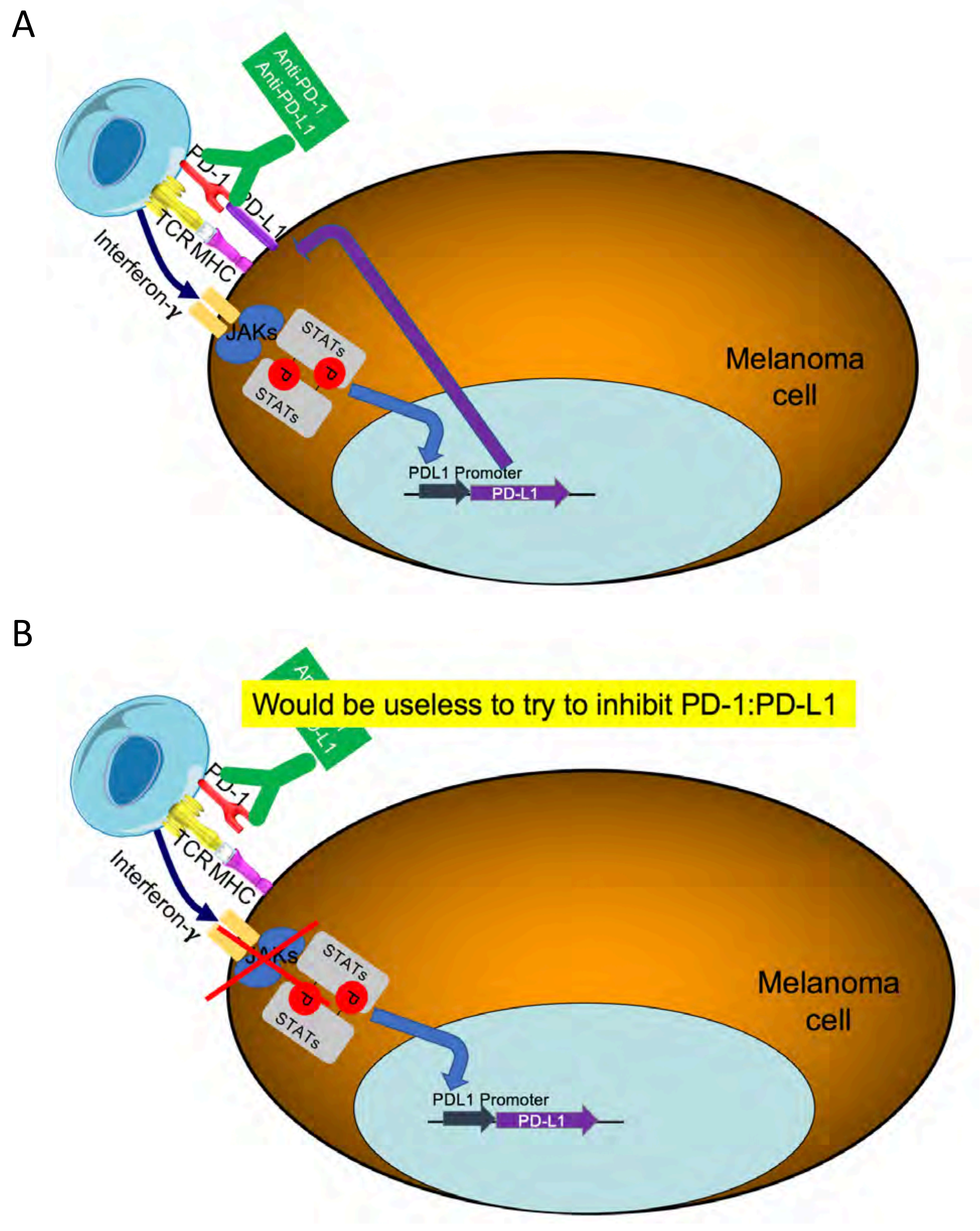

Would be useless to try to inhibit PD-1:PD-L1

Supplementary Table 1. Demographic and baseline patient clinical characteristics.

	Total patients 23	
	Responders	Non-responders
Number of patients (M/F)	14 (13/1)	9 (5/4)
Mean age (M/F)	62 (63/53)	59 (67/54)
Stage		
M0	1	0
M1a	0	0
M1b	2	1
M1c	11	8
ECOG performance status		
0	11	8
1	3	1
Brain metastasis		
Yes	1	0
No	13	9
LDH		
Normal	10	5
Elevated	4	4
BRAF and other mutational status		
Wild type	7	5
BRAF V600E	6	4
BRAF 597	1	0
NRAS mutated (from BRAF wild type)	0	1
RAF1 amplified (from BRAF wild type)	0	1
Prior treatment		
None	1	0
Radiation only	2	0
Chemotherapy only	0	0
Immunotherapy	8	10
BCG	1	0
GM-CSF	1	0
Interferon	1	2
Ipilimumab	6	9
Ipilimumab + Interferon	1	2
Ipilimumab + IL-2	1	0
Targeted therapy (vemurafenib or dabrafenib)	5	4
Adoptive cell therapy TCR or TIL therapy)	2	1
Toxicities (Adverse effects)		
Fatigue (grade 1-2)	2	2
Colitis (grade 1-3)	2	1
Pneumonitis (grade 1-2)	1	1
Myalgia (grade 1-2)	0	1
Vitiligo	3	1
Diverticulitis (grade 1-2)	1	0
Liver function test abnormality, grade 3	0	1
Acute renal insufficiency, grade 4	1	0
Response		
Partial response (PR)	11	-
Complete response (CR)	3	-
Progression of disease (PD)	-	9

Chapter 4:

High response to PD1 blockade in desmoplastic melanoma

High response rate to PD-1 blockade in desmoplastic melanomas

Zeynep Eroglu[1,2]*, Jesse M. Zaretsky[1]*, Siwen Hu-Lieskovan[1]*ɣ, Dae Won Kim[2,3], Alain Algazi[4], Douglas B. Johnson[5], Elizabeth Liniker[6], Ben Kong[7], Rodrigo Munhoz[8], Suthee Rapisuwon[9], Pier Federico Gherardini[10], Bartosz Chmielowski[1], Xiaoyan Wang[1], I. Peter Shintaku[1], Cody Wei[1], Jeffrey A. Sosman[5], Richard Joseph[13], Michael A. Postow[8], Jane Messina[2], Richard A. Scolyer[6,11,12], Alistair J. Cochran[1], Matteo S Carlino[6,7,11], Wen-Jen Hwu[3], Georgina V. Long[6,11,14], Antoni Ribas[1]ɣ

*Equal contribution as first authors

ɣCorresponding authors

Author Affiliations: [1]University of California Los Angeles; Los Angeles, CA; [2]Moffitt Cancer Center and University of South Florida, Tampa, FL; [3]The University of Texas-MD Anderson Cancer Center, Houston, TX; [4]University of California San Francisco, San Francisco, CA; [5]Vanderbilt Ingram Cancer Center, Nashville, TN; [6]Melanoma Institute Australia, Sydney, Australia; [7]Westmead Hospital, Sydney, Australia; [8]Memorial Sloan Kettering Cancer Center, and Weill Cornell Medical College, New York, NY; [9]Georgetown Lombardi Cancer Center, Washington D.C.; [10]Parker Institute for Cancer Immunotherapy, San Francisco, CA [11]The University of Sydney, Sydney, Australia; [12]Royal Prince Alfred Hospital, Sydney, Australia; [13]Mayo Clinic, Jacksonville, FL.; [14]Royal North Shore Hospital, Sydney, Australia

Desmoplastic melanoma (DM) is a rare subtype of melanoma characterized by dense fibrous stroma, resistance to chemotherapy and a lack of actionable driver mutations, but is highly associated with ultraviolet light DNA damage. We analysed 57 patients with advanced DM treated with programmed cell death 1 (PD-1) or PD-1 ligand (PD-L1) blocking antibody therapy. Objective tumour responses were observed in 40 of the 57 patients (70%, 95% confidence interval 58-82%), including 18 patients (32% overall) with a complete response. Whole-exome sequencing revealed a high mutational load and frequent *NF-1* mutations (14/17 cases). Immunohistochemistry (IHC) analysis from 19 DM and 13 non-DM revealed a higher percentage of PD-L1 positive cells in the tumour parenchyma in DM ($p = 0.04$), highly associated with increased CD8 density and PD-L1 expression in the tumour invasive margin. Therefore, patients with metastatic DM derive significant clinical benefit from PD-1/PD-L1 immune checkpoint blockade therapy despite being a cancer defined by its dense desmoplastic fibrous stroma. The benefit is likely derived from the high mutational burden and a frequent pre-existing adaptive immune response limited by PD-L1 expression.

Desmoplastic melanoma (DM) accounts for less than 4% of melanomas, and is characterized histologically by spindle-shaped melanoma cells within abundant collagenous stroma with scattered lymphoid aggregates. It is strongly associated with ultraviolet light radiation damage resulting in a high mutational burden[1], but is generally without known actionable genes for targeted therapies.[1] Anti-PD-1 and anti-PD-L1 antibodies, such as atezolizumab, avelumab, durvalumab, nivolumab and pembrolizumab have been approved in many countries for the treatment of patients with advanced melanoma and other cancers.[2] By blocking the PD-1/PD-L1 checkpoint at the last step of anti-tumour T cell effector function, T cells mediate tumour-cell killing, resulting in an overall response rate of 33-40% in patients with metastatic melanoma.[3,4] Studies suggest that recognition of neoantigens resultant from somatic mutations may be important as a higher somatic non-synonymous mutation burden may be associated with improved clinical response to anti-PD-1/anti-PD-L1 therapy.[5-8] Therefore, in view of the higher mutational burden reported in DM and the recent evidence that more aggressive primary skin DM lesions had higher frequency of PD-L1 expression and CD8 infiltration[9], we hypothesized that patients with DM may have higher tumour response rates to anti-PD-1 or anti-PD-L1 therapies compared to other patients with metastatic melanoma.

We conducted a retrospective review of the pathology reports from 1058 patients with advanced melanoma treated with anti-PD-1/anti-PD-L1 immunotherapies between 2011 and 2016 at 10 international sites with high volume melanoma clinical trials. We identified 57 patients with advanced unresectable DM who received PD-1/PD-L1 blockade therapy (Expanded Data Tables 1 and 2). Thirty-five patients (61%) had visceral metastases or elevated lactate dehydrogenase (M1c disease), which are recognized makers of poor prognosis.[10] Histological features were reported by the local pathologists sub-classified as pure (n = 23), mixed (n = 29) or indeterminate (n = 5) DM histopathologic subtypes.[11,12] All cases had the distinctive diagnostic features of DM with abundant connective tissue surrounding the tumour cells, which can be highlighted by Masson's trichrome stain (examples in Figure 1a, with the collagenous stroma stained in blue). Forty-one patients (72%) had received prior systemic treatment, most frequently with the cytotoxic T lymphocyte antigen-4 (CTLA-4) blocking antibody ipilimumab (Expanded Data Tables 1 and 3). The most frequently administered anti-PD-1/anti-PD-L1 drug was pembrolizumab in 43 (75%) of patients, while eight (14%) received nivolumab, three (5%) the anti-PD-L1 antibody BMS-936559, and an additional three (5%) received a combination of nivolumab or pembrolizumab with ipilimumab.

With a median follow up of 20 months, 40 out of the 57 patients (70%, 95% Clopper-Pearson CI of 57 to 82%) had an objective response by RECIST 1.1 criteria (Figure 1b and c). This included

18 (32%) complete responses and 22 (39%) partial responses; nine patients with a partial response eventually progressed but none of the patients with complete response have progressed. When the 3 patients treated with an anti-PD1/ipilimumab doublet were excluded, responses were seen in 37 out of 54 (69%) patients. Twelve patients (21%) had progressive disease, and 5 (9%) had stable disease; two of these patients eventually progressed. Median time to best response was 4.1 months (range 1.3 – 22.6 months). Three patients with isolated progression (including two who had a partial response) underwent surgery and subsequently had no evidence of melanoma for 1.8, 5.2, and 5.3 years, respectively. With median follow-up of 20 months, median progression free survival (PFS) was not reached; estimated one-year PFS rate was 66% (95% CI 56-80) and two-year PFS rate was 62% (95% CI 51-77), indicating the durability of the responses (Extended Data Figure 1a). Median overall survival (OS) was not reached (Extended Data Figure 1b). Kaplan-Meier estimated one-year OS was 85% (95% CI 78-98) and two-year OS was 74% (95% CI 64-89). OS ranged from 3.6 months to 5.3+ years (Extended Data Figure 1b). For patients censored on the Kaplan-Meier curve, median follow-up was 27+ months. There were no statistically significant differences in either ORR (65% vs 69%), or OS between patients with the two DM histological subtypes, pure or mixed.

Given the high clinical activity noted in this series of patients with DM, we wanted to better understand the underlying biology that may lead to improved outcomes in patients. Whole exome sequencing from 17 cases in our DM cohort revealed that mutations in *NF-1* in the absence of *BRAF*/*RAS* hotspot mutations were the most common driving genetic event (82.4%, 14/17 samples), along with an enrichment for loss-of-function mutations in *TP53* and *ARID2* (Figure 2a, Extended Data Figure 2a). The high frequency of *NF-1* mutations is similar to previously published series of DM[1,13] and characteristic of a recently defined *NF-1* subtype that makes up 8-12% of melanoma.[14,15] *NF-1* subtype melanoma from sun-exposed, (but not acral[16]) sites have a mutation rate that is more than double the *BRAF*, *RAS*, or triple wild-type subtypes.[14,15] Correspondingly, our DM cohort displayed a similarly high mutational load (median 1282 nonsynonymous mutations compared with 1052 in TCGA *NF-1* subtype, rank sum p = 0.71) that was significantly greater than non-*NF-1* subtype melanoma in TCGA data or combined data from two anti-PD1 treated cohorts[17,18] (rank sum p = 2.3e-9 and p= 0.0006 respectively, Figure 2b). In a prior cohort[1], 45% of DM were of a high mutational load triple wild-type subtype; however, we only identified two such samples, one of which may be a false negative due to low tumour purity and coverage (Extended Data Table 1). Regardless of subtype, all DM samples contained >82% C>T transitions as part of a strong signature of ultraviolet light induced DNA damage that is common to cutaneous melanoma.[1,19] (Extended Data Figure 2b-c).

Although DM has high mutational load and a high anti-PD-1 overall response rate, non-responders (n=5) showed no difference in mutational load from responders (rank sum p = 0.91, Figure 2b), a finding which is also true of two previous anti-PD1 treated cohorts,[17,18] in contrast to anti-CTLA4 treated melanoma[20] (Extended Data Figure 2d). Among the few samples with an NF1 subtype in these other immunotherapy-treated cohorts, 4 out of 6 had response to anti-PD1 and 5 out of 10 had response to anti-CTLA4 (Figure 2d, Extended Data Figure 2c).

Genes mutated more frequently in DM non-responders or responders are reported in Extended Data Figure 3a, though none passed false-discovery-rate cutoffs due to the small number of samples per group and high number of mutations, We did not find any significantly recurrent (n > 3) point mutations, and only one sample in our cohort harboured a mutation in *NFKBIE*, the chr6:44,233,400 C>T hotspot previously reported to be mutated at frequently in DM.[1] We analysed potential detrimental mutations in the interferon receptor pathway that may result in innate or acquired resistance to anti-PD-1 therapy[17,21] and detected potentially homozygous interferon pathway mutations in one case with a mixed clinical response who progressed due to new bone metastases (Extended Data Figure 3b). We did not detect any mutations in *B2M* nor complete loss-of-function mutations in other critical non-redundant antigen presentation machinery molecules (Extended Data Figure 3b).

Previous work showed that pre-existing intratumoral CD8+ T cells, in particular when co-localized with PD-1 and PD-L1 expression at the invasive tumour margin or tumour periphery, may predict response to anti-PD1/L1 therapy.[22] The presence of lymphoid aggregates within and at the periphery of the tumour are an important histopathologic hallmark of DM that may provide a substrate for response to anti-PD1/L1 therapy. In order to evaluate whether the presence of CD8+ T cells at the tumour periphery in DM predicts response to anti-PD1/L1 therapy, we analysed 19 available pre-treatment tumour biopsies from our DM cohort for digital quantitative immunohistochemistry (IHC) analyses of PD-L1 and CD8. S100 expression was used to define the invasive tumour margin (stromal-tumour edge) and inside tumour parenchyma (tumour centre). Thirteen baseline biopsies of patients with metastatic non-DM also treated with anti-PD-1 therapies were used for comparison (7 with a complete or partial response, 6 with progressive disease). Overall, biopsies of patients with DM (including both responders and non-responders), had a strikingly higher percentage of PD-L1 positive cells in the tumour parenchyma when compared to non-DM cases ($p = 0.04$, Figure 3b). There were no significant differences in the density of CD8+ cells between DM and non-DM cases in the tumour parenchyma, and CD8+ and PD-L1+ cells in the invasive margin ($p = 0.12$, $p = 0.41$, $p = 0.16$, Figure 3a, 3c and 3d). Consistent with our previous observation, the strongest correlation with clinical benefit (defined as having a complete or partial response, or prolonged stable disease for >12 months) was baseline density of CD8+ T cells in the invasive margin in non-DM melanoma. ($p=0.002$, Extended Data Figure 4a, b, c and d).

The higher density of intra-tumour PD-L1 expression in DM, especially in the biopsies of patients with a clinical response, could be due to reactive PD-L1 expression in response to T cells producing interferon gamma, which is termed adaptive immune resistance, [23,24] or due to intrinsic genetic alterations leading to constitutive PD-L1 expression.[25] This prompted us to investigate the association between CD8+ and PD-L1+ cell densities in the invasive margin and tumour parenchyma. As shown in Extended Data Figure 5, in DM samples PD-L1 expression in the tumour parenchyma was significantly associated with CD8 density (p=0.007) and PD-L1 expression in the invasive margin, but not CD8 density inside of the tumour parenchyma (p=0.15). Similarly, PD-L1 expression in the invasive margin was significantly correlated with CD8 density in the invasive margin (p=0.0003), CD8 density in the tumour parenchyma (p=0.04), and PD-L1 expression in the tumour parenchyma (p=0.0003). Among cases for which we had exome sequencing, we did not detect many of the reported genetic mechanisms reported to cause constitutive PD-L1 expression among our DM samples, including amplification of the PD-L1/PD-L2/JAK2 (PDJ) locus or MYC, EGFR mutation or amplification, or CDK5 disruption.[26-29] With respect to the PI3K/AKT pathway,[30,31] we observed one case with a *PIK3CA E542K* activating hotspot mutation, in which 22% of intra-tumour cells were PD-L1 positive, and one with an *AKT2 P45L* mutation of uncertain significance, whose intra-tumour cells were 11% PD-L1 positive. The PD-L1 3’ UTR was not well captured in our exome sequencing, and disruption could not be assessed.[32]

We also observed a striking difference in the pattern of PD-L1 expression in DM samples when compared to the non-DM samples. Analysis of CD8+ cell infiltration and PD-L1 expression level in the invasive margin and tumour parenchyma resulted in six different patterns (Figure 4a to f). Twelve out of 14 patients (86%) with DM and six out of seven patients (86%) with non-DM who derived a clinical benefit to anti-PD1/L1 treatments had one of the three patterns that included high CD8+ cells. Ten out of 17 DM cases displayed high PD-L1 in both the tumour parenchyma and invasive margins. Six out of seven cases of non-DM with clinical benefit to anti-PD1/L1 treatment had high PD-L1 expression in the invasive margin (Figure 4g).[22] Patients without a tumour response tended to have low CD8+ cells regardless of the status of PD-L1 (Figure 4g), although occasionally (2 out of 9) patients whose tumours had low baseline CD8 infiltrates responded to therapy.

We generated a heat map to integrate the data of CD8 and PD-L1 expression in biopsies with response and mutational load, allowing cases of DM and non-DM to self-organize based on this data (Extended Data Figure 6). Biopsies with higher CD8+ invasive margin density clustered together usually with higher PD-L1 expression both intratumoral and in the invasive margin, and were enriched for patients with an objective tumour response. The DM and non-DM cases did not segregate from each other and were distributed among the different clusters of cases; however the majority of cases with high PD-L1 expression in the tumour parenchyma were DM. Mutational load, which was relatively high in all these cases, did not cluster with any particular pattern of CD8 or PD-L1 expression, or with response to therapy.

Desmoplastic melanoma is defined by its clinically and pathologically evident desmoplasia. Clinically, these lesions present as solid masses that are adherent to surrounding tissues and require large defiguring surgeries for resection. Dense collagenous stroma has been thought to be a major limitation for immune infiltration, as it has been described for pancreatic cancer.[33-36] However, our data challenges this notion as there are indeed pre-existing T cell infiltrates in the invasive edge of DM lesions, and a much higher response rate to anti-PD1 therapy than any other subtypes of melanoma. In fact, the response rate of 70% is among the highest to single agent PD-1 blockade therapy in any pathologically-defined cancer, together with relapsed Hodgkin's disease and Merkel cell carcinomas.[26,37] With a high mutational load and a high frequency of intratumoral PD-L1 expression that is highly associated with CD8 T cell density in the invasive margin, it suggests that DM responds to PD-1 blockade therapy due to having a more dynamic pre-existing adaptive immune response process.

Methods

Analysis of clinical data

To conduct this retrospective analysis, records of 1054 patients with advanced melanoma treated with anti-PD1/PDL1 therapy were reviewed across ten institutions to identify those with a diagnosis of DM. Each institution conducted its own search to find patients who fit these criteria. All patients had signed a local written informed consent form for research analyses. Consent to obtain photographs was obtained.

Immunohistochemistry (IHC) analysis

Patients were selected for IHC analysis if they had adequate pre-treatment tumour samples and had signed a local written informed consent form for research analyses. Tumour samples were obtained from eight different institutions. Slides cut from frozen or FFPE tissue samples were stained with haematoxylin and eosin, Masson's Trichrome stain, or anti-S100, anti-CD8, and anti-PD-L1 at the UCLA Anatomic Pathology Immunohistochemistry and Histology Laboratory (CLIA-certified). Antibodies used included rabbit polyclonal S100 (DAKO, 1/1000 dilution, low pH retrieval), CD8 clone C8/144B (Dako, 1/100, low pH retrieval), and PD-L1 (Sp142, 1/200 dilution with High pH retrieval Spring Biosciences, Pleasanton, CA). IHC was performed on Leica Bond III autostainer using Bond ancillary reagents and Refine Polymer Detection system. Slides were examined for the presence of CD8 and PD-L1 within the tumour parenchyma and the connective tissue surrounding the tumour (invasive margin). We defined the invasive margin (or leading edge) as the interfaces between individual tumour bundles and the fibrotic regions, as opposed to the intra-tumour staining, which is within the capsule of individual tumours. All slides were scanned at an absolute magnification of ×200 (resolution of 0.5 μm per pixel). An algorithm was designed based on pattern recognition that quantified immune cells within S100-positive areas (tumour) and S100-negative areas (invasive margin). The algorithm calculated the percentage cellularity (% positive cells/all nucleated cells) using the Halo platform (Indica Labs, Corrales, NM). This analysis system was not able to differentiate between tumour cell or infiltrating immune cell PD-L1 staining.[38] Immunohistochemical variables were compared between biopsies of patients who responded or progressed using Wilcoxon-Mann-Whitney test.

Genetic analyses

In brief, whole exome sequencing was performed at the UCLA Clinical Microarray Core using the Roche Nimblegen SeqCap EZ Human Exome Library v3.0 targeting 65 Mb of genome. Mutation calling was performed as previously described.[17,21] Out of 22 biopsies of DM sequenced, 17 cases (3 complete responses, 8 partial responses, 1 stable disease, 5 progressive disease) could be analysed by meeting quality control criteria for minimum coverage (50x tumour, 30x normal), tumour content (10%), and effective depth (12x purity*coverage, representing >80% probability to detect heterozygous mutations with at least 4 reads). These were compared with exome sequencing from the TCGA[14], a prior DM cohort[1], and two anti-PD-1 monotherapy treated cohorts, one from our group[17] with 23 cases which included a mix of responders and non-responders, and the second a subset of 30 patients post-CTLA-4 non-response. From that cohort to include one sample per patient, we excluded on-treatment samples in the setting of response; then we selected the biopsy with the highest tumour purity, regardless of timepoint, since most patients with >1 biopsy had <10% variance in their mutational loads. Response was defined as CR, PR, or SD >6 months by RECIST1.1 in both cohorts. Mutation calling methods between cohorts all used MuTect at their core, and only non-synonymous mutations (Nonsense, Missense, Splice_Site, Frameshift indels, In-frame indels, Start_Codon indels or SNPs, and Stoploss/Nonstop variants) were assessed to minimize differences between exon-capture kits. An additional filter was applied to all data sets to exclude mutations at sites of known germline variation with an allele frequency >0.0005 in the Exome

Aggregation Consortium (ExAC) database v0.3.1. Tumour purity was estimated by Sequenza, or as 2 * median variant allele frequency if less than 30%. Loss-of-function burden was determined using the LOF SIgRank algorithm [1], with the simulation run for 1000 iterations and synonymous mutations for background mutation rate defined as silent, 3'UTR, 5'UTR, or exon-flanking intronic mutations. Single nucleotide variants and their flanking contexts were analysed for mutation signatures for the DM and UCLA non-DM[17] cohorts together using a published tool.[19]

Statistical analyses

Kaplan-Meier method and Greenwood's formula were used for the estimation of survival probabilities (survival rates and overall survival) and the corresponding 95% confidence intervals (CIs). Progression-free survival was defined from start of treatment to disease progression or death from any cause. Overall survival was defined from start of treatment to death from any cause. The objective response rate was reported as proportion along with Clopper-Pearson exact CIs. The chi-square and Fisher's exact test were used to test for differences between groups for categorical variables. The Wilcoxon-Mann-Whitney rank sum test was used to compare mutation rate between groups. Statistical analyses of the pathological data were performed using GraphPad Prism and mutation data using R v3.2.5. All tests were two-sided; *P* values < 0.05 were considered statistically significant.

Acknowledgements

This study was funded in part by the Grimaldi Family Fund, the Parker Institute for Cancer Immunotherapy, NIH grants R35 CA197633 and P01 CA168585, the Ressler Family Fund, the Samuels Family Fund and the Garcia-Corsini Family Fund (to A.R.). A.R. is supported by a Stand Up To Cancer – Cancer Research Institute Cancer Immunology Dream Team Translational Research Grant (SU2C-AACR-DT1012). Stand Up To Cancer is a program of the Entertainment Industry Foundation administered by the American Association for Cancer Research. Z.E. is supported in part by the Moffitt Cancer Center NCI Skin SPORE (5P50CA168536). J.M.Z. is part of the UCLA Medical Scientist Training Program supported by NIH training grant GM08042. S.H-L. was supported by a Young Investigator Award and a Career Development Award from the American Society of Clinical Oncology (ASCO), a Tower Cancer Research Foundation Grant, and a Dr. Charles Coltman Fellowship Award from the Hope Foundation. We acknowledge the Translational Pathology Core Laboratory (TPCL) and Rongqing Guo, Wang Li, Jia Pang and Mignonette H. Macabali from UCLA for blood and biopsy processing, and Xinmin Li, Ling Dong, Janice Yoshizawa, and Jamie Zhou from the UCLA Clinical Microarray Core for sequencing expertise. GVL supported is by an NHMRC Fellowship and The University of Sydney Medical Foundation. RAS is supported by an NHMRC Fellowship.

Author Contributions. Z.E., J.M.Z., S.H-L. and A.R. developed the concepts. Z.E., S.H-L, J.M.Z., and A.R. designed the experiments. Z.E., J.M.Z., S.H-L. and A.R. interpreted the data. S.H-L., P.S. and Z.E. performed IHC analyses. J.M.Z. performed genomic analyses. A.R., B.C., Z.E., A.A., D.J., E.L., B.K., R.M., S.R., J.A., R.J., M.P., M.S.C, W.H., and G.V.L. clinically evaluated patients and contributed tumour samples. R.A.S., J.M., and A.C. evaluated tumour samples. P.F.G. conducted the heat map analysis. C.W. evaluated the CM clinical data. Z.E., J.M.Z., S.H-L. and A.R. wrote the manuscript. S.H-L. and A.R. supervised the project. All authors contributed to the manuscript and approved the final version.

Author Information. Reprints and permissions information is available at www.nature.com/reprints. Correspondence and requests for materials should be addressed to S.H-L. (shu-lieskovan@mednet.ucla.edu) or A.R. (aribas@mednet.ucla.edu).

Figure Legends

Figure 1. High response rate to PD-1 blockade in patients with desmoplastic melanoma (DM). A) Histological examples of three cases of DM compared with two cases of non-desmoplastic cutaneous melanoma (non-DM) stained with Masson's Trichrome stain to highlight the collagenous stroma characteristic of DM. Top panel: S100 stains (brown). Lower panel: Masson's trichrome stain (blue collagenous stroma, red cytoplasm and brown nucleus). B) Images of three cases of DM with response to anti-PD-1/L1 therapy. Left: baseline images; right: images while on anti-PD-1 therapy. C) Waterfall plot of best response on therapy of 54 DM patients treated with anti-PD-1 or anti-PD-L1 antibodies (data was not available for 3 patients, two who had progressive disease and one who had a partial response).

Figure 2. High mutational load and similarity to NF1 subtype in desmoplastic melanoma. A) Top bar graph represents mutational load. Tiling plot shows mutations in a given gene (rows) per sample (columns). In the tiling plot, top line represents response, as either primary resistance/progressive disease (red) or response (partial or complete response and stable disease > 6 months, dark blue). Colour indicates mutation type, with truncating mutations (frameshift, nonsense, splice-site) in red, missense in green, and synonymous in beige. Darker colour intensity indicates potentially homozygous mutations, with variant allele frequency >1.5 times the sample median. * = biopsy from responding lesion despite a mixed response and eventual progression. o = patient showed no evidence of disease for > 1year after surgical resection of a progressing lesion. B) Non-synonymous mutations determined by whole exome sequencing (WES) from the current DM cohort, two pooled studies of anti-PD1 treated cutaneous melanoma[17,18] and TCGA data. Each cohort is split by driver mutation subtype, colour indicates anti-PD1 response (red = progression, blue = response), and shape represents desmoplastic pure vs mixed subtype. P values = Wilcoxon-Mann-Whitney rank sum test.

Figure 3. CD8 density and PD-L1 expression in the tumour parenchyma and invasive margins in biopsies of patients with desmoplastic (DM) and non-desmoplastic cutaneous melanoma (non-DM). A) CD8 staining in the tumour centre (non-DM: 2CR/5PR/6PD; DM: 7CR/7PR/1SD/3PD). B) PD-L1 staining in the tumour centre (non-DM: 1CR/5PR/5PD; DM: 7CR/6PR/1SD/3PD). C) CD8 staining in the invasive margin (non-DM: 2CR/5PR/6PD; DM: 6CR/7PR/1SD/3PD). D) PD-L1 staining in the invasive margin (non-DM: 1CR/5PR/5PD; DM: 6CR/6PR/1SD/3PD). Percentage of positively stained cells in all nucleated cells are presented. PD: progressive disease; SD: stable disease; CR: complete response; PR: partial response. * Indicates statistical significance.

Figure 4. Patterns of CD8 infiltration and PD-L1 expression in biopsies of patients with desmoplastic (DM) and non-desmoplastic cutaneous melanoma (non-DM). Using cut off of >10% for high CD8 density in either parenchyma or invasive margins and >15% for high PD-L1 expression, six different patterns were identified: A) High CD8 density, high PD-L1 tumour parenchyma > invasive margins. B) High CD8 density, high PD-L1 invasive margins > tumour parenchyma. C) High CD8 density, high PD-L1 in the invasive margins only. D) Low CD8 density, high PD-L1 in the invasive margins only. E) Low CD8 infiltration, high PD-L1 expression tumour parenchyma > invasive margins. F) Low CD8 density, low PD-L1 expression. G) Heat map summary of patterns of CD8 and PD-L1 expression in biopsies of patients with DM and CM based on their response to therapy with anti-PD-1/L1; CB: clinical benefit; PD: progressive disease. Intensity of colour coding indicates number of cases in each category.

Expanded Data

Expanded Data Table 1. Details of individual patient characteristics and samples analysed from each patient.

Pt	Histologic subtype	Age	Gender	Stage	Prior ipilimumab	Treatment	Biopsy location	ORR	PFS	OS	IHC	WES	Tumour Source	Normal Source	Sequencing Platform	Tumour Depth	Normal Depth	Estimated Tumour Cellularity (fraction)	Effective Tumour Depth	Nonsynonymous Mutations	Exonic Sequencing Footprint (Mb)	Mutations/Megabase
1	Mixed	61	M	M1c	Yes	Pembrolizumab	primary	CR	26.7	26.7	Yes	No	NA	NA	NA	NA	NA	NA	NA	NA	NA	NA
2	Pure	70	M	M1a	Yes	Pembrolizumab	locally advanced	CR	9.9	9.9	Yes	No	NA	NA	NA	NA	NA	NA	NA	NA	NA	NA
3	Mixed	54	M	M1b	No	BMS-936559 (anti-PD-L1)	metastatic	CR	55.3	55.3	Yes	No	NA	NA	NA	NA	NA	NA	NA	NA	NA	NA
4	Pure	62	F	M1b	Yes	Pembrolizumab	metastatic	CR	42.4	42.4	Yes	No	NA	NA	NA	NA	NA	NA	NA	NA	NA	NA
5	Pure	83	M	M1c	Yes	Pembrolizumab	metastatic	CR	14.1	14.1	Yes	Yes	FFPE	PBMC	HiSeq 2500 2x100	223	151	0.38	88.54	3058	27.6	110.8
6	Pure	73	M	M1b	No	Pembrolizumab	metastatic	CR	31.5	31.5	Yes	No	NA	NA	NA	NA	NA	NA	NA	NA	NA	NA
7	Mixed	74	M	M1c	Yes	Pembrolizumab	metastatic	CR	25	25	Yes	Yes	FFPE	FFPE	HiSeq 2500 2x100	136.8	33.9	0.51	69.77	1310	27.6	47.46
8	Mixed	75	F	M1b	No	Nivolumab + ipilimumab	primary	PR	13.9	36.9	Yes	No	NA	NA	NA	NA	NA	NA	NA	NA	NA	NA
9	Pure	79	F	M1b	No	Nivolumab	locally advanced	PR	10	63	Yes	Yes	Fresh Frozen	PBMC	HiSeq 2500 2x100	199.84	171.26	0.27	53.96	1868	27.6	67.68
10	Pure	67	F	M1b	Yes	Pembrolizumab	locally advanced	PR	28.2	42	Yes	Yes	FFPE	FFPE	HiSeq 2500 2x100	57.55	215.8	0.26	14.82	670	27.6	18.3
11	Mixed	63	M	M1c	Yes	Pembrolizu	prim	PR	49.7	49.7	Yes	No	NA	NA	NA	NA	NA	NA	NA	NA	NA	NA

						mab	ary															
12	Mixed	75	F	M1c	Yes	Pembrolizumab	locally advanced	PR	8.9	16	Yes	Yes	FFPE	FFPE	HiSeq 2500 2x100	64.24	55.69	0.18	11.56	212	27.6	7.68
13	Mixed	52	F	M1c	Yes	Pembrolizumab	metastatic	PR	20.6	20.6	Yes	Yes	FFPE	FFPE	HiSeq 2500 2x100	130.7	25	0.75	93.24	1688	27.6	61.16
14	Mixed	66	M	M1c	No	Pembrolizumab	primary	PD	2.7	18.2	No	Yes	FFPE	FFPE	HiSeq 2500 2x100	121	67.1	0.18	21.78	525	27.6	19.02
15	Pure	60	M	M1c	Yes	Pembrolizumab	metastatic	PD	3.4	20.7	Yes	Yes	FFPE	FFPE	HiSeq 2500 2x100	143.25	70	0.21	30.08	1695	27.6	61.41
16	Pure	85	M	M1b	Yes	Pembrolizumab	locally advanced	PD	3.6	11.7	Yes	Yes	FFPE	FFPE	HiSeq 2500 2x100	48.8	42	0.45	21.96	659	27.6	23.88
17	Pure	62	M	M1c	Yes	Pembrolizumab	locally advanced	PD	3.3	7.5	Yes	Yes	FFPE	FFPE	HiSeq 3000 2x150	201	77.6	0.38	76.38	1717	27.6	62.21
18	Pure	67	M	M1c	Yes	Pemrbolizumab with ipilimumab	locally advanced	PR	20	20	Yes	Yes	FFPE	FFPE	HiSeq 2500 2x100	60	73.6	0.27	16.2	824	27.6	29.86
19	Mixed	59	M	M1c	No	Pembrolizumab	metastatic	SD	12.4	12.4	Yes	Yes	Fresh Frozen	PBMC	HiSeq 2500 2x100	217	235	0.49	106.33	1533	27.6	55.54
20	Mixed	85	M	M1c	No	Pembrolizumab	metastatic	PR	8	9.1	No	Yes	Fresh Frozen	PBMC	HiSeq 2500 2x100	159.08	159.25	0.14	22.27	1395	27.6	50.54
21	unknown	33	F	M1c	No	Nivolumab	metastatic	PR	8	62.6	No	Yes	FFPE	PBMC	HiSeq 2500 2x100	152.1	171.26	0.64	96.64	509	27.6	18.44
22	Pure	60	M	M1b	No	Pembrolizumab	locally advanced	PR	31.5	31.5	No	Yes	Fresh Frozen	PBMC	HiSeq 2500 2x100	195.33	181.39	0.14	27.35	1282	27.6	46.45

23	Mixed	61	M	M1b	Yes	Pembrolizumab	locally advanced	PD	2.8	5.6	No	Yes	Fresh Frozen	PBMC	HiSeq 2500 2x100	93.56	125	0.59	55.46	1129	27.6	40.91
24	Pure	79	M	2B*	No	Pembrolizumab	unresectable primary	CR	14.8	14.8	Yes	Yes	FFPE	PBMC	HiSeq 2500 2x100	94.5	131	0.16	15.12	462	27.6	16.74

*Patient not included in 57 patients for whom PFS/OS was analysed

Expanded Data Table 2. Summary of patient characteristics

Characteristics (n=57)	**N (%)**
Age (median/range)	71 (26-86)
Gender (male)	47 (82%)
Stage IIIC	1 (2%)
Stage IV	
M1a	3 (4%)
M1b	20 (35%)
M1c	33 (58%)
Desmoplastic subtype	
Pure	23 (40%)
Mixed	29 (51%)
Unknown	5 (9%)
BRAF V600 mutation (+)	1 (2%)
ECOG	
0	28 (49%)
1	29 (51%)
LDH	
Elevated	11 (19%)
Normal	46 (81%)
Sites of metastases (may have multiple)	
Brain	2 (4%)
Lung	33 (58%)
Liver	18 (32%)
Bone	11 (19%)
Prior lines of therapy for metastatic disease	
0	16 (28%)
1	30 (53%)
2	11 (19%)
Prior ipilimumab therapy	29 (51%)
Response rate to prior ipilimumab therapy	2 (7%)

Expanded Data Table 3. Summary of systemic drug treatments received by each patient.

Treatment Received (n=57)	**N (%)**
Pembrolizumab	
2 mg/kg	31 (54%)
10 mg/kg	10 (18%)
Dose not known	2 (4%)
Nivolumab	
0.1 mg/kg	2 (4%)
3 mg/kg	5 (9%)
10 mg/kg	1 (2%)
Nivolumab (1 mg/kg) + ipilimumab (3 mg/kg)	2 (4%)
Pembrolizumab (2 mg/kg) + ipilimumab (1 mg/kg)	1 (2%)
BMS-936559 (anti-PDL1)	
0.1 mg/kg	1 (2%)
0.3 mg/kg	2 (4%)
Cycles of therapy (median/range)	12 (1-73)
Length of follow-up (median)	20 months
Duration of response (median)	17 months
Received subsequent systemic therapy	4 (7%)
Received surgical excision for isolated progression	3 (5%)

Extended Data Figures.

Extended Data Figure 1. Survival data of the desmoplastic melanoma cohort. A) Progression free survival (PFS), n = 57, median not reached, range = 1.2 months to 4.7 years. B) Overall survival (OS), n=57, median not reached, range = 3.6 months to 5.3 years.

Extended Data Figure 2. Sequencing characteristics of desmoplastic cohort. A) Scores from the loss-of-function (LOF) SigRank algorithm[1] show enrichment for LOF mutations (nonsense, frameshift, splice-site or damaging missense) compared to the expected number based on the rate of LOF mutations in the cohort. Solid line corresponds to observed/expected ratio of 1.0. B) Cumulative percentage per DM sample of single nucleotide mutations by transition/transversion substitution. C) Mutation signature analysis[19] on combined DM and non-DM cohort.[17] All show the predominant C>T rich signature 7 characteristic of UV damage. D) Mutational load in the vanAllen[20] anti-CTLA4 treated cohort separated by driver subtype and coloured by response.

Extended Data Figure 3. Mutations in antigen presenting machinery or enriched by response in the desmoplastic cohort. A) Mutations in genes enriched in responders (blue) or non-responders (red). B) Mutations in antigen presenting machinery genes. P-values = Unadjusted Fisher exact test of number of samples with a non-synonymous mutation per gene, cutoffs 0.015 for and 0.05. Tiling plot shows mutations in a given gene (rows) per sample (columns). Colour indicates mutation type, with truncating mutations (frameshift, nonsense, splice-site) in red, missense in green, and synonymous in beige. Darker colour intensity indicates potentially homozygous mutations, with variant allele frequency >1.5 times the sample median.

Extended Data Figure 4. CD8 density and PD-L1 expression in the tumour parenchyma and invasive margins in biopsies of patients with desmoplastic and non-desmoplastic melanoma. A) CD8 staining in the invasive margin. B) PD-L1 staining in the invasive margin. C) CD8 staining in the tumour centre. D) PD-L1 staining in the tumour centre. Percentage of positively stained cells in all nucleated cells are presented. CB: clinical benefit; PD: progressive disease; SD: stable disease; CR: complete response; PR: partial response. * Indicates statistical significance.

Extended Data Figure 5. Correlation of CD8 and PD-L1 in the invasive margin or tumour parenchyma in desmoplastic melanoma. IM: Invasive margin; Centre: tumour centre.

	p value linear regression	p value Spearman correlation
CD8 IM vs PDL1 Tumor	0.007	0.01
CD8 Tumor vs PDL1 Tumor	0.15	0.11
CD8 IM vs PDL1 IM	0.0003	0.0002
CD8 Tumor vs PDL1 IM	0.04	0.03
CD8 Tumor vs CD8 IM	<0.0001	0.0006
PDL1 Tumor vs PDL1 IM	0.0003	0.0002

Extended Data Figure 6. Hierarchical clustering of desmoplastic melanoma and non-desmoplastic cutaneous melanoma based on CD8 and PD-L1 expression in the invasive margin and tumour parenchyma.

References

1 Shain, A. H. *et al.* Exome sequencing of desmoplastic melanoma identifies recurrent NFKBIE promoter mutations and diverse activating mutations in the MAPK pathway. *Nature genetics* **47**, 1194-1199, doi:10.1038/ng.3382 (2015).

2 Sharma, P. & Allison, J. P. The future of immune checkpoint therapy. *Science (New York, N.Y.)* **348**, 56-61, doi:10.1126/science.aaa8172 (2015).

3 Robert, C. *et al.* Nivolumab in previously untreated melanoma without BRAF mutation. *The New England journal of medicine* **372**, 320-330, doi:10.1056/NEJMoa1412082 (2015).

4 Ribas, A. *et al.* Association of Pembrolizumab With Tumor Response and Survival Among Patients With Advanced Melanoma. *Jama* **315**, 1600-1609, doi:10.1001/jama.2016.4059 (2016).

5 Rizvi, N. A. *et al.* Cancer immunology. Mutational landscape determines sensitivity to PD-1 blockade in non-small cell lung cancer. *Science (New York, N.Y.)* **348**, 124-128, doi:10.1126/science.aaa1348 (2015).

6 Le, D. T. *et al.* PD-1 Blockade in Tumors with Mismatch-Repair Deficiency. *The New England journal of medicine* **372**, 2509-2520, doi:10.1056/NEJMoa1500596 (2015).

7 Hugo, W. *et al.* Genomic and Transcriptomic Features of Response to Anti-PD-1 Therapy in Metastatic Melanoma. *Cell* **165**, 35-44, doi:10.1016/j.cell.2016.02.065 (2016).

8 Rosenberg, J. E. *et al.* Atezolizumab in patients with locally advanced and metastatic urothelial carcinoma who have progressed following treatment with platinum-based chemotherapy: a single-arm, multicentre, phase 2 trial. *Lancet (London, England)* **387**, 1909-1920, doi:10.1016/S0140-6736(16)00561-4 (2016).

9 Frydenlund, N. *et al.* Tumoral PD-L1 expression in desmoplastic melanoma is associated with depth of invasion, tumor-infiltrating CD8 cytotoxic lymphocytes and the mixed cytomorphological variant. *Modern pathology : an official journal of the United States and Canadian Academy of Pathology, Inc* **30**, 357-369, doi:10.1038/modpathol.2016.210 (2017).

10 Han, D. *et al.* Clinicopathologic predictors of survival in patients with desmoplastic melanoma. *PloS one* **10**, e0119716, doi:10.1371/journal.pone.0119716 (2015).

11 Busam, K. J. *et al.* Cutaneous desmoplastic melanoma: reappraisal of morphologic heterogeneity and prognostic factors. *The American journal of surgical pathology* **28**, 1518-1525 (2004).

12 Murali, R. *et al.* Prognostic factors in cutaneous desmoplastic melanoma: a study of 252 patients. *Cancer* **116**, 4130-4138, doi:10.1002/cncr.25148 (2010).

13 Wiesner, T. *et al.* NF1 Mutations are Common in Desmoplastic Melanoma. *The American journal of surgical pathology* **39**, 1357-1362, doi:10.1097/pas.0000000000000451 (2015).

14 Akbani, R. *et al.* Genomic Classification of Cutaneous Melanoma. *Cell* **161**, 1681-1696, doi:10.1016/j.cell.2015.05.044.

15 Krauthammer, M. *et al.* Exome sequencing identifies recurrent mutations in NF1 and RASopathy genes in sun-exposed melanomas. *Nature genetics* **47**, 996-1002, doi:10.1038/ng.3361

16 Hayward, N. K. *et al.* Whole-genome landscapes of major melanoma subtypes. *Nature* **advance online publication**, doi:10.1038/nature22071

http://www.nature.com/nature/journal/vaop/ncurrent/abs/nature22071.html#supplementary-information (2017).

17 Shin, D. S. *et al.* Primary Resistance to PD-1 Blockade Mediated by JAK1/2 Mutations. *Cancer discovery*, doi:10.1158/2159-8290.CD-16-1223 (2016).

18 Roh, W. *et al.* Integrated molecular analysis of tumor biopsies on sequential CTLA-4 and PD-1 blockade reveals markers of response and resistance. *Science translational medicine* **9**, doi:10.1126/scitranslmed.aah3560 (2017).

19 Alexandrov, L. B. Signatures of mutational processes in human cancer. **500**, 415-421, doi:10.1038/nature12477 (2013).

20 Van Allen, E. M. *et al.* Genomic correlates of response to CTLA-4 blockade in metastatic melanoma. *Science (New York, N.Y.)* **350**, 207-211, doi:10.1126/science.aad0095 (2015).

21 Zaretsky, J. M. *et al.* Mutations Associated with Acquired Resistance to PD-1 Blockade in Melanoma. *The New England journal of medicine* **375**, 819-829, doi:10.1056/NEJMoa1604958 (2016).

22 Tumeh, P. C. *et al.* PD-1 blockade induces responses by inhibiting adaptive immune resistance. *Nature* **515**, 568-571, doi:10.1038/nature13954 (2014).

23 Taube, J. M. *et al.* Colocalization of inflammatory response with B7-h1 expression in human melanocytic lesions supports an adaptive resistance mechanism of immune escape. *Science translational medicine* **4**, 127ra137, doi:10.1126/scitranslmed.3003689 (2012).

24 Pardoll, D. M. The blockade of immune checkpoints in cancer immunotherapy. *Nature reviews. Cancer* **12**, 252-264, doi:10.1038/nrc3239 (2012).

25 Ribas, A. & Hu-Lieskovan, S. What does PD-L1 positive or negative mean? *The Journal of experimental medicine* **213**, 2835-2840, doi:10.1084/jem.20161462 (2016).

26 Ansell, S. M. *et al.* PD-1 blockade with nivolumab in relapsed or refractory Hodgkin's lymphoma. *The New England journal of medicine* **372**, 311-319, doi:10.1056/NEJMoa1411087 (2015).

27 Akbay, E. A. *et al.* Activation of the PD-1 pathway contributes to immune escape in EGFR-driven lung tumors. *Cancer discovery* **3**, 1355-1363, doi:10.1158/2159-8290.CD-13-0310 (2013).

28 Casey, S. C. *et al.* MYC regulates the antitumor immune response through CD47 and PD-L1. *Science (New York, N.Y.)* **352**, 227-231, doi:10.1126/science.aac9935 (2016).

29 Dorand, R. D. *et al.* Cdk5 disruption attenuates tumor PD-L1 expression and promotes antitumor immunity. *Science (New York, N.Y.)* **353**, 399-403, doi:10.1126/science.aae0477 (2016).

30 Parsa, A. T. *et al.* Loss of tumor suppressor PTEN function increases B7-H1 expression and immunoresistance in glioma. *Nature medicine* **13**, 84-88, doi:10.1038/nm1517 (2007).

31 Lastwika, K. J. *et al.* Control of PD-L1 Expression by Oncogenic Activation of the AKT-mTOR Pathway in Non-Small Cell Lung Cancer. *Cancer Res* **76**, 227-238, doi:10.1158/0008-5472.CAN-14-3362 (2016).

32 Kataoka, K. *et al.* Aberrant PD-L1 expression through 3'-UTR disruption in multiple cancers. *Nature* **534**, 402-406, doi:10.1038/nature18294 (2016).

33 Olive, K. P. *et al.* Inhibition of Hedgehog signaling enhances delivery of chemotherapy in a mouse model of pancreatic cancer. *Science (New York, N.Y.)* **324**, 1457-1461, doi:10.1126/science.1171362 (2009).

34 Provenzano, P. P. *et al.* Enzymatic targeting of the stroma ablates physical barriers to treatment of pancreatic ductal adenocarcinoma. *Cancer Cell* **21**, 418-429, doi:10.1016/j.ccr.2012.01.007 (2012).

35 Feig, C. *et al.* Targeting CXCL12 from FAP-expressing carcinoma-associated fibroblasts synergizes with anti-PD-L1 immunotherapy in pancreatic cancer. *Proceedings of the National Academy of Sciences of the United States of America* **110**, 20212-20217, doi:10.1073/pnas.1320318110 (2013).

36 Jiang, H. *et al.* Targeting focal adhesion kinase renders pancreatic cancers responsive to checkpoint immunotherapy. *Nature medicine* **22**, 851-860, doi:10.1038/nm.4123 (2016).

37 Nghiem, P. T. *et al.* PD-1 Blockade with Pembrolizumab in Advanced Merkel-Cell Carcinoma. *New England Journal of Medicine* **374**, 2542-2552, doi:10.1056/NEJMoa1603702 (2016).

38 Rittmeyer, A. *et al.* Atezolizumab versus docetaxel in patients with previously treated non-small-cell lung cancer (OAK): a phase 3, open-label, multicentre randomised controlled trial. *The Lancet* **389**, 255-265, doi:10.1016/S0140-6736(16)32517-X.

Figure 1

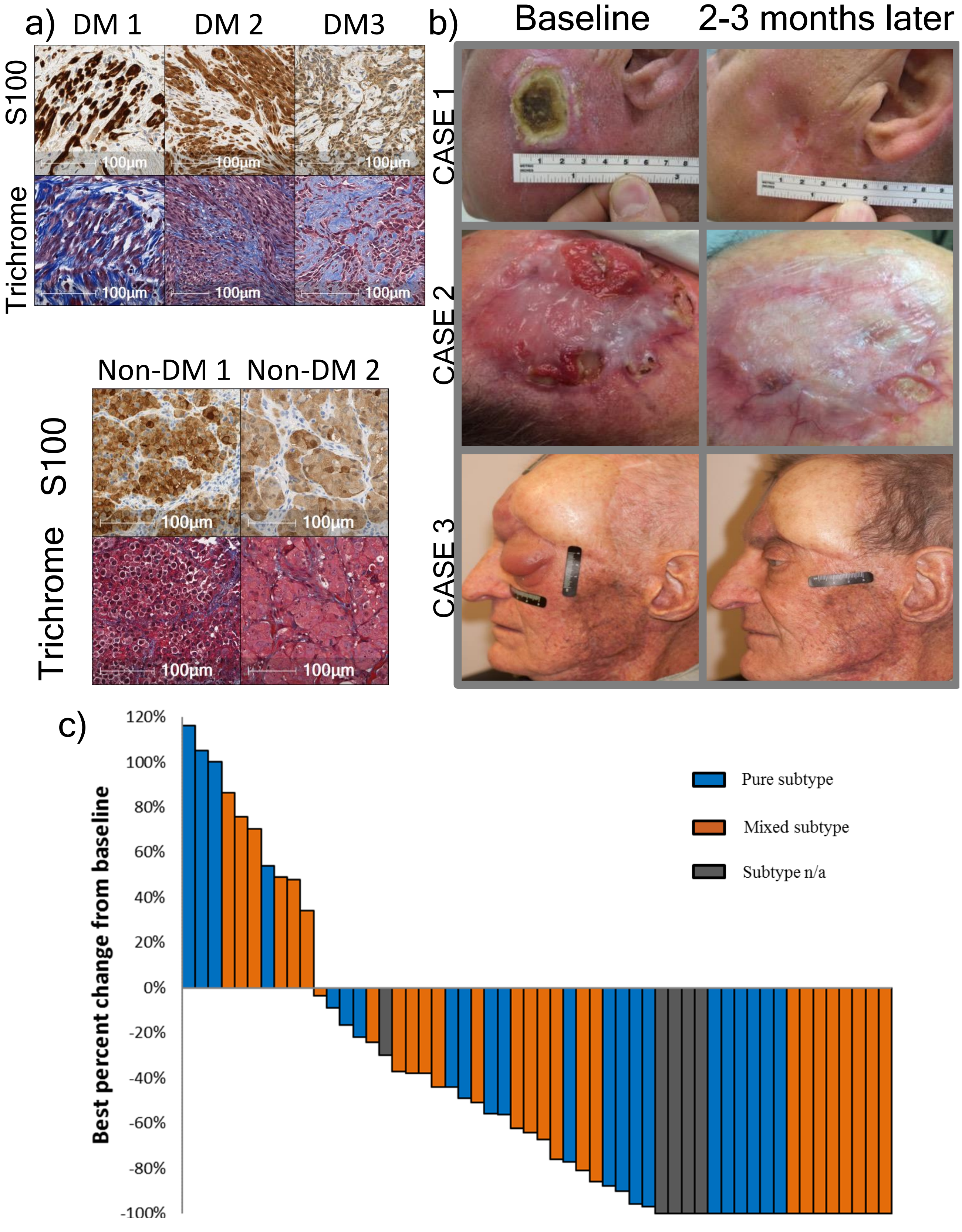
a)
DM 1
DM 2
DM3
S100
Trichrome
100µm
Non-DM 1
Non-DM 2
S100
Trichrome
100µm
b)
Baseline
2-3 months later
CASE 1
CASE 2
CASE 3
c)
Best percent change from baseline
120%
100%
80%
60%
40%
20%
0%
-20%
-40%
-60%
-80%
-100%
Pure subtype
Mixed subtype
Subtype n/a

Figure 2

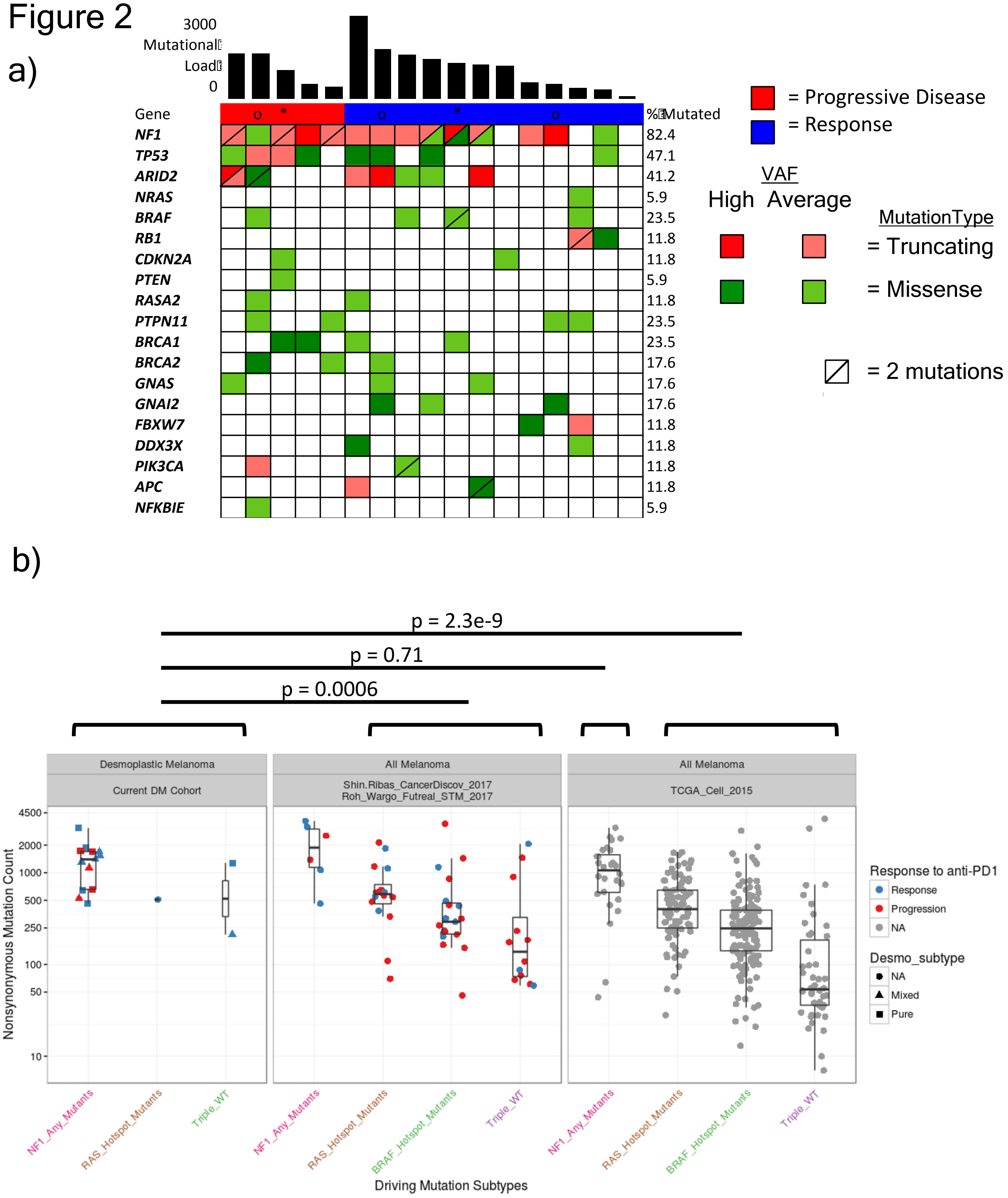
a)
3000
Mutational Load
0
Gene
o
*
o
*
o
% Mutated
NF1 82.4
TP53 47.1
ARID2 41.2
NRAS 5.9
BRAF 23.5
RB1 11.8
CDKN2A 11.8
PTEN 5.9
RASA2 11.8
PTPN11 23.5
BRCA1 23.5
BRCA2 17.6
GNAS 17.6
GNAI2 17.6
FBXW7 11.8
DDX3X 11.8
PIK3CA 11.8
APC 11.8
NFKBIE 5.9
= Progressive Disease
= Response
VAF
High
Average
MutationType
= Truncating
= Missense
= 2 mutations
b)
p = 2.3e-9
p = 0.71
p = 0.0006
Desmoplastic Melanoma
Current DM Cohort
All Melanoma
Shin.Ribas_CancerDiscov_2017
Roh_Wargo_Futreal_STM_2017
All Melanoma
TCGA_Cell_2015
Nonsynonymous Mutation Count
4500
2000
1000
500
250
100
50
10
NF1_Any_Mutants
RAS_Hotspot_Mutants
Triple_WT
NF1_Any_Mutants
RAS_Hotspot_Mutants
BRAF_Hotspot_Mutants
Triple_WT
NF1_Any_Mutants
RAS_Hotspot_Mutants
BRAF_Hotspot_Mutants
Triple_WT
Driving Mutation Subtypes
Response to anti-PD1
Response
Progression
NA
Desmo_subtype
NA
Mixed
Pure

Figure 3

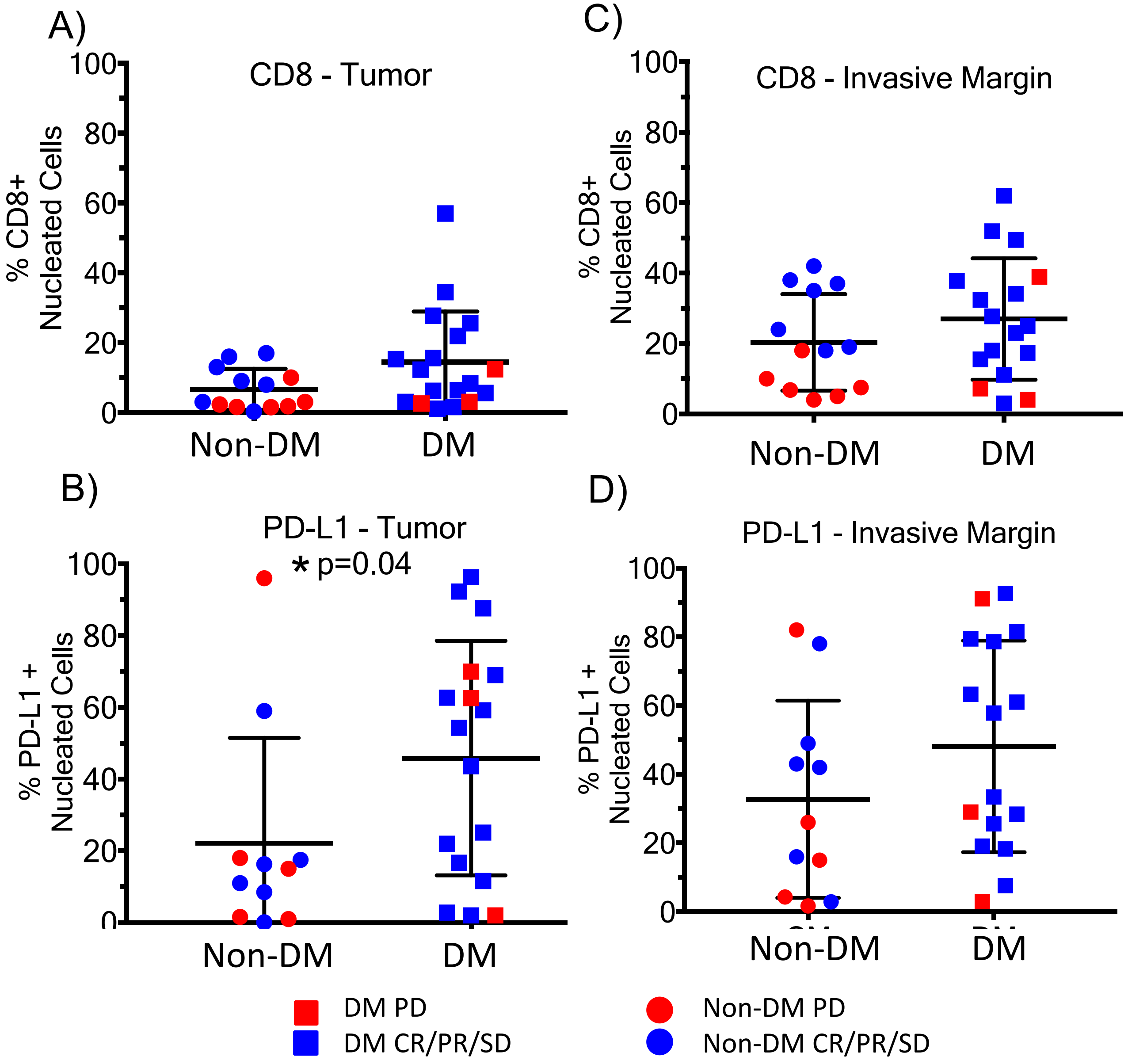
A)
CD8 - Tumor
% CD8+ Nucleated Cells
100
80
60
40
20
0
Non-DM
DM
B)
PD-L1 - Tumor
* p=0.04
% PD-L1 + Nucleated Cells
100
80
60
40
20
0
Non-DM
DM
C)
CD8 - Invasive Margin
% CD8+ Nucleated Cells
100
80
60
40
20
0
Non-DM
DM
D)
PD-L1 - Invasive Margin
% PD-L1 + Nucleated Cells
100
80
60
40
20
0
Non-DM
DM
DM PD
DM CR/PR/SD
Non-DM PD
Non-DM CR/PR/SD

Figure 4

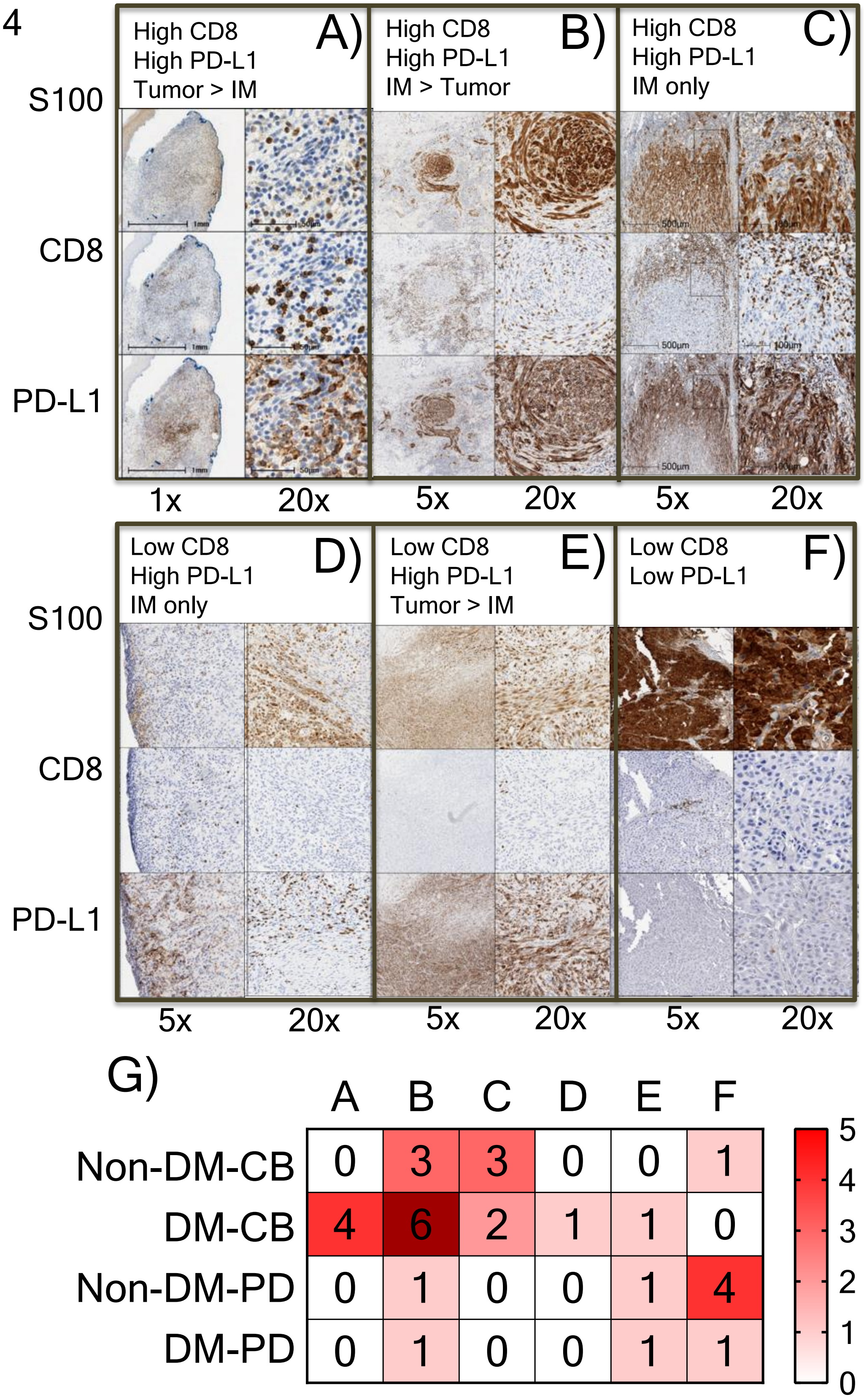

	A	B	C	D	E	F
Non-DM-CB	0	3	3	0	0	1
DM-CB	4	6	2	1	1	0
Non-DM-PD	0	1	0	0	1	4
DM-PD	0	1	0	0	1	1

Extended Data Figure 1

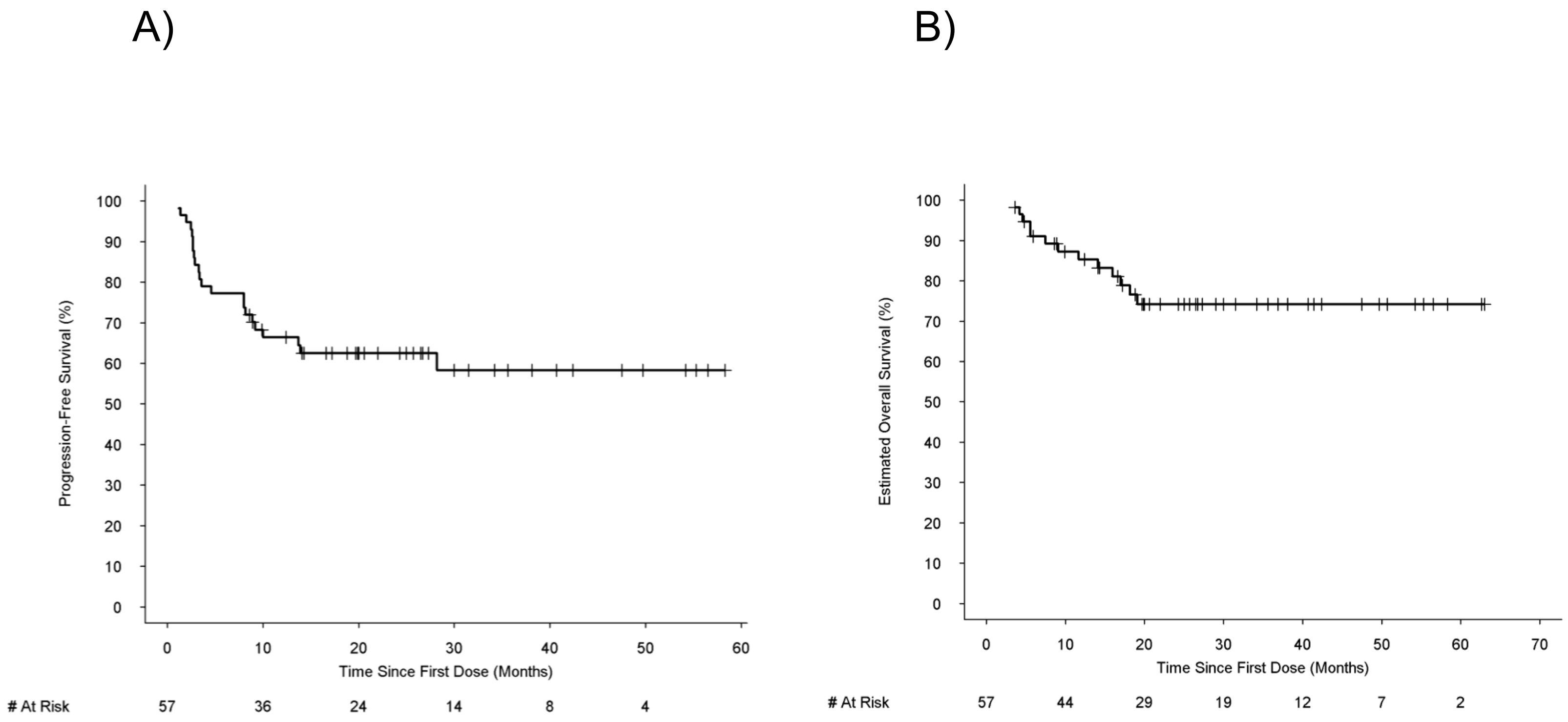

Extended Data Figure 2

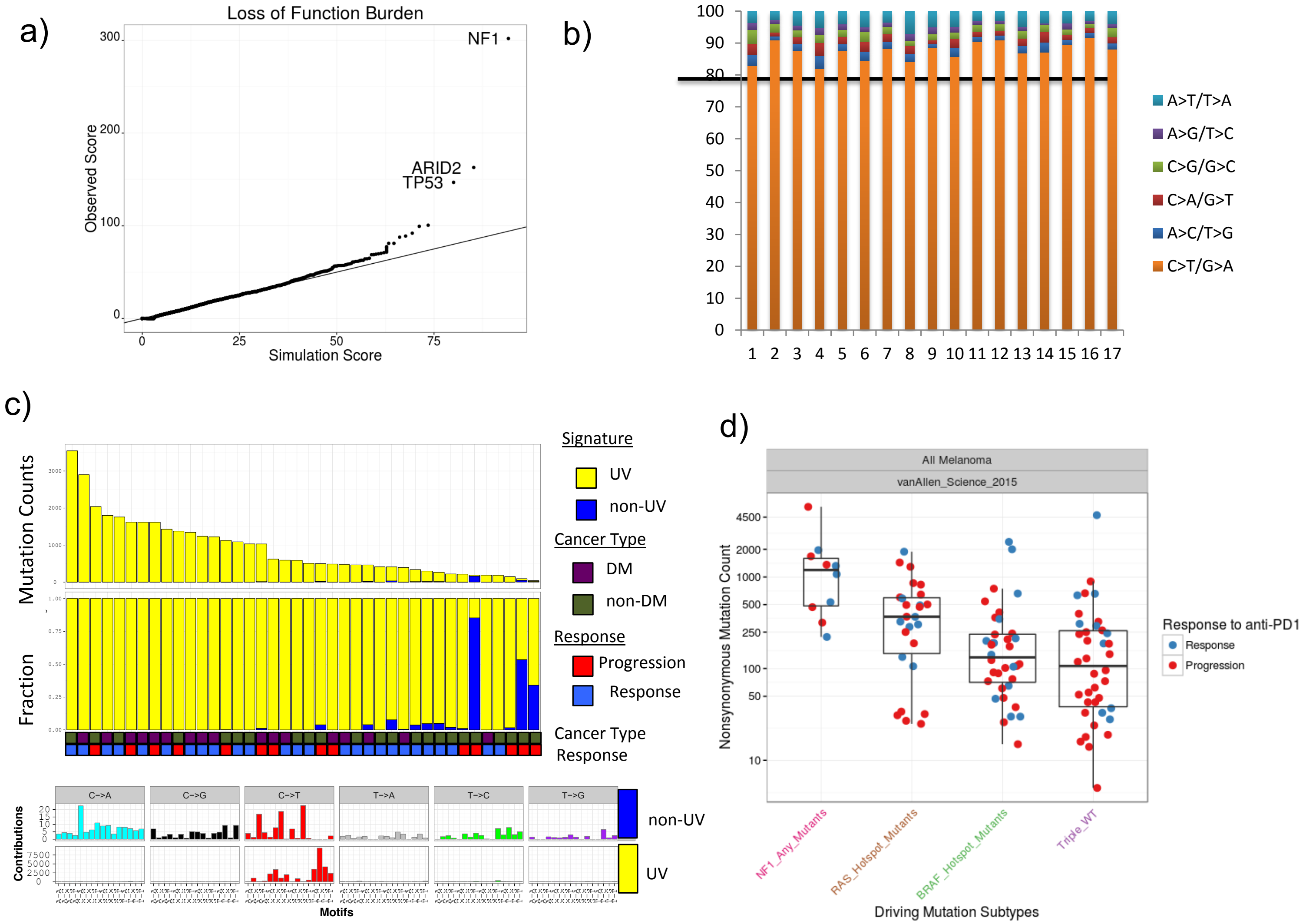

Extended Data Figure 3

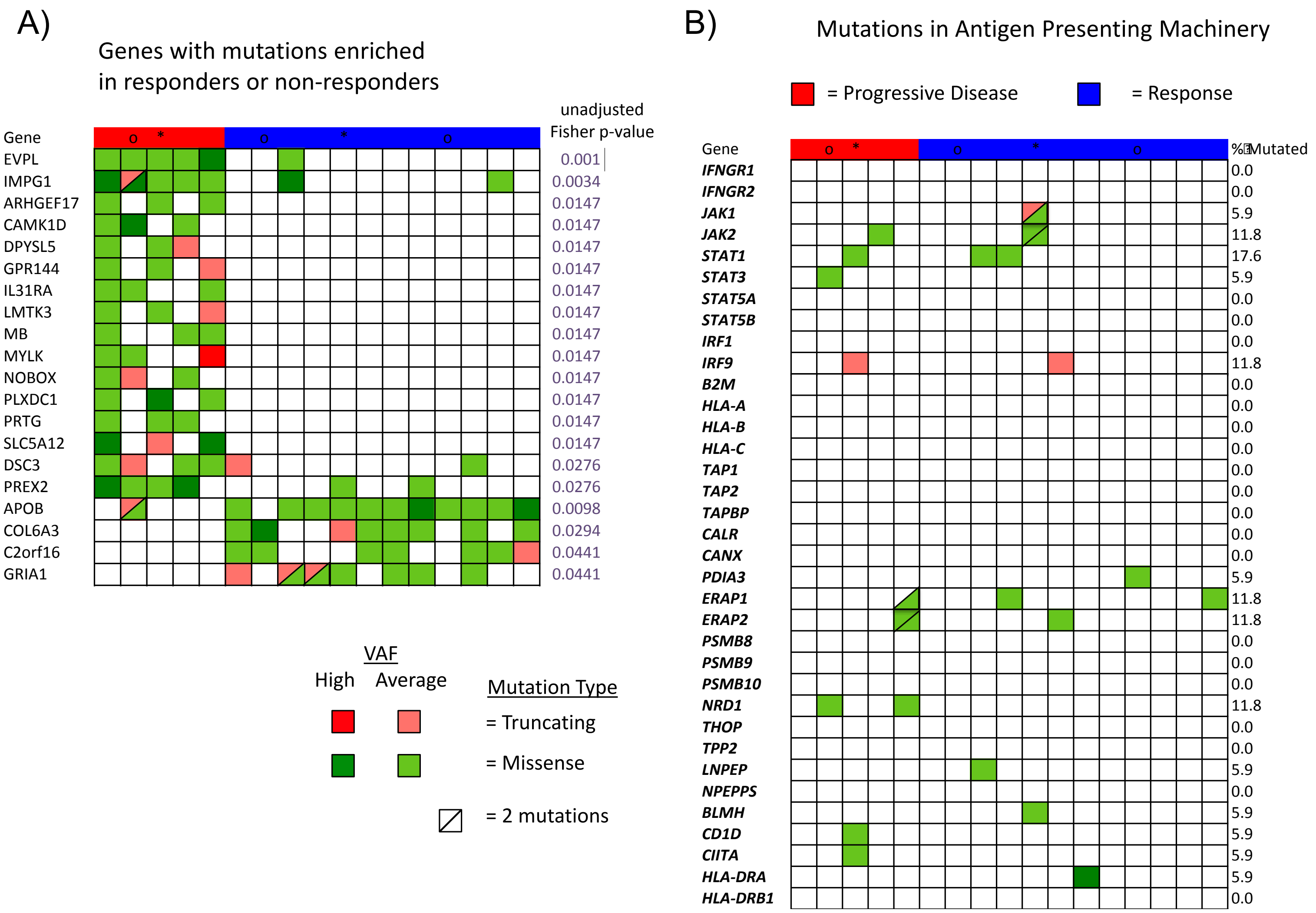

Gene	unadjusted Fisher p-value
EVPL	0.001
IMPG1	0.0034
ARHGEF17	0.0147
CAMK1D	0.0147
DPYSL5	0.0147
GPR144	0.0147
IL31RA	0.0147
LMTK3	0.0147
MB	0.0147
MYLK	0.0147
NOBOX	0.0147
PLXDC1	0.0147
PRTG	0.0147
SLC5A12	0.0147
DSC3	0.0276
PREX2	0.0276
APOB	0.0098
COL6A3	0.0294
C2orf16	0.0441
GRIA1	0.0441

Gene	% Mutated
IFNGR1	0.0
IFNGR2	0.0
JAK1	5.9
JAK2	11.8
STAT1	17.6
STAT3	5.9
STAT5A	0.0
STAT5B	0.0
IRF1	0.0
IRF9	11.8
B2M	0.0
HLA-A	0.0
HLA-B	0.0
HLA-C	0.0
TAP1	0.0
TAP2	0.0
TAPBP	0.0
CALR	0.0
CANX	0.0
PDIA3	5.9
ERAP1	11.8
ERAP2	11.8
PSMB8	0.0
PSMB9	0.0
PSMB10	0.0
NRD1	11.8
THOP	0.0
TPP2	0.0
LNPEP	5.9
NPEPPS	0.0
BLMH	5.9
CD1D	5.9
CIITA	5.9
HLA-DRA	5.9
HLA-DRB1	0.0

Extended Data Figure 4

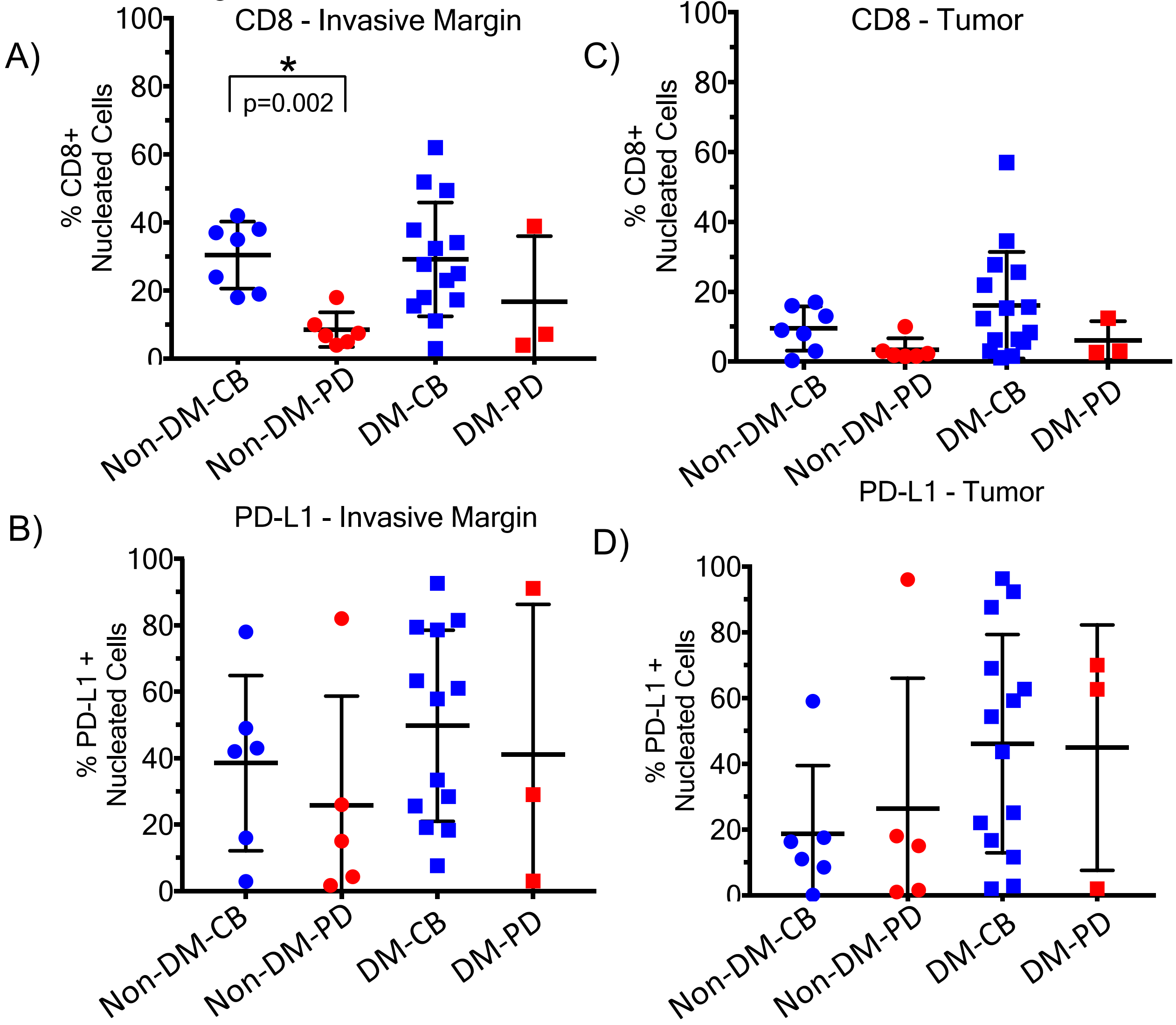

Extended Data Figure 5

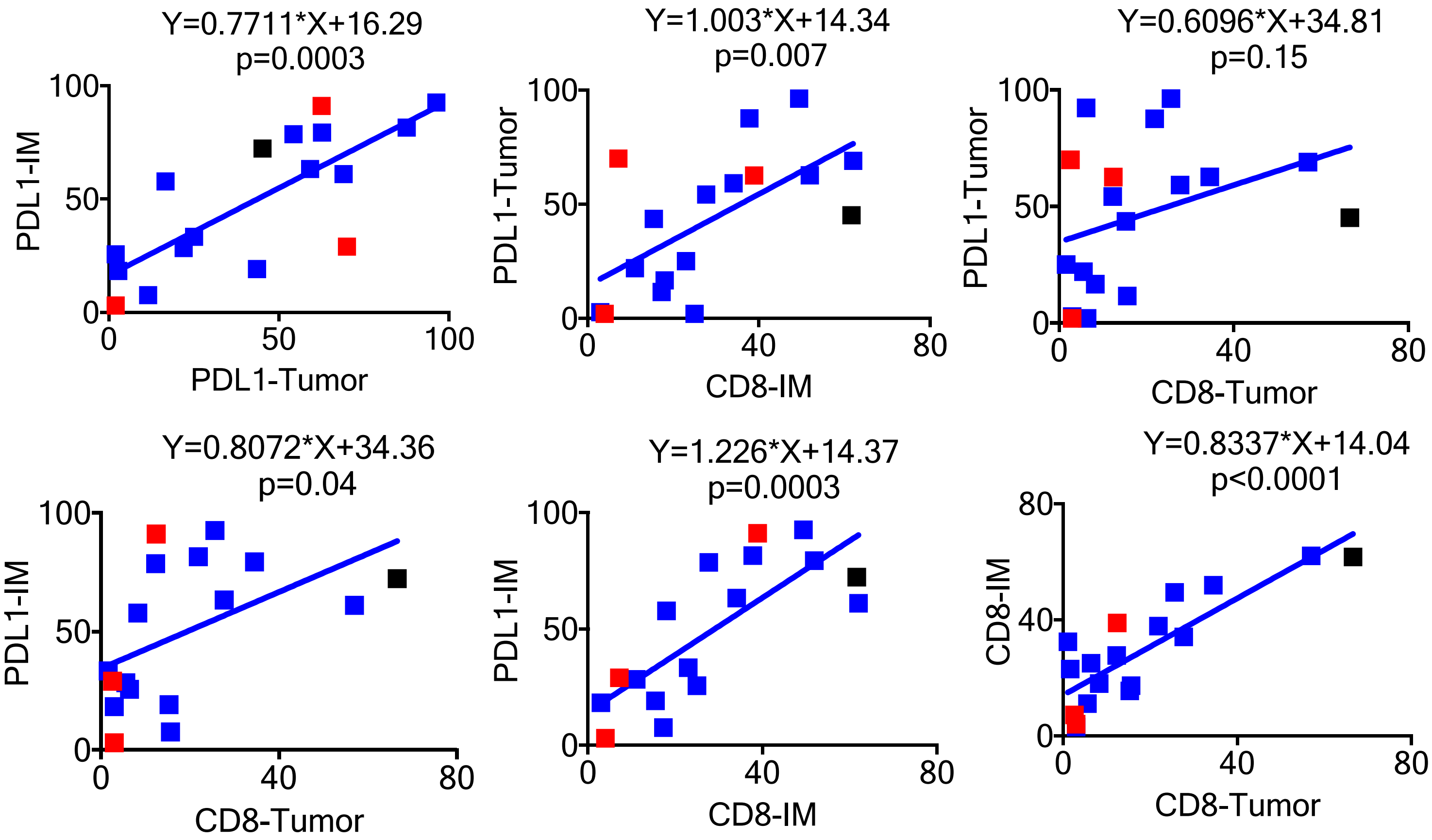

Extended Data Figure 6

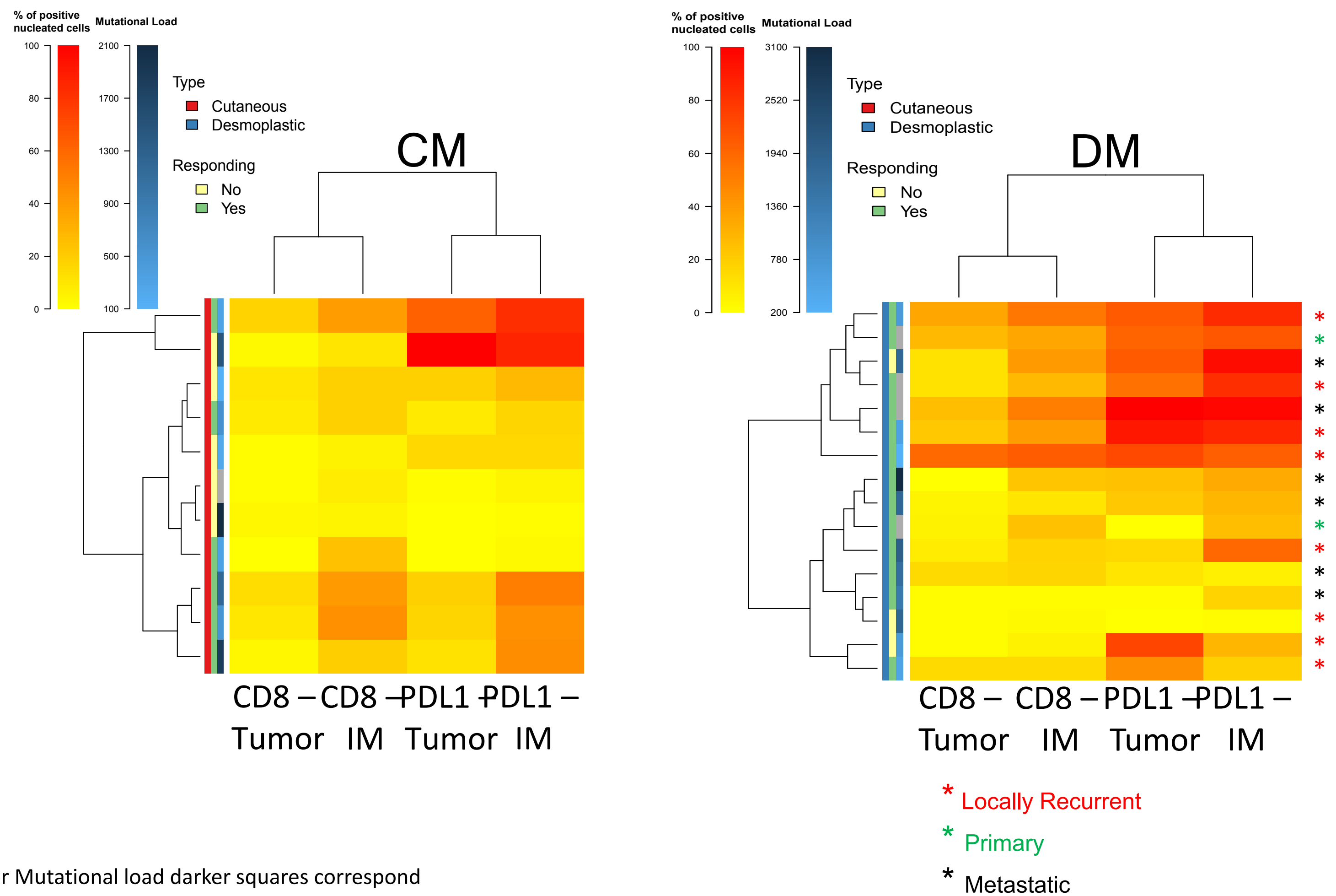

For Mutational load darker squares correspond to higher mutational load. Gray squares are missing data points

Chapter 5:

Genomic and transcriptomic features of response to anti-PD-1 therapy in metastatic melanoma

Cell

Genomic and Transcriptomic Features of Response to Anti-PD-1 Therapy in Metastatic Melanoma

Willy Hugo,[1,6,9] Jesse M. Zaretsky,[2,6,9] Lu Sun,[1,6] Chunying Song,[1,6] Blanca Homet Moreno,[3] Siwen Hu-Lieskovan,[3] Beata Berent-Maoz,[3] Jia Pang,[3] Bartosz Chmielowski,[3] Grace Cherry,[3] Elizabeth Seja,[3] Shirley Lomeli,[1,6] Xiangju Kong,[1,6] Mark C. Kelley,[7] Jeffrey A. Sosman,[8] Douglas B. Johnson,[8] Antoni Ribas,[2,3,4,5,6] and Roger S. Lo[1,2,5,6,*]

[1]Division of Dermatology, Department of Medicine
[2]Department of Molecular and Medical Pharmacology
[3]Division of Hematology & Oncology, Department of Medicine
[4]Division of Surgical Oncology, Department of Surgery
[5]Jonsson Comprehensive Cancer Center
[6]David Geffen School of Medicine
University of California, Los Angeles, CA 90095-1662, USA
[7]Department of Surgery, Vanderbilt-Ingram Cancer Center, Nashville, TN 37232, USA
[8]Department of Medicine, Vanderbilt-Ingram Cancer Center, Nashville, TN 37232, USA
[9]Co-first authors
*Correspondence: rlo@mednet.ucla.edu

http://dx.doi.org/10.1016/j.cell.2016.02.065

SUMMARY

PD-1 immune checkpoint blockade provides significant clinical benefits for melanoma patients. We analyzed the somatic mutanomes and transcriptomes of pretreatment melanoma biopsies to identify factors that may influence innate sensitivity or resistance to anti-PD-1 therapy. We find that overall high mutational loads associate with improved survival, and tumors from responding patients are enriched for mutations in the DNA repair gene *BRCA2*. Innately resistant tumors display a transcriptional signature (referred to as the IPRES, or innate anti-PD-1 resistance), indicating concurrent up-expression of genes involved in the regulation of mesenchymal transition, cell adhesion, extracellular matrix remodeling, angiogenesis, and wound healing. Notably, mitogen-activated protein kinase (MAPK)-targeted therapy (MAPK inhibitor) induces similar signatures in melanoma, suggesting that a non-genomic form of MAPK inhibitor resistance mediates cross-resistance to anti-PD-1 therapy. Validation of the IPRES in other independent tumor cohorts defines a transcriptomic subset across distinct types of advanced cancer. These findings suggest that attenuating the biological processes that underlie IPRES may improve anti-PD-1 response in melanoma and other cancer types.

INTRODUCTION

PD-1 immune checkpoint blockade therapy induces a high rate of anti-melanoma response and provides unprecedented clinical benefits (Hamid et al., 2013; Topalian et al., 2012). This therapeutic approach has also been shown to be active against a growing list of human malignancies, and clinical testing of combinations of PD-1 (or PD-L1) with other treatment targets has already begun (Sharma and Allison, 2015). However, effective clinical use of anti-PD-1 agents is encumbered by a high rate of innate resistance (60%–70%) in advanced metastatic melanoma. The mechanistic basis for the variation in response patterns or in long-term clinical benefits (i.e., survival) remains poorly explained.

In melanoma, the extent of pretreatment and especially treatment-induced intra-tumoral T cell infiltration correlates with clinical responses (Tumeh et al., 2014), supporting unleashing of tumor-specific T cells as the primary mechanistic basis of anti-PD-1 therapy. Preliminary retrospective analyses of clinical data hinted at prior failure of mitogen-activated protein kinase (MAPK)-targeted therapy being a negative factor for subsequent response to immune checkpoint blockade in melanoma (Puzanov et al., 2015, Pigment Cell Melanoma Res., abstract; Ramanujam et al., 2015, Pigment Cell Melanoma Res., abstract; Simeone et al., 2015, Pigment Cell Melanoma Res., abstract). In this context, acquired resistance to MAPK-targeted therapy has been correlated with depletion of intra-tumoral T cells, exhaustion of CD8 T cells, and loss of antigen presentation (Hugo et al., 2015).

At the genomic level, the overall mutation load has been correlated with clinical responses to anti-PD-1 therapy and linked to smoking in non-small-cell lung cancer or mismatch repair deficiency in colon cancer. (Le et al., 2015; Rizvi et al., 2015). Whether it was non-small-cell lung tumors on anti-PD-1 therapy or melanoma tumors on anti-CTLA-4 therapy (Snyder et al., 2014; Van Allen et al., 2015), the range of somatic mutation and neoepitope loads of the responding pretreatment tumors overlapped significantly with that of the non-responding tumors, despite statistically significant differences in their medians. As such, the lack of high mutational loads did not necessarily preclude clinical responses, and conversely, the presence of high mutational loads does not always correlate with responses. Thus, additional genomic or non-genomic features seem likely to contribute to anti-PD-1 response patterns. Here, we sought to assess omic-scale features related to clinical response and survival patterns in order to gain insights into potential strategies for patient stratification and identification of anti-PD-1 combinatorial therapies.

RESULTS AND DISCUSSION

High Mutational Load Does Not Associate with Tumor Response but Correlates with Improved Patient Survival

We analyzed the whole-exome sequences (WES) of 38 pretreatment (pembrolizumab and nivolumab) melanoma tumors (responding, n = 21; non-responding, n = 17; total 34 of 38 pretreatment; 4 of 38 early on-treatment; 14 of 38 patients with prior MAPK inhibitor (MAPKi) treatment; Table S1A) and patient-matched normal tissues for germline references. Responding pretreatment tumors were derived from patients who went on to have complete or partial responses or stable disease control (with mixed responses excluded) in response to anti-PD-1 therapy. Non-responding tumors were derived from patients who had progressive disease. These response patterns were based on irRECIST (Hoos et al., 2015; Wolchok et al., 2009). We also analyzed the transcriptomes through RNA-seq of responding (n = 15) and non-responding (n = 13) pretreatment tumors (total 27 of 28 pretreatment; 1 of 28 early on-treatment) with available high-quality RNA. WES achieved a median of 140× coverage in both tumor and normal tissues (Table S1B). We detected a median of 489 non-synonymous somatic mutations in the 38 tumors (range, 73 to 3,985, which is similar to that in a different set of melanoma tissues; Van Allen et al., 2015).

We found that responding pretreatment tumors on anti-PD-1 therapy harbored more non-synonymous single nucleotide variants (nsSNVs) compared to the non-responding tumors, albeit the statistical significance cutoff was not met (median nsSNVs responding = 495 and non-responding = 281, p = 0.30, Mann-Whitney; Table S1B). Increased predicted HLA (human leukocyte antigen) class I and class II neoepitope loads were also detected in the responding pretreatment tumors, although these differences were not statistically significant either (median HLA class I neoepitopes responding = 231 and non-responding = 156, p = 0.41; median HLA class II neoepitopes responding = 130 and non-responding = 95, p = 0.36, Mann-Whitney; Table S1B). Even when we considered only expressed nsSNV and neoepitope loads, the statistical significance of the differences between the responding versus non-responding tumors was not augmented. The comparison of these two groups of tumors was not likely biased by small differences in mean tumor purities or depth of sequencing (Figures S1A and S1B). The numbers of predicted HLA class I and II neoepitopes were strongly correlated with the number of nsSNVs (Figure S1C). We did not identify any recurrent predicted neoepitope or experimentally validated neoantigens (Table S1C). Previous work analyzing melanoma tumors sampled prior to anti-CTLA-4 antibody therapy had associated responses with a tetrapeptide signature (Snyder et al., 2014). However, we did not observe enrichment of this peptide motif in the pretreatment tumors that responded to anti-PD-1 therapy (Figure S1D). Likewise, analysis of an independent cohort of 110 melanoma tumors' pre-anti-CTLA-4 therapy also did not yield enrichment of this tetrapeptide motif among responding tumors (Van Allen et al., 2015).

In addition to examining the relationship between non-synonymous somatic mutational loads in pretreatment tumors and anti-tumor responses elicited by anti-PD-1 antibodies, we also examined the potential influences of somatic mutational loads on clinical benefits derived from anti-PD-1 immunotherapy as reflected by patient survival. Notably, a mutational load in the top third (compared to the bottom third) was significantly associated with improved survival (Figure 1A). We also observed a trend toward higher mutational load being associated with better survival among melanoma patients not treated with anti-PD-1 antibodies (Cancer Genome Atlas Network, 2015), although this association did not reach statistical significance (Figure S1E), suggesting that the prognostic power of a high mutational load is augmented in the setting of anti-PD-1 therapy. As expected, a positive association between objective tumor responses and survival was highly statistically significant (Figure 1B). Moreover, when we divided each non-responding and responding tumor group into sub-groups with low or high mutational loads (i.e., below or above the median total somatic nsSNVs of each response group; Figure 1C), patients with responding tumors of low mutation loads significantly outlived patients with non-responding tumors of high mutation loads (Figure 1D). This is despite the fact that mutational loads of these two groups were significantly different, with no overlap across the two distributions (Figure 1C). Hence, factors beyond the mutational load also influence shorter-term tumor response patterns and longer-term patient survival.

Enrichment for *BRCA2* Mutations in Anti-PD-1 Responsive Melanoma

We then sought to identify mutations (nsSNVs and small insertion-and-deletions [indels]; Table S1D) that (1) were recurrently and selectively associated with either responding or non-responding tumors (recurrence $\geq$ 25% in one group and, at most, one hit in the other group) and (2) occurred in genes at rates higher than background rates (Fisher's exact test, false discover rate [FDR]-corrected $p \leq 0.05$; Figure 1E; Table S1E). The background mutation rate of each gene was calculated from the WES data of 469 melanoma tumors (Hodis et al., 2012; Cancer Genome Atlas Network, 2015). Analysis of copy-number variations (CNVs) did not identify any recurrent alteration exclusive to either group. *BRCA2* harbored nsSNVs in 6 of 21 responding tumors (28%), but only 1 of 17 non-responding tumors (6%; Figure 1E). With a background mutational rate estimated at 6% (28 of 469 melanoma tumors), *BRCA2* was significantly more frequently mutated in the responding tumors than expected (Fisher p = 0.002, odds ratio = 6.2). The pattern of mutations in disparate BRCA2 protein domains suggested loss-of-function mutations (Figure 1F): one in the N-terminal NPM1-interacting region, one in the POLH-interacting domain, and four in the helical domain critical for FANCD2 interaction. Intriguingly, the somatic mutational load of the tumors with *BRCA2* nsSNVs was

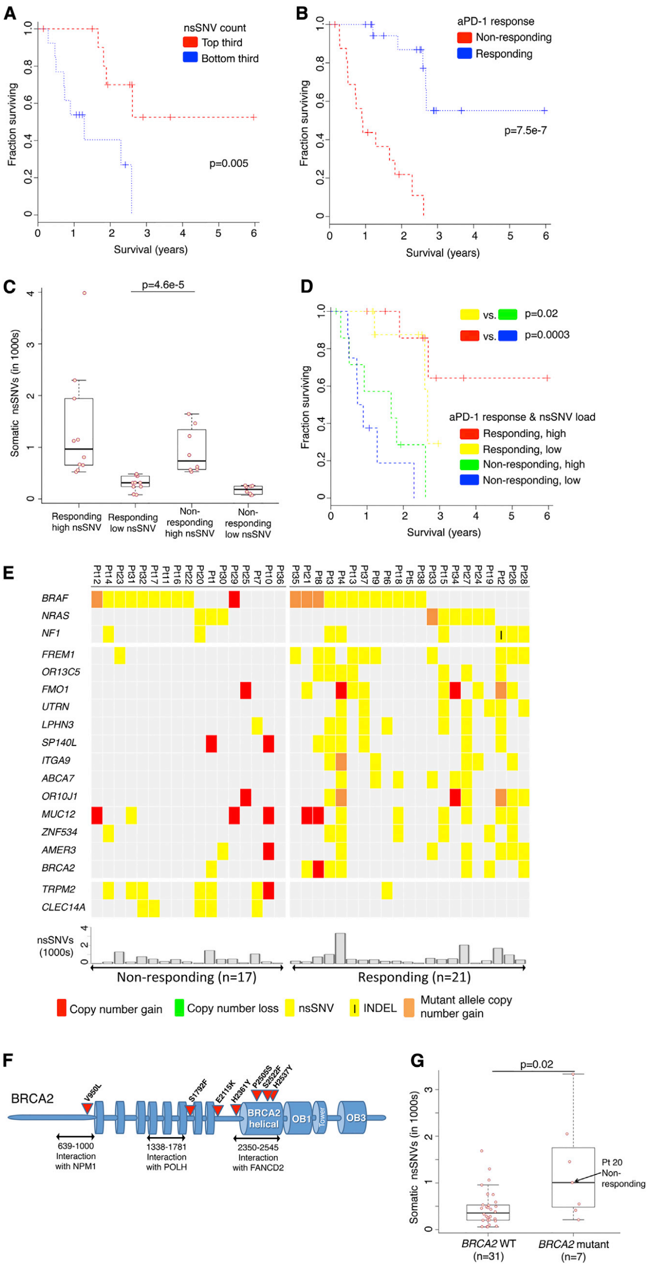

Figure 1. Mutational Correlates of Innate Sensitivity to Anti-PD-1 Therapy

(A) Overall survival of anti-PD-1-treated patients whose melanoma tumors harbored high (top third) versus low (bottom third) mutational (somatic nsSNVs) loads; p values, log-rank test.

(B) Overall survival of anti-PD-1-treated melanoma patients whose pretreatment tumors responded (n = 20) or did not respond (n = 17); p value, log-rank test.

(C) Total number of nsSNVs detected in anti-PD-1 responding and non-responding melanoma tumors harboring high (above the respective group's median) or low (below the group's median) mutational loads; p value, Mann Whitney test.

(D) Overall survival of anti-PD-1-treated melanoma patients harboring high (above the group median) or low (below the group median) mutational loads and whose pretreatment tumors responded or did not respond; p value, log-rank test.

(E) Recurrent exomic alterations (nsSNVs and small INDELs) in pretreatment tumors of responding versus non-responding patients on anti-PD-1 therapy. Copy-number alterations were annotated for the same genes as a reference. Top, mutations of melanoma signature genes. Middle, mutations recurrent in responding versus non-responding tumors (recurrence in 25% in one group and at most one occurrence in the opposite group, Fisher's exact test, FDR-corrected $p \leq 0.05$ on enrichment against the background mutation frequency). Bottom, the total nsSNV load of each melanoma tumor.

(F) Schematics of impact of missense mutations in the BRCA2 protein and its domains.

(G) Total number of nsSNVs detected in melanomas with or without *BRCA2* non-synonymous mutations; p value, Mann Whitney test.

See also Table S1 and Figure S1.

significantly higher than that with wild-type *BRCA2* in this cohort of tumors (Figure 1G), as well as two additional cohorts of melanoma tumors (Figure S1F). Thus, *BRCA2* loss-of-function mutations, which are expected to produce defects in homologous recombination and double-stranded DNA break repair (Holloman, 2011), may produce specific mutational signatures or unknown effects (e.g., induction of cell death) that contribute to anti-PD-1 responsiveness.

Co-enriched Transcriptomic Signatures in a Major Subset of Anti-PD-1 Resistant Melanoma

We then addressed whether transcriptomic features would differentiate between responding ($n = 15$) versus non-responding ($n = 13$) tumors sampled prior to anti-PD-1 therapy (total 27 of 28 pretreatment tumors and 1 of 28 early on-treatment). We compared the transcriptomes of the two tumor groups using two approaches: (1) analysis of differentially expressed genes (DEGs; Figures 2A, top, and 2B) across the two aggregate groups (Table S2A) coupled with GO term enrichment analysis of DEGs (Figure 2C) and (2) differential signature enrichment based on single-sample gene set variance analysis, or GSVA, scores using publicly available (C2 chemical and genetic perturbation, C6 oncogenic, and C7 immunologic subsets of the Molecular Signature Database, Broad Institute) and self-curated (see below) perturbation-induced gene signatures (Figure 2D; Table S2B).

From analysis of DEGs (cutoff, 2-fold difference between the absolute medians of normalized expressions in the two groups; nominal Mann-Whitney $p \leq 0.1$), we made observations suggesting that mesenchymal and inflammatory tumor phenotypes may be associated with innate anti-PD-1 resistance. First, 693 genes were differentially expressed between the responding versus non-responding pretreatment tumors, and the transcriptomes of non-responding tumors were dominated by relative gene up-expression events compared with the transcriptomes of responding tumors (Figure 2A, top, showing only genes whose differential expression met nominal Mann-Whitney $p \leq 0.05$; Table S2A). Second, DEGs that were expressed higher in non-responding pretreatment tumors included mesenchymal transition genes (*AXL, ROR2, WNT5A, LOXL2, TWIST2, TAGLN, FAP*), immunosuppressive genes (*IL10, VEGFA, VEGFC*), and monocyte and macrophage chemotactic genes (*CCL2, CCL7, CCL8 and CCL13*; Figures 2A and 2B). In addition to mesenchymal genes, genes associated with wound healing and angiogenesis, which are considered T cell suppressive (Motz and Coukos, 2011; Schäfer and Werner, 2008; Voron et al., 2014), were expressed higher among non-responding relative to responding pretreatment tumors. Interestingly, a recent study using a mouse melanoma model showed that *VEGFA* and *CCL2* expression was associated with innate anti-PD-1 resistance (Peng et al., 2016). *CDH1*, which is typically down-expressed by mesenchymal cancer cells, was also down-expressed by non-responding (versus responding) pretreatment tumors. Third, genes with putative roles in modulating immune checkpoint sensitivity were not differentially expressed between responding versus non-responding tumor groups (Figures 2A, bottom, and S2A). *GZMA, PRF1* (CD8 T cell cytolytic score), *PDCD1LG2* (*PD-L2*), and *CTLA4* were expressed higher in the pretreatment melanoma tumors of patients who derived benefit from CTLA-4 antibodies (Van Allen et al., 2015). However, these genes, along with other T cell related genes such as *CD8A*/*B*, *PD-L1, LAG3* (T cell checkpoint genes), and *IFNG,* did not present higher expression in anti-PD-1-responsive tumors (Figures 2A, bottom, and S2A). Similarly, we did not observe higher enrichment of multiple interferon signatures in the anti-PD-1-responsive group (Figure 2D, bottom). Previously, an interferon gamma signature was found to be differentially up-expressed in the pretreatment tumor biopsies from responding patients when a restricted set of immune genes were analyzed (Ribas et al., 2015, J. Clin. Oncol., abstract). However, the technical approach may not be comparable to our whole tumor transcriptomic approach. We did note that the expression levels of HLA class I genes (*HLA-A*, *-B*, or *-C*) trended higher among the responding tumors, although the differences were not statistically significant. Lastly, the complete loss of *PTEN* was reported to promote resistance to immune checkpoint blockade (Peng et al., 2016), but there was only one case of homozygous *PTEN* deletion (with nearly undetectable *PTEN* mRNA expression; Figure S2A) in our cohort (in the non-responsive sub-group), limiting our ability to draw meaningful associations in this dataset. Generally, we did not observe a statistically significant difference in *PTEN* expression between anti-PD-1 responding versus non-responding tumors. Thus, individual gene-based expression analysis suggested mesenchymal and T cell suppressive inflammatory or angiogenic tumor phenotypes as being associated with innate anti-PD-1 resistance.

We then queried biological processes represented by DEGs. While gene ontology (GO) enrichment analysis of genes up-expressed among responding tumors produced no significantly enriched terms, genes up-expressed among non-responding tumors were enriched for cell adhesion, extracellular matrix (ECM) organization, wound healing, and angiogenesis (FDR-adjusted p values of GO gene sets shown in Figure 2C). Using independently derived perturbation-based transcriptomic signatures (Molecular Signature Database; Table S2C), we sought after differentially enriched processes in the responding versus non-responding pretreatment tumors (cutoff, 10% difference between the absolute medians of GSVA scores in the two groups; FDR-corrected Welch t test $p \leq 0.25$). Gene sets meeting these standard cutoffs formed the core set (Figure 2D, top, in bold) from which we compiled additional concurrently enriched (nominal Welch t test $p \leq 0.1$) and functionally related gene sets (Figure 2D, top; Table S2B). We considered these statistically weaker gene set enrichments biologically meaningful given the functional coherence of these gene signatures with the core signatures (Subramanian et al., 2005).

Importantly, a group of 26 transcriptomic signatures were co-enriched en bloc in 9 of 13 non-responding versus 1 of 15 responding pre-anti-PD-1 tumors (see Experimental Procedures). Co-enrichment of these signatures, collectively referred to as the innate anti-PD-1 resistance (IPRES) signature, again indicated heightened mesenchymal transition, angiogenesis, hypoxia, and wound healing. The concurrence of a tumor cell mesenchymal phenotype with an angiogenesis- and wound-healing-related inflammatory microenvironment has been documented in the literature (Chen et al., 2014, 2015; Mak et al.,

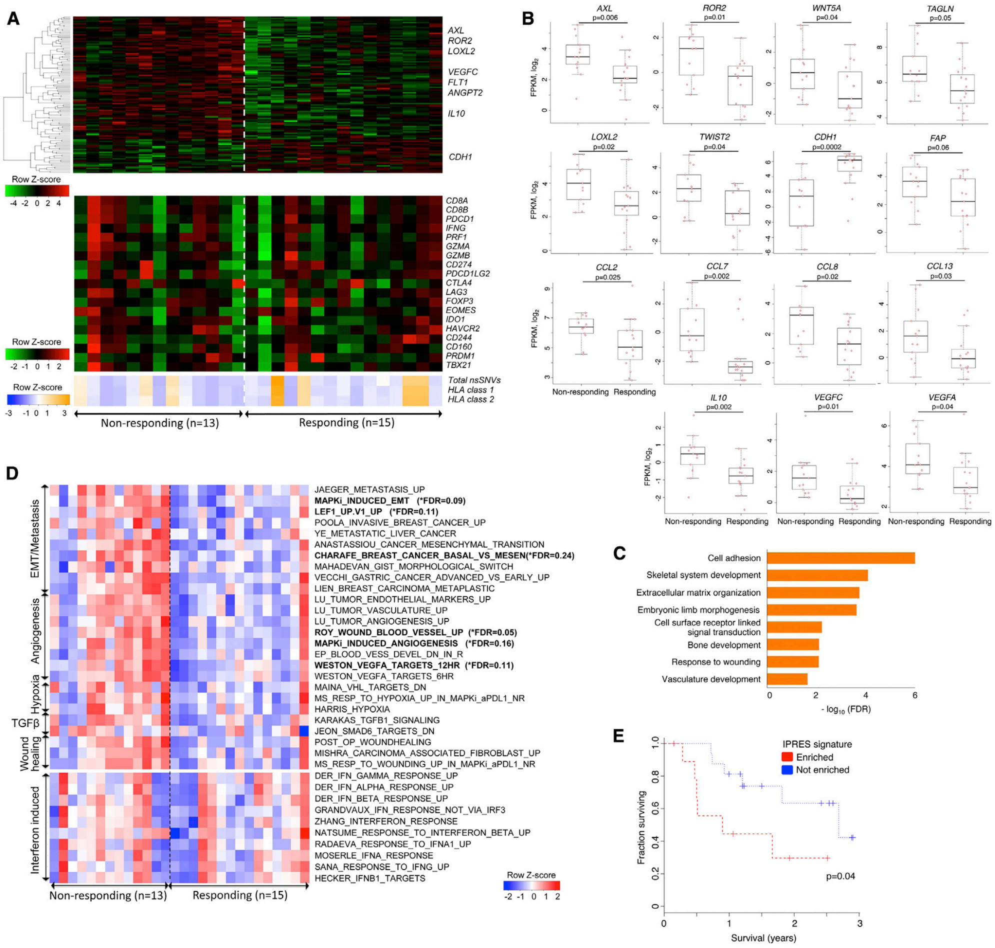

Figure 2. Transcriptomic Signatures of Innate Resistance to Anti-PD-1 Therapy

(A) Top, heatmap showing differentially expressed genes in the pretreatment tumors derived from patients who responded versus who did not respond to anti-PD-1 treatment (gene expression with inter-quartile range [IQR] ≥ 2; median fold-change [FC] difference ≥ 2; Mann Whitney p ≤ 0.05). Middle, mRNA expression levels of genes with hypothetical roles in modulating response patterns to anti-PD-1 therapy. Bottom, overall number of nsSNVs and HLA class 1 and 2 neoepitopes (predicted).

(B) mRNA levels of genes (which control tumor cell mesenchymal transition, tumor angiogenesis, and macrophage and monocyte chemotaxis) that were differentially expressed between the responding versus non-responding pretreatment tumors; p values, Mann Whitney test.

(C) GO enrichment of genes that were expressed higher in the non-responding tumors.

(D) Heatmap showing the gene set variance analysis (GSVA) scores of gene signatures differentially enriched in the responding versus non-responding pre-anti-PD-1 tumors (absolute median GSVA score difference ≥ 10%, FDR-corrected Welch t test p ≤ 0.25 or nominal Welch t test p ≤ 0.1). For comparison, enrichment scores of interferon signatures are also displayed.

(E) Overall survival of anti-PD-1-treated melanoma patients with presence (n = 10) or absence (n = 16) of co-enriched innate anti-PD-1 resistance (IPRES) signatures; p value, log-rank test.

See also Table S2 and Figure S2.

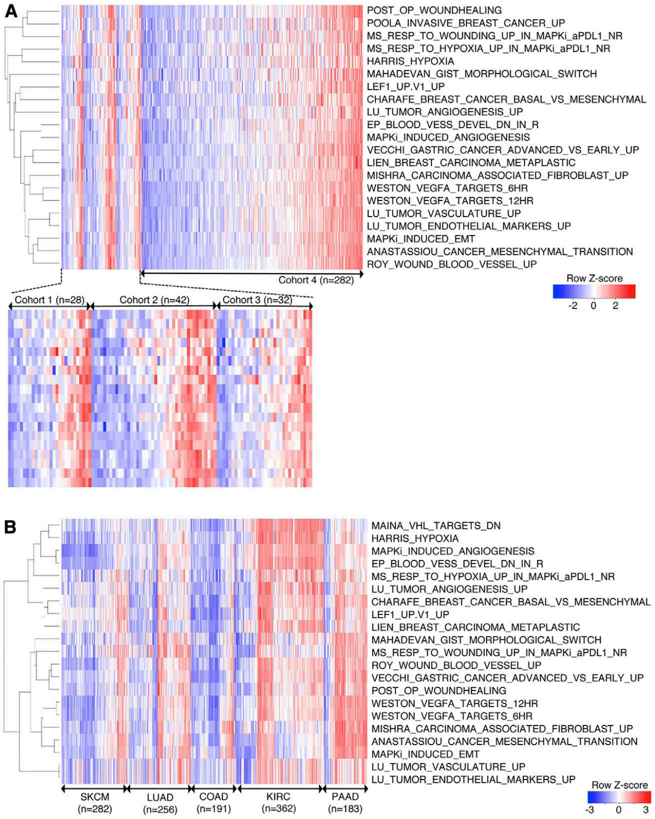

Figure 3. Co-enrichment of Innate Anti-PD-1 Resistance-Associated Signatures Defines a Transcriptomic Subset in Melanoma and Multiple Cancers

(A) Heatmap showing GSVA scores of IPRES signatures across four independent RNA-seq datasets derived from metastatic melanoma. Cohort 1, pretreatment (anti-PD-1) tumors; cohort 2, pretreatment (anti-CTLA-4) tumors; cohort 3, pretreatment (MAPKi) tumors; cohort 4, TCGA cutaneous melanoma (metastatic only).

(B) Heatmap showing GSVA scores of IPRIM signatures across TCGA RNA-seq datasets (metastatic melanoma, SKCM; lung adenocarcinoma, LUAD; colon adenocarcinoma, COAD; kidney clear cell carcinoma, KIRC; and pancreatic adenocarcinoma, PAAD).

See also Figure S3.

2016). Interestingly, this set of 26 IPRES signatures included signatures induced by MAPKi treatment of melanoma tumors and cell lines (Table S2C). We have shown recently that MAPKi treatment of melanoma cells induces transcriptome-wide reprogramming, leading to concurrent phenotype switches (C.S., L.S., W.H., and R.S.L., unpublished data). Notably, MAPKi-induced signatures of mesenchymal-invasive transition, angiogenesis, and wound-healing signatures were detected in the residual melanoma tumors from patients on MAPKi therapy, suggesting that induction of these signatures may negatively impact responsiveness to combinatorial anti-PD-1/L1 therapy.

IPRES Signatures Define a Transcriptomic Subset across Cancers

The observations that IPRES content signatures were co-enriched in the same tumors (Figure 2D) and that MAPKi induced these signatures concurrently (Table S2C) implied co-regulated tumor phenotypes that together define a transcriptomic subset. To evaluate whether co-enrichment of IPRES content signatures was an exclusive feature of our cohort, we queried three additional cohorts of metastatic melanoma-derived RNA-seq (Hugo et al., 2015; Cancer Genome Atlas Network, 2015; Van Allen et al., 2015), including a cohort consisting of only ^{V600}*BRAF* mutant melanomas (cohort 3; Hugo et al., 2015). We found that IPRES content signatures co-enriched not only in the same tumors, but also in about a third of total samples in each of the four independent transcriptomic datasets (cohort 1 from this study, 10 IPRES-enriched tumors of 28 total tumors; cohort 2, 15 of 42; cohort 3, 11 of 32; cohort 4, 90 of 282; Figure 3A). Considering 126 among 384 total tumors as the background prevalence for co-enrichment of IPRES content signatures in metastatic melanoma, we determined that this IPRES-enriched transcriptomic subset was over-represented among the anti-PD-1 non-responding pretreatment tumors (Fisher p = 0.013, odds ratio = 4.6) and under-represented among the responding pretreatment tumors (Fisher p = 0.04, odds ratio = 0.15) within cohort 1. In contrast, co-enrichment of IPRES signatures was neither over- nor under-represented among the responding or non-responding pre-anti-CTLA-4 melanoma tumors in cohort 2 (Figure S2B; Van Allen et al., 2015), which suggests that mechanisms of innate resistance to anti-PD-1 and anti-CTLA-4 are not necessarily similar.

Furthermore, co-enrichment of the IPRES signatures defined a transcriptomic subset within not only melanoma, but also all major common human malignancies analyzed (Figure 3B). The IPRES-enriched transcriptomic subset of certain cancers, such as pancreatic adenocarcinoma, made up the majority of tumors. Within a side-by-side comparison, only 6 of 69 primary cutaneous melanomas showed co-enrichment of IPRES signatures, in contrast to 90 of 282 metastatic (The Cancer Genome Atlas [TCGA]) melanomas ($p = 3.9e^{-5}$, odds ratio = 0.2; Figure S3), consistent with mesenchymal transition and metastasis gene sets among IPRES signatures. Thus, co-enrichment of IPRES signatures defines a distinct transcriptomic program that exists across distinct cancer histologies.

This study highlights the utility of both exome and transcriptome sequencing data generated from pretreatment tumor samples for the identification of potential determinants of response to anti-PD-1. Although the overall somatic mutational loads of anti-PD-1-responsive melanoma tumors were not significantly higher than those of non-responsive tumors, higher mutational loads associated significantly with better survival after anti-PD-1 therapy. This finding is still consistent with the notion that neoepitopes derived from somatic non-synonymous mutations are critical for deriving clinical benefits from anti-PD-1 therapy in melanoma. However, objective tumor responses, although strongly associated with survival benefits, did not appear to be driven overwhelmingly by the overall somatic mutational loads. That is to say, a relatively low mutational load did not preclude a tumor response. This is consistent with findings from gastrointestinal cancers where low mutational loads did not preclude tumor infiltration by mutation-reactive, class I- and II-restricted T cells (Tran et al., 2015). Thus, overall somatic or predicted neoepitope loads of pretreatment melanoma tumors are not enough to predict response patterns to anti-PD-1 therapy.

In our cohort, responsive tumors were significantly enriched for (likely) loss-of-function mutations in *BRCA2*. As one would predict from the known function of BRCA2 in DNA repair, *BRCA2*-mutated melanomas harbored higher mutational loads than *BRCA2*-wild-type melanomas. Although it is conceivable that defective BRCA2-DNA repair results in specific mutational motifs (rather than or in addition to the general increase in mutational load) that enhance responsiveness, it is also possible that cellular stress resulting from defective DNA repair could lead to increased cell death and anti-tumor immunity. Moreover, these data support the notion that tumor cell phenotypic plasticity (i.e., mesenchymal transition) and the resultant impacts on the microenvironment (e.g., ECM remodeling, cell adhesion, and angiogenesis features of immune suppressive wound healing) are critical barriers to anti-PD-1 responses. The limited number of patients in our melanoma cohort posed certain challenges to our analysis. For example, we relaxed the statistical stringency in single gene-based differential expression analysis (bypassing multiple hypothesis correction) to derive enough genes for GO enrichment analysis. However, converging findings from alternative analysis (i.e., GSVA) of the transcriptome data helped to mitigate potential caveats. Finally, in separate work, we found that mutation-targeted therapy (i.e., MAPKi) induces tumor cell-autonomous changes (e.g., mesenchymal transition; C.S., L.S., W.H., and R.S.L., unpublished data) and upregulates anti-PD-1 resistance-associated processes in residual tumors that have regressed in response to MAPKi treatment. Thus, while our findings in this study necessitate confirmation in independent tissue cohorts, the identification of transcriptomic features associated with anti-PD-1 resistance suggests that mitigation of IPRES-related biological processes may enhance response rates to anti-PD-1 (and anti-PD-1 plus MAPKi) therapy.

EXPERIMENTAL PROCEDURES

Tumor Specimens and Profiling

All tissues in this study were obtained with the approval of institutional review boards and patients' consents. All patients received either pembrolizumab or nivolumab as the anti-PD-1 therapy for their metastatic melanoma. 38 melanoma specimens (32 pre-treatment tumors, 2 pretreatment tumor-derived cultures, 3 early on-treatment tumors without response, and 1 early on-treatment tumor with response) and their patient-matched normal tissues were analyzed by WES. Among these 38 samples with WES data, 28 with sufficient RNA quality were also analyzed by RNA sequencing (RNA-seq). This set included another RNA-seq dataset derived from a second-site, pre-treatment tumor biopsy from patient #27. However, this second-site, pre-treatment tumor-derived WES dataset was excluded in our aggregate mutation analysis to avoid double counting two tumor exomes from the same patient (Table S1A).

38 tumor specimens and their respective normal tissues were subjected to WES (Table S1A). WES was performed using pair-end sequencing with read length of 2 × 100 bps based on the Illumina HiSeq2000 platform. RNA from a subset of 28 tumors were pair-end sequenced with read length of 2 × 100 bps (Illumina HiSeq2000). We included two tumors from patient #27 for transcriptomic analyses, but not for mutation and neoepitope analyses, since the tumors may not share the same transcriptomic profile, but they essentially contain the same set of non-synonymous somatic mutations.

Whole Exome Sequencing

We called single nucleotide variant (SNV) and INDEL as reported (Shi et al., 2014) using a stand-alone version of Oncotator (Ramos et al., 2015). Copy numbers were called using the intersection of the copy-number calls derived from Sequenza (Favero et al., 2015) and VarScan2 (Koboldt et al., 2012). Tumor purities and ploidies (Table S1B) were calculated based on the calls of Sequenza using WES data with default parameters. The impact of *BRCA2* nsSNVs was visualized using the domain information in the INTERPRO protein domain database (Mitchell et al., 2015).

HLA Types and Neoepitopes

The four-digit HLA class 1 and 2 types of each patient were called using ATHLATES (Liu et al., 2013) using the WES-sequencing reads from the normal tissue. To ensure concordance, we manually compared ATHLATES' calls of the normal versus tumor samples and ascertained that there was at least no two-digit HLA typing discrepancy between any normal tumor pair. For each non-synonymous coding mutation from a tumor, we predicted its impact on the patient's HLA class I and II binding using the standalone version of the programs NetMHCpan v2.8 (Hoof et al., 2009; Nielsen et al., 2007) and NetMHCIIpan v3.0 (Karosiene et al., 2013), respectively. Specifically, for HLA class I binding prediction using netMHCpan v2.8, we tested all 9-11-mer peptides containing the mutated amino acids for binding to the patient's HLA-A, -B, and -C. A peptide was defined as a neoepitope based on two criteria: (1) predicted binding affinity $\leq$ 500nM and (2) rank percentage $\leq$ 2% (default cutoff). For HLA class II binding prediction using netMHCIIpan v3.0, we tested the 9-19-mers containing the mutated amino acids for binding to the patient-specific, ATHLATES-predicted DPA-DPB, DQA-DQB, and DRA-DRB allele pairs. We also applied the same predicted binding affinity and rank percentage cutoff as we did for HLA class I to nominate the HLA class-II-binding neoepitopes. Expressed non-synonymous mutations and neoepitopes were defined based on corresponding genes with normalized expression levels $\geq$ 1 (in fragments per kilobase of transcripts per million mapped reads [FPKM]). Statistical differences of nsSNV, HLA class I and II neoepitopes, WES coverages, and tumor purities were computed using two-sided Mann-Whitney test.

Mutation Recurrence

To estimate the statistical significance of the recurrence of gene mutations in the responding or non-responding tumors, we used an independent batch of 469 melanomas' whole-exome sequence datasets (Hodis et al., 2012; Cancer Genome Atlas Network, 2015) to estimate each gene's background mutation frequency. Significance was computed by Fisher's exact test followed by FDR adjustment for multiple hypothesis testing. We listed genes that fulfilled the criteria: (1) recurrence in at least 25% of the responder/non-responder, (2) occurrence of at most once in the opposite group, and (3) Fisher's exact test FDR-adjusted p value ≤ 0.05. These genes were illustrated in Figure 1A, and all genes that fulfilled the first and second criteria and tested for multiple hypotheses were listed in Table S1E. The association between *BRCA2* nsSNVs and overall nsSNV counts were tested using two-sided Mann Whitney test and validated in independent WES datasets (Hodis et al., 2012; Cancer Genome Atlas Network, 2015).

RNA-Seq and Gene Set Enrichment

Paired-end transcriptome reads were mapped to the UCSC hg19 reference genome using Tophat2 (Kim et al., 2013). Normalized expression levels of genes were expressed in FPKM values as generated by cuffquant and cuffnorm (Trapnell et al., 2012). The program was run with the option "–frag-bias-correct" and "–multi-read-correct" to improve sensitivity (Roberts et al., 2011). A gene was defined as differentially expressed between the responding and non-responding tumor groups when its median expression differed by at least 2-fold between the groups with a nominal two-sided Mann-Whitney p value ≤ 0.1 (Table S2A). Applying multiple hypothesis correction of FDR p ≤ 0.25 only yielded three differentially expressed genes: *ALDH1L2* and *MFAP2* in the non-responding and *CDH1* (E-cadherin) in the responding group. As such, the genes meeting the uncorrected, nominal Mann-Whitney p value ≤ 0.1 that were expressed higher either in the responding or non-responding group were separately analyzed for GO term enrichments using the online functional annotation tools DAVID (Huang et al., 2009a). Enriched GO terms were selected from the GO biological process terms in DAVID's fat database (Huang et al., 2009b). GO terms which were highly overlapping, as defined by functional clustering in DAVID's website, were represented by the terms with the best FDR-adjusted p values.

To calculate single-sample gene set enrichment, we used the GSVA program (Hänzelmann et al., 2013) to derive the absolute enrichment scores of previously experimentally validated gene signatures as follows: (1) the C2 CGP (chemical and genetic perturbation sets), (2) the C6 and C7 subset of the Molecular Signature Database version 4.0 (Subramanian et al., 2005), (3) self-curated MAPKi-induced gene signatures using cell lines and patient-derived tumors (C.S., L.S., W.H., and R.S.L., unpublished data), (4) post-operation wound signature (Inkeles et al., 2015), and (5) melanoma invasive/proliferative signatures (Hoek et al., 2008). To derive the GSVA score of each signature in each tumor sample, we computed from raw RNA-seq read counts by HTSEQ COUNT program and then normalized them to $\log_2$ counts per million (CPM) values using EdgeR (McCarthy et al., 2012). We removed batch effects using the edgeR function RemoveBatchEffect when we combined RNA-seq data from multiple experiments (Figure 3A). The normalized $\log_2$ CPM values were then passed on as input for GSVA in the RNA-seq mode. Differentially enriched core gene sets between the responding and non-responding tumor groups were defined by GSVA score differences of $\geq 10\%$ and FDR-corrected, two-sided Welch t test p value ≤ 0.25 (we used t test because the GSVA scores were normally distributed around zero). Two gene sets, INGRAM_SHH_TARGETS_DN and WONG_ENDMETRIUM_CANCER_DN, were not included in the core set because they did not specifically point to a cellular process and/or relate to the other six gene sets in the core set (Table S2B, top eight). We also collected gene sets that met the GSVA score differences of $\geq 10\%$ and nominal Welch t test p value ≤ 0.1 (Table S2B) and included those which were concordantly enriched and functionally related to the core gene sets to make up the full list of IPRES signatures (Figure 2D).

To compare co-enrichment of IPRES signatures across multiple melanoma cohorts, we combined and batch-corrected the $\log_2$ CPM values of four melanoma transcriptome cohorts: (1) our current pre-anti-PD-1 tumors (n = 28), (2) pre-anti-CTLA-4 tumors (n = 42), (3) pre-MAPKi tumors (n = 32), and (4) the metastatic subset of TCGA melanoma (n = 282). We row-normalized the GSVA scores of each gene set in the IPRES signature across the samples from the four cohorts. For this comparative study, we excluded the gene sets JAEGER_METASTASIS_UP, YE_METASTATIC_LIVER_CANCER, KARAKAS_TGFB1_SIGNALING, and JEON_SMAD6_ TARGETS_ DN from the IPRES set because they showed weaker co-enrichment with rest of the gene sets (see Figure 2D, top). The IPRES (enrichment) score was defined as the average *Z* score across all gene sets in the IPRES signature, and we applied an average *Z* score of 0.35 as the cutoff for IPRES signature enrichment in a tumor sample. This resulted in IPRES co-enrichment in nine non-responding tumors and one responding tumor in our anti-PD-1 cohort (this cutoff was chosen because it provided the largest average *Z* score separation between the samples with and without IPRES co-enrichment). Since the IPRES score was not comparable across analyses in Figures 3A, 3B, and S3 (since the IPRES score is *Z* score-base), we used the 90th highest IPRES score in the TCGA metastatic melanoma cohort as the IPRES score cutoff (since there were 90 of 282 tumors showing IPRES co-enrichment in this TCGA metastatic cohort; Figure 3A) for analyses performed to yield Figures 3B and S3. This allowed for a non-parametric comparison across multiple TCGA datasets at the IPRES co-enrichment level established in our anti-PD-1 cohort.

Source Data

Analysis of differential non-synonymous mutational hits in responders versus non-responders to ipilimumab was based on the mutation calls as reported (Van Allen et al., 2015). We curated published CD8 T cell exhaustion genes (Wherry, 2011) to minimize those likely to be expressed by melanoma cells by excluding genes whose maximum $\log_2$ FPKM was 1 in an in-house melanoma cell-line-derived RNA-seq database (n = 26 cell lines). This resulted in the inclusion of genes for surface receptors *PDCD1 (PD-1)*, *LAG3*, *HAVCR2 (Tim-3)*, *CD160*, and *CD244* as well as transcription factors *EOMES*, *PRDM1 (Blimp-1)*, and *TBX21 (T-bet)*. We assessed co-enrichment of IPRES content signatures in the (1) anti-CTLA-4 pretreatment cohort (Van Allen et al., 2015), (2) MAPKi pretreatment cohort (Hugo et al., 2015; C.S., L.S., W.H., and R.S.L., unpublished data), (3) TCGA melanoma (metastatic and primary subsets separately analyzed; Cancer Genome Atlas Network, 2015), (4) TCGA pancreatic ductal adenocarcinoma (TCGA, provisional, see https://tcga-data.nci.nih.gov/tcga/tcgaHome2.jsp), (5) TCGA lung adenocarcinoma (Cancer Genome Atlas Research Network, 2014), (6) TCGA colorectal adenocarcinoma (Cancer Genome Atlas Network, 2012), and (7) TCGA kidney clear cell carcinoma (Cancer Genome Atlas Research Network, 2013).

ACCESSION NUMBERS

The accession number for the transcriptome data is GEO: GSE78220. The whole-exome sequencing data has been deposited to the Sequence Read Archive (https://www.ncbi.nlm.nih.gov/sra), under the accession numbers SRA: SRP067938 (UCLA samples) and SRA: SRP090294 (Vanderbilt samples).

SUPPLEMENTAL INFORMATION

Supplemental Information includes three figures and two tables and can be found with this article online at http://dx.doi.org/10.1016/j.cell.2016.02.065.

AUTHOR CONTRIBUTION

W.H., J.M.Z., L.S., C.S., A.R., and R.S.L. generated, analyzed, and interpreted the data. S.H.-L., B.H.M., B.C., G.C., E.S., M.C.K., J.A.S., D.B.J., A.R., and R.S.L. evaluated patients and provided tissue reagents. B.B.-M., J.P., S.L., and X.K. processed tissues for analysis. All authors contributed to manuscript preparation. W.H. and R.S.L. developed the concepts, supervised the project, and wrote the paper.

ACKNOWLEDGMENTS

This work has been funded by the NIH (R35 CA197633 to A.R., P01 CA168585 to A.R. and R.S.L., 1R01CA176111 to R.S.L., and K12CA0906525 to D.B.J.), the Ressler Family Foundation (to R.S.L. and A.R.), the Grimaldi Family Fund (to A.R. and R.S.L.), the Burroughs Wellcome Fund (to R.S.L.), the Ian Copeland Melanoma Fund (to R.S.L.), the Wade F.B. Thompson/Cancer Research Institute CLIP Grant (to R.S.L.), the Steven C. Gordon Family Foundation (to R.S.L.), the American Skin Association (to W.H.), the Dr. Robert Vigen Memorial Fund (to A.R.), the Garcia-Corsini Family Fund (to A.R.), the ASCO Conquer

Cancer Career Development Award (to D.B.J.), and the American Cancer Society Research Professorship (to J.A.S.). Informed consents were obtained from patients for the research performed in this study.

Received: December 25, 2015
Revised: January 30, 2016
Accepted: February 29, 2016
Published: March 17, 2016; corrected online January 18, 2017

REFERENCES

Cancer Genome Atlas Network (2012). Comprehensive molecular characterization of human colon and rectal cancer. Nature *487*, 330–337.

Cancer Genome Atlas Network (2015). Genomic Classification of Cutaneous Melanoma. Cell *161*, 1681–1696.

Cancer Genome Atlas Research Network (2013). Comprehensive molecular characterization of clear cell renal cell carcinoma. Nature *499*, 43–49.

Cancer Genome Atlas Research Network (2014). Comprehensive molecular profiling of lung adenocarcinoma. Nature *511*, 543–550.

Chen, L., Gibbons, D.L., Goswami, S., Cortez, M.A., Ahn, Y.H., Byers, L.A., Zhang, X., Yi, X., Dwyer, D., Lin, W., et al. (2014). Metastasis is regulated via microRNA-200/ZEB1 axis control of tumour cell PD-L1 expression and intratumoral immunosuppression. Nat. Commun. *5*, 5241.

Chen, L., Heymach, J.V., Qin, F.X., and Gibbons, D.L. (2015). The mutually regulatory loop of epithelial-mesenchymal transition and immunosuppression in cancer progression. OncoImmunology *4*, e1002731.

Favero, F., Joshi, T., Marquard, A.M., Birkbak, N.J., Krzystanek, M., Li, Q., Szallasi, Z., and Eklund, A.C. (2015). Sequenza: allele-specific copy number and mutation profiles from tumor sequencing data. Ann. Oncol. *26*, 64–70.

Hamid, O., Robert, C., Daud, A., Hodi, F.S., Hwu, W.J., Kefford, R., Wolchok, J.D., Hersey, P., Joseph, R.W., Weber, J.S., et al. (2013). Safety and tumor responses with lambrolizumab (anti-PD-1) in melanoma. N. Engl. J. Med. *369*, 134–144.

Hänzelmann, S., Castelo, R., and Guinney, J. (2013). GSVA: gene set variation analysis for microarray and RNA-seq data. BMC Bioinformatics *14*, 7.

Hodis, E., Watson, I.R., Kryukov, G.V., Arold, S.T., Imielinski, M., Theurillat, J.P., Nickerson, E., Auclair, D., Li, L., Place, C., et al. (2012). A landscape of driver mutations in melanoma. Cell *150*, 251–263.

Hoek, K.S., Eichhoff, O.M., Schlegel, N.C., Döbbeling, U., Kobert, N., Schaerer, L., Hemmi, S., and Dummer, R. (2008). In vivo switching of human melanoma cells between proliferative and invasive states. Cancer Res. *68*, 650–656.

Holloman, W.K. (2011). Unraveling the mechanism of BRCA2 in homologous recombination. Nat. Struct. Mol. Biol. *18*, 748–754.

Hoof, I., Peters, B., Sidney, J., Pedersen, L.E., Sette, A., Lund, O., Buus, S., and Nielsen, M. (2009). NetMHCpan, a method for MHC class I binding prediction beyond humans. Immunogenetics *61*, 1–13.

Hoos, A., Wolchok, J.D., Humphrey, R.W., and Hodi, F.S. (2015). CCR 20th Anniversary Commentary: Immune-Related Response Criteria–Capturing Clinical Activity in Immuno-Oncology. Clin. Cancer Res. *21*, 4989–4991.

Huang, W., Sherman, B.T., and Lempicki, R.A. (2009a). Systematic and integrative analysis of large gene lists using DAVID bioinformatics resources. Nat. Protoc. *4*, 44–57.

Huang, W., Sherman, B.T., and Lempicki, R.A. (2009b). Bioinformatics enrichment tools: paths toward the comprehensive functional analysis of large gene lists. Nucleic Acids Res. *37*, 1–13.

Hugo, W., Shi, H., Sun, L., Piva, M., Song, C., Kong, X., Moriceau, G., Hong, A., Dahlman, K.B., Johnson, D.B., et al. (2015). Non-genomic and Immune Evolution of Melanoma Acquiring MAPKi Resistance. Cell *162*, 1271–1285.

Inkeles, M.S., Scumpia, P.O., Swindell, W.R., Lopez, D., Teles, R.M., Graeber, T.G., Meller, S., Homey, B., Elder, J.T., Gilliet, M., et al. (2015). Comparison of molecular signatures from multiple skin diseases identifies mechanisms of immunopathogenesis. J. Invest. Dermatol. *135*, 151–159.

Karosiene, E., Rasmussen, M., Blicher, T., Lund, O., Buus, S., and Nielsen, M. (2013). NetMHCIIpan-3.0, a common pan-specific MHC class II prediction method including all three human MHC class II isotypes, HLA-DR, HLA-DP and HLA-DQ. Immunogenetics *65*, 711–724.

Kim, D., Pertea, G., Trapnell, C., Pimentel, H., Kelley, R., and Salzberg, S.L. (2013). TopHat2: accurate alignment of transcriptomes in the presence of insertions, deletions and gene fusions. Genome Biol. *14*, R36.

Koboldt, D.C., Zhang, Q., Larson, D.E., Shen, D., McLellan, M.D., Lin, L., Miller, C.A., Mardis, E.R., Ding, L., and Wilson, R.K. (2012). VarScan 2: somatic mutation and copy number alteration discovery in cancer by exome sequencing. Genome Res. *22*, 568–576.

Le, D.T., Uram, J.N., Wang, H., Bartlett, B.R., Kemberling, H., Eyring, A.D., Skora, A.D., Luber, B.S., Azad, N.S., Laheru, D., et al. (2015). PD-1 Blockade in Tumors with Mismatch-Repair Deficiency. N. Engl. J. Med. *372*, 2509–2520.

Liu, C., Yang, X., Duffy, B., Mohanakumar, T., Mitra, R.D., Zody, M.C., and Pfeifer, J.D. (2013). ATHLATES: accurate typing of human leukocyte antigen through exome sequencing. Nucleic Acids Res. *41*, e142.

Mak, M.P., Tong, P., Diao, L., Cardnell, R.J., Gibbons, D.L., William, W.N., Skoulidis, F., Parra, E.R., Rodriguez-Canales, J., Wistuba, I.I., et al. (2016). A Patient-Derived, Pan-Cancer EMT Signature Identifies Global Molecular Alterations and Immune Target Enrichment Following Epithelial-to-Mesenchymal Transition. Clin. Cancer Res. *22*, 609–620.

McCarthy, D.J., Chen, Y., and Smyth, G.K. (2012). Differential expression analysis of multifactor RNA-Seq experiments with respect to biological variation. Nucleic Acids Res. *40*, 4288–4297.

Mitchell, A., Chang, H.Y., Daugherty, L., Fraser, M., Hunter, S., Lopez, R., McAnulla, C., McMenamin, C., Nuka, G., Pesseat, S., et al. (2015). The InterPro protein families database: the classification resource after 15 years. Nucleic Acids Res. *43*, D213–D221.

Motz, G.T., and Coukos, G. (2011). The parallel lives of angiogenesis and immunosuppression: cancer and other tales. Nat. Rev. Immunol. *11*, 702–711.

Nielsen, M., Lundegaard, C., Blicher, T., Lamberth, K., Harndahl, M., Justesen, S., Røder, G., Peters, B., Sette, A., Lund, O., and Buus, S. (2007). NetMHCpan, a method for quantitative predictions of peptide binding to any HLA-A and -B locus protein of known sequence. PLoS ONE *2*, e796.

Peng, W., Chen, J.Q., Liu, C., Malu, S., Creasy, C., Tetzlaff, M.T., Xu, C., McKenzie, J.A., Zhang, C., Liang, X., et al. (2016). Loss of PTEN promotes resistance to T cell-mediated immunotherapy. Cancer Discov. *6*, 202–216.

Ramos, A.H., Lichtenstein, L., Gupta, M., Lawrence, M.S., Pugh, T.J., Saksena, G., Meyerson, M., and Getz, G. (2015). Oncotator: cancer variant annotation tool. Hum. Mutat. *36*, E2423–E2429.

Rizvi, N.A., Hellmann, M.D., Snyder, A., Kvistborg, P., Makarov, V., Havel, J.J., Lee, W., Yuan, J., Wong, P., Ho, T.S., et al. (2015). Cancer immunology. Mutational landscape determines sensitivity to PD-1 blockade in non-small cell lung cancer. Science *348*, 124–128.

Roberts, A., Trapnell, C., Donaghey, J., Rinn, J.L., and Pachter, L. (2011). Improving RNA-Seq expression estimates by correcting for fragment bias. Genome Biol. *12*, R22.

Schäfer, M., and Werner, S. (2008). Cancer as an overhealing wound: an old hypothesis revisited. Nat. Rev. Mol. Cell Biol. *9*, 628–638.

Sharma, P., and Allison, J.P. (2015). Immune checkpoint targeting in cancer therapy: toward combination strategies with curative potential. Cell *161*, 205–214.

Shi, H., Hugo, W., Kong, X., Hong, A., Koya, R.C., Moriceau, G., Chodon, T., Guo, R., Johnson, D.B., Dahlman, K.B., et al. (2014). Acquired resistance and clonal evolution in melanoma during BRAF inhibitor therapy. Cancer Discov. *4*, 80–93.

Snyder, A., Makarov, V., Merghoub, T., Yuan, J., Zaretsky, J.M., Desrichard, A., Walsh, L.A., Postow, M.A., Wong, P., Ho, T.S., et al. (2014). Genetic basis for clinical response to CTLA-4 blockade in melanoma. N. Engl. J. Med. *371*, 2189–2199.

Subramanian, A., Tamayo, P., Mootha, V.K., Mukherjee, S., Ebert, B.L., Gillette, M.A., Paulovich, A., Pomeroy, S.L., Golub, T.R., Lander, E.S., and Mesirov, J.P. (2005). Gene set enrichment analysis: a knowledge-based approach for interpreting genome-wide expression profiles. Proc. Natl. Acad. Sci. USA *102*, 15545–15550.

Topalian, S.L., Hodi, F.S., Brahmer, J.R., Gettinger, S.N., Smith, D.C., McDermott, D.F., Powderly, J.D., Carvajal, R.D., Sosman, J.A., Atkins, M.B., et al. (2012). Safety, activity, and immune correlates of anti-PD-1 antibody in cancer. N. Engl. J. Med. *366*, 2443–2454.

Tran, E., Ahmadzadeh, M., Lu, Y.C., Gros, A., Turcotte, S., Robbins, P.F., Gartner, J.J., Zheng, Z., Li, Y.F., Ray, S., et al. (2015). Immunogenicity of somatic mutations in human gastrointestinal cancers. Science *350*, 1387–1390.

Trapnell, C., Roberts, A., Goff, L., Pertea, G., Kim, D., Kelley, D.R., Pimentel, H., Salzberg, S.L., Rinn, J.L., and Pachter, L. (2012). Differential gene and transcript expression analysis of RNA-seq experiments with TopHat and Cufflinks. Nat. Protoc. *7*, 562–578.

Tumeh, P.C., Harview, C.L., Yearley, J.H., Shintaku, I.P., Taylor, E.J., Robert, L., Chmielowski, B., Spasic, M., Henry, G., Ciobanu, V., et al. (2014). PD-1 blockade induces responses by inhibiting adaptive immune resistance. Nature *515*, 568–571.

Van Allen, E.M., Miao, D., Schilling, B., Shukla, S.A., Blank, C., Zimmer, L., Sucker, A., Hillen, U., Foppen, M.H., Goldinger, S.M., et al. (2015). Genomic correlates of response to CTLA-4 blockade in metastatic melanoma. Science *350*, 207–211.

Voron, T., Marcheteau, E., Pernot, S., Colussi, O., Tartour, E., Taieb, J., and Terme, M. (2014). Control of the immune response by pro-angiogenic factors. Front. Oncol. *4*, 70.

Wherry, E.J. (2011). T cell exhaustion. Nat. Immunol. *12*, 492–499.

Wolchok, J.D., Hoos, A., O'Day, S., Weber, J.S., Hamid, O., Lebbé, C., Maio, M., Binder, M., Bohnsack, O., Nichol, G., et al. (2009). Guidelines for the evaluation of immune therapy activity in solid tumors: immune-related response criteria. Clin. Cancer Res. *15*, 7412–7420.

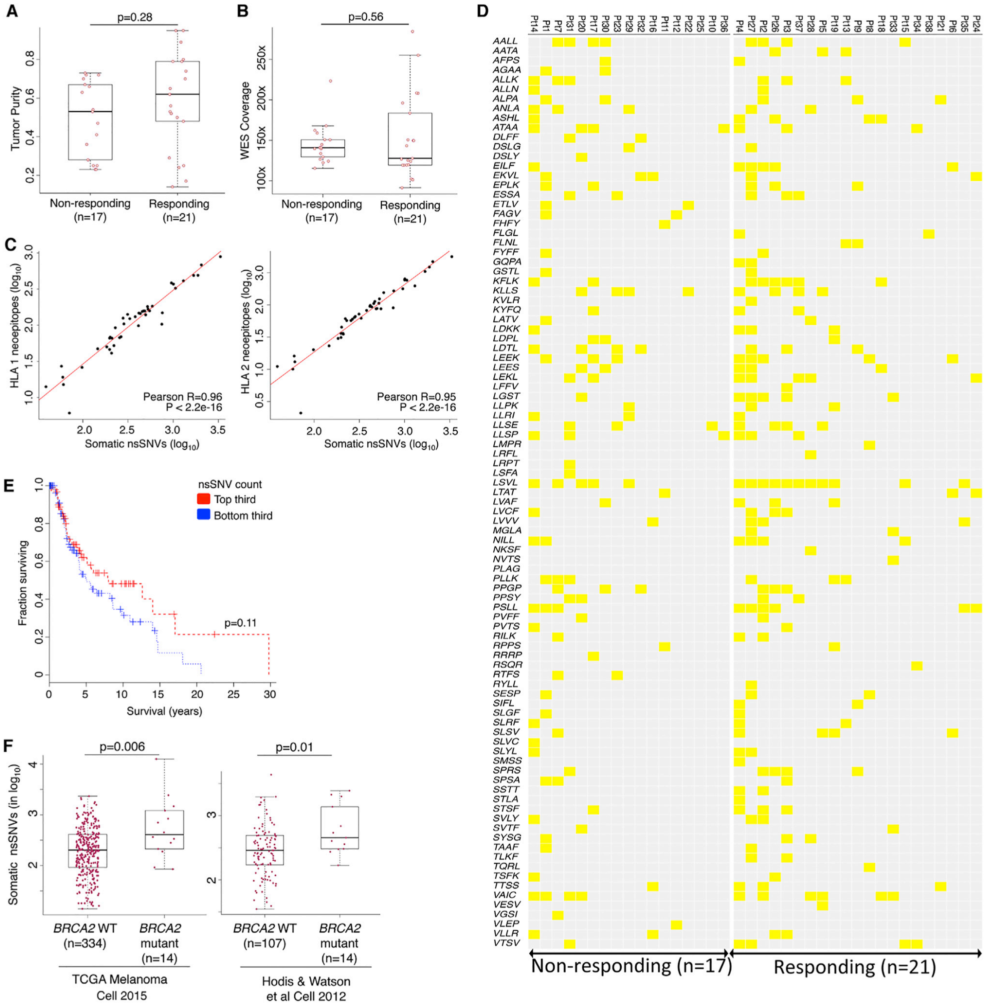

Figure S1. Genomic Features of Melanoma Tumors from Patients Treated with Anti-PD-1 Therapy, Related to Figure 1

(A) The difference of tumor purities between the responding versus non-responding tumors with WES; p value, Mann Whitney test.

(B) The difference of WES coverages between the responding versus non-responding tumors; p value, Mann Whitney test.

(C) Correlations between the number of somatic nsSNVs and the number of predicted HLA class 1 (left) or class 2 (right) neoepitopes. Correlation, Pearson, p values, Student's t test.

(D) Recurrence of tetrapeptides (previously reported as enriched in responding pre-anti-CTLA-4 tumors) in non-responding and responding pre-anti-PD-1 tumors.

(E) Overall survival of TCGA melanoma patients whose tumors harbored high (top third) versus low (bottom third) mutational (somatic nsSNVs) loads; p value, log-rank test.

(F) Mutational loads (somatic nsSNVs) detected in melanoma with or without *BRCA2* somatic nsSNVs in two datasets; p values, Mann Whitney test.

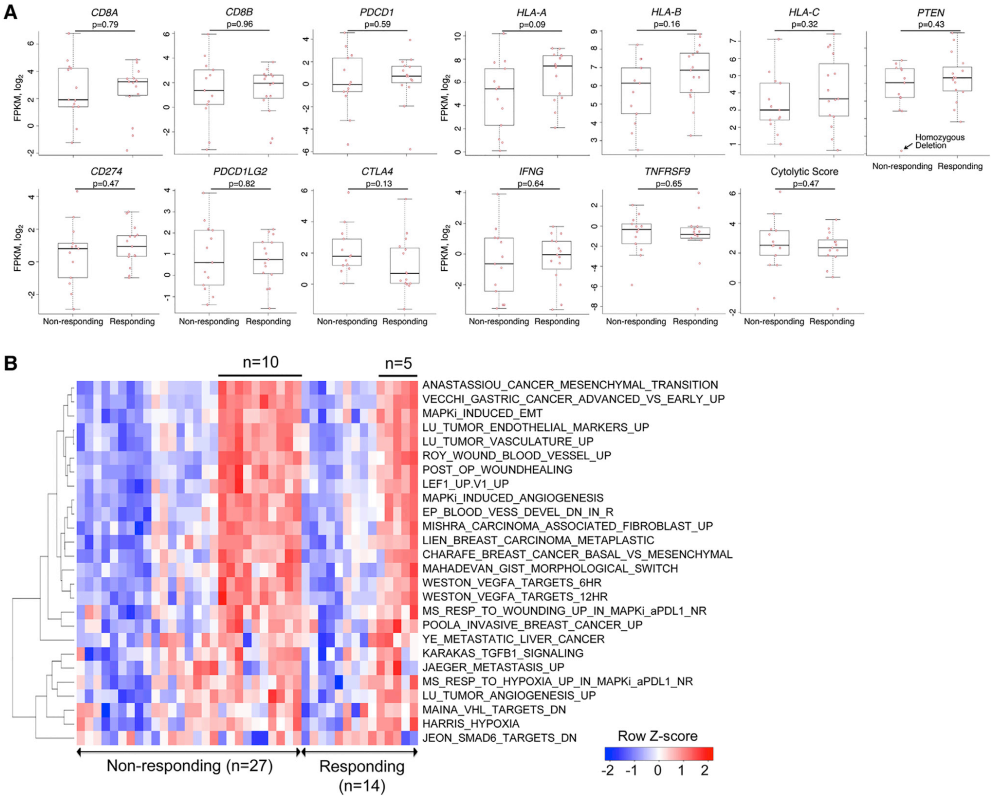

Figure S2. Gene or Signature Expression Patterns in Pretreatment Melanoma Tumors on Anti-PD-1 or Anti-CTLA-4 Therapies, Related to Figure 2

(A) mRNA levels of genes (CD8 T cell markers, effectors, cytolytic scores; immune checkpoints, MHC class 1, and *PTEN*) between the responding versus non-responding pretreatment tumors; p values, Mann Whitney test.

(B) Heatmap showing GSVA scores of IPRES signatures across responding (n = 14) versus non-responding (n = 27) pre-anti-CTLA-4 tumors.

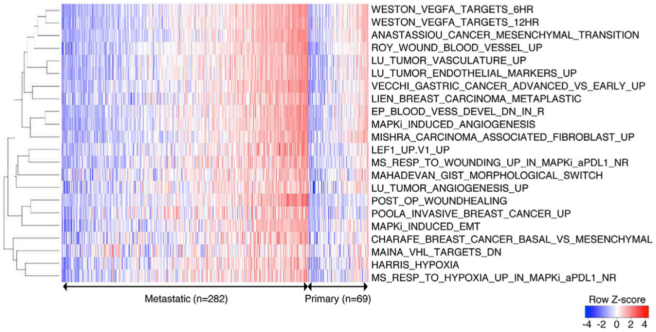

Figure S3. Co-enrichment of IPRES Signatures in Metastatic versus Primary Cutaneous Melanoma, Related to Figure 3
Heatmap showing GSVA scores of IPRES signatures across TCGA primary and metastatic melanoma tumors.

Chapter 6:

Sensitive, non-destructive detection of neoantigen-specific T cell populations from tumors and blood

Sensitive, non-destructive detection and analysis of neoantigen-specific T cell populations from tumors and blood

Songming Peng[a,*], Jesse M. Zaretsky[b,*], Michael T. Bethune[c], Alice Hsu[c], Elizabeth Holman[a], Xiaozhe Ding[a,c], Katherine Guo[a], Jungwoo Kim[a], Alexander M. Xu[a], John E. Heath[a], Won Jun Noh[c], Jing Zhou[a], Yapeng Su[a], Jami McLaughlin[4], Donghui Cheng[d], Owen N. Witte[d,e,f], David Baltimore[c], Antoni Ribas[b], and James R. Heath[a g]

[a]Division of Chemistry and Chemical Engineering, California Institute of Technology, 1200 East California Blvd, Pasadena, CA 91125

[b]Department of Medicine, University of California Los Angeles and Jonsson Comprehensive Cancer Center 10833 Le Conte Avenue, Los Angeles, California 90095, USA

[c]Division of Biology and Biological Engineering, California Institute of Technology, 1200 East California Boulevard, Pasadena, CA 91125, USA

[d]Eli and Edythe Broad Center of Regenerative Medicine and Stem Cell Research, [e]Department of Microbiology, Immunology and Molecular Genetics, and [f]Howard Hughes Medical Institute, University of California, Los Angeles, CA 90095

*These authors contributed equally to this work.

[g]Correspondence to: heath@caltech.edu

Lead Contact: James R. Heath heath@caltech.edu

Summary: Tumor neoantigens are fragments of mutated proteins that contain the mutation, and can be presented by major histocompatibility complex molecules on tumor cells, where they are surveyed by T cells. The rapid and sensitive identification of neoantigen-specific T cell populations from tumor tissues or blood has proven challenging. A microchip platform for the non-destructive identification of neoantigen-specific CD8+ T cells is described. The method utilizes a library of neoantigen/MHC tetramers linked to a magnetic nanoparticle via a DNA barcode. The neoantigen-specificity of the T cells is determined by decoding the barcode through sequential fluorescent microscopy reads. The captured T cells may be further characterized for function, or via matching the neoantigen-specificity with the T cell receptor gene. Tumor infiltrating lymphocytes and non-expanded peripheral blood mononuclear cells collected from melanoma patients at various time points across an anti-PD1 therapy regimen are shown to contain overlapping neoantigen-specific T cell populations.

Keywords: Neoantigens, Cancer Immunotherapy, Nanotechnology, Microfluidics, T cell receptor

Highlights:

A nanotechnology plus microfluidics tool captures neoantigen-specific T cell populations

Neoantigen-specific T cells may be paired with the T cell receptor gene

Neoantigen-specific T cell populations in blood reflect those in the tumor

The kinetics neoantigen-specific T cell populations may reflect therapy response

Introduction:

Tumor neoantigens have been implicated as playing important roles in the recognition of cancer cells by the immune system (McGranahan et al., 2016; Schumacher and Schreiber, 2015) and are candidate targets for personalized cancer vaccines.(Carreno et al., 2015; Gubin et al., 2014) Neoantigens (also called neoepitopes) are fragments of mutated proteins that contain the mutation, and can be presented in the cleft of Major Histocompatibility Complex (MHC) Class I molecules on the surfaces of cells within the tumor, where they are surveyed by CD8+ T cells. The tumor-specificity of neoantigens, coupled with the ability of neoantigen-specific T cells to specifically kill cancer cells(Lu et al., 2014; Robbins et al., 2013), have made them increasingly important for cancer immunotherapy. Furthermore, T cell receptors (TCRs) that recognize specific neoantigens are candidates for TCR-engineered cell based therapies.(Stroncek et al., 2012)

Putative neoantigens can be identified by tumor exome analysis,(Lu et al., 2014; Robbins et al., 2013; Rooij et al., 2013; Yadav et al., 2014) and then rank-ordered according to MHC binding strength(Fritsch et al., 2014; Nielsen et al., 2007), as well as filtered by accounting for gene expression. However, finding which candidates actively promote T cell tumor recognition is challenging on several fronts. First, a patient tumor that has a mutation density of 10 per 1 million expressed DNA base pairs might have more than 100 putative neoantigens that exhibit a calculated binding constant (k_d) to a given HLA genotype MHC of 500 nM or stronger. Further, any particular neoantigen-specific T cell population is likely to exist in low abundance. Additional challenges are associated with pairing neoantigens to their cognate TCRs. Nevertheless, such interactions are the core of cancer immunotherapy,(Coulie et al., 2014) and so there has been significant effort towards meeting these challenges. One approach involves expressing the nucleotide sequences of the putative neoantigens within antigen-presenting target cells that are HLA-genotype matched with the patient, and then incubating those cells with tumor infiltrating lymphocytes (TILs) or T cells from peripheral blood mononuclear cells (PBMCs) to identify populations of T cells that are reactive against those neoantigens.(Linnemann et al., 2015; Robbins et al., 2013) This approach, while laborious, can identify the presence of neoantigen-specific T cell populations, but does not provide a quantitative enumeration of those populations. A second approach, reported by the Schumacher group, involves the use of MHC tetramers, each labeled with multiple fluorophores to enable colorimetric multiplexing in a flow cytometry-based detection scheme.(Andersen et al., 2012) This technique has been used for the analysis of T cell populations from *in vitro* expanded TILs and PBMCs.(Rizvi et al., 2015) A related mass cytometry variant, which uses mass labels in place of the fluorophores has also been reported,(Newell et al., 2013), as has a DNA-labeled tetramer approach the combines flow cytometry with PCR amplification of the labels.(Bentzen et al., 2016) As discussed below, these flow cytometry methods have limitations when used to quantitate small populations of antigen-specific T cells from small biospecimens. This can be partially addressed by in vitro expansion of the T cells, but such expansion can significantly alter T cell population profiles. Further, expansion significantly extends the time required for the analysis. For a tumor with a high mutational burden, these methods typically identify a few neoantigen-specific CD8+ T cell populations for a given HLA genotype.(McGranahan et al., 2016)

A further measurement challenge is to match the neoantigen-specificity of a T cell with the TCR genes. The TCR protein is a heterodimer composed of a variable α chain and a variable β chain, with the matched α/β chains defining the T cell antigen specificity. The (single cell) pairSEQ technique recently reported by Robins' group(Howie et al., 2015) provides an elegant approach for assembling the full TCR gene sequence from separate measurements of α and β chains from a population of T cells. However, this method does not establish the antigen specificity of that gene, and is likely challenging to employ when analyzing small populations of T cells with a variety of antigen specificities. In general, the dual challenge of identifying neoantigen-specific T cells and matching them with their cognate TCR genes increases in difficulty as abundance of the individual T cell populations drops.

Here, we report a method, which we call barcoded nanoparticle-nucleic acid cell sorting (barcoded NP-NACS), for the highly sensitive enumeration of neoantigen-specific T cell populations from TILs or non-expanded PBMCs collected from cancer patients. Once paired with a neoantigen, the T cells may be further analyzed at the functional or genetic level.

Results

Capture of antigen-specific T cells using magnetic nanoparticles surface-coated with antigen/MHC tetramers MHC tetramers coupled onto magnetic nanoparticle (NP) surfaces provide an excellent platform for sorting antigen-specific T cells, since the high loading of tetramers achievable on individual NPs builds upon the cooperative binding advantage that the tetramer scaffold itself provides. We tested this hypothesis by analyzing a sample of Jurkat T lymphocyte cells that were spiked with between 1 and 1000 NY-ESO TCR-specific Jurkats, within a constant cell count of 10,000. The NY-ESO antigen is a cancer testis antigen that has been targeted in various adoptive cell therapy trials (Rapoport et al., 2015; Robbins et al., 2011). We compared the sensitivity of magnetic capture of the NP-tetramer labeled cells to what could be achieved using the multi-color flow cytometry staining scheme (Andersen et al., 2012) (Figure 1 A,B). This assay was also used to optimize the size of the NP. Smaller NPs, such as those below radius (r)=50 nm, require strong magnetic fields for cell enrichment. To achieve such fields, columns filled with steel beads are utilized to increase the magnetic field gradient to maximize separation efficiency. We found that such columns greatly reduced cell recovery when handling small (10^4) cell numbers. On the other hand, particles of r>1 micrometer tend to precipitate from solution due to gravity, and so are difficult to handle. NPs of r = 500 nm avoided both of these issues and so were selected. Each 500 nm NP presents 10^5 sites or more (see STAR Methods) for attaching the antigen-MHC tetramer.

The antigen-MHC constructs used for FC analysis and magnetic capture were identical (Fig 1A, B). In both cases, they were assembled onto a streptavidin scaffold to form a tetramer. For flow cytometry analysis, the streptavidin was dye labeled with one of two fluorophores, following literature protocols(Andersen et al., 2012). For magnetic capture, the tetramer scaffold utilized cysteine-modified streptavidin(SAC) (Ramachandiran et al., 2007) to facilitate site-specific incorporation of ssDNA linkers (Kwong et al., 2009) for connecting to the NP via DNA hybridization (see STAR Methods).

Flow cytometry analysis of the spiked samples was done using both tight (conservative) and loose gating schemes. (see STAR Methods and Supplementary Figure S1.A). NY-ESO TCR specific Jurkat cells were identified as those cells that stained positive for both dyes. For the NP-tetramer detection, we used a Calcein AM fluorescent live cell stain so that when the captured cells were viewed on a hemocytometry chip, they could be counted using fluorescence microscopy (Fig S1.B). Both flow cytometry gating schemes, as well as the NP-tetramer capture, yielded excellent linear performance for detecting the NY-ESO TCR-specific Jurkat cells over the full spiked range of 10^3 (Figure S1.C). For the flow cytometry method, when a loose gate was utilized to achieve maximum sensitivity for double-fluorescent positive NY-ESO Jurkat cells, some false-positives were counted. Thus, the numbers of cells detected was slightly above (103%) what was spiked. On the other hand, when a tight gate was utilized to minimize false positives, sensitivity for double-fluorescent positive NY-ESO Jurkat cells was sacrificed (Fig. S1. A), and 64% of the spiked cells were detected. A key finding was that over the extreme dilution range of 0-10 spiked cells, the NP-tetramer method yielded quantitatively superior performance (Figure 1C) to either of the FC gating schemes. The sensitivity of the flow cytometry was consistent with expectations from literature(Bentzen et al., 2016). This data illustrates that 500 nm radius magnetic NPs, surface coated with antigen/MHC Class I tetramers, provide a highly sensitive method for the capture of antigen-specific CD8+ T cells that outperforms the gold standard FC method for very low abundance cells from small samples sizes (10^4 cells).

The barcoded NP-NACS library method for analysis of neoantigen-specific T cells

We modified the NP-tetramer capture approach to permit the parallel capture of multiple populations of antigen-specific CD8+ T cells collected from patient materials. To this end, we altered the process flow of Figure 1B in three ways, as illustrated in Figures 2A, B. First, we utilized the well-established method of conditional antigen exchange (Bakker et al., 2008; Celie et al., 2009) to enable the rapid construction of a library of antigen-MHC tetramers (see STAR Methods). Second, we expanded the DNA linker that connects the antigen/MHC complex to the magnetic NP to incorporate an ssDNA barcode. Third, we developed a microfluidic platform for isolating those individual T cells that are magnetically captured, so as to permit a fluorescence microscopy-based decoding of each barcoded T cell. The chemical process associated with barcode readout is demonstrated in supplementary figure S2. We used an ssDNA barcode designed with 3 positions, each of which have 3 possible sequences. For each position, the specific sequence is read using ssDNA oligomers labeled with one of 3 fluorophores. Only one of those oligomers will hybridize. For a full list of the ssDNA reagents and their corresponding barcode usage, refer to supplementary tables S1 and S2, respectively. Thus, the labeled cell will fluoresce red, green or yellow, depending upon the sequence at that position. Once a position is read, the fluorescent ssDNA oligomer is removed using a displacement ssDNA oligomer, and the next position is read. In this way, an n-color, m-position barcoded yields n^m multiplexing capability. Figure 2C, as an example, lists the barcodes assigned to 26 neoantigens plus the MART-1 melanosomal antigen for patient #1. This decoding process is efficient (Supplementary figure S2), but requires that the captured cells be held in place as various solutions are introduced, flushed, etc. Because virtually all reagents used here will stick to dead cells, the cells must also remain viable throughout the capture and barcode readout process. We constructed an elastomer-based microfluidic chip designed with a series of microchambers, each of which contained 10 separate single cell traps (Fig 2B, Supplementary figure S3). Once a T cell is labeled with tetramer/DNA/NP constructs, the T cell is considered barcoded. We named the full approach of antigen-specific T cell labeling, capture and readout as barcoded nanoparticle nucleic acid cell sorting, or barcoded-NP NACS.

Analysis of tumor infiltrating lymphocytes from melanoma cancer patient biopsies

We used the above methods to analyze human CD8+ cells expanded from tumor infiltrating lymphocytes (TILs) collected from tumor biopsies of three patients with metastatic melanoma who were being treated with checkpoint inhibitor therapy at the time of biopsy (Supplementary Patient Information). These patients were treated with the anti-PD-1 antibody pembrolizumab within a phase I trial.(Ribas et al., 2016) Therapy responses were mediated by tumor infiltrating CD8+ cells.(Tumeh et al., 2014) The response of patient #1 to the therapy is illustrated in the images of Figure 3A, and in the timeline of Figure 3B. The points at which various biospecimens were collected from patient #1 are also indicated in Fig 3B. For all 3 patients, a pre-treatment biopsy was analyzed for both the tumor exome and gene expression (see STAR Methods). *In silico* analysis was carried out to prepare rank-ordered lists of putative neoantigens for HLA-A*0201, with respect to MHC binding affinity (see STAR Methods, and Supplementary Tables S3-S8). Those lists were unique for each patient and informed the construction of the barcoded NP-NACS libraries. For patient #1 the tightest binding 50 putative neoantigens plus the MART-1 melanoma antigen were tested. The list of Fig 2C includes the top 26 neoantigens from those 50. For neoantigen numbers 3, 5, 11, 26, 31, 34, 36, 37, 46 and 48, the corresponding transcripts for those proteins yielded zero mutation reads (Supplementary Table S6). Thus, these non-expressed neoantigens provided controls that spanned the sampled range of neoantigen/MHC binding affinities.

The barcoded NP-NACS library elements were combined and used to capture 4.5-5% of the CD8+ TILs. We also recorded a 0.5% non-selective capture, based upon testing the library against CD4+ T cells from the same TILs sample (Supplementary Fig. S4). Two separate runs on different vials of expanded patient #1 TILs, were similarly analyzed and yielded the same seven neoantigen-specific T cell populations (plus MART-1 specific cells, which provided a positive control) (Supplementary Fig. S5). All but very low-abundance populations (1 or 2 incidents per analysis) were detected in both assays. The most abundant population (1.2% of CD8+ cells) was specific for neoantigen #12. We further analyzed patient #1 TILS for specificities against neoantigens ranked 28-50 (k_d values up to 500 nM). Two additional populations were detected (#'s 38 and 45). Figure 2B provides some of the single cell fluorescent readouts that were used to assign populations. Some traps will capture 2 cells (see Fig 2B trap #4). Microscopic inspection will typically permit at least one of those cells to be distinguished for barcoding. Typically, we either get a high fidelity read or a nonsense read which we discard (see trap #8 in Fig 2B). This lends a very low noise level to the approach. We defined detected neoantigen-specific T cell populations as those identified by 3 or more unambiguous reads, or detected in both analyses of patient #1 TILs. The summed analysis of patient #1 TILs is provided in Fig. 3C (top histogram).

For comparison, some biospecimens were analyzed using the serial hemocytometry approach of Figure 1B. Like barcoded NP-NACS, this approach is also highly efficient in the use of available cells. Neoantigen-specific T cells are precipitated from a population of, for example, 10,000 CD8+ T cells, but that same population is then re-interrogated using the next NP-NACS library element. The method is particularly useful for analysis of non-expanded PBMCs, where neoantigen-specific T cell populations are particularly rare (see below). In such cases, it can be challenging to remove all of the unbound magnetic NPs while not also losing some of the barcoded cells. This removal is necessary for the fluorescent readout, since unbound NPs will interfere with the barcoded NP-NACs process. However, such unbound particles do not interfere with the hemocytometry approach (supplementary Fig S1.B). To characterize the non-specific pulldown rate of this approach, we used the barcoded NP-NACS library designed for patient #1 to analyze expanded TILs from an unrelated patient with metastatic melanoma on the same clinical trial, as well as PBMCs from a healthy volunteer. The list of neoantigens should be unique to patient #1 and so should not capture T cell populations from the control patient samples. The results for both controls were similar. The patient #1 neo-antigen library captured on average 2 cells per library element from a total of 10,000 CD8+ T cells, with a standard deviation of 1.4 (Supplementary Fig. S6). Thus, for the hemocytometry approach, we set a noise level of 5 cells (2 standard deviations above the mean). For either control sample, no library element captured more than 5 cells, and there was no correlation between the controls (Supplementary Fig. S6), indicating that no patient #1 library elements are of intrinsically low-selectivity. Using the barcoded NP-NACS library for patient #2, serial analysis of that patient's TILs yielded a similar number of neoantigen-specific T cell populations as were found for patient #1. (Supplementary Fig. S7).

The above TILs analyses revealed a larger number of neoantigen-specific T cell populations than have been reported using multiplex flow cytometry analysis.*(1-4)* We thus analyzed the expanded patient #1 TILs using the multiplex flow method.(Andersen et al., 2012) For that analysis, we prepared a 14-element tetramer library presenting putative neoantigens 1-8, 12, 14, 15, 19, 27 and MART-1 (8 of which were detected using barcoded NP-NACS) (see STAR Methods). When using loose gate to obtain maximum sensitivity, 7 different neo-antigens were detected. This is significantly higher than what was found from a control flow cytometry analysis of CD8+ T cells from a healthy donor (Supplementary Fig. S8-S9). However, if a tight gate is utilized, only T cells specific to neoantigen #12 were detected in two and only two colors (Supplementary Fig. S8). The abundance of neoantigen #12 specific T cells detected by flow cytometry vs barcoded NP-NACS, was different (4% versus 1.2%). This likely arises from the subset of CD8+ T cells analyzed by the two methods (see STAR Methods and Supplementary Fig S10). In particular, all neoantigen #12-specific T cells identified using flow cytometry were from the subset of those cells that were CD8++. For the vial that was expanded for flow cytometry analysis, this CD8++ population was 20% of the live, CD3+ cells. In the vial expanded for barcoded NP-NACS analysis, the corresponding percentage was 8%. These results indicate that the sensitivity of the barcoded NP-NACS method, coupled with the selective identification of individual cells through the barcoding process, allows the detection of neoantigen-specific CD8+ T cell populations that are not detected using flow cytometry.

Barcoded NP-NACS for the analysis of non-expanded PBMCs

The sensitivity of the barcoded NP-NACS method prompted us to analyze peripheral blood from patient #1 and patient #3 (Fig. 3 and Supplementary Figs. S11-S13). We did not expand these T cells *in vitro*, so as to avoid any accompanying population bias. We used the 49-element neoantigen library to interrogate patient #1 PBMCs collected at four time points. Two time points (Days 187 and 208, Fig 3A) were collected during therapy response while tumors were shrinking, and corresponded closely to the date of the tumor biopsy (Day 187) from which the TILs were collected. For those samples, the total abundance of detected neoantigen-specific T cell levels was well below those found in the TILs (1% of all CD8+ PBMCs vs 7% of all CD8+ TILs), but we positively detected several populations at levels of >5 cells per 10^4 CD8+ PBMCs. Most PBMC populations coincided with those detected from the TILs, with two new populations (specific to neoantigens #15 and #33) identified. Analysis of PBMCs at Day 439, at the end of tumor regression, detected no such populations (Supplementary Fig. S11). This last point emphasizes the selectivity of the method, and again indicates that none of the library elements were intrinsically low selectivity.

Day 41 PBMCs correspond to a time close to the biopsy from which the exome and transcriptome measurements were taken, but also during a period of pseudo-progression for patient #1 prior to response (Fig 3A). Analyzing PBMCs at this time point was pure discovery science, as we could not formulate a hypothesis for whether or not neoantigen-specific CD8+ T cell populations would be detected. In fact, we identified 2-fold higher numbers of neoantigen-specific T cells relative to later time points when the tumors were regressing. Similar populations were detected at Days 187 and 208, and provided a subset of those detected at Day 41.

Several of the detected T cell populations from patient #1 PBMCs correspond to relatively weak (k_d > 50 nM) neoantigen/MHC binding affinities. The corresponding mutation-containing reads from the pre-treatment transcriptome analysis are provided in the bottom graph of Fig 3C. There is a striking correspondence between the appearance of T cell populations specific to weaker binding neoantigens, and the expression levels of the corresponding mutated proteins. For example, 8 of the top 12 neoantigens, as ranked by mRNA expression level, were detected (Supplementary Table S6). Further, for the 10 neoantigens in the panel for which corresponding mRNA levels were measured to be zero, only the strong binding neoantigen #5 was associated with any detected populations (TILs and Day 41 PBMCs).

For patient #3, we used a 34-element neoantigen-MHC tetramer library (Supplemental Table S5) to analyze expanded TILs and non-expanded PBMCs. A baseline noise level was established by testing this library against a different patient's PBMCs (Supplementary Fig S12). Unlike patients #1 and #2, the patient #3 TILs were from a biopsy collected 29 days prior to start of therapy (Supplementary Fig. S13A). Patient #3 also had a very different response profile to anti-PD1 therapy. CD8+ cells from the TILs expanded very slowly compared to CD4+ TILs, so only 5000 cells were used for each analysis. Only two neoantigen-specific CD8+ TIL populations were detected (#13 and #20) (Supplementary Fig. S13B). However, the most dominant population (#13) was also observed in PBMCs during therapy response. Four additional neo-antigen populations were detected from PBMCs during early treatment when tumors were rapidly shrinking (Day 25), while only #13 and #14 were detected at a time point (Day 87) close to maximum therapeutic response (Supplementary Fig S13B). All neoantigen-MHC library elements tested for patient #3 were calculated to exhibit strong binding (k_d<50 nM). Similar to the case for patient #1, the correspondence between mutant mRNA reads and the detected T cell populations specific to these strong binding neoantigen-MHCs is weak (Supplementary Fig S13B).

Functional and Genetic Analysis of Identified Neoantigen-specific CD8+ T cell Populations

Exposure of antigen-specific CD8+ T cells to their cognate antigen/MHC complex should lead to T cell activation, and so an assay that probes for such activation can provide an independent validation of the population analysis methods reported here. To this end, we used ELISpot single cell assays of interferon-γ release, to confirm that the neoantigen-specific CD8+ populations from patient #1, day 41 PBMC were functionally activated following exposure to antigen (Fig 3D, Supplementary Table S9). This assay provides a confirmation that the barcoded NP-NACS method is, in fact, working as described.

Barcoded T cells are still viable, and so we took advantage of this and designed a cell capture microchip with a low-density of cell traps (Supplementary Figure S14). This design permits a single barcoded cell to be decoded using fluorescence imaging, and then punched from the device for single cell sequencing of the α and β chains of the TCR (Fig 4). A CD8+ T cell from patient #1 was captured in a microfluidic trap (Supplementary Fig. S14) and barcoded to identify the neo-antigen identity (Fig. 4A). RT-PCR was used on the retrieved cell to obtain the TCR α and β gene sequences, which were then cloned into a retroviral vector. Jurkat cells transduced to express that TCR were found to bind to the cognate neoantigen tetramer (Fig. 4B).

Discussion

The rarity of individual populations of neoantigen-specific T cells in often-precious patient tumor tissues or blood can make them extremely challenging to detect and validate. Nevertheless, an in-depth knowledge of those populations can provide guidance for various vaccination (Gubin et al., 2014) or cell based cancer immunotherapies(Tran et al., 2016). The serial (NP-NACS) method, which relies on the use of MHC tetramers attached to 500 nanometer radius magnetic NPs, is simple to implement, and yet significantly outperforms state-of-the-art multicolor flow cytometry for the detection of low-abundance (<10) cells in small (10^4 cells) sample sizes. The barcoded NP-NACS parallel analysis method is an extension of the technique that features two additional advantages. First, the method permits a library of putative neoantigens to be tested simultaneously. Second, it offers the advantage that the barcode is decoded via imaging individual cells. This microscopic analysis adds additional fidelity to the identification process, so that that false positive reads may be ruled out. Third, it allows for the direct recovery of viable individual cells, for either functional analysis or sequencing for the identification of antigen/TCR pairs.

Analysis of tumors of three patients responding to anti-PD1 therapy reveals that 5-25% of the top predicted neoantigens for HLA A*0201 can be paired with T cell populations. With peptide/MHC binding strength cutoffs of 5×10^{-7} M and 5×10^{-8} M, we still accounted for 7% and 5% of the CD8+ TILs for patient #1 and #2, respectively. It is likely that including weaker binding neoantigens would yield additional T cell populations. Both those patients express 5 additional HLA genotypes (Supplementary Patient Information). Although the actual representation of those genotypes needs to be tested, the implication is that 30-50% of the CD8+ TILs within these patient tumors may well be neoantigen-specific. This number is significantly larger than would have been inferred using alternative analytic methods, but is consistent with a prior result in mice (Gubin et al., 2014). Further, the neoantigen-specific T cell population numbers detected here are consistent with immune responses to tumor antigens that have been observed in healthy donors(Stronen et al., 2016). In that work, PBMCs from the healthy donor were expanded in the presence of a library of neoantigens, so as to amplify those extremely rare populations that exhibit specificity against library elements. The direct detection of such populations in non-expanded PBMCs, as reported here, emphatically highlights the importance of neoantigen-specific T cell populations as major effectors in anti-PD-1 cancer immunotherapy. A second observation is that the measured spectrum of neoantigen-specific T cell populations only correlates loosely with the predicted rank-order of putative neoantigens. However, an additional correlation with mRNA expression levels was found, especially for weaker binding neoantigens. This is consistent with recent work on antigen profiling(Abelin et al., 2017). These data should facilitate refining such prediction algorithms. A third observation is that the same neoantigen-specific populations detected in the tumor are also detected in the blood, albeit at a lower relative abundance to all CD8+ PBMCs. In the analysis for patient #1, those populations are detected a full 2 months prior to traditional clinical measures (via radiographic computed tomography (CT) imaging) of actual tumor shrinkage. Finally, the patients analyzed here had highly mutated tumors which responded to immunotherapy. The sensitivity of the barcoded NP- NACS method may permit the detection of neoantigen-specific T cell populations in low mutation burden tumors where immunotherapy has had less success. In high mutation burden tumors, this method should allow the detection of lower affinity antigens that may have significant value as truncal mutations. In either case, there may be clinical benefits to this approach, as it can rapidly define personalized neoantigen-specific T cell based therapies or personalized neoantigen-derived vaccines.

Author contributions: SP, JMZ, MTB, ONW, DB, AR and JRH designed the experiments. Patient samples were from trials that were run by AR. SP, JMZ, MTB, AH, EH, XD, KG, JK, AMX, JEH, WJN, JZ, YS, JM, and DC did the experiments. SP, JMZ, MTB, AR, and JRH wrote the paper.

Acknowledgments: We acknowledge the following agencies and foundations for support: The Stand Up to Cancer Foundation and the Cancer Research Institute (A.R. and J.R.H.), the National Cancer Institute (1U54 CA199090 and R01-CA170689 to J.R.H. and A.R., R35 CA197633 to A.R.), the Jean Perkins Foundation (J.R.H. PI), the Prostate Cancer Foundation (15CHAL02 to D.B., O.N.W., and M.T.B.), and Caltech internal support through a CI2 grant. E. H. acknowledges a National Science Foundation Graduate Research Fellowship. A.M.X. acknowledges the NIH for a fellowship (1F32CA213966). M.T.B is the recipient of a Jane Coffin Childs Postdoctoral Fellowship. O.N.W. is supported by the Eli and Edythe Broad Center of Regenerative Medicine and Stem Cell Research.

References

Abelin, J.G., Keskin, D.B., Sarkizova, S., Hartigan, C.R., Zhang, W., Sidney, J., Stevens, J., Lane, W., Zhang, G.L., Eisenhaure, T.M.*, et al.* (2017). Mass Spectrometry Profiling of HLA-Associated Peptidomes in Mono-allelic Cells Enables More Accurate Epitope Prediction. Immunity *46*, 315-326.

Andersen, R.S., Kvistborg, P., Frosig, T.M., Pedersen, N.W., Lyngaa, R., Bakker, A.H., Shu, C.J., Straten, P.t., Schumacher, T.N., and Hadrup, S.R. (2012). Parallel detection of antigen-specific T cell responses by combinatorial encoding of MHC multimers. Nat Protocols *7*, 891-902.

Bakker, A.H., Hoppes, R., Linnemann, C., Toebes, M., Rodenko, B., Berkers, C.R., Hadrup, S.R., van Esch, W.J., Heemskerk, M.H., Ovaa, H.*, et al.* (2008). Conditional MHC class I ligands and peptide exchange technology for the human MHC gene products HLA-A1, -A3, -A11, and -B7. Proc Nat Acad Sci *105*, 3825-3830.

Bentzen, A.K., Marquard, A.M., Lyngaa, R., Saini, S.K., Ramskov, S., Donia, M., Such, L., Furness, A.J.S., McGranahan, N., Rosenthal, R.*, et al.* (2016). Large-scale detection of antigen-specific T cells using peptide-MHC-I multimers labeled with DNA barcodes. Nat Biotech *34*, 1037-1045.

Carreno, B.M., Magrini, V., Becker-Hapak, M., Kaabinejadian, S., Hundal, J., Petti, A.A., Ly, A., Lie, W.R., Hildebrand, W.H., Mardis, E.R.*, et al.* (2015). A dendritic cell vaccine increases the breadth and diversity of melanoma neoantigen-specific T cells. Science *348*, 803-808.

Celie, P.H., Toebes, M., Rodenko, B., Ovaa, H., Perrakis, A., and Schumacher, T.N. (2009). UV-induced ligand exchange in MHC class I protein crystals. Journal of the American Chemical Society *131*, 12298.

Coulie, P.G., Van den Eynde, B.J., van der Bruggen, P., and Boon, T. (2014). Tumour antigens recognized by T lymphocytes: at the core of cancer immunotherapy. Nat Rev Cancer *14*, 135-146.

Fritsch, E.F., Rajasagi, M., Ott, P.A., Brusic, V., Hacohen, N., and Wu, C.J. (2014). HLA-Binding Properties of Tumor Neoepitopes in Humans. Cancer Immunology Research *2*, 522-529.

Gubin, M.M., Zhang, X., Schuster, H., Caron, E., Ward, J.P., Noguchi, T., Ivanova, Y., Hundal, J., Arthur, C.D., Krebber, W.-J.*, et al.* (2014). Checkpoint blockade cancer immunotherapy targets tumour-specific mutant antigens. Nature *515*, 577-581.

Howie, B., Sherwood, A.M., Berkebile, A.D., Berka, J., Emerson, R.O., Williamson, D.W., Kirsch, I., Vignali, M., Rieder, M.J., Carlson, C.S.*, et al.* (2015). High-throughput pairing of T cell receptor α and β sequences. Science Translational Medicine *7*, 301ra131-301ra131.

Kwong, G.A., Radu, C.G., Hwang, K., Shu, C.J., Koya, R., Comin-Anduix, B., Hadrup, S.R., Witte, O.N., Schumacher, T.N., Ribas, A.*, et al.* (2009). Modular Nucleic Acid Assembled p/MHC microarrays for Multiplexed Sorting of Antigen-Specific Lymphophocytes. Journal of the American Chemical Society *131*, 9695-9703.

Linnemann, C., van Buuren, M.M., Bies, L., Verdegaal, E.M.E., Schotte, R., Calis, J.J.A., Behjati, S., Velds, A., Hilkmann, H., Atmioui, D.e.*, et al.* (2015). High-throughput epitope discovery reveals frequent recognition of neo-antigens by CD4+ T cells in human melanoma. Nat Med *21*, 81-85.

Lu, Y.-C., Yao, X., Crystal, J.S., Li, Y.F., El-Gamil, M., Gross, C., Davis, L., Dudley, M.E., Yang, J.C., Samuels, Y.*, et al.* (2014). Efficient Identification of Mutated Cancer Antigens Recognized by T Cells Associated with Durable Tumor Regressions. Clinical Cancer Research *20*, 3401-3410.

McGranahan, N., Furness, A.J.S., Rosenthal, R., Ramskov, S., Lyngaa, R., Saini, S.K., Jamal-Hanjani, M., Wilson, G.A., Birkbak, N.J., Hiley, C.T.*, et al.* (2016). Clonal neoantigens elicit T cell immunoreactivity and sensitivity to immune checkpoint blockade. Science.

Newell, E.W., Sigal, N., Nair, N., Kidd, B.A., Greenberg, H.B., and Davis, M.M. (2013). Combinatorial tetramer staining and mass cytometry analysis facilitate T-cell epitope mapping and characterization. Nat Biotech *31*, 623-629.

Nielsen, M., Lundegaard, C., Blicher, T., Lamberth, K., Harndahl, M., Justesen, S., Røder, G., Peters, B., Sette, A., Lund, O.*, et al.* (2007). *NetMHCpan*, a Method for Quantitative Predictions of Peptide Binding to Any HLA-A and -B Locus Protein of Known Sequence. PLoS ONE *2*, e796.

Ramachandiran, V., Grigoriev, V., Lan, L., Ravkov, E., Mertens, S.A., and Altman, J.D. (2007). A Robust Method for Production of MHC Tetramers with Small Molecule Fluorophores. Journal of Immunological Methods *319*, 13-20.

Rapoport, A.P., Stadtmauer, E.A., Binder-Scholl, G.K., Goloubeva, O., Vogl, D.T., Lacey, S.F., Badros, A.Z., Garfall, A., Weiss, B., Finklestein, J.*, et al.* (2015). NY-ESO-1-specific TCR-engineered T cells mediate sustained antigen-specific antitumor effects in myeloma. Nat Med *21*, 914-921.

Ribas, A., Hamid, O., Daud, A., and et al. (2016). ASsociation of pembrolizumab with tumor response and survival among patients with advanced melanoma. JAMA *315*, 1600-1609.

Rizvi, N.A., Hellmann, M.D., Snyder, A., Kvistborg, P., Makarov, V., Havel, J.J., Lee, W., Yuan, J.D., Wong, P., Ho, T.S.*, et al.* (2015). Mutational landscape determines sensitivity to PD-1 blockade in non-small cell lung cancer. Science *348*, 124-128.

Robbins, P.F., Lu, Y.-C., El-Gamil, M., Li, Y.F., Gross, C., Gartner, J., Lin, J.C., Teer, J.K., Cliften, P., Tycksen, E.*, et al.* (2013). Mining exomic sequencing data to identify mutated antigens recognized by adoptively transferred tumor-reactive T cells. Nature Medicine *19*, 747-752.

Robbins, P.F., Morgan, R.A., Feldman, S.A., Yang, J.C., Sherry, R.M., Dudley, M.E., Wunderlich, J.R., Nahvi, A.V., Helman, L.J., Mackall, C.L.*, et al.* (2011). Tumor regression in patients with metastatic synovial cell sarcoma and melanoma using genetically engineered lymphocytes reactive with NY-ESO-1. Journal of Clinical Oncology *29*, 917-924.

Rooij, N.v., Van Buuren, M.M., Philips, D., Velds, A., Toebes, M., Heemskerk, B., van Dijk, L.J.A., Behjati, S., Hilkmann, H., el Atmioui, D.*, et al.* (2013). Tumor Exome Analysis Reveals Neoantigen-Specific T-Cell Reactivity in an Ipilimumab-Responsive Melanoma. Journal of Clinical Oncology *31*, doi: 10.1200/JCO.2012.1247.7521.

Schumacher, T.N., and Schreiber, R.D. (2015). Neoantigens in cancer immunotherapy. Science *348*, 69-74.

Stroncek, D.F., Berger, C., Cheever, M.A., Childs, R.W., Dudley, M.E., Flynn, P., Gattinoni, L., Heath, J.R., Kalos, M., Marincola, F.M.*, et al.* (2012). New directions in cellular therapy of cancer: a summary of the summit on cellular therapy for cancer. Journal of Translational Medicine *10*, 48-52.

Stronen, E., Toebes, M., Kelderman, S., Van Buuren, M.M., Yang, W., Van Rooij, N., Donia, M., Boschen, M.-L., Lund-Johansen, F., Olweus, J.*, et al.* (2016). Targeting of cancer neoantigens with donor-derived T cell receptor repertoires. Science *352*, 1337-1341.

Tran, E., Robbins, P.F., Lu, Y.-C., Prickett, T.D., Gartner, J.J., Jia, L., Pasetto, A., Zheng, Z., Ray, S., Groh, E.M.*, et al.* (2016). T-Cell Transfer Therapy Targeting Mutant KRAS in Cancer. New England Journal of Medicine *375*, 2255-2262.

Tumeh, P.C., Harview, C.L., Yearley, J.H., Shintaku, I.P., Taylor, E.J.M., Robert, L., Chmielowski, B., Spasic, M., Henry, G., Ciobanu, V.*, et al.* (2014). PD-1 blockade induces responses by inhibiting adaptive immune resistance. Nature *515*, 568-571.

Yadav, M., Jhunjhunwala, S., Phung, Q.T., Lupardus, P., Tanguay, J., Bumbaca, S., Franci, C., Cheung, T.K., Fritsche, J., Weinschenk, T.*, et al.* (2014). Predicting immunogenic tumour mutations by combining mass spectrometry and exome sequencing. Nature *515*, 572-576.

Figure Captions

Figure 1. Sensitivity comparison of multi-color flow cytometry (FC) and tetramer-functionalized magnetic nanoparticle (NP) cell capture for NY-ESO TCR specific Jurkat T lymphocytes spiked into Jurkat cells. A. Preparation of MHC-antigen tetramer FC reagents for cell identification. A NY-ESO TCR-specific T cell is identified as one that fluoresces in both red and green. B. Preparation of MHC-antigen tetramer functionalized magnetic NPs. All cells are fluorescently stained with a live-cell stain. Those Jurkat cells that are captured with the magnet are spread on a hemocytometry chip for enumeration via fluorescence microscopy. C. For 1-10 NY-ESO TCR-specific T cells spiked into 10,000 Jurkat cells, results are plotted for the numbers of cells detected versus the numbers of spiked cells. The top two plots are for the multi-color FC detection. For the top plot, a loose gate was defined (all double fluorescent cells are recorded). For the middle plot, a tight gate was defined (all non-double fluorescent cells are strictly excluded). The bottom plot is for the NP-tetramer hemocytometry. Each plot includes a straight-line fit, the fitted slope and intercept (bottom right of each plot), and the R^2 fitting metric. All data was collected in triplicate. Some data points appear missing, but are actually just repeated observations of the same value, and so the points overlap.

Figure 3. Analysis of neoantigen-specific CD8+ T cell populations from patient #1 TILs and PBMCs over the course of treatment with anti-PD1. **A.** Patient #1 had metastatic melanoma to the chest wall, pleura and lung progressing after three prior lines of therapy with high dose interleukin-2, vemurafenib and TIL adoptive cell therapy. Upon start on pembrolizumab the patient had a transient progression for three months, with increase in size of the chest wall masses and pleural effusion (Dec 2012), followed by a long-lasting tumor regression. **B.** The timeline of the lesion size. Day 0 is the start of treatment. A baseline tumor biopsy was collected for genomic and transcriptomic analysis at d ay -28 (star symbol). Black dots represent CT-scan measurement dates, while the arrows correspond to points of analysis, and are color coded for the bar graphs in part C. **C.** Neoantigen-specific T cell populations detected from Day 187 TILs (top graph) and PBMCs over the course of the therapy, along with mutation-containing mRNA read counts for the mutant proteins (bottom graph) from the baseline RNA-seq. PBMCs analyzed at day 439 (black arrow on panel B) yielded no detected neoantigen-specific populations. The horizontal dashed lines in the PBMC analysis graphs represent the signal threshold above which the identification of a T cell population is statistically significant. The vertical light green dashed lines indicate T cell populations detected across the different time points and patient materials, while the vertical orange dashed lines connect transcripts to corresponding T cell populations detected at day 41. For the TILs analysis, the MART-1 tumor antigen is library element #50, while for all PBMCs, that library element is the conditional antigen (MHC-J). **D.** ELISpot single cell assays of IFN-γ secretion from each of the neoantigen-specific T cell populations detected from Day 41 PBMCs. The baseline (dashed line) was established as the average background level using an identical number of CD8+ T cells from a healthy donor. The right y-axis represents the populations detected (part C) and the left y-axis represents, in an analysis of a different vial of CD8+ PBMCs, the numbers of

ELISpots detected. Neoantigens 1 and 10 (red font x-axis label) are controls. Micrographs of represented ELISpot assays are shown for a healthy donor and for a neoantigen-specific T cell population.

Figure 2. Construction and use of the barcoded NP-NACS library for antigen specific T cell capture and analysis. **A.** The conditional antigen approach is employed to convert a single batch of photo-cleavable antigen-MHC complexes into a library, where each MHC library element presents a unique antigen. In the drawing, neoantigens are represented as 9-mer string beads, with a single red circle indicating a point mutation at that residue. The library elements are combined with DNA-labeled, cysteine-modified streptavidin (SAC) to form a library of DNA-labeled tetramers. Each tetramer library element is coupled, via DNA-hybridization, to a magnetic nanoparticle (NP) that has been chemically modified to present a DNA-barcode. Shown is a 3-color, 3-position DNA barcode which also has a 4th segment for hybridization to the tetramer. Each antigen is associated with a specific barcode. All elements of the barcoded NP-NACS library are combined, and then, with a magnet, used to separate antigen-specific T cell populations from a biological sample, such as TILs or PBMCs. **B.** Single cell analysis of captured neoantigen-specific T cells collected from a sample of expanded TILS from patient #1. The far-left image is an optical micrograph of a microfluidic chamber equipped with 10 cell traps, 9 of which contain single barcoded T cells. The T cells appear black due to the NP barcodes that decorate their surface. This microchip has 60 such cell capture microchambers. The fluorescent micrograph series are the sequential reads of the three barcode positions, with the colorimetric readouts for the 9 trapped cells provided below (R = red, G = green; Y = yellow). The cell at position #8 does not provide a clean read, while the cell at position #9 was lost during the process. Some traps contain 2 cells (for example, #4), and so reads are only done on those cells that are clearly delineated in the images. **C.** The barcode key. Each of the $3^3=27$ color sequences correspond to a neoantigen or, at position #8, to the MART-1 tumor antigen. For example, the cell at position #3 reads ‘YRG’ and corresponds to neoantigen #12. The Y(D) notation (red font) implies a Y for D mutation in the neoantigen sequence.

Figure 4. Demonstration that the barcoded NP-NACS approach permits matching of neoantigen specificities and TCR genes for individual cells. **A.** The process flow. The optical micrographs show a captured barcoded T cell from patient #1, followed by the 3 sequential fluorescent readout steps to identify specificity against neoantigen #12. Scale bars are 20 μm. The captured single T cell was punched out to perform RT-PCR to obtain TCRα and TCRβ gene sequences (DNA ladder: 100bp). The obtained TCR gene was then assembled and transferred into a retroviral vector, and delivered into Jurkat T cells for analysis by flow cytometry. **B.** Flow cytometry results for untransduced Jurkats (left), Jurkats transduced with LNGFR expression reporter (center) and Jurkats transduced with both NGFR and the TCR specific for neo-antigen 12 (right).

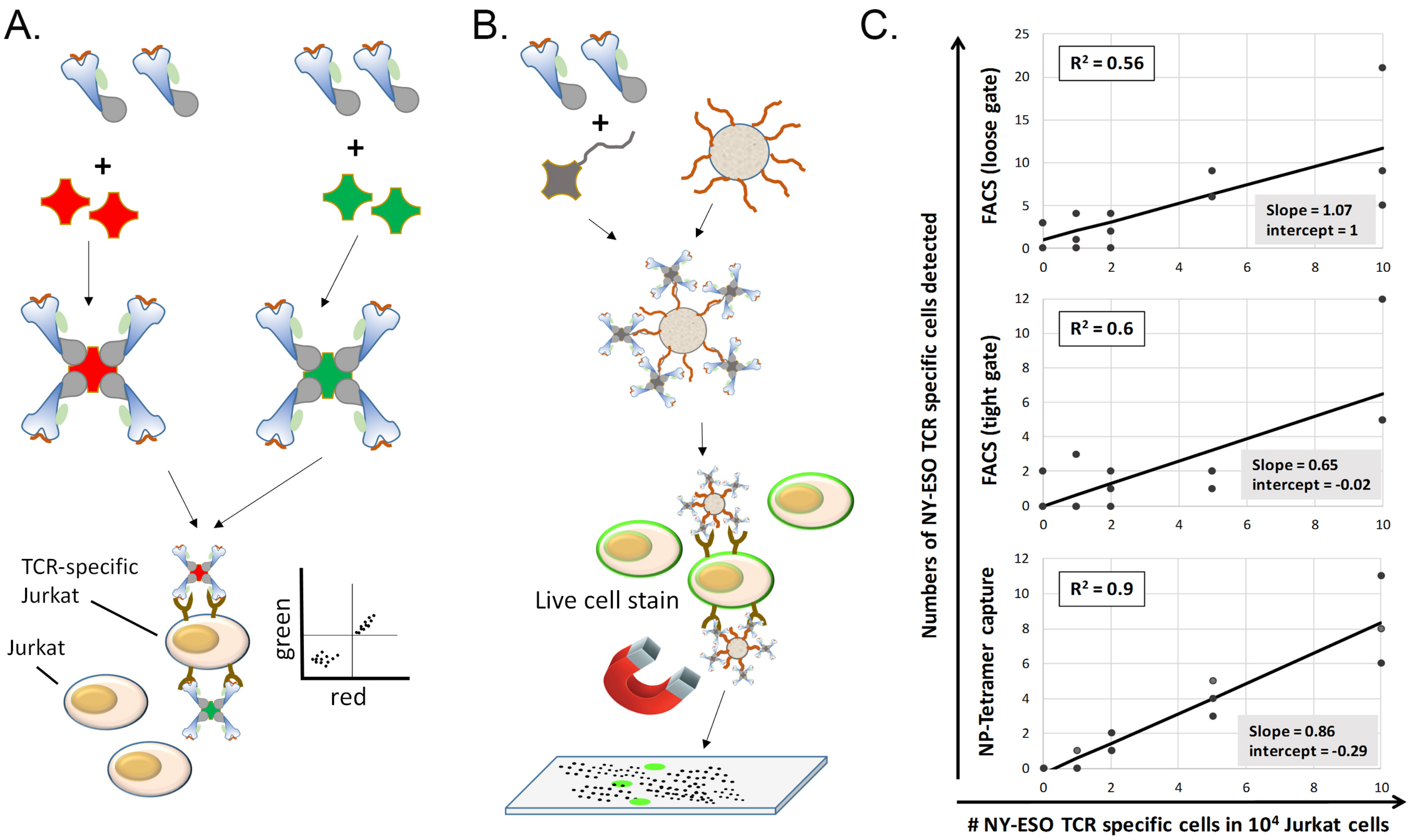
A.
+
+
TCR-specific
Jurkat
Jurkat
green
red
B.
+
Live cell stain
C.
Numbers of NY-ESO TCR specific cells detected
FACS (loose gate)
R² = 0.56
Slope = 1.07
intercept = 1
0 5 10 15 20 25
0 2 4 6 8 10
FACS (tight gate)
R² = 0.6
Slope = 0.65
intercept = -0.02
0 2 4 6 8 10 12
0 2 4 6 8 10
NP-Tetramer capture
R² = 0.9
Slope = 0.86
intercept = -0.29
0 2 4 6 8 10 12
0 2 4 6 8 10
NY-ESO TCR specific cells in 10⁴ Jurkat cells

Fig. 1

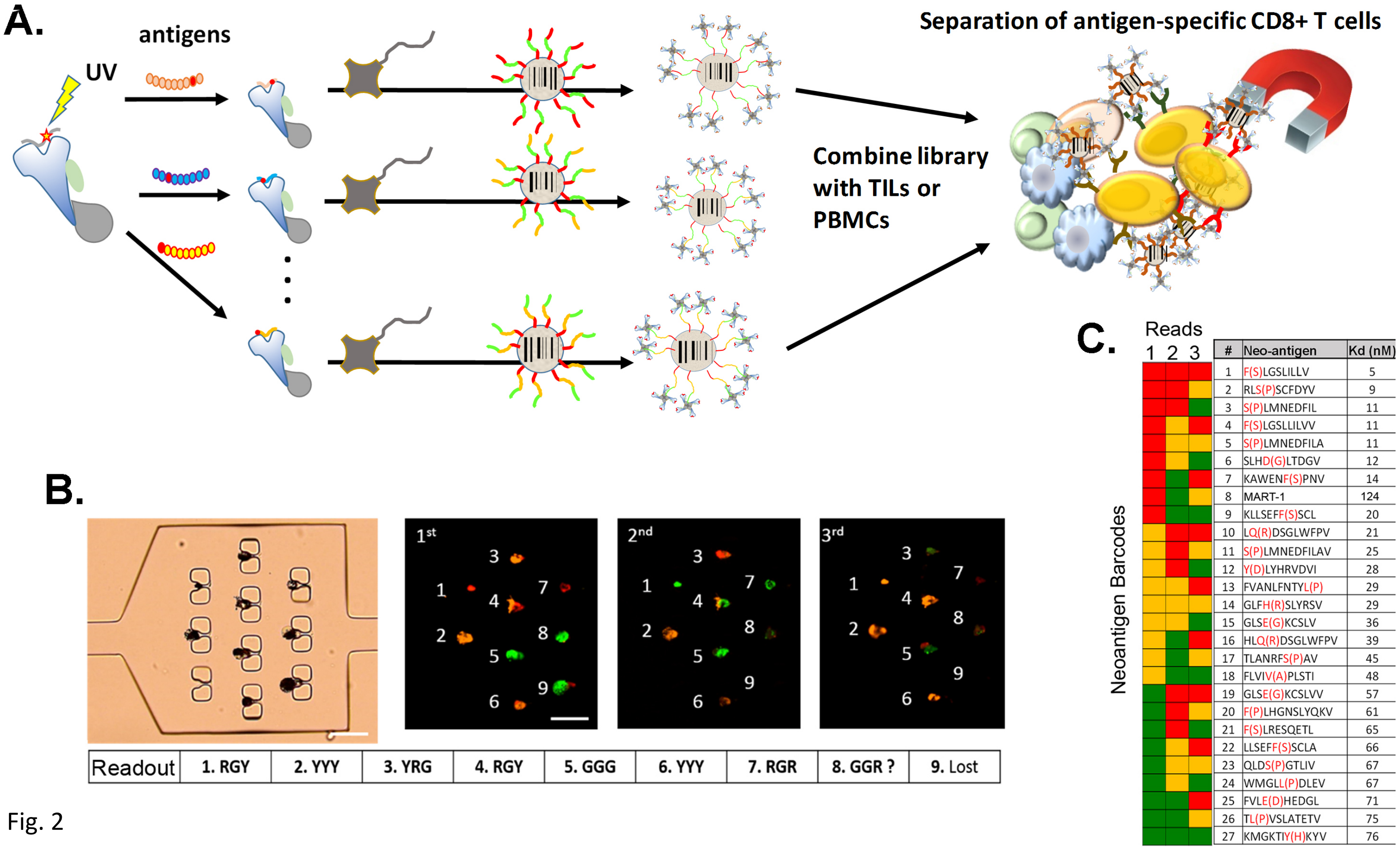

Readout	1. RGY	2. YYY	3. YRG	4. RGY	5. GGG	6. YYY	7. RGR	8. GGR ?	9. Lost

Reads 1	2	3	#	Neo-antigen	Kd (nM)
🟥	🟥	🟥	1	F(S)LGSLILLV	5
🟥	🟥	🟨	2	RLS(P)SCFDYV	9
🟥	🟥	🟩	3	S(P)LMNEDFIL	11
🟥	🟨	🟥	4	F(S)LGSLLILVV	11
🟥	🟨	🟨	5	S(P)LMNEDFILA	11
🟥	🟨	🟩	6	SLHD(G)LTDGV	12
🟥	🟩	🟥	7	KAWENF(S)PNV	14
🟥	🟩	🟨	8	MART-1	124
🟥	🟩	🟩	9	KLLSEFF(S)SCL	20
🟨	🟥	🟥	10	LQ(R)DSGLWFPV	21
🟨	🟥	🟨	11	S(P)LMNEDFILAV	25
🟨	🟥	🟩	12	Y(D)LYHRVDVI	28
🟨	🟨	🟥	13	FVANLFNTYL(P)	29
🟨	🟨	🟨	14	GLFH(R)SLYRSV	29
🟨	🟨	🟩	15	GLSE(G)KCSLV	36
🟨	🟩	🟥	16	HLQ(R)DSGLWFPV	39
🟨	🟩	🟨	17	TLANRFS(P)AV	45
🟨	🟩	🟩	18	FLVIV(A)PLSTI	48
🟩	🟥	🟥	19	GLSE(G)KCSLVV	57
🟩	🟥	🟨	20	F(P)LHGNSLYQKV	61
🟩	🟥	🟩	21	F(S)LRESQETL	65
🟩	🟨	🟥	22	LLSEFF(S)SCLA	66
🟩	🟨	🟨	23	QLDS(P)GTLIV	67
🟩	🟨	🟩	24	WMGLL(P)DLEV	67
🟩	🟩	🟥	25	FVLE(D)HEDGL	71
🟩	🟩	🟨	26	TL(P)VSLATETV	75
🟩	🟩	🟩	27	KMGKTIY(H)KYV	76

Fig. 2

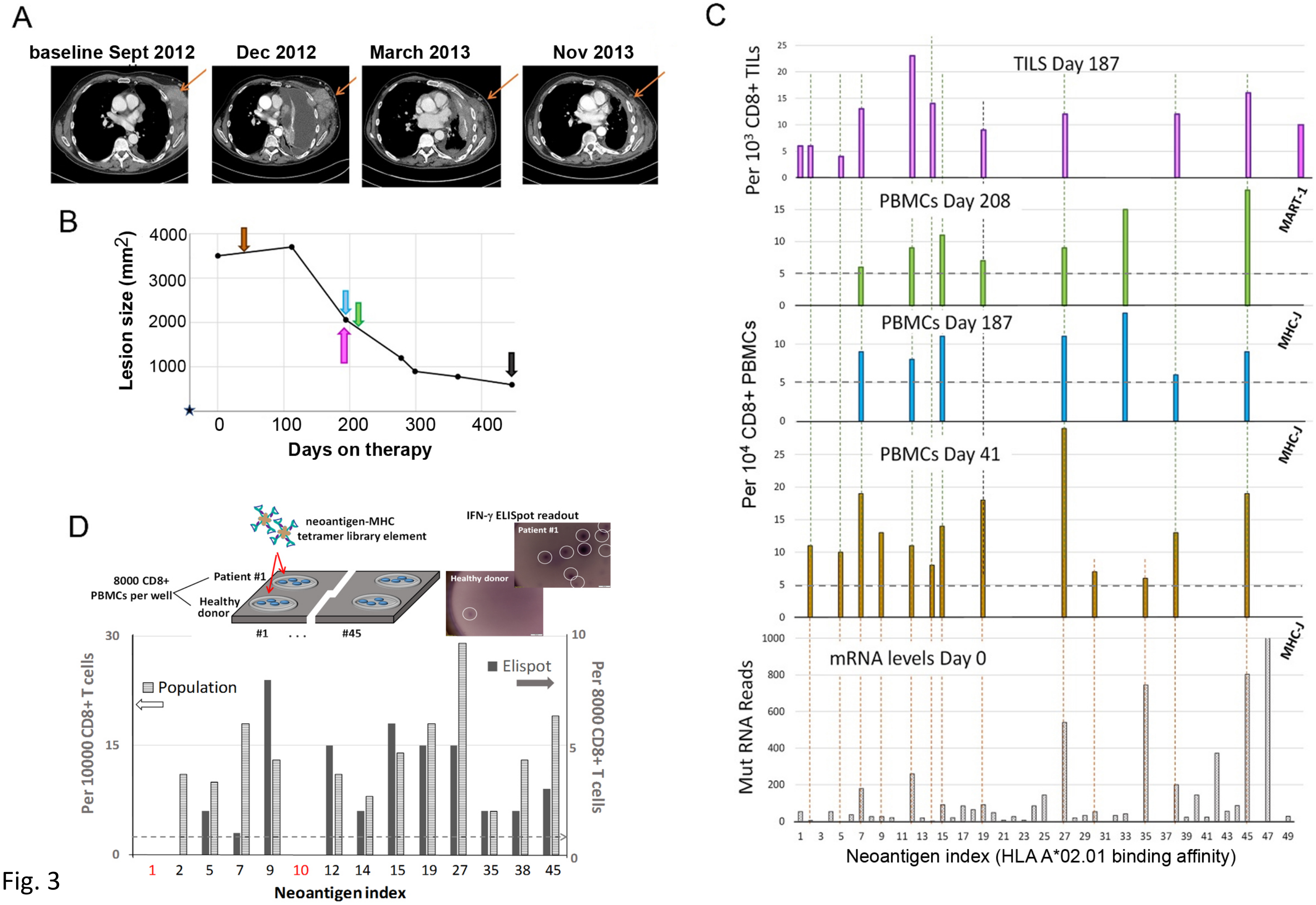
A
baseline Sept 2012
Dec 2012
March 2013
Nov 2013
B
Lesion size (mm^2)
4000
3000
2000
1000
0
100
200
300
400
Days on therapy
C
Per 10^3 CD8+ TILs
TILS Day 187
PBMCs Day 208
MART-1
Per 10^4 CD8+ PBMCs
PBMCs Day 187
MHC-I
PBMCs Day 41
Mut RNA Reads
mRNA levels Day 0
Neoantigen index (HLA A*02.01 binding affinity)
D
neoantigen-MHC
tetramer library element
IFN-γ ELISpot readout
Patient #1
Healthy donor
8000 CD8+
PBMCs per well
#1
. . .
#45
Per 10000 CD8+ T cells
Population
Elispot
Per 8000 CD8+ T cells
1
2
5
7
9
10
12
14
15
19
27
35
38
45
Neoantigen index

Fig. 3

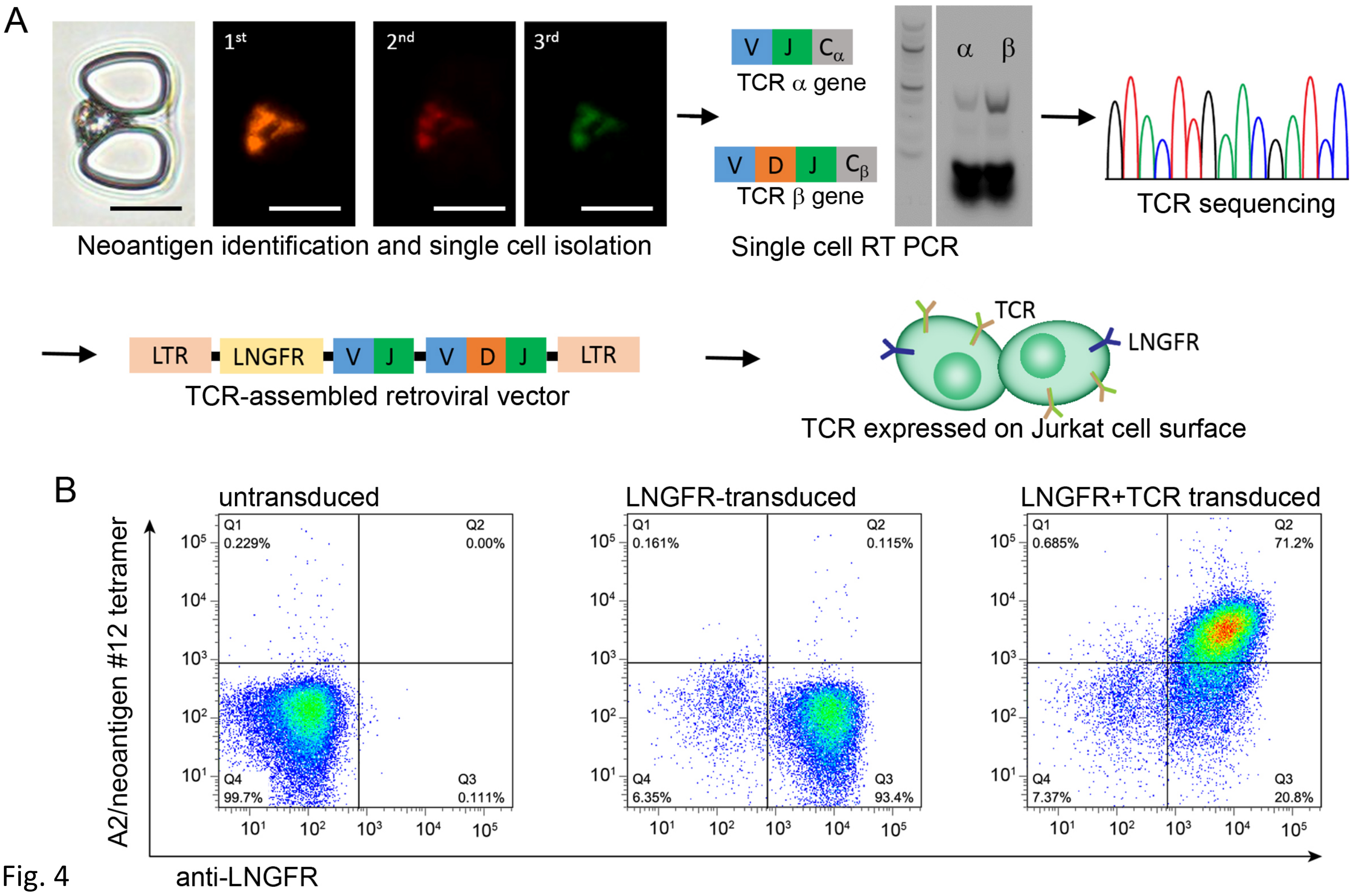
A
1st
2nd
3rd
Neoantigen identification and single cell isolation
V J Cα
TCR α gene
V D J Cβ
TCR β gene
α β
Single cell RT PCR
TCR sequencing
LTR LNGFR V J V D J LTR
TCR-assembled retroviral vector
TCR
LNGFR
TCR expressed on Jurkat cell surface
B
untransduced
LNGFR-transduced
LNGFR+TCR transduced
Q1 0.229%
Q2 0.00%
Q4 99.7%
Q3 0.111%
Q1 0.161%
Q2 0.115%
Q4 6.35%
Q3 93.4%
Q1 0.685%
Q2 71.2%
Q4 7.37%
Q3 20.8%
A2/neoantigen #12 tetramer
anti-LNGFR

Fig. 4

STAR Methods

Patients, treatment, and specimen collection

Patients with metastatic melanoma were selected for the current analysis by being HLA-A*02:01 positive, having an adequate baseline biopsy as well as an on-treatment biopsy, and exhibiting an objective tumor response while participating in a phase 1 trial of pembrolizumab. Patients #1 and #2 received single agent pembrolizumab intravenously 10 mg/kg every 3 weeks (10Q3W). Tumor responses were evaluated starting at 12 weeks, confirmed 4 weeks after first response, and imaged every 12 weeks thereafter. Response was characterized by both the Response Evaluation Criteria in Solid Tumors (RECIST) and the immune-related response criteria (irRC). Tumour biopsy and peripheral blood cell collection and analyses were approved by UCLA IRBs 11-001918 and 11-003066. Tumor biopsies from the patients analyzed were obtained at baseline and on therapy and were processed with one aliquot immediately fixed in formalin followed by paraffin embedding for pathological analyses, a second aliquot snap frozen by immediate immersion in liquid nitrogen for genetic analyses, and a third aliquot minced fresh under sterile condition followed by DNAse/collagenase digestion to create single cell suspensions (s.c.s) before cryopreservation in liquid nitrogen. Peripheral blood mononuclear cells (PBMCs) were prepared from fresh whole blood by Ficoll-Paque density gradient centrifugation and cryopreserved.

TIL isolation and expansion

Tumor infiltrating lymphocytes were expanded from cryopreserved s.c.s using anti-CD3 antibody (OKT3, 50ng/mL, 48hr exposure) and IL-2 (300IU/mL) and re-cyropreserved at $5x10^6$ cells/mL after 2-4 weeks. TILs were thawed and treated with DNAse for 45 min the morning of use, and stained with antibodies to CD4 (BV510, BioLegend, San Diego, CA) and CD8+ (BV605, BioLegend, San Diego, CA). Live (7AAD-negative) populations of CD4 and CD8+ single-positive cells were sorted using a FACS Cell Sorter (BD Biosciences, San Jose, CA).

Whole exome sequencing (WES), mutation calling and HLA-typing

Both DNA and RNA were extracted simultaneously from snap-frozen tumor biopsies (Qiagen AllPrep Kit). DNA from tumors and matched normal blood samples were sequenced at the UCLA Clinical Microarray Core. Paired-end 2x100bp sequencing was carried out on the HiSeq 2000 platform (Illumina, San Diego, CA) following exon capture using the Nimblegen SeqCap EZ Human Exome Library v3.0 (Roche), which targets 65 Mb of genome. Sequencing generated 6-10 billion reads per sample, with each targeted base covered by an average of 90-150 reads. Sequences were aligned to the UCSC hg19 human genome reference using BWA-mem algorithm (v0.7.9). Preprocessing followed the GATK Best Practices Workflow v3, including duplicate removal (Picard Tools), indel realignment, and base quality score recalibration. Somatic mutations were called with methods modified from[1], using MuTect (v1.1.7)[2], Varscan2 Somatic (v2.3.6)[3], and the GATK-HaplotypeCaller (HC, v3.3). Only high-confidence mutations were retained, defined as those identified by at least two out of three programs. For the GATK-HC, somatic variants were determined using one-sided Fisher's Exact Test (P value cut-off ≤ 0.01) between tumor/normal pairs. Variants were annotated by Oncotator[4], with non-synonymous mutations being those classified as Nonsense, Missense, Splice_Site, or Nonstop Mutations, as well as Frame_Shift, In_Frame, or Start_Codon altering insertions/deletions. HLA-typing was performed by ATHLATES from the whole exome sequencing data.

RNA sequencing

RNA sequencing was performed using the Illumina HiSeq 2500 platform on 100-bp paired-end libraries prepared using the IlluminaTruSeq RNA sample preparation kit per the manufacturer's instructions. Reads were mapped to hg19 using TopHat2 v2.0,[5] and were quantified and normalized using Cufflinks v2.2.1[6] program and CuffNorm to generate normalized expression tables by library size (fragments per kilobase of exon per million fragments mapped, FPKM) using the geometric normalization method. Mutation-containing RNA reads were identified by a custom Python (v2.7.3) script utilizing the Biopython and pysam packages, and verified by visual inspection in the Integrated Genomics Viewer (IGV).

Peptide HLA binding prediction and neoantigen candidate identification

Peptide binding predictions to HLA-A02:01 were generated by netMHC3.4[7] for 9-mer and 10-mer peptides in a sliding window around each non-synonymous amino acid-altering mutation. (Peptide sequences were derived from Ensembl GRCh37 release 74.) Candidate peptides were binned by 1) those with mutations-containing reads identified by RNA-seq, 2) those with RNA expression (FPKM > 0) but no identified mutated reads, and 3) all others without detectable RNA-seq expression. Peptides were ranked and sorted by HLA binding affinity within each bin.

Production of ssDNA-SAC conjugates

The ssDNA-SAC conjugate was produced following previous published protocol.[8] Briefly, SAC was first expressed from the pTSA-C plasmid containing the SAC gene (Addgene).[9] Before conjugation to DNA, SAC (1 mg/ml) was buffer exchanged to PBS containing Tris(2-Carboxyethyl) phosphine Hydrochloride (TCEP, 5 mM) using zeba desalting columns (Pierce). Then MHPH (3-N-Maleimido-6-hydraziniumpyridine hydrochloride, 100 mM, Solulink) in DMF was added to SAC at a molar excess of 300:1. In the meantime, SFB (succinimidyl 4-formylbenzoate, 100mM, Solulink) in DMF was added to 5'-amine modified ssDNA (500 μM) in a 40:1 molar ratio. After reacting at rt for 4 hours, MHPH-labeled SAC and SFB-labeled DNA were buffer exchanged to citrated (50 mM sodium citrate, 150 mM NaCl, pH 6.0), and then mixed in a 20:1 ratio of DNA to SAC to react at rt overnight. DNA-SAC conjugate was purified using the Superdex 200 gel filtration column (GE health) and concentrated with 10K MWCO ultra-centrifuge filters (Millipore).

Human MHC class I neoantigen library construction

MHC library was generated using the UV-mediated peptide exchange method.[10] The photo-labile peptide KILGFVFJV and other neo-antigen peptides were synthesized with standard automated Fmoc-peptide synthesis methodology (J, (S)-3-(Fmoc-amino)-3-(2-nitrophenyl)propionic acid, is the photo-labile amino acid residue). Plasmids encoding human MHC class I heavy chain and human β_2m containing bacterial strain were kind gifts from Ton N M Schumacher. MHC photo-labile protein was folded from MHC heavy chain inclusion body, β_2m inclusion body and photo-labile peptide according to the previously published protocol[11] and then biotinylated using the BirA biotin ligase. Mixture of MHC photo-labile protein (0.5 μM) and neo-antigen peptide (50 μM) was exposed to 365 nm UV light for 1 hour to generate the MHC neo-antigen library.

NP MHC neo-antigen library construction

Streptavidin coated magnetic NPs (1 μm diameter, Invitrogen Dynabeads MyOne T1) were used. Each of these NPs can present up to 3×10^5 ssDNA oligomers on their surface, according to the manufacturer specifications. These NPs were mixed with biotin-DNA at 1:20 ratio to obtain NP-DNA. Excess DNA was removed by washing the magnetic NP for 3 times. In parallel, MHC neo-antigen library was added to ssDNA-SAC at 4:1 ratio to form the DNA-MHC tetramer. Equal amount (in terms of DNA ratio) of NP-DNA and DNA-MHC tetramer were hybridized at 37 ºC for 30 min to generate the NP MHC neo-antigen library. An even simpler fashion of the library was constructed by incubating the Streptavidin magnetic NP with biotinylated MHC monomer at a ratio of 1:4 to 1:8 at rt for 30min. Excessive MHC monomer wash removed by washing the magnetic NP for 1-2X with PBS, 0.1% BSA. As obtained library has been used to analyze sample from Patient #3.

Cell-trapping microfluidic device fabrication

First, a master mold with cell traps (multiple traps or single traps) was prepared using the SU-8 2025 photoresist. Sylgard 184 (A:B = 10:1) mixture was then poured onto the mold, degassed and cured at 80 ºC for 2 hours. In the meantime, a thin layer of PDMS was spun coated onto a glass slide at 2000 rpm/min and cured at 80 ºC for 1 hour. The PDMS device and PDMS-coated glass were treated with O_2 plasma for 1 min and bound together to get the final cell-trapping microfluidic device.

TIL pulldown and barcode

NP MHC neo-antigen library was added to CD 8+ human T cells for 15-30 min at rt. The NP-bound T cells were magnetically enriched and washed by PBS with 0.1% BSA to remove any non-specifically pulled T cells. The cells were then loaded into costar transwell polycarbonate membrane (5 μm pore) to remove free NPs. Then, the cells were loaded into the cell-trapping microfluidic device and sequentially barcoded. First, 3 different DNA-dyes (cy3, cy5 and Alex 488) were loaded to the device to hybridize with the DNA on the NP at 37 ºC for 15 min. After a brief washing, fluorescent images were taken to obtain the first round barcode. Displacement DNAs were added to the device at 37 ºC for 15 min to remove the first round DNA dyes. Similar procedures were employed to obtain the second and third round barcoding images.

CD8+ T cell pulldown from PBMC

CD8+ T cells from PBMC were sorted by FACS. CD8+ T cells were then stained with Calcein AM (a green-fluorescent live/dead stain, ThermoFisher) and incubated with each individual NP-NACS library at rt for 15-30 min. Neo-antigen specific cells were enriched by magnet pulldown. The non-captured T cells in the supernatant was collected for further incubation with other NP-NACS library element. The enriched T cells were washed by PBS once to remove any non-specific cell pulldown. Cells were then loaded into a cell hemocytometer. The whole area in the hemocytometer chip was imaged to obtain the total pulldown cell number. Healthy donor PBMC and/or PBMC from an unrelated male melanoma patient were used as control to obtain the background.

ELISPOT assay

8000 CD8+ T cells from PBMC (Day 41 from patient #1 or heathy donor, 100 μl in RPMI based media supplemented with 300 IU/ml IL-2) were stimulated with 0.1 μM final concentration of neo-antigen tetramers for 26 hours in a 37 ºC CO_2 incubator. Secreted human IFN-γ were detect by the ELISpot assay

(R & D) following the manufacturer's suggested protocol, except with more stringent washing by increasing the repeated washing to 6 times in each washing step.

Sensitivity comparison of NP-barcoded NACS and Multicolor flow cytometry

Varying numbers (0, 1, 2, 5, 10, 20, 50, 100, 200, 500 and 1000) of NY-ESO transduced Jurkat T cells were spiked into Jurkat T cells to generate samples comprised of a total number of 10 000 cells. Such samples were prepared and analyzed in triplicate. For multicolor flow analysis, cells were stained with R-Phycoerythrin-NY-ESO (PE-NY-ESO) tetramer, Allophycocyanin-NY-ESO (APC-NY-ESO) tetramer (antigen: SLLMWITQV), 7-Aminoactinomycin D (7AAD) and analyzed by flow cytometry. Single stain of NY-ESO Jurkat T cells and Jurkat T cells were used as controls.

For the NP-barcoded NACS comparison, similar samples of NY-ESO transduced Jurkat T cells (stained with Calcein AM, only live cell will be stained with green fluorescence) spiked into Jurkat T cells to obtain a total number of 10 000 cells were prepared and analyzed in triplicate. Cells were incubated with NY-ESO NP- NACS library element at rt for 15-30min. The magnetically labeled T cells were enriched using a magnet, washed with 100 μl PBS with 0.1% BSA, re-suspended in 10 μl PBS with 0.1% BSA, and loaded into a plastic hemocytometer (Incyto). The numbers of captured cells were counted using fluorescence microscopy by using the green fluorescent NY-ESO Jurkat T cells as signal.

Comparison of NP-barcoded NACS and multicolor flow cytometry for analysis of Patient #1 expanded TILs. In Figure 3C (top panel) of the main text we present an analysis of patient #1 expanded TILs using the NP-barcoded NACS approach. We analyzed a different vial of those similarly expanded TILs using multicolor flow cytometry method of Schumacher. For the flow analysis, we present, in Figure S8, multiple workups of the patient #1 TILs data set, in which we select the CD8++ live cells for workup using a tight or loose gating strategy, or we select all CD8+ live cells for workup, also using a tight or loose gating strategy. The top table (Fig. S8A) provides the dye labels that define each neoantigen-specific barcode. For example, a T cell that is dyed for both APC and PE will be identified as specific to neoantigen #1. In Fig. S8B-S8E, the bottom left table provides the numbers of cells that were detected positive for only single colors. The bottom right table provides the numbers of cells that were detected as positive for two colors. For example, Fig S9B represents the most stringent selection process – only CD8++ cells, with a tight gating strategy, were selected for analysis. Under this condition, one population of cells (#12) was stained with both BV-421 and PE dyes, and 699 such cells were detected. Only a total of 4 other cells are detected as stained with just a single dye.

A more promiscuous gating strategy is CD8+ live cells, tight gate (Fig. S8C). In that analysis, 702 cells are detected as specific against neoantigen #12. This indicates that the neoantigen #12 specific T cell population resides exclusively in the CD8++ pool of cells. Only 3 other cells are found to stain with 2 colors, although a large number stain positive for only BV421. Note that for the most promiscuous selection (CD8+, loose gate) the numbers of doubly positive cells increases for a few populations. For the singly stained cells, BV421 and APC are over-represented. Thus, there may be some neoantigen specific populations within the CD8+ pool, but they do not express sufficient TCR to be detected as doubly stained.

Figures S9 are analogous workups of a data set from a healthy donor PBMC control, and Figure S10 provides the flow cytometry selection criteria for the patient #1 TILs analyzed by barcoded NP-NACS. In the main text we indicate that only T cells specific to neoantigen #12 are detected using the flow method. Here we discuss that result in more detail.

Figure S10 presents the gating strategy used to select cells for the barcoded NP-NACS analysis. This is analogous to CD8+ with a loose gate, but the barcoding and microscopy analysis permits additional restrictions to be added. Note that in this vial of expanded TILs, the CD8++ population is proportionately less than it is for Figures S9A-D (roughly 1/5 of the CD8+ cells versus 43% of the CD8+ cells that were analyzed by flow). This accounts for most of the discrepancy between those T cells identified as neoantigen specific. In other words, the neoantigen #12 specific cells identified by flow are CD8++. The fraction of CD8++ cells in the vial analyzed by flow is more than 2x higher than the corresponding fraction of those cells in the vial analyzed by NP-barcoded NACS.

Single cell TCR cloning

Neo-antigen specific T cells were trapped in the microfluidic device with single cell traps (Supplementary Fig. S13). The cells were then recovered by PDMS puncher. Brief sonication was applied to release the cell from the punched-out PDMS to cell lysis buffer (10mM Tris, pH=8, with 1U/µl RNAse inhibitor, Promega). Rearranged Vα and Vβ domain genes were cloned from single cells using a OneStep RT PCR kit (Qiagen) with multiplexed forward primers that bind TRAV and TRBV gene segments (Supplementary Tables S10 and S11) and reverse primers that bind the constant Cα (5'-GCCACAGCACTGTTGCTCTTGAAGTCC-3') and Cβ (5'-CCACCAGCTCAGCTCCACGTG-3') domain genes. cDNA products were used as templates in a second semi-nested amplification with a universal set of primers (alpha forward primer: 5'-TGGCCTGCTTTGTTTGCCGTGGTTACAGGAAGCCTCAGCA-3', alpha reverse primer: 5'-GCCACAGCACTGTTGCTCTTGAAGTCCATAG-3'; beta forward primer: 5'-CGGGCTCCTTTGCCTACCGTGCCTGCAGGAGGGCTCGGCA-3', beta reverse primer: 5'-CGTGCTGACCCCACTGTGCACCTCCTTCCCATTCACCCACCAGCTCAGCTCCACGTGGTC-3'). Vα and Vβ cDNA were sequenced and reamplified using single TRAV/TRBV forward primers to correct mispriming artifacts introduced through multiplexed PCR. Retroviral vectors were constructed for functional testing through PCR assembly. The Vα and Vβ domain genes were assembled with human growth hormone (HGH) signal peptides, constant regions of the TCRα and TCRβ chains, and a 2A ribosomal skipping sequence, then digested with restriction enzymes and ligated into a MSCV-based non-replicative retroviral backbone.

To produce retrovirus, HEK-293T/17 cells were transfected via calcium phosphate precipitation with the TCR vector, a packaging vector encoding gag-pol, and a pseudotyping vector encoding RD114 envelope glycoprotein. Media was replaced 24 hours following transfection and viral supernatant was collected 48 hours following transfection. An equal volume of viral supernatant was added to Jurkat T cells in RPMI-based medium (final density: 0.5 x 10^6 cells/mL) and polybrene was added to a final concentration of 5 µg/mL. Cells were spinfected at 1350xg for 90 minutes at 30 °C, and then incubated with virus overnight at 37 °C, 5% CO2. Half of the media was replaced 24 hours following infection and cells were assayed for TCR specificity 48 hours following infection via flow cytometry using cognate fluorescent peptide-MHC tetramers.

Sensitive, non-destructive detection of neoantigen-specific T cell populations from tumors and blood

Supporting Figures and Tables

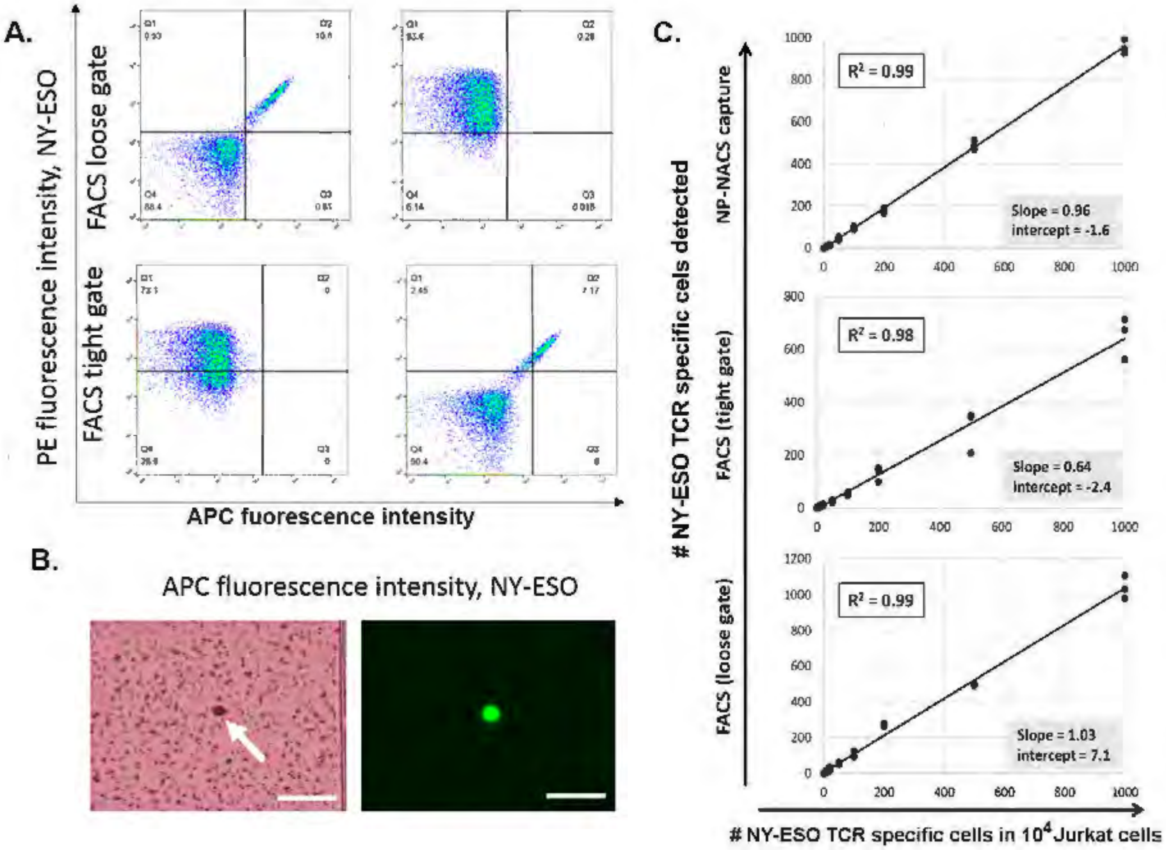

Fig. S1. Sensitivity comparison of NP-NACS and FACS methods. **A.** FACS plots for loose gate and tight gate controls. The loose gate is determined by visual separation of double-fluorescent positive Jurkat T cells from double-fluorescent negative Jurkat T cells (upper left). The tight gate is set to eliminate any possible leak of double-fluorescent positive signals from non-stained Jurkat T cells, as well as PE-NY-ESO or APC-NY-ESO single stain controls (lower left). **B.** Typical image from the NP-NACS capture, as recorded using a hemocytometry microchip. The single T cell shown was captured with a magnet, along with unbound tetramer-functionalized magnetic NPs. The captured cell appears black in the bright field image, because it is covered by barcoded magnetic NPs. It appears green in the fluorescent image due to the live cell/dead cell stain calcein AM (Life Tech) (right). Scale bar is 50 µm. **C.** Plot of number of NY-ESO Jurkat T cells detected by NP-NACS capture, and by FACS, with both loose gate and tight gate definitions. For the measurements, a known number, between 0 and 1000, of NY-ESO TCR-specific Jurkat T cells were spiked into a background of non-transfected Jurkat cells, keeping the total cell count at 10,000. Each plot provides linear regression fits to the data (solid curve) over the full spiking range. The fitted slope and intercept, and statistical uncertainties (given as standard error) are provided on each plot. The x-axis is the numbers of cells spiked, while the y-axis is the numbers of cells detected. All measurements are in triplicate for each spiking condition.

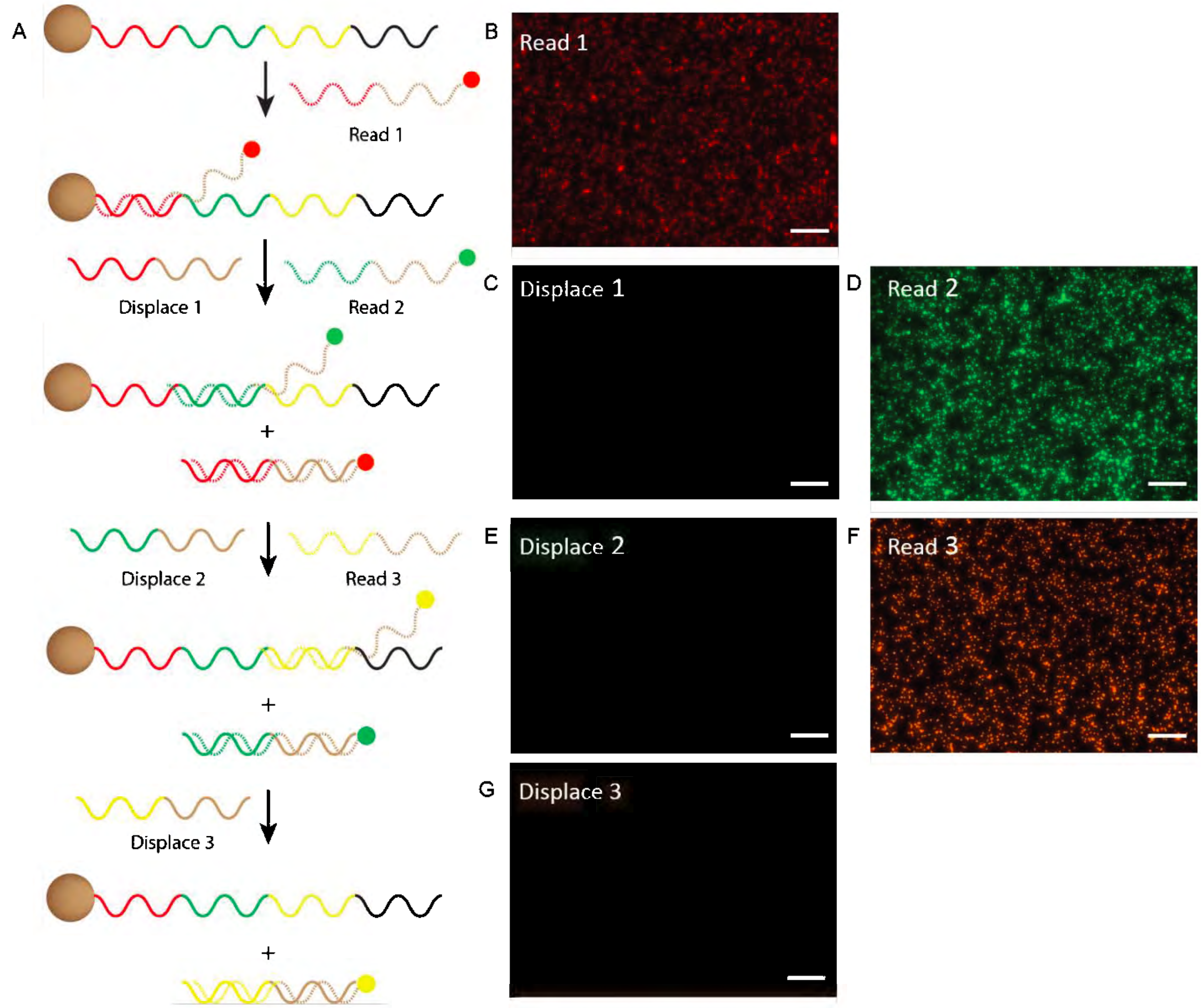

Fig. S2. DNA sequential barcode readout process. **A.** Schematic illustration of the barcode readout. NP-DNA is first hybridized to Read 1 DNA to give red fluorescence (**B**). Displace 1 DNA and Read 2 DNA are introduced to remove Read 1 DNA (**C**) and yield green fluorescence (**D**). Similar process is repeated to remove Read 2 DNA (**E**) and generate the third yellow fluorescence signal (**F**). The third yellow fluorescence can also be removed by adding Displace 3 DNA (**G**). Additional rounds of barcoding can be introduced as needed to increase library multiplexing capabilities. Scale bar: 50 µm.

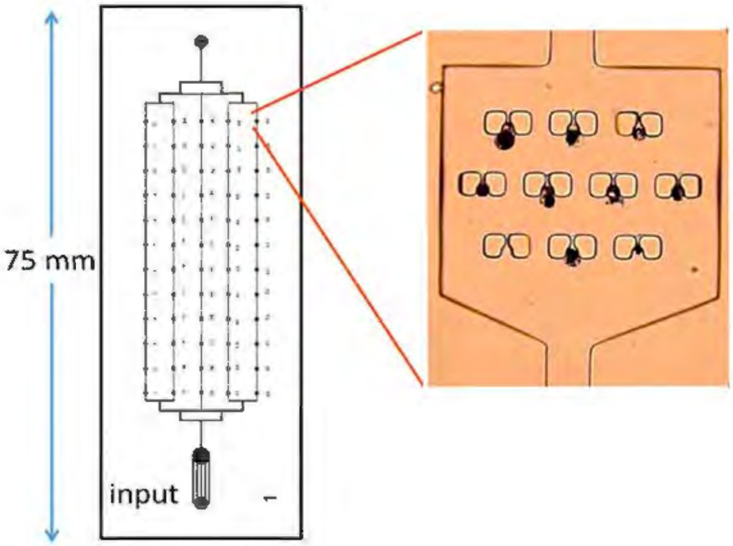

Fig. S3. Design of microchip for the capture and isolation of antigen-specific T cells. Cells are injected into the input, and flow through one of 5 channels, before exiting to waste. Each channel contains 12 microchambers, each of which has 10 cell traps. The micrograph at right shows one of those microchambers, with 9 of the 10 cell traps filled. The trapped cells appear black, because of the numbers of NP barcodes that coat the cell surface.

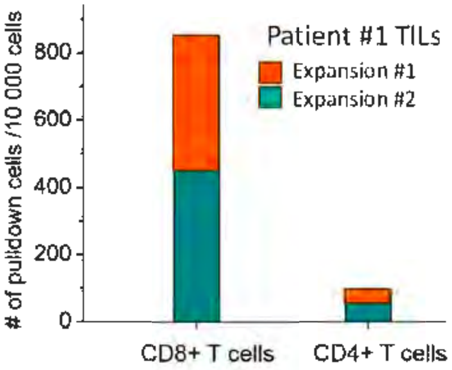

Fig. S4. Capture percentage of neoantigen-specific CD8+ cells T for patient #1 using two independent cell captures with NP-barcoded NACS library 1-27. Non-selective capture is estimated to be around 0.5%, as gauged by the relative numbers of CD4+ T cells that were captured using the same method. The two independent captures were carried out more than one week apart.

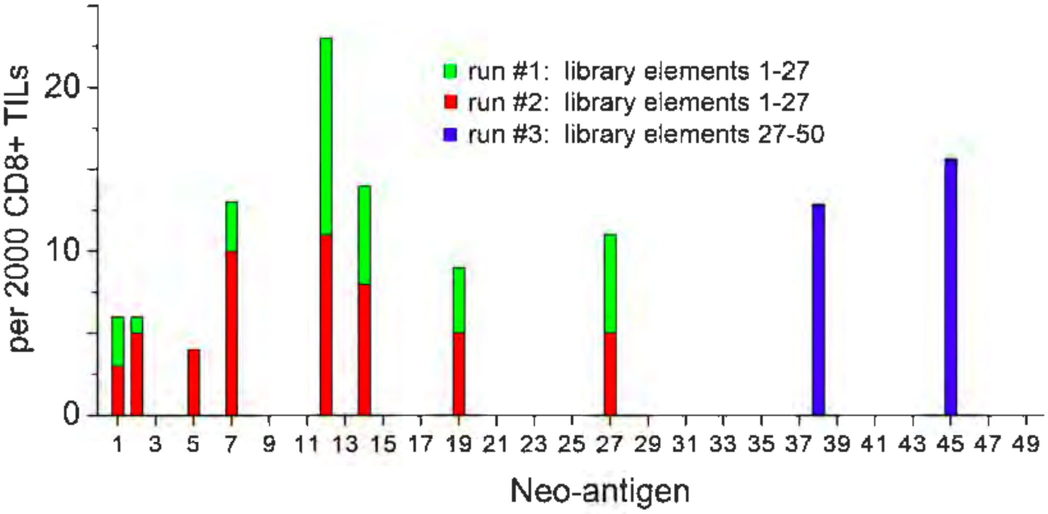

Fig. S5. Neoantigen population detected from expanded TILs from the tumor of patient #1. For each run, approximately 10,000 CD8+ TILs were analyzed per run, and isolated within the cell capture chambers of the microfluidic chip for fluorescence-based readouts of the attached NP-barcodes. Capture efficiency within the microfluidic chip was about 10%. Runs #1 and #2 utilized the same 27-element NP-barcoded NACS library, corresponding to the top-ranked 27 putative neoantigens. All populations shown for runs #1 and #2 were detected in both runs, excepting neoantigen #5, which was detected in 4 clean reads only in run #2. Run #3 utilized a NP-barcoded NACS library designed to capture CD8+ T cells specific to neoantigens rank ordered 28-50.

.

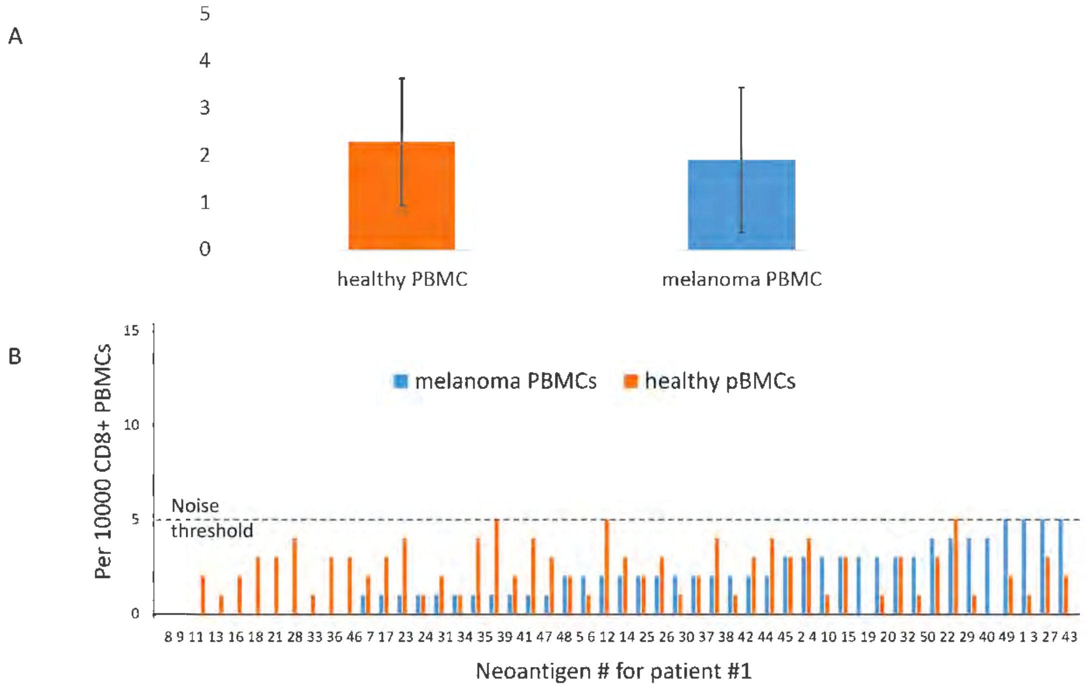

Fig. S6. Results of control experiments in which the NP-barcoded NACS library designed for patient #1 was utilized to capture CD8+ PBMCs from a different melanoma cancer patient (blue) and from a healthy donor (orange). **A.** Average numbers of pulled-down T cells, per library element, from healthy donor PBMC and PBMC from an unrelated melanoma patient, on the same clinical trial as patient #1. Data was presented as mean ± standard deviation. **B.** The numerical labels on the x-axis corresponds to the rank-order of the putative neoantigens. The data has been sorted according to frequency of detection for the melanoma patient, so as to illustrate that there is no correlation between these two controls. A correlation would likely indicate capture by non-selective library elements. The noise threshold was set at the average plus two standard deviations.

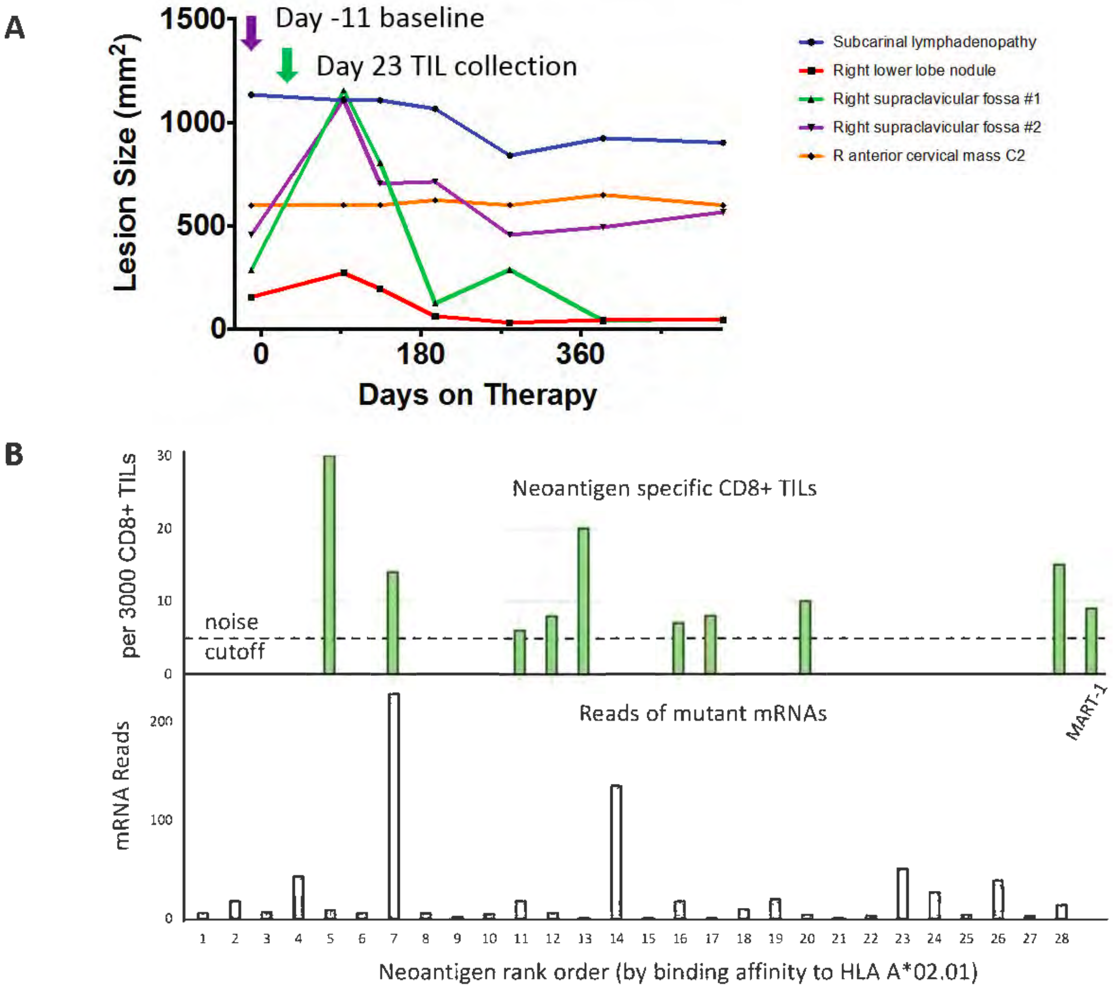

Fig. S7. TIL analysis of Patient #2 over the course of response to anti-PD-1 therapy, using the NP-barcoded NACS library to enumerate neoantigen-specific CD8+ T cell populations. **A.** The timeline of the lesion size of subcarinal lymph node, supraclavicular lymph node, and neck in Patient #2. Day 0 corresponds to the start of anti-PD-1 therapy. A baseline tumor biopsy (indicated by the purple arrow) was collected for genomic and transcriptomic analysis at day -11. Black dots represent CT-scan measurement dates, while the green arrow corresponds to the time point of analysis. **B**. Analysis of patient #2 TILs for neoantigen-specific CD8+ T cell populations using a NP-barcode NACS library based upon the top 28 putative neoantigens predicted for patient #2, plus the MART-1 tumor antigen. Only T cell populations detected at more than 5 cells per 3000 TILs are considered statistically significant. The bottom graph shows the mRNA copies measured for the mutated proteins from which the neoantigens derive.

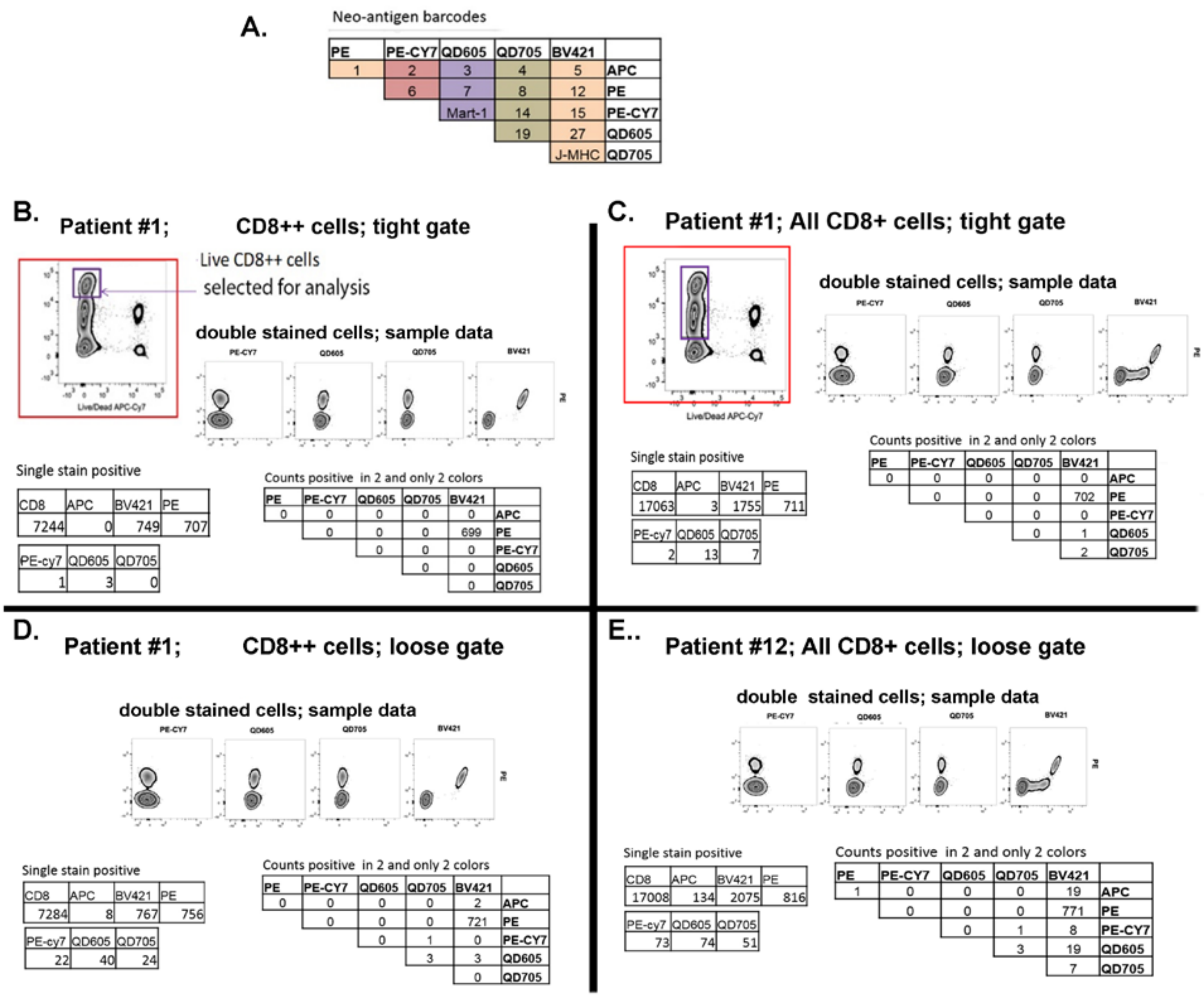

A.

Neo-antigen barcodes

PE	PE-CY7	QD605	QD705	BV421	
1	2	3	4	5	APC
	6	7	8	12	PE
		Mart-1	14	15	PE-CY7
			19	27	QD605
				J-MHC	QD705

B. Patient #1; CD8++ cells; tight gate

double stained cells; sample data

Single stain positive

CD8	APC	BV421	PE
7244	0	749	707

PE-cy7	QD605	QD705
1	3	0

Counts positive in 2 and only 2 colors

PE	PE-CY7	QD605	QD705	BV421	
0	0	0	0	0	APC
	0	0	0	699	PE
		0	0	0	PE-CY7
			0	0	QD605
				0	QD705

C. Patient #1; All CD8+ cells; tight gate

double stained cells; sample data

Single stain positive

CD8	APC	BV421	PE
17063	3	1755	711

PE-cy7	QD605	QD705
2	13	7

Counts positive in 2 and only 2 colors

PE	PE-CY7	QD605	QD705	BV421	
0	0	0	0	0	APC
	0	0	0	702	PE
		0	0	0	PE-CY7
			0	1	QD605
				2	QD705

D. Patient #1; CD8++ cells; loose gate

double stained cells; sample data

Single stain positive

CD8	APC	BV421	PE
7284	8	767	756

PE-cy7	QD605	QD705
22	40	24

Counts positive in 2 and only 2 colors

PE	PE-CY7	QD605	QD705	BV421	
0	0	0	0	2	APC
	0	0	0	721	PE
		0	1	0	PE-CY7
			3	3	QD605
				0	QD705

E.. Patient #12; All CD8+ cells; loose gate

double stained cells; sample data

Single stain positive

CD8	APC	BV421	PE
17008	134	2075	816

PE-cy7	QD605	QD705
73	74	51

Counts positive in 2 and only 2 colors

PE	PE-CY7	QD605	QD705	BV421	
1	0	0	0	19	APC
	0	0	0	771	PE
		0	1	8	PE-CY7
			3	19	QD605
				7	QD705

Figure S8. Multi-color staining flow cytometry analysis of patient #1. A. Color encoding scheme of neoantigen-MHC tetramers. For example, neoantigen #7 tetramer is stained with QD605 and PE. B-E. detection statistics for two selections of CD8+ T cells. The CD8++ subpopulation is analyzed in panels B and D. All CD8+ T cells are analyzed in panel C and E. Each panel incorporated either a tight or loose gating condition for counting those cells that stain with 2 and only 2 colors. Each panel provides the numbers of cells analyzed (single stain positive for CD8), as well as the numbers of cells that stained positive for single stains and two stains. Note that neoantigen #12 specific CD8+ T cells are almost completely localized within the CD8++ subpopulation.

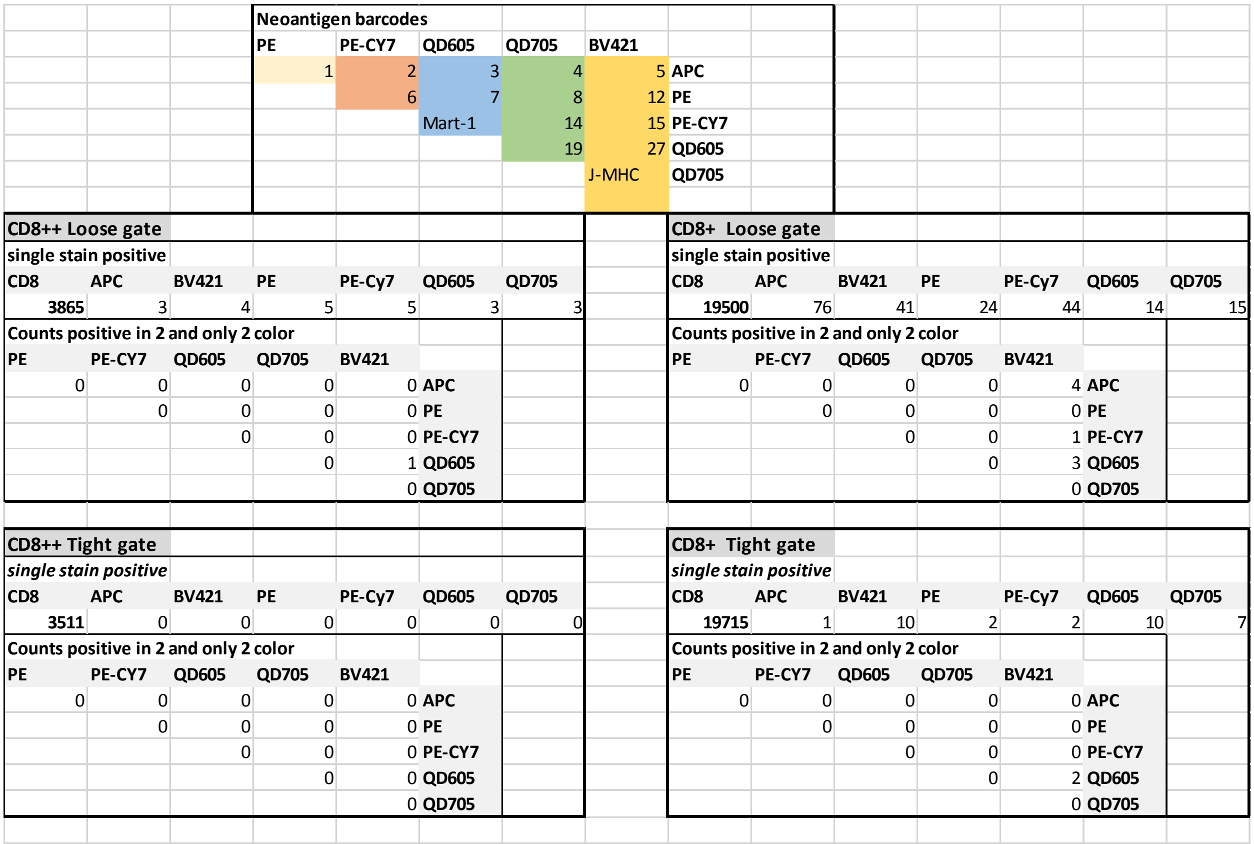

Neoantigen barcodes

PE	PE-CY7	QD605	QD705	BV421	
1	2	3	4	5	APC
	6	7	8	12	PE
		Mart-1	14	15	PE-CY7
			19	27	QD605
				J-MHC	QD705

CD8++ Loose gate

single stain positive

CD8	APC	BV421	PE	PE-Cy7	QD605	QD705
3865	3	4	5	5	3	3

Counts positive in 2 and only 2 color

PE	PE-CY7	QD605	QD705	BV421	
0	0	0	0	0	APC
	0	0	0	0	PE
		0	0	0	PE-CY7
			0	1	QD605
				0	QD705

CD8+ Loose gate

single stain positive

CD8	APC	BV421	PE	PE-Cy7	QD605	QD705
19500	76	41	24	44	14	15

Counts positive in 2 and only 2 color

PE	PE-CY7	QD605	QD705	BV421	
0	0	0	0	4	APC
	0	0	0	0	PE
		0	0	1	PE-CY7
			0	3	QD605
				0	QD705

CD8++ Tight gate

single stain positive

CD8	APC	BV421	PE	PE-Cy7	QD605	QD705
3511	0	0	0	0	0	0

Counts positive in 2 and only 2 color

PE	PE-CY7	QD605	QD705	BV421	
0	0	0	0	0	APC
	0	0	0	0	PE
		0	0	0	PE-CY7
			0	0	QD605
				0	QD705

CD8+ Tight gate

single stain positive

CD8	APC	BV421	PE	PE-Cy7	QD605	QD705
19715	1	10	2	2	10	7

Counts positive in 2 and only 2 color

PE	PE-CY7	QD605	QD705	BV421	
0	0	0	0	0	APC
	0	0	0	0	PE
		0	0	0	PE-CY7
			0	2	QD605
				0	QD705

Figure S9. Flow Cytometry analysis of control patient PBMCs using the neoantigen library of patient #1. The top table presents which neoantigen library elements were dyed with which fluorophores. For example, neoantigen #9 is dyed with QD605 and PE. The lower 4 tables list the numbers of cells that were analyzed (indicated by the number under CD8), and then the numbers of cells that detected as staining positive for a single fluorphore, as well as those that stained positive for two and only two fluorphores. Four different gating conditions are provided. The terms 'tight gate' and 'loose gate' refer to the gating levels set on the 2-color detected cells, not on the CD8 selection. The CD8 selection was either done for CD8+ (right two tables) or the CD8++ subset of the CD8+ cells (left two tables).

I

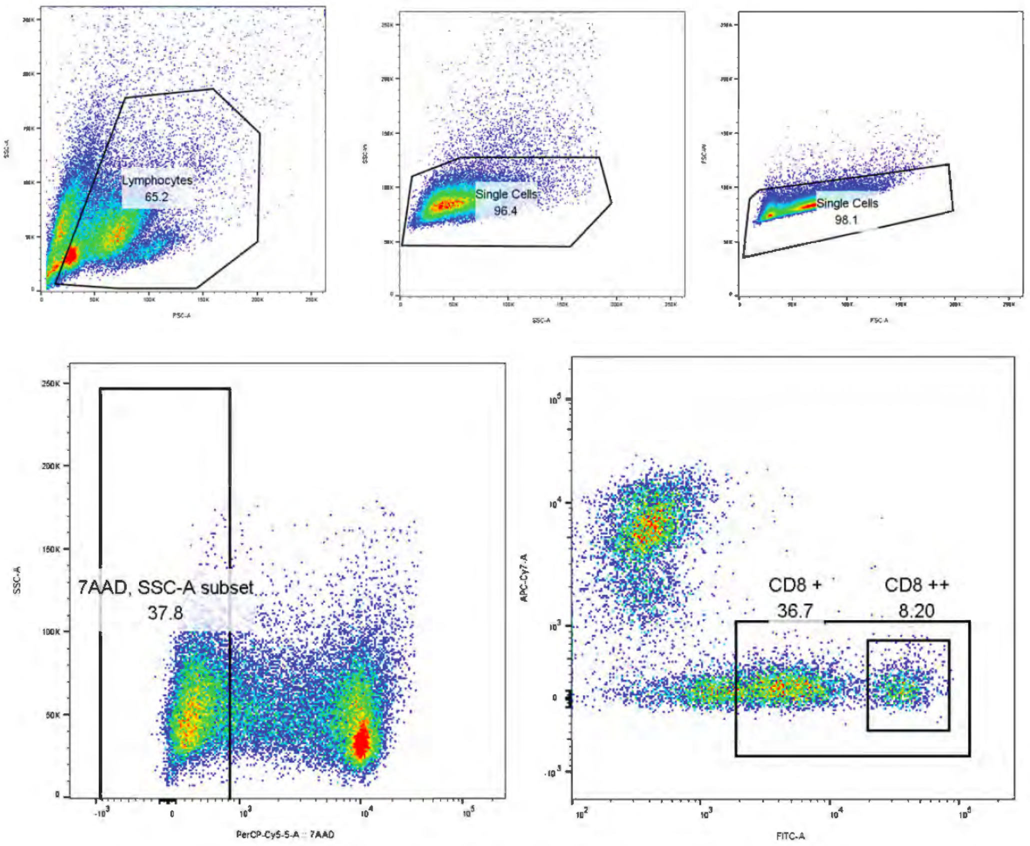

Selection of CD8+ cells for NP-barcoded NACS analysis.

Fig. S10. CD8 + T cells used in the NP-barcoded NACS analysis. TILs tested were expanded long-term (37 days) in-vitro following anti-CD3 (OKT3) + IL-2 stimulation. Chronic stimulation can lead to CD8 and TCR downregulation[1], which we observed as CD8 ++ and CD8 + populations with a 4-fold difference in median fluorescence intensity.

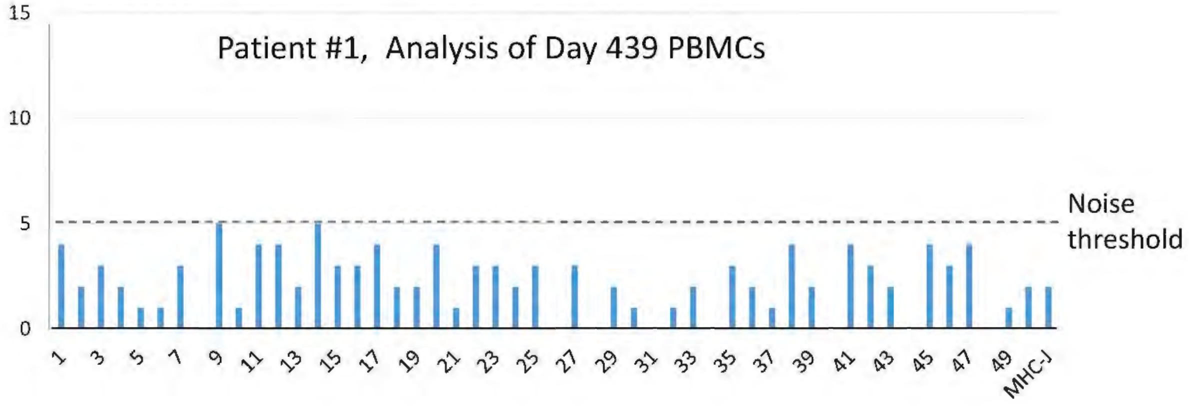

Fig S11. Analysis of patient #1 PBMCs from a blood draw collected 439 days following the start of anti-PD-1 therapy. No populations above two standard deviations of the mean (2.2±1.4 cells per library element) were recorded.

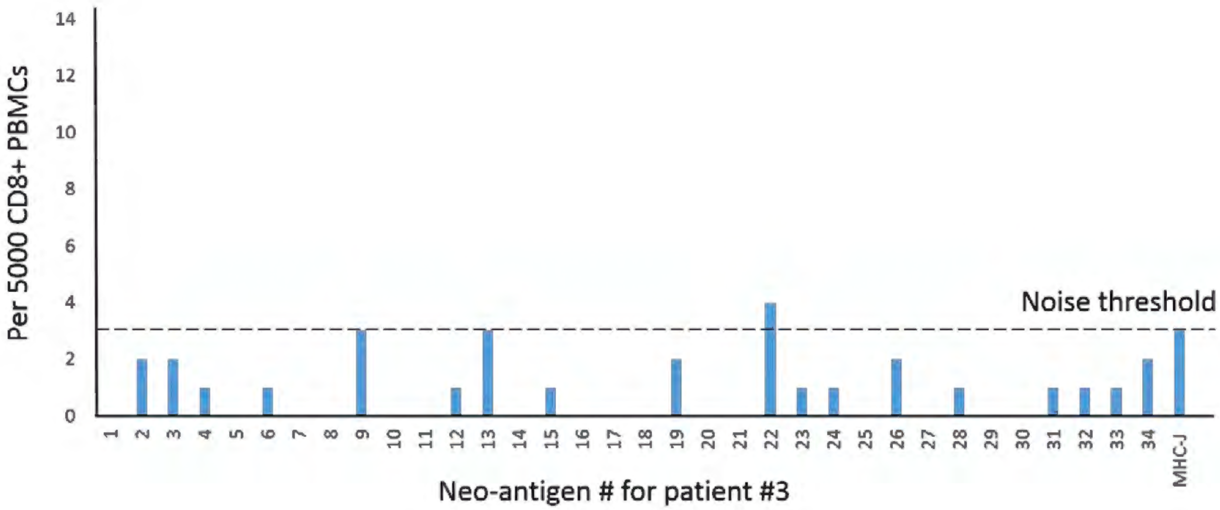

Fig. S12. Results of control experiments in which the NP-barcoded NACS library designed for patient #3 was utilized to capture CD8+ PBMCs from a healthy donor. Average pulled-down T cells from healthy donor PBMC was 0.9 ± 1.1 (mean ± standard deviation). The noise threshold was set at average plus two standard deviations.

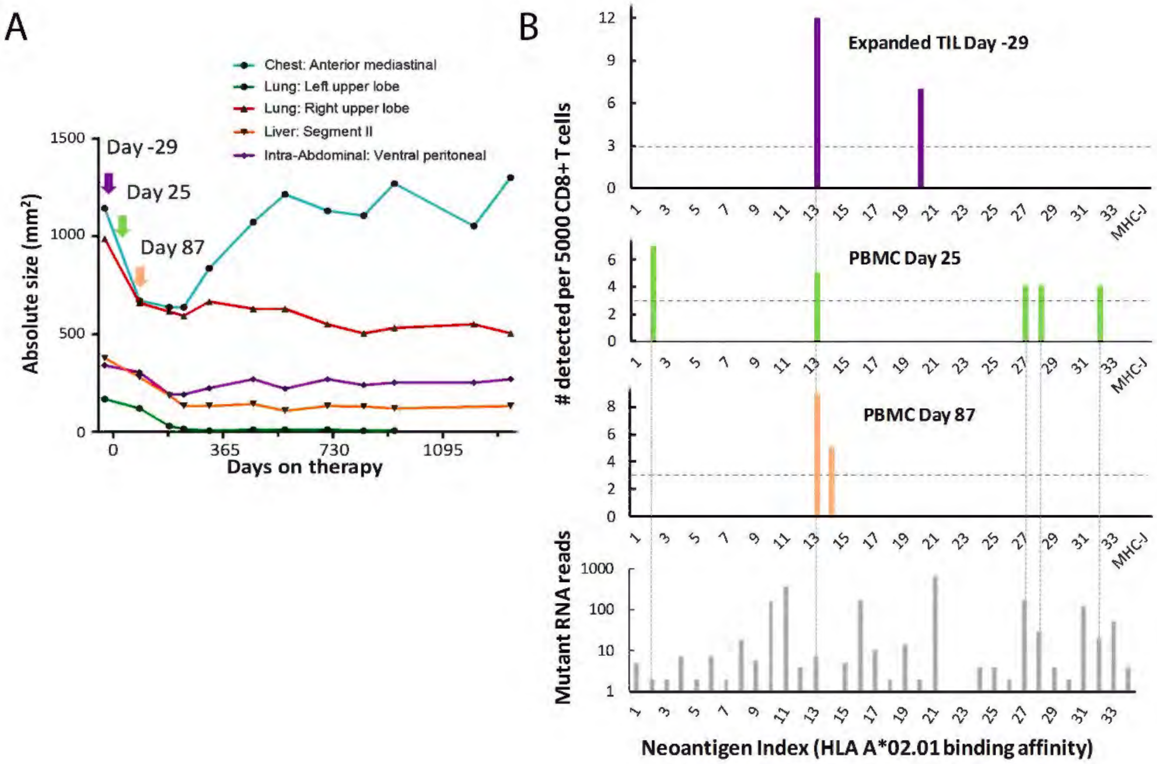

Fig. S13. TIL and PBMC analysis of Patient #3 over the course of response to anti-PD-1 therapy, using the barcoded NP-NACS library to enumerate neoantigen-specific CD8+ T cell populations. **A.** The timeline of the lesion size of chest, lung, liver and intra-abdominal in Patient #3. Day 0 corresponds to the start of anti-PD-1 therapy. A baseline tumor biopsy (indicated by the purple arrow) was collected for genomic and transcriptomic analysis at day -29. Black dots represent CT-scan measurement dates, while the arrows correspond to the time points of analysis, and are color coded for the bar graphs in part B. **B.** Neoantigen-specific T cell populations detected from expanded TILs collected from baseline (top graph) and PBMCs over the course of the therapy (middle two graphs), along with mutation-containing mRNA read counts for the mutant proteins (bottom graph) from the baseline RNA-seq. The horizontal dashed lines in the TIL and PBMC analysis graphs represent the signal threshold above which the identification of a T cell population is statistically significant, which is determined in Fig. S7. The vertical gray dashed lines indicate T cell populations detected across the different time points and patient materials, and their correlation with RNA transcripts reads. Conditional antigen (MHC-J) was used as an internal control.

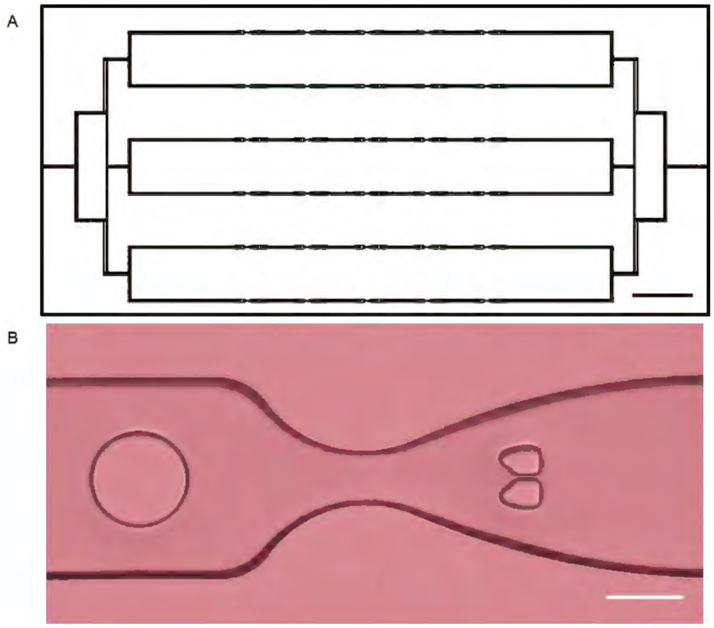

Fig. S14. Microchip design for capture and recovery of NP-barcoded cells for TCR sequencing. **A.** Schematic illustration of the single cell trap device. The single cell traps are designed to be 2 mm apart from each other, which allows the isolation of the specific trapped cell by 1 mm cell puncher without disturbing other trapped cells. **B.** Microscope image of the zoomed in single cell traps. Scale bars for A and B are 2 mm and 50 µm, respectively.

Supplementary Tables

Supplementary Table S1. DNA sequence for constructing library and barcoding

#	Name	DNA sequence
DNA for NP modification (5’-biotin-)		
1	D1-D5-D9	AA AAA AAA A GTG ATG AGT TTC AA ATC AGT CAA GAG AA CTC GTT CAC TAT AA CTG AAT CCT CGG GAT GCC TA
2	D1-D5-D10	AA AAA AAA A GTG ATG AGT TTC AA ATC AGT CAA GAG AA CTT ACG AGT GTA AA CTG AAT CCT CGG GAT GCC TA
3	D1-D5-D11	AA AAA AAA A GTG ATG AGT TTC AA ATC AGT CAA GAG AA TGT CTC TAA GTG AA CTG AAT CCT CGG GAT GCC TA
4	D1-D6-D9	AA AAA AAA A GTG ATG AGT TTC AA GTA TTC GTC ATC AA CTC GTT CAC TAT AA CTG AAT CCT CGG GAT GCC TA
5	D1-D6-D10	AA AAA AAA A GTG ATG AGT TTC AA GTA TTC GTC ATC AA CTT ACG AGT GTA AA CTG AAT CCT CGG GAT GCC TA
6	D1-D6-D11	AA AAA AAA A GTG ATG AGT TTC AA GTA TTC GTC ATC AA TGT CTC TAA GTG AA CTG AAT CCT CGG GAT GCC TA
7	D1-D7-D9	AA AAA AAA A GTG ATG AGT TTC AA GTC AGA TAG TTC AA CTC GTT CAC TAT AA CTG AAT CCT CGG GAT GCC TA
8	D1-D7-D10	AA AAA AAA A GTG ATG AGT TTC AA GTC AGA TAG TTC AA CTT ACG AGT GTA AA CTG AAT CCT CGG GAT GCC TA
9	D1-D7-D11	AA AAA AAA A GTG ATG AGT TTC AA GTC AGA TAG TTC AA TGT CTC TAA GTG AA CTG AAT CCT CGG GAT GCC TA
10	D2-D5-D9	AA AAA AAA A CTA TGT CGA TAC AA ATC AGT CAA GAG AA CTC GTT CAC TAT AA CTG AAT CCT CGG GAT GCC TA
11	D2-D5-D10	AA AAA AAA A CTA TGT CGA TAC AA ATC AGT CAA GAG AA CTT ACG AGT GTA AA CTG AAT CCT CGG GAT GCC TA
12	D2-D5-D11	AA AAA AAA A CTA TGT CGA TAC AA ATC AGT CAA GAG AA TGT CTC TAA GTG AA CTG AAT CCT CGG GAT GCC TA
13	D2-D6-D9	AA AAA AAA A CTA TGT CGA TAC AA GTA TTC GTC ATC AA CTC GTT CAC TAT AA CTG AAT CCT CGG GAT GCC TA
14	D2-D6-D10	AA AAA AAA A CTA TGT CGA TAC AA GTA TTC GTC ATC AA CTT ACG AGT GTA AA CTG AAT CCT CGG GAT GCC TA
15	D2-D6-D11	AA AAA AAA A CTA TGT CGA TAC AA GTA TTC GTC ATC AA TGT CTC TAA GTG AA CTG AAT CCT CGG GAT GCC TA
16	D2-D7-D9	AA AAA AAA A CTA TGT CGA TAC AA GTC AGA TAG TTC AA CTC GTT CAC TAT AA CTG AAT CCT CGG GAT GCC TA
17	D2-D7-D10	AA AAA AAA A CTA TGT CGA TAC AA GTC AGA TAG TTC AA CTT ACG AGT GTA AA CTG AAT CCT CGG GAT GCC TA
18	D2-D7-D11	AA AAA AAA A CTA TGT CGA TAC AA GTC AGA TAG TTC AA TGT CTC TAA GTG AA CTG AAT CCT CGG GAT GCC TA
19	D3-D5-D9	AA AAA AAA A TAC ATC CAA GAC AA ATC AGT CAA GAG AA CTC GTT CAC TAT AA CTG AAT CCT CGG GAT GCC TA
20	D3-D5-D10	AA AAA AAA A TAC ATC CAA GAC AA ATC AGT CAA GAG AA CTT ACG AGT GTA AA CTG AAT CCT CGG GAT GCC TA

21	D3-D5-D11	AA AAA AAA A TAC ATC CAA GAC AA ATC AGT CAA GAG AA TGT CTC TAA GTG AA CTG AAT CCT CGG GAT GCC TA
22	D3-D6-D9	AA AAA AAA A TAC ATC CAA GAC AA GTA TTC GTC ATC AA CTC GTT CAC TAT AA CTG AAT CCT CGG GAT GCC TA
23	D3-D6-D10	AA AAA AAA A TAC ATC CAA GAC AA GTA TTC GTC ATC AA CTT ACG AGT GTA AA CTG AAT CCT CGG GAT GCC TA
24	D3-D6-D11	AA AAA AAA A TAC ATC CAA GAC AA GTA TTC GTC ATC AA TGT CTC TAA GTG AA CTG AAT CCT CGG GAT GCC TA
25	D3-D7-D9	AA AAA AAA A TAC ATC CAA GAC AA GTC AGA TAG TTC AA CTC GTT CAC TAT AA CTG AAT CCT CGG GAT GCC TA
26	D3-D7-D10	AA AAA AAA A TAC ATC CAA GAC AA GTC AGA TAG TTC AA CTT ACG AGT GTA AA CTG AAT CCT CGG GAT GCC TA
27	D3-D7-D11	AA AAA AAA A TAC ATC CAA GAC AA GTC AGA TAG TTC AA TGT CTC TAA GTG AA CTG AAT CCT CGG GAT GCC TA
DNA for barcoding		
	M1	5-Cy5-AGC ACA GGG AAA CTC ATC AC
	M2	5-Cy3- GCA TCA TCG TAT CGA CAT AG
	M3	5-Alex488-ATG GTT CGG TCT TGG ATG TA
	M5	5-Cy5-CGC CAA TGC TCT TGA CTG AT
	M6	5-Cy3- AGG ACT TCG ATG ACG AAT AC
	M7	5-Alex488-ATC CTT GCG AAC TAT CTG AC
	M9	5-Cy5-GCC GTA TCA TAG TGA ACG AG
	M10	5-Cy3- CCA GCG ATT ACA CTC GTA AG
	M11	5-Alex488-CAG ACC TGC ACT TAG AGA CA
DNA for displacement		
	M1 comp	GTG ATG AGT TTC CCT GTG CT
	M2 comp	CTA TGT CGA TAC GAT GAT GC
	M3 comp	TAC ATC CAA GAC CGA ACC AT
	M5 comp	ATC AGT CAA GAG CAT TGG CG
	M6 comp	GTA TTC GTC ATC GAA GTC CT
	M7 comp	GTC AGA TAG TTC GCA AGG AT
	M9 comp	CTC GTT CAC TAT GAT ACG GC
	M10 comp	CTT ACG AGT GTA ATC GCT GG
	M11 comp	TGT CTC TAA GTG CAG GTC TG
DNA for streptavidin labeling		
	DNA-SAC	5-NH_2-AAA AAA AAA A TAG GCA TCC CGA GGA TTC AG

Supplementary Table S2. Fluorescent decoding table

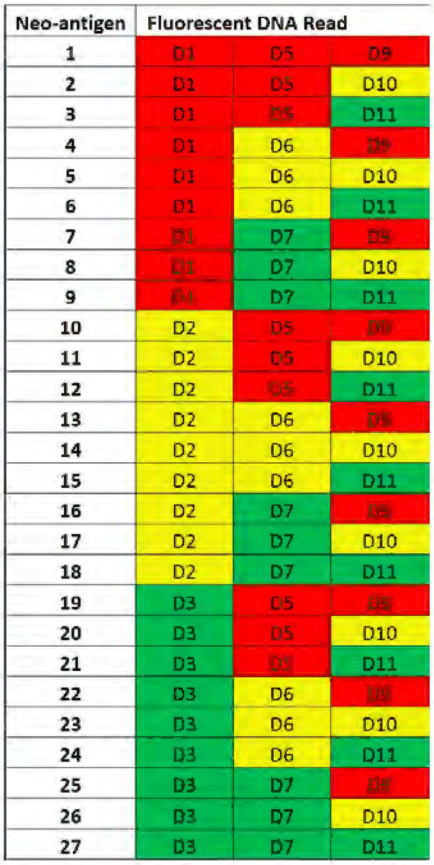

Neo-antigen	Fluorescent DNA Read		
1	D1	D5	D9
2	D1	D5	D10
3	D1	D5	D11
4	D1	D6	D9
5	D1	D6	D10
6	D1	D6	D11
7	D1	D7	D9
8	D1	D7	D10
9	D1	D7	D11
10	D2	D5	D9
11	D2	D5	D10
12	D2	D5	D11
13	D2	D6	D9
14	D2	D6	D10
15	D2	D6	D11
16	D2	D7	D9
17	D2	D7	D10
18	D2	D7	D11
19	D3	D5	D9
20	D3	D5	D10
21	D3	D5	D11
22	D3	D6	D9
23	D3	D6	D10
24	D3	D6	D11
25	D3	D7	D9
26	D3	D7	D10
27	D3	D7	D11

Supplementary Table S3. Putative neo-antigens for Patient #1

#	Neo-antigen	K_d (nM)	#	Neo-antigen	K_d (nM)
1	F(S)LGSLILV	5	27	KMGKTIYKY(H)V	76
2	RLS(P)SCFDYV	9	28	NLFNTYL(P)CL	77
3	S(P)LMNEDFIL	11	29	RLSEV(A)MARM	82
4	F(S)LGSLLILVV	11	30	VLTEIF(S)LGSL	105
5	S(P)LMNEDFILA	11	31	ALYKEE(G)EQEPV	133
6	SLHD(G)LTDGV	12	32	VLIDLIQRTKV(D)	134
7	KAWENF(S)PNV	14	33	MVC(R)TFCPPPL	138
8	LLSEFF(S)SCL	18	34	LLFHS(P)PRAHL	139
9	KLLSEFF(S)SCL	20	35	V(M)LLHAFEGYNV	147
10	LQ(R)DSGLWFPV	21	36	VTSSIVTL(P)V	158
11	S(P)LMNEDFILAV	25	37	SL(P)APPRTPEL	212
12	Y(D)LYHRVDVI	28	38	F(S)FVEASMSV	223

13	FVANLFNTYL(P)	29	39	S(C)MLTARSWDSV	248
14	GLFH(R)SLYRSV	29	40	FVLE(D)HEDGLNL	261
15	GLSE(G)KCSLV	36	41	SLQT(A)NVQRL	273
16	HLQ(R)DSGLWFPV	39	42	KVKCIPF(Y)AV	313
17	TLANRFS(P)AV	45	43	FVFSKYC(R)HRA	366
18	FLVIV(A)PLSTI	48	44	S(N)LVPEDEANI	368
19	GLSE(G)KCSLVV	57	45	ILPFF(L)YLGSA	380
20	F(P)LHGNSLYQKV	61	46	RI(N)AGEEVTLTV	416
21	F(S)LRESQETL	65	47	VLT(A)RLALLQL	418
22	LLSEFF(S)SCLA	66	48	LLEYRI(S)SENPV	440
23	QLDS(P)GTLIV	67	49	MQQPSPQ(P)IPPV	449
24	WMGLL(P)DLEV	67	50	GLFH(R)SLYRS	463
25	FVLE(D)HEDGL	71			
26	TL(P)VSLATETV	75			

-Letter in the bracket indicates the native peptide.

Supplementary Table S4. Putative neo-antigens for Patient #2

#	Neo-antigen	K_d (nM)	#	Neo-antigen	K_d (nM)
1	LLTDLLFL(S)I	4	15	TVLGTPF(S)EV	26
2	RLMERSIY(H)SA	7	16	SIY(H)SARYIFV	26
3	FLVNDWLL(S)V	8	17	YLAHWLYY(H)Y	27
4	FLDSC(S)PHLPL	8	18	KIS(P)SQPPPV	28
5	KMNELNY(H)CI	10	19	KL(S)STFLMKA	29
6	RLLTDLLFL(S)I	10	20	FTLFELAF(S)L	31
7	RLANLIW(R)RA	11	21	FLPRKENI(S)SV	31
8	RLLTDLLFL(S)	12	22	VLQGC(R)LPCPV	31
9	RIYTEMC(R)FTV	13	23	F(S)LANSGGWV	33
10	VL(P)FEKKDFV	16	24	YILLYKN(D)GV	37
11	KIFCASF(S)RI	17	25	F(S)LYKSQGEI	40
12	FL(S)IETDIQM	17	26	FIS(P)WGPASI	44
13	QLFQL(P)YNFEL	23	27	LL(S)YELQPGT	44
14	VLYFN(H)HYFPA	24	28	NLY(H)EEDALL	45

-Letter in the bracket indicates the native peptide.

Supplementary Table S5. Putative neo-antigens for Patient #3

#	Neo-antigen	K_d (nM)	#	Neo-antigen	K_d (nM)
1	F(S)LDVALFLL	6	18	KLTELLFS(P)YI	19

2	F(S)LLGLPNPA	7	19	SLTAHF(S)LLPL	21
3	S(P)MDDLISLL	7	20	FS(P)MDDLISL	22
4	ALKE(G)YLYAV	7	21	FLKLCEK(E)WPV	26
5	F(S)LLGLPNPAL	8	22	KLAQTF(L)GLEV	27
6	SMI(M)EKSELV	9	23	LLC(R)PYPASL	28
7	YLLEAI(V)REGL	9	24	IIFS(P)ILSNPV	31
8	ILASC(R)CLHV	10	25	LMGTSLHLI(V)	32
9	TL(S)MGDMPSA	10	26	VLQR(G)LSLEV	32
10	CLNS(P)FVYIV	12	27	GMGKIL(P)SAV	41
11	FS(P)GEYIPTV	14	28	KLLLRLPV(A)L	43
12	TLMGTSLHLI(V)	14	29	SLHLI(V)FQMGV	45
13	SMMGHK(E)VKV	15	30	FS(P)MDDLISLL	45
14	R(G)MDEQLTSL	15	31	TMFQNLFS(P)SI	46
15	MV(A)ADGLFFQV	15	32	ALC(R)AAQHWV	49
16	KIL(P)SAVSTV	16	33	F(S)QLVACTKV	50
17	L(P)LIKYFAEA	17	34	TLAK(E)GTFTPL	50

-Letter in the bracket indicates the native peptide.

Supplementary Table S6. Full analysis of neoantigens and mutated genes for Patient #1.

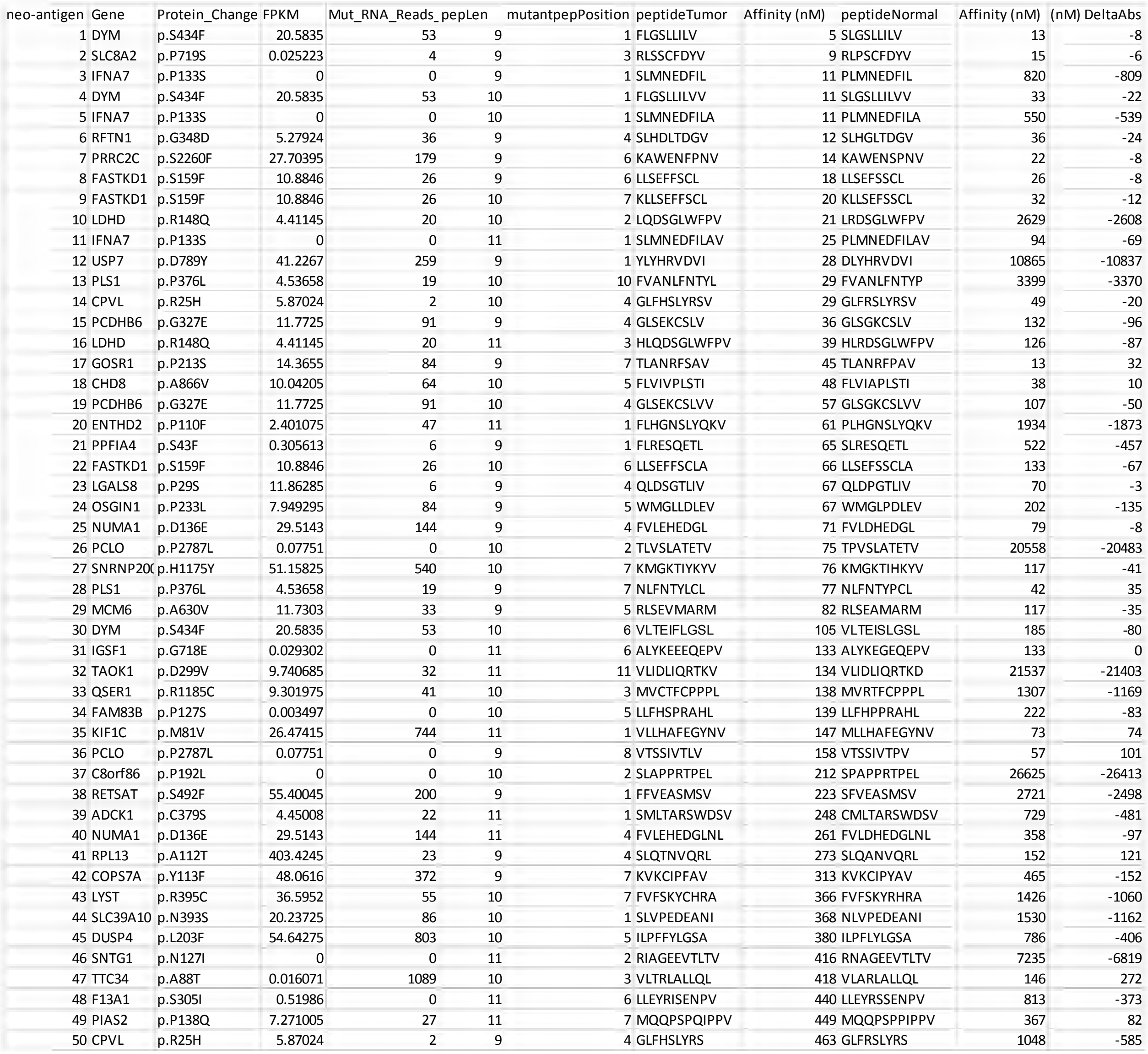

neo-antigen	Gene	Protein_Change	FPKM	Mut_RNA_Reads_	pepLen	mutantpepPosition	peptideTumor	Affinity (nM)	peptideNormal	Affinity (nM)	(nM) DeltaAbs
1	DYM	p.S434F	20.5835	53	9	1	FLGSLLILV	5	SLGSLLILV	13	-8
2	SLC8A2	p.P719S	0.025223	4	9	3	RLSSCFDYV	9	RLPSCFDYV	15	-6
3	IFNA7	p.P133S	0	0	9	1	SLMNEDFIL	11	PLMNEDFIL	820	-809
4	DYM	p.S434F	20.5835	53	10	1	FLGSLLILVV	11	SLGSLLILVV	33	-22
5	IFNA7	p.P133S	0	0	10	1	SLMNEDFILA	11	PLMNEDFILA	550	-539
6	RFTN1	p.G348D	5.27924	36	9	4	SLHDLTDGV	12	SLHGLTDGV	36	-24
7	PRRC2C	p.S2260F	27.70395	179	9	6	KAWENFPNV	14	KAWENSPNV	22	-8
8	FASTKD1	p.S159F	10.8846	26	9	6	LLSEFFSCL	18	LLSEFSSCL	26	-8
9	FASTKD1	p.S159F	10.8846	26	10	7	KLLSEFFSCL	20	KLLSEFSSCL	32	-12
10	LDHD	p.R148Q	4.41145	20	10	2	LQDSGLWFPV	21	LRDSGLWFPV	2629	-2608
11	IFNA7	p.P133S	0	0	11	1	SLMNEDFILAV	25	PLMNEDFILAV	94	-69
12	USP7	p.D789Y	41.2267	259	9	1	YLYHRVDVI	28	DLYHRVDVI	10865	-10837
13	PLS1	p.P376L	4.53658	19	10	10	FVANLFNTYL	29	FVANLFNTYP	3399	-3370
14	CPVL	p.R25H	5.87024	2	10	4	GLFHSLYRSV	29	GLFRSLYRSV	49	-20
15	PCDHB6	p.G327E	11.7725	91	9	4	GLSEKCSLV	36	GLSGKCSLV	132	-96
16	LDHD	p.R148Q	4.41145	20	11	3	HLQDSGLWFPV	39	HLRDSGLWFPV	126	-87
17	GOSR1	p.P213S	14.3655	84	9	7	TLANRFSAV	45	TLANRFPAV	13	32
18	CHD8	p.A866V	10.04205	64	10	5	FLVIVPLSTI	48	FLVIAPLSTI	38	10
19	PCDHB6	p.G327E	11.7725	91	10	4	GLSEKCSLVV	57	GLSGKCSLVV	107	-50
20	ENTHD2	p.P110F	2.401075	47	11	1	FLHGNSLYQKV	61	PLHGNSLYQKV	1934	-1873
21	PPFIA4	p.S43F	0.305613	6	9	1	FLRESQETL	65	SLRESQETL	522	-457
22	FASTKD1	p.S159F	10.8846	26	10	6	LLSEFFSCLA	66	LLSEFSSCLA	133	-67
23	LGALS8	p.P29S	11.86285	6	9	4	QLDSGTLIV	67	QLDPGTLIV	70	-3
24	OSGIN1	p.P233L	7.949295	84	9	5	WMGLLDLEV	67	WMGLPDLEV	202	-135
25	NUMA1	p.D136E	29.5143	144	9	4	FVLEHEDGL	71	FVLDHEDGL	79	-8
26	PCLO	p.P2787L	0.07751	0	10	2	TLVSLATETV	75	TPVSLATETV	20558	-20483
27	SNRNP20(	p.H1175Y	51.15825	540	10	7	KMGKTIYKYV	76	KMGKTIHKYV	117	-41
28	PLS1	p.P376L	4.53658	19	9	7	NLFNTYLCL	77	NLFNTYPCL	42	35
29	MCM6	p.A630V	11.7303	33	9	5	RLSEVMARM	82	RLSEAMARM	117	-35
30	DYM	p.S434F	20.5835	53	10	6	VLTEIFLGSL	105	VLTEISLGSL	185	-80
31	IGSF1	p.G718E	0.029302	0	11	6	ALYKEEEQEPV	133	ALYKEGEQEPV	133	0
32	TAOK1	p.D299V	9.740685	32	11	11	VLIDLIQRTKV	134	VLIDLIQRTKD	21537	-21403
33	QSER1	p.R1185C	9.301975	41	10	3	MVCTFCPPPL	138	MVRTFCPPPL	1307	-1169
34	FAM83B	p.P127S	0.003497	0	10	5	LLFHSPRAHL	139	LLFHPPRAHL	222	-83
35	KIF1C	p.M81V	26.47415	744	11	1	VLLHAFEGYNV	147	MLLHAFEGYNV	73	74
36	PCLO	p.P2787L	0.07751	0	9	8	VTSSIVTLV	158	VTSSIVTPV	57	101
37	C8orf86	p.P192L	0	0	10	2	SLAPPRTPEL	212	SPAPPRTPEL	26625	-26413
38	RETSAT	p.S492F	55.40045	200	9	1	FFVEASMSV	223	SFVEASMSV	2721	-2498
39	ADCK1	p.C379S	4.45008	22	11	1	SMLTARSWDSV	248	CMLTARSWDSV	729	-481
40	NUMA1	p.D136E	29.5143	144	11	4	FVLEHEDGLNL	261	FVLDHEDGLNL	358	-97
41	RPL13	p.A112T	403.4245	23	9	4	SLQTNVQRL	273	SLQANVQRL	152	121
42	COPS7A	p.Y113F	48.0616	372	9	7	KVKCIPFAV	313	KVKCIPYAV	465	-152
43	LYST	p.R395C	36.5952	55	10	7	FVFSKYCHRA	366	FVFSKYRHRA	1426	-1060
44	SLC39A10	p.N393S	20.23725	86	10	1	SLVPEDEANI	368	NLVPEDEANI	1530	-1162
45	DUSP4	p.L203F	54.64275	803	10	5	ILPFFYLGSA	380	ILPFLYLGSA	786	-406
46	SNTG1	p.N127I	0	0	11	2	RIAGEEVTLTV	416	RNAGEEVTLTV	7235	-6819
47	TTC34	p.A88T	0.016071	1089	10	3	VLTRLALLQL	418	VLARLALLQL	146	272
48	F13A1	p.S305I	0.51986	0	11	6	LLEYRISENPV	440	LLEYRSSENPV	813	-373
49	PIAS2	p.P138Q	7.271005	27	11	7	MQQPSPQIPPV	449	MQQPSPPIPPV	367	82
50	CPVL	p.R25H	5.87024	2	9	4	GLFHSLYRS	463	GLFRSLYRS	1048	-585

Supplementary Table S7. Full analysis of neoantigens and mutated genes for Patient #2.

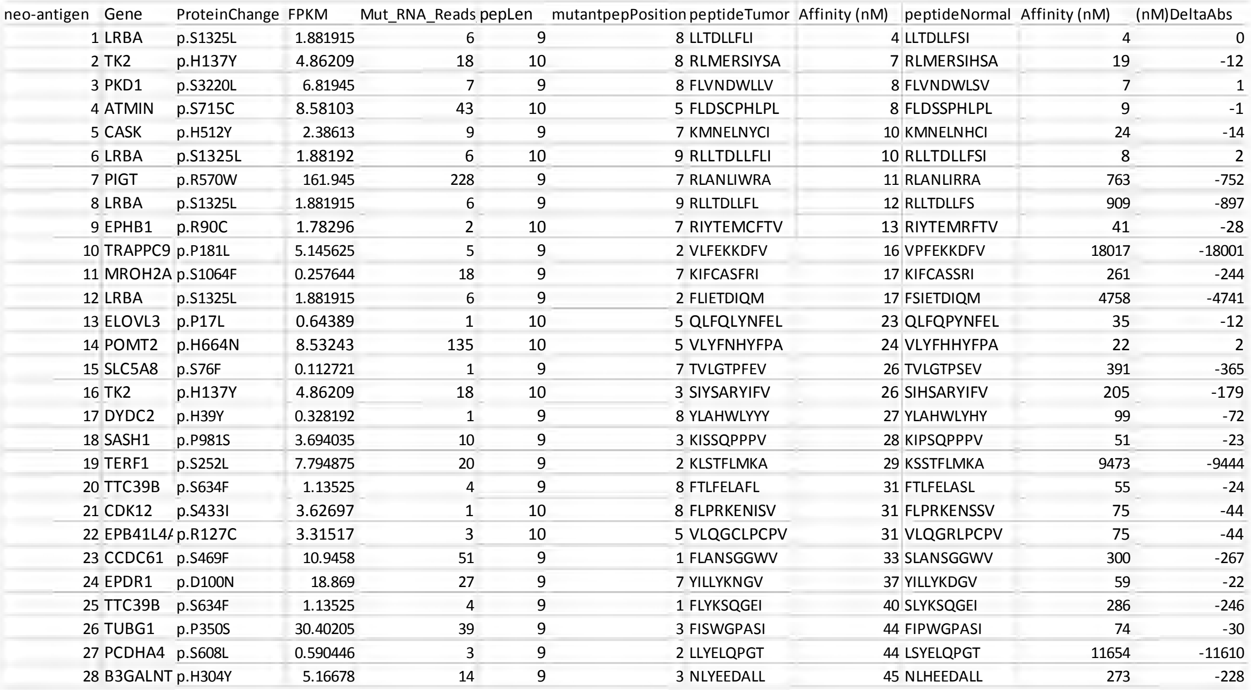

neo-antigen	Gene	ProteinChange	FPKM	Mut_RNA_Reads	pepLen	mutantpepPosition	peptideTumor	Affinity (nM)	peptideNormal	Affinity (nM)	(nM)DeltaAbs
1	LRBA	p.S1325L	1.881915	6	9	8	LLTDLLFLI	4	LLTDLLFSI	4	0
2	TK2	p.H137Y	4.86209	18	10	8	RLMERSIYSA	7	RLMERSIHSA	19	-12
3	PKD1	p.S3220L	6.81945	7	9	8	FLVNDWLLV	8	FLVNDWLSV	7	1
4	ATMIN	p.S715C	8.58103	43	10	5	FLDSCPHLPL	8	FLDSSPHLPL	9	-1
5	CASK	p.H512Y	2.38613	9	9	7	KMNELNYCI	10	KMNELNHCI	24	-14
6	LRBA	p.S1325L	1.88192	6	10	9	RLLTDLLFLI	10	RLLTDLLFSI	8	2
7	PIGT	p.R570W	161.945	228	9	7	RLANLIWRA	11	RLANLIRRA	763	-752
8	LRBA	p.S1325L	1.881915	6	9	9	RLLTDLLFL	12	RLLTDLLFS	909	-897
9	EPHB1	p.R90C	1.78296	2	10	7	RIYTEMCFTV	13	RIYTEMRFTV	41	-28
10	TRAPPC9	p.P181L	5.145625	5	9	2	VLFEKKDFV	16	VPFEKKDFV	18017	-18001
11	MROH2A	p.S1064F	0.257644	18	9	7	KIFCASFRI	17	KIFCASSRI	261	-244
12	LRBA	p.S1325L	1.881915	6	9	2	FLIETDIQM	17	FSIETDIQM	4758	-4741
13	ELOVL3	p.P17L	0.64389	1	10	5	QLFQLYNFEL	23	QLFQPYNFEL	35	-12
14	POMT2	p.H664N	8.53243	135	10	5	VLYFNHYFPA	24	VLYFHHYFPA	22	2
15	SLC5A8	p.S76F	0.112721	1	9	7	TVLGTPFEV	26	TVLGTPSEV	391	-365
16	TK2	p.H137Y	4.86209	18	10	3	SIYSARYIFV	26	SIHSARYIFV	205	-179
17	DYDC2	p.H39Y	0.328192	1	9	8	YLAHWLYYY	27	YLAHWLYHY	99	-72
18	SASH1	p.P981S	3.694035	10	9	3	KISSQPPPV	28	KIPSQPPPV	51	-23
19	TERF1	p.S252L	7.794875	20	9	2	KLSTFLMKA	29	KSSTFLMKA	9473	-9444
20	TTC39B	p.S634F	1.13525	4	9	8	FTLFELAFL	31	FTLFELASL	55	-24
21	CDK12	p.S433I	3.62697	1	10	8	FLPRKENISV	31	FLPRKENSSV	75	-44
22	EPB41L4	p.R127C	3.31517	3	10	5	VLQGCLPCPV	31	VLQGRLPCPV	75	-44
23	CCDC61	p.S469F	10.9458	51	9	1	FLANSGGWV	33	SLANSGGWV	300	-267
24	EPDR1	p.D100N	18.869	27	9	7	YILLYKNGV	37	YILLYKDGV	59	-22
25	TTC39B	p.S634F	1.13525	4	9	1	FLYKSQGEI	40	SLYKSQGEI	286	-246
26	TUBG1	p.P350S	30.40205	39	9	3	FISWGPASI	44	FIPWGPASI	74	-30
27	PCDHA4	p.S608L	0.590446	3	9	2	LLYELQPGT	44	LSYELQPGT	11654	-11610
28	B3GALNT	p.H304Y	5.16678	14	9	3	NLYEEDALL	45	NLHEEDALL	273	-228

Supplementary Table S8. Full analysis of neoantigens and mutated genes for Patient #3.

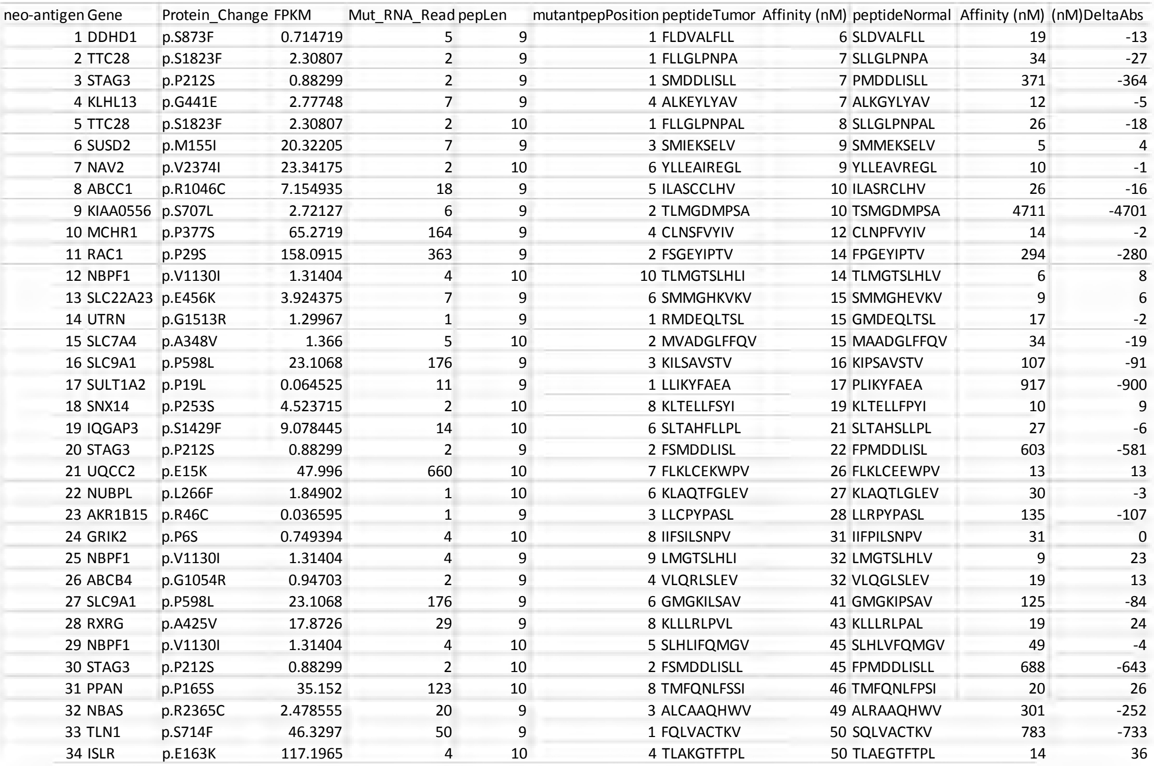

neo-antigen	Gene	Protein_Change	FPKM	Mut_RNA_Read	pepLen	mutantpepPosition	peptideTumor	Affinity (nM)	peptideNormal	Affinity (nM)	(nM)DeltaAbs
1	DDHD1	p.S873F	0.714719	5	9	1	FLDVALFLL	6	SLDVALFLL	19	-13
2	TTC28	p.S1823F	2.30807	2	9	1	FLLGLPNPA	7	SLLGLPNPA	34	-27
3	STAG3	p.P212S	0.88299	2	9	1	SMDDLISLL	7	PMDDLISLL	371	-364
4	KLHL13	p.G441E	2.77748	7	9	4	ALKEYLYAV	7	ALKGYLYAV	12	-5
5	TTC28	p.S1823F	2.30807	2	10	1	FLLGLPNPAL	8	SLLGLPNPAL	26	-18
6	SUSD2	p.M155I	20.32205	7	9	3	SMIEKSELV	9	SMMEKSELV	5	4
7	NAV2	p.V2374I	23.34175	2	10	6	YLLEAIREGL	9	YLLEAVREGL	10	-1
8	ABCC1	p.R1046C	7.154935	18	9	5	ILASCCLHV	10	ILASRCLHV	26	-16
9	KIAA0556	p.S707L	2.72127	6	9	2	TLMGDMPSA	10	TSMGDMPSA	4711	-4701
10	MCHR1	p.P377S	65.2719	164	9	4	CLNSFVYIV	12	CLNPFVYIV	14	-2
11	RAC1	p.P29S	158.0915	363	9	2	FSGEYIPTV	14	FPGEYIPTV	294	-280
12	NBPF1	p.V1130I	1.31404	4	10	10	TLMGTSLHLI	14	TLMGTSLHLV	6	8
13	SLC22A23	p.E456K	3.924375	7	9	6	SMMGHKVKV	15	SMMGHEVKV	9	6
14	UTRN	p.G1513R	1.29967	1	9	1	RMDEQLTSL	15	GMDEQLTSL	17	-2
15	SLC7A4	p.A348V	1.366	5	10	2	MVADGLFFQV	15	MAADGLFFQV	34	-19
16	SLC9A1	p.P598L	23.1068	176	9	3	KILSAVSTV	16	KIPSAVSTV	107	-91
17	SULT1A2	p.P19L	0.064525	11	9	1	LLIKYFAEA	17	PLIKYFAEA	917	-900
18	SNX14	p.P253S	4.523715	2	10	8	KLTELLFSYI	19	KLTELLFPYI	10	9
19	IQGAP3	p.S1429F	9.078445	14	10	6	SLTAHFLLPL	21	SLTAHSLLPL	27	-6
20	STAG3	p.P212S	0.88299	2	9	2	FSMDDLISL	22	FPMDDLISL	603	-581
21	UQCC2	p.E15K	47.996	660	10	7	FLKLCEKWPV	26	FLKLCEEWPV	13	13
22	NUBPL	p.L266F	1.84902	1	10	6	KLAQTFGLEV	27	KLAQTLGLEV	30	-3
23	AKR1B15	p.R46C	0.036595	1	9	3	LLCPYPASL	28	LLRPYPASL	135	-107
24	GRIK2	p.P6S	0.749394	4	10	8	IIFSILSNPV	31	IIFPILSNPV	31	0
25	NBPF1	p.V1130I	1.31404	4	9	9	LMGTSLHLI	32	LMGTSLHLV	9	23
26	ABCB4	p.G1054R	0.94703	2	9	4	VLQRLSLEV	32	VLQGLSLEV	19	13
27	SLC9A1	p.P598L	23.1068	176	9	6	GMGKILSAV	41	GMGKIPSAV	125	-84
28	RXRG	p.A425V	17.8726	29	9	8	KLLLRLPVL	43	KLLLRLPAL	19	24
29	NBPF1	p.V1130I	1.31404	4	10	5	SLHLIFQMGV	45	SLHLVFQMGV	49	-4
30	STAG3	p.P212S	0.88299	2	10	2	FSMDDLISLL	45	FPMDDLISLL	688	-643
31	PPAN	p.P165S	35.152	123	10	8	TMFQNLFSSI	46	TMFQNLFPSI	20	26
32	NBAS	p.R2365C	2.478555	20	9	3	ALCAAQHWV	49	ALRAAQHWV	301	-252
33	TLN1	p.S714F	46.3297	50	9	1	FQLVACTKV	50	SQLVACTKV	783	-733
34	ISLR	p.E163K	117.1965	4	10	4	TLAKGTFTPL	50	TLAEGTFTPL	14	36

Supplementary Table S9: ELISpot count for healthy PBMC T cells and Day 41 PBMC for patient #1.

Neo-antigen tetramer	Count for PBMC from patient #1	Count for healthy PBMC T cells
1	0	2
2	0	0
5	2	1
7	1	0
9	8	1
10	0	1
12	5	3
14	2	0
15	6	1
19	5	0
27	5	0
35	2	1
38	2	2
45	3	1

The average background noise level from healthy PBMC T cells were detected as 1 spot.

Supplementary Table S10: single cell TCRα cloning primers

Vα-gene-specific primers for cloning TCRα genes		
TRAV gene	**Signal peptide sequence**	**TRAV gene-specific sequence**
TRAV1-1*01	5'-TACAGGAAGCCTCAGCA	GGACAAAGCCTTGAGCAGCCCTC-3'
TRAV1-2*01	5'-TACAGGAAGCCTCAGCA	GGACAAAACATTGACCAGCCCACTG-3'
TRAV2*01	5'-TACAGGAAGCCTCAGCA	AAGGACCAAGTGTTTCAGCCTTCCAC-3'
TRAV3*01	5'-TACAGGAAGCCTCAGCA	GCTCAGTCAGTGGCTCAGCCGGA-3'
TRAV4*01	5'-TACAGGAAGCCTCAGCA	CTTGCTAAGACCACCCAGCCCATC-3'
TRAV5*01	5'-TACAGGAAGCCTCAGCA	GGAGAGGATGTGGAGCAGAGTCTTTTCC-3'
TRAV6*01	5'-TACAGGAAGCCTCAGCA	AGCCAAAAGATAGAACAGAATTCCGAGGC-3'
TRAV6*03	5'-TACAGGAAGCCTCAGCA	GAGGCCCTGAACATTCAGGAGGG-3'
TRAV7*01	5'-TACAGGAAGCCTCAGCA	GAAAACCAGGTGGAGCACAGCCC-3'
TRAV8-1*01	5'-TACAGGAAGCCTCAGCA	GCCCAGTCTGTGAGCCAGCATAACC-3'
TRAV8-2*01	5'-TACAGGAAGCCTCAGCA	GCCCAGTCGGTGACCCAGCTTG-3'
TRAV8-2*02	5'-TACAGGAAGCCTCAGCA	GCCCAGTCGGTGACCCAGCTTAG-3'
TRAV8-3*01	5'-TACAGGAAGCCTCAGCA	GCCCAGTCAGTGACCCAGCCTG-3'
TRAV8-4*06	5'-TACAGGAAGCCTCAGCA	CTCTTCTGGTATGTGCAATACCCCAACC-3'
TRAV8-4*07	5'-TACAGGAAGCCTCAGCA	GTTGAACCATATCTCTTCTGGTATGTGCAATACC-3'
TRAV8-6*01	5'-TACAGGAAGCCTCAGCA	GCCCAGTCTGTGACCCAGCTTGAC-3'
TRAV8-7*01	5'-TACAGGAAGCCTCAGCA	ACCCAGTCGGTGACCCAGCTTG-3'
TRAV9-1*01	5'-TACAGGAAGCCTCAGCA	GGAGATTCAGTGGTCCAGACAGAAGGC-3'
TRAV9-2*01	5'-TACAGGAAGCCTCAGCA	GGAAATTCAGTGACCCAGATGGAAGG-3'
TRAV9-2*02	5'-TACAGGAAGCCTCAGCA	GGAGATTCAGTGACCCAGATGGAAGG-3'
TRAV10*01	5'-TACAGGAAGCCTCAGCA	AAAAACCAAGTGGAGCAGAGTCCTCAGTC-3'
TRAV11*01	5'-TACAGGAAGCCTCAGCA	CTACATACACTGGAGCAGAGTCCTTCATTCC-3'
TRAV12-1*01	5'-TACAGGAAGCCTCAGCA	CGGAAGGAGGTGGAGCAGGATCC-3'

TRAV12-2*01	5'-TACAGGAAGCCTCAGCA	CAGAAGGAGGTGGAGCAGAATTCTGG-3'
TRAV12-2*03	5'-TACAGGAAGCCTCAGCA	GGACCCCTCAGTGTTCCAGAGGG-3'
TRAV12-3*01	5'-TACAGGAAGCCTCAGCA	CAGAAGGAGGTGGAGCAGGATCCTG-3'
TRAV13-1*02	5'-TACAGGAAGCCTCAGCA	GGAGAGAATGTGGAGCAGCATCCTTC-3'
TRAV13-2*01	5'-TACAGGAAGCCTCAGCA	GGAGAGAGTGTGGGGCTGCATCTTC-3'
TRAV14/DV4*01	5'-TACAGGAAGCCTCAGCA	GCCCAGAAGATAACTCAAACCCAACCAG-3'
TRAV14/DV4*04	5'-TACAGGAAGCCTCAGCA	CAGAAGATAACTCAAACCCAACCAGGAATG-3'
TRAV16*01	5'-TACAGGAAGCCTCAGCA	GCCCAGAGAGTGACTCAGCCCGA-3'
TRAV17*01	5'-TACAGGAAGCCTCAGCA	AGTCAACAGGGAGAAGAGGATCCTCAGG-3'
TRAV18*01	5'-TACAGGAAGCCTCAGCA	GGAGACTCGGTTACCCAGACAGAAGG-3'
TRAV19*01	5'-TACAGGAAGCCTCAGCA	GCTCAGAAGGTAACTCAAGCGCAGACTG-3'
TRAV20*01	5'-TACAGGAAGCCTCAGCA	GAAGACCAGGTGACGCAGAGTCCC-3'
TRAV21*01	5'-TACAGGAAGCCTCAGCA	AAACAGGAGGTGACGCAGATTCCTGC-3'
TRAV22*01	5'-TACAGGAAGCCTCAGCA	GGAATACAAGTGGAGCAGAGTCCTCCAG-3'
TRAV23/DV6*01	5'-TACAGGAAGCCTCAGCA	CAGCAGCAGGTGAAACAAAGTCCTCA-3'
TRAV23/DV6*04	5'-TACAGGAAGCCTCAGCA	CAGCAGGTGAAACAAAGTCCTCAATCTTTG-3'
TRAV24*01	5'-TACAGGAAGCCTCAGCA	ATACTGAACGTGGAACAAAGTCCTCAGTCAC-3'
TRAV25*01	5'-TACAGGAAGCCTCAGCA	GGACAACAGGTAATGCAAATTCCTCAGTACC-3'
TRAV26-1*01	5'-TACAGGAAGCCTCAGCA	GATGCTAAGACCACCCAGCCCCC-3'
TRAV26-1*02	5'-TACAGGAAGCCTCAGCA	GATGCTAAGACCACCCAGCCCACC-3'
TRAV26-2*01	5'-TACAGGAAGCCTCAGCA	GATGCTAAGACCACACAGCCAAATTCAATG-3'
TRAV27*01	5'-TACAGGAAGCCTCAGCA	ACCCAGCTGCTGGAGCAGAGCC-3'
TRAV29/DV5*01	5'-TACAGGAAGCCTCAGCA	GACCAGCAAGTTAAGCAAAATTCACCATC-3'
TRAV30*01	5'-TACAGGAAGCCTCAGCA	CAACAACCAGTGCAGAGTCCTCAAGC-3'
TRAV34*01	5'-TACAGGAAGCCTCAGCA	AGCCAAGAACTGGAGCAGAGTCCTCAG-3'
TRAV35*01	5'-TACAGGAAGCCTCAGCA	GGTCAACAGCTGAATCAGAGTCCTCAATC-3'
TRAV36/DV7*01	5'-TACAGGAAGCCTCAGCA	GAAGACAAGGTGGTACAAAGCCCTCTATCTC-3'
TRAV36/DV7*02	5'-TACAGGAAGCCTCAGCA	GAAGACAAGGTGGTACAAAGCCCTCAATC-3'
TRAV38-1*01	5'-TACAGGAAGCCTCAGCA	GCCCAGACAGTCACTCAGTCTCAACCAG-3'
TRAV38-1*04	5'-TACAGGAAGCCTCAGCA	GCCCAGACAGTCACTCAGTCCCAGC-3'
TRAV38-2/DV8*01	5'-TACAGGAAGCCTCAGCA	GCTCAGACAGTCACTCAGTCTCAACCAGAG-3'
TRAV39*01	5'-TACAGGAAGCCTCAGCA	GAGCTGAAAGTGGAACAAAACCCTCTGTTC-3'
TRAV40*01	5'-TACAGGAAGCCTCAGCA	AGCAATTCAGTCAAGCAGACGGGC-3'
TRAV41*01	5'-TACAGGAAGCCTCAGCA	AAAAATGAAGTGGAGCAGAGTCCTCAGAAC-3'

Supplementary Table S11: single cell TCRβ cloning primers.

Vβ-gene-specific primers for cloning TCRα genes		
TRBV gene	**Signal peptide sequence**	**TRBV gene-specific sequence**
TRBV1*01	5'-CAGGAGGGCTCGGCA	GATACTGGAATTACCCAGACACCAAAATACCTG-3'
TRBV2*01	5'-CAGGAGGGCTCGGCA	GAACCTGAAGTCACCCAGACTCCCAG-3'
TRBV3-1*01	5'-CAGGAGGGCTCGGCA	GACACAGCTGTTTCCCAGACTCCAAAATAC-3'
TRBV3-2*01	5'-CAGGAGGGCTCGGCA	GACACAGCCGTTTCCCAGACTCCA-3'
TRBV4-1*01	5'-CAGGAGGGCTCGGCA	GACACTGAAGTTACCCAGACACCAAAACAC-3'
TRBV4-1*02	5'-CAGGAGGGCTCGGCA	CACCTGGTCATGGGAATGACAAATAAGAAG-3'
TRBV4-2*01	5'-CAGGAGGGCTCGGCA	GAAACGGGAGTTACGCAGACACCAAG-3'

TRBV4-3*04	5'-CAGGAGGGCTCGGCA	AAGAAGTCTTTGAAATGTGAACAACATCTGGG-3'
TRBV5-1*01	5'-CAGGAGGGCTCGGCA	AAGGCTGGAGTCACTCAAACTCCAAGATATC-3'
TRBV5-1*02	5'-CAGGAGGGCTCGGCA	AGGGCTGGGGTCACTCAAACTCC-3'
TRBV5-3*01	5'-CAGGAGGGCTCGGCA	GAGGCTGGAGTCACCCAAAGTCCC-3'
TRBV5-4*01	5'-CAGGAGGGCTCGGCA	GAGACTGGAGTCACCCAAAGTCCCAC-3'
TRBV5-4*03	5'-CAGGAGGGCTCGGCA	CAGCAAGTGACACTGAGATGCTCTTCTCAG-3'
TRBV5-4*04	5'-CAGGAGGGCTCGGCA	ACTGTGTCCTGGTACCAACAGGCCCT-3'
TRBV5-5*01	5'-CAGGAGGGCTCGGCA	GACGCTGGAGTCACCCAAAGTCC-3'
TRBV5-8*01	5'-CAGGAGGGCTCGGCA	GAGGCTGGAGTCACACAAAGTCCCAC-3'
TRBV5-8*02	5'-CAGGAGGGCTCGGCA	AGGACAGCAAGCGACTCTGAGATGC-3'
TRBV6-1*01	5'-CAGGAGGGCTCGGCA	AATGCTGGTGTCACTCAGACCCCA-3'
TRBV6-4*01	5'-CAGGAGGGCTCGGCA	ATTGCTGGGATCACCCAGGCAC-3'
TRBV6-4*02	5'-CAGGAGGGCTCGGCA	ACTGCTGGGATCACCCAGGCAC-3'
TRBV7-1*01	5'-CAGGAGGGCTCGGCA	GGTGCTGGAGTCTCCCAGTCCCTG-3'
TRBV7-2*01	5'-CAGGAGGGCTCGGCA	GGAGCTGGAGTCTCCCAGTCCCC-3'
TRBV7-2*04	5'-CAGGAGGGCTCGGCA	GGAGCTGGAGTTTCCCAGTCCCC-3'
TRBV7-3*01	5'-CAGGAGGGCTCGGCA	GGTGCTGGAGTCTCCCAGACCC-3'
TRBV7-3*05	5'-CAGGAGGGCTCGGCA	TGGGAGCTCAGGTGTGATCCAATTTC-3'
TRBV7-4*01	5'-CAGGAGGGCTCGGCA	GGTGCTGGAGTCTCCCAGTCCC-3'
TRBV7-6*01	5'-CAGGAGGGCTCGGCA	GGTGCTGGAGTCTCCCAGTCTCCC-3'
TRBV7-9*01	5'-CAGGAGGGCTCGGCA	GATACTGGAGTCTCCCAGAACCCCAG-3'
TRBV7-9*03	5'-CAGGAGGGCTCGGCA	GATACTGGAGTCTCCCAGGACCCCAG-3'
TRBV7-9*04	5'-CAGGAGGGCTCGGCA	ATATCTGGAGTCTCCCACAACCCCAGAC-3'
TRBV7-9*07	5'-CAGGAGGGCTCGGCA	CACAACCGCCTTTATTGGTACCGACAG-3'
TRBV9*01	5'-CAGGAGGGCTCGGCA	GATTCTGGAGTCACACAAACCCCAAAGC-3'
TRBV10-1*01	5'-CAGGAGGGCTCGGCA	GATGCTGAAATCACCCAGAGCCCAAG-3'
TRBV10-2*01	5'-CAGGAGGGCTCGGCA	GATGCTGGAATCACCCAGAGCCCA-3'
TRBV10-2*02	5'-CAGGAGGGCTCGGCA	AAGGCAGGTGACCTTGATGTGTCACC-3'
TRBV11-1*01	5'-CAGGAGGGCTCGGCA	GAAGCTGAAGTTGCCCAGTCCCC-3'
TRBV11-2*01	5'-CAGGAGGGCTCGGCA	GAAGCTGGAGTTGCCCAGTCTCCCAG-3'
TRBV11-3*01	5'-CAGGAGGGCTCGGCA	GAAGCTGGAGTGGTTCAGTCTCCCAGA-3'
TRBV11-3*03	5'-CAGGAGGGCTCGGCA	GGTCTCCCAGATATAAGATTATAGAGAAGAAACAGC-3'
TRBV12-1*01	5'-CAGGAGGGCTCGGCA	GATGCTGGTGTTATCCAGTCACCCAGG-3'
TRBV12-2*01	5'-CAGGAGGGCTCGGCA	GATGCTGGCATTATCCAGTCACCCAAG-3'
TRBV12-3*01	5'-CAGGAGGGCTCGGCA	GATGCTGGAGTTATCCAGTCACCCC-3'
TRBV12-5*01	5'-CAGGAGGGCTCGGCA	GATGCTAGAGTCACCCAGACACCAAGG-3'
TRBV13*01	5'-CAGGAGGGCTCGGCA	GCTGCTGGAGTCATCCAGTCCCC-3'
TRBV14*01	5'-CAGGAGGGCTCGGCA	GAAGCTGGAGTTACTCAGTTCCCCAGC-3'
TRBV15*01	5'-CAGGAGGGCTCGGCA	GATGCCATGGTCATCCAGAACCCAAG-3'
TRBV16*01	5'-CAGGAGGGCTCGGCA	GGTGAAGAAGTCGCCCAGACTCCA-3'
TRBV17*01	5'-CAGGAGGGCTCGGCA	GAGCCTGGAGTCAGCCAGACCC-3'
TRBV18*01	5'-CAGGAGGGCTCGGCA	AATGCCGGCGTCATGCAGAAC-3'
TRBV19*01	5'-CAGGAGGGCTCGGCA	GATGGTGGAATCACTCAGTCCCCAAAG-3'
TRBV20-1*01	5'-CAGGAGGGCTCGGCA	GGTGCTGTCGTCTCTCAACATCCGAG-3'
TRBV20/OR9-2*01	5'-CAGGAGGGCTCGGCA	AGTGCTGTCGTCTCTCAACATCCGAG-3'
TRBV21-1*01	5'-CAGGAGGGCTCGGCA	GACACCAAGGTCACCCAGAGACCTAGAC-3'

TRBV21/OR9-2*01	5'-CAGGAGGGCTCGGCA	GACACCAAGGTCACCCAGAGACCTAGATTTC-3'
TRBV23-1*01	5'-CAGGAGGGCTCGGCA	CATGCCAAAGTCACACAGACTCCAGG-3'
TRBV24-1*01	5'-CAGGAGGGCTCGGCA	GATGCTGATGTTACCCAGACCCCAAG-3'
TRBV25-1*01	5'-CAGGAGGGCTCGGCA	GAAGCTGACATCTACCAGACCCCAAGATAC-3'
TRBV26*01	5'-CAGGAGGGCTCGGCA	GATGCTGTAGTTACACAATTCCCAAGACACAG-3'
TRBV26/OR9-2*01	5'-CAGGAGGGCTCGGCA	GATGCTGTAGTTACACAATTCTCAAGACACAGAATC-3'
TRBV27*01	5'-CAGGAGGGCTCGGCA	GAAGCCCAAGTGACCCAGAACCC-3'
TRBV28*01	5'-CAGGAGGGCTCGGCA	GATGTGAAAGTAACCCAGAGCTCGAGATATC-3'
TRBV29-1*01	5'-CAGGAGGGCTCGGCA	AGTGCTGTCATCTCTCAAAAGCCAAGC-3'
TRBV29-1*03	5'-CAGGAGGGCTCGGCA	ACGATCCAGTGTCAAGTCGATAGCCAAG-3'
TRBV30*01	5'-CAGGAGGGCTCGGCA	TCTCAGACTATTCATCAATGGCCAGCG-3'
TRBV30*04	5'-CAGGAGGGCTCGGCA	ACTATTCATCAATGGCCAGCGACCC-3'

Supplementary Patient Information

	Patient #1	Patient #2	Patient #3
irRECIST	Partial Response	Partial Response	Partial Response
Study	Merck MK-3475-001	Merck MK-3475-001	Merck MK-3475-001
Age at Tx start	61	70	70
Sex	M	M	M
ECOG Status at Baseline	0	0	0
Disease Status at Baseline	M1c	M1b	M1c
BRAF/NRAS	BRAF V600E	NRAS G13D	NRAS Q61K
Melanoma Sub-Type	Cutaneous	Cutaneous	Cutaneous
HLA Type	HLA-A*02:01, HLA-A*68:01 HLA-B*15:07, HLA-B*44:02 HLA-C*03:03, HLA-C*07:04	HLA-A*02:01, HLA-A*24:02 HLA-B*51:01, HLA-B*58:01 HLA-C*01:02, HLA-C*03:02	HLA-A*02:01, HLA-A*03:01 HLA-B*07:02, HLA-B*51:01 HLA-C*02:02, HLA-C*07:02
Prior Systemic Therapies	1. Vemurafenib 2. Ipilimumab 3. Chemotherapy+IL-2 4. TIL adoptive cell transfer	1. Adjuvant GM-CSF	1. Ipilimumab
Date of first evidence of tumor regression	Day 166	Day 134	Day 87
Date of first irRECIST Response (-50%)	Day 250	Day 280	Day 186
Site of Baseline Biopsy	Left Chestwall	Subclavicular Lymph Node	Right Chestwall
Date of Baseline Biopsy for Exome/RNA-seq	Day -28	Day -11	Day -29

# Somatic Nonsynonymous Mutations	350	745	660
Date of Biopsy for TIL collection	Day 187	Day 23	Day -29
Date of PBMCs Sampled	Day 41, Day 166, Day 187, Day 208, Day 439	N/A	Day 25, Day 87

Chapter 7:

Conclusion and Future Directions

In the preceding chapters, we presented a series of studies that sought to identify mechanisms and biomarkers of resistance to anti-PD1 therapy. We did this by exploring mutational changes in melanoma lesions previously responsive to therapy, as well as by examining differences in baseline genomic or transcriptomic characteristics in tumor biopsies from patients with differential response. The description of selection for JAK1/2 or B2M mutations in the acquired resistance setting and the definition of the IPRES signature were some of the first resistance-associated biology reported out of the PD1 clinical trials. However, many questions remain.

Frequency and sufficiency of interferon insensitivity as a path to resistance

Though the JAK1/2 mutations (or more generally interferon insensitivity) were seen in two early cases with a carefully selected clinical course of acquired resistance, none were seen in 10 further cases of late progression (data not shown), and they exist at relatively low frequency in large melanoma datasets from the pre-anti-PD1 era, as seen in chapter 3. How often will tumors become resistant by this mechanism? Furthermore, though the clinical presentation was suggestive, proof that interferon insensitivity is *sufficient* for immune resistance was lacking, as JAK mutation could have been accompanied by other mutations or immune system dynamics not initially appreciated.

Subsequent publications from other groups fill some of these gaps and support the importance of interferon resistance in tumor-immune resistance. First, IFNGR1 knockout (KO) in B16 melanoma cells conferred a degree of primary resistance to anti-CTLA4 therapy [1]. Similarly a competitive screen with pooled CRISPR libraries, also in a B16 model, showed that hits to key signaling components in the interferon pathway (STAT1, JAK1/2, IFNGR1/2) were enriched in resistant tumors following anti-PD1+vaccine combination therapy and knockout of these genes individually led to primary resistance as well [2]. Finally, a very recent study also identified JAK1/2 homozygous loss-of-function mutations in 4/47 cell lines, all four of which were derived after exposure to older immunotherapies (IL2, IFNa, DC vaccine) [3]. Some pre-immunotherapy cell lines from the same patient lacked the JAK mutation, and intriguingly this group presented evidence that loss-of-heterozygosity (LOH) of the wild-type allele occurred first, and the JAK mutation arose later in the single remaining copy. 75% of their cell lines had LOH at chr 9p (the JAK2 locus), as did 68% of our patient-derived biopsy panel, suggesting a large number of melanomas may be at risk. This is in contrast to 10% and 16%, respectively at the JAK1 locus on chromosome 1. p16/CDKN2A is also on chr 9p, 17Mb away from JAK2, and there may be a synergistic selective pressure for LOH at that locus, as it would potentiate the 2-hit loss of both this traditional tumor-suppressor as well as the JAK2 “immune-related tumor suppressor”.

Direct mechanistic connection between interferon insensitivity or IPRES signature and immune resistance or escape. While the lack of growth arrest was suggestive, interferon gamma upregulates hundreds of downstream genes genes [4]. Which of these are necessary for tumor control remains to be elucidated, and many may be involved in indirect or surprising ways. Experiments to identify downstream genes that phenocopy JAK loss in immunotherapy resistance might be a fruitful avenue for future research.

The IPRES signature, and epithelial-to-mesenchymal transition in particular, continues to be associated with poor immunotherapy response/survival in further studies [5], but as an amalgam of possibly disparate biological processes (EMT, angiogenesis, macrophage chemotaxis, etc), presents an even more complex scenario for determining the direct affect on T-cell activity.

T-cell focused considerations

While both interferon resistance and the IPRES signature are primarily defined in the tumor compartment (though IPRES may incorporate features of the microenvironment), mechanisms focused on T-cell activity were not addressed by this work. The role of other immune suppressive cells (tumor-associated macrophages, Tregs), metabolism in the tumor microenvironment (IDO1/tryptophan, adenosine), and other checkpoint signals also remain attractive explanations for resistance [6].

Similarly we focused on resistance in the setting of an anti-tumor immune response, but lack of an initial productive immune response may play a large role in primary resistance. Absence of T-cells at the tumor margin is a poor prognostic factor [7], but reasons for this were also not addressed in this work. Lack of good tumor antigens is one explanation, but may be less likely in melanoma where we noted a poor correlation with anti-PD1 response and mutational load in chapters 4 and 5. A second and rising hypothesis for absence of a T-cell response is a lack of tumor-associated dendritic cells and/or co-stimulation [8-10].

Finally, in almost all cases we've studied of response and late progression, T-cells have been found in abundance at the tumor margin. Significant questions remain regarding these T-cells, including whether they are still tumor-antigen specific, and their exact phenotype (memory vs terminal effectors, active vs exhausted). The technology described in chapter 5 can provide the tools help address antigen specificity, while dissociation of fresh biopsies into single cell suspensions with high dimensional mass-cytometry or single-cell RNA-seq [11] of TILs may help address phenotype questions.

Possible Interventions

The ultimate goal in understanding mechanisms of resistance is to find a way to overcome it. Several strategies warrant further investigation. While B2M and HLA loss have long been known or suspected as a route to resistance, the precise reason for failure of NK-cell surveillance is unknown, but strategies to reverse it remain attractive.

Tumors that have become insensitive to interferon, especially at the receptor/kinase level, may benefit from interferon-independent activation of downstream genes. Alternatively, interferon insensitivity may open unanticipated synergies. For example oncolytic viral therapy may be more effective without the anti-viral activity of interferon-response genes and reactive PD-L1 expression. The fact that interferon insensitive cancer cells could still by killed in short term in-vitro co-culture T-cells was also an intriguing result. One possible explanation is that killing is perforin/granzyme mediated early in an immune response, but interferon becomes important to tumor control *in-vivo* when local T-cell count or activation strength is low (i.e. with chronic exhaustion/equilibrium). Methods to alter T-cell dose/activation to restore or favor perforin/granzyme mediated killing might therefore be an attractive avenue warranting further study.

References

1. Gao, J, LZ Shi, H Zhao, et al. 2016. Loss of IFN-γ Pathway Genes in Tumor Cells as a Mechanism of Resistance to Anti-CTLA-4 Therapy. *Cell* 167: 397–404.e9.

2. Mangruso RT, Pope HW, Zimmer MD, et al. In vivo CRISPR screening identifieds Ptpn2 as a target for cancer immunotherapy. AACR Annual Meeting 2017 Abstratct #1019

3. Sucker, A, F Zhao, N Pieper, et al. 2017. Acquired IFNγ Resistance Impairs Anti-Tumor Immunity and Gives Rise to T-Cell-Resistant Melanoma Lesions. *Nat Commun* 8: 15440.

4. Schneider, WM, MD Chevillotte, and CM Rice. 2014. Interferon-Stimulated Genes: a Complex Web of Host Defenses. *Annu Rev Immunol* 32: 513–45.

5. Shields, BD, F Mahmoud, EM Taylor, et al. 2017. Indicators of Responsiveness to Immune Checkpoint Inhibitors. *Sci Rep* 7: 807.

6. Sharma, P, S Hu-Lieskovan, JA Wargo, and A Ribas. 2017. Primary, Adaptive, and Acquired Resistance to Cancer Immunotherapy. *Cell* 168: 707–23.

7. Tumeh, PC, CL Harview, JH Yearley, et al. 2014. PD-1 Blockade Induces Responses by Inhibiting Adaptive Immune Resistance. *Nature* 515: 568–71.

8. Spranger S, Bao R, Gajewski TF. Melanoma-intrinsic β-catenin signalling prevents anti-tumour immunity.. *Nature* 2015; **523**:231–5.

9. Homet MB, Zaretsky JM, Garcia-Diaz A, et al.. Response to Programmed Cell Death-1 Blockade in a Murine Melanoma Syngeneic Model Requires Costimulation, CD4, and CD8 T Cells.. *Cancer Immunol Res* 2016; **4**:845–857.

10. Kamphorst AO, Wieland A, Nasti T*, et al.*. Rescue of exhausted CD8 T cells by PD-1-targeted therapies is CD28-dependent.. *Science* 2017; **355**:1423–1427.

11. Singer, M, C Wang, L Cong, et al. 2016. A Distinct Gene Module for Dysfunction

Uncoupled from Activation in Tumor-Infiltrating T Cells. *Cell* 166: 1500–1511.e9.